Investigation of Doped Graphene Properties using Density Functional Theory and its Applications in Gas Sensing

THESIS

Submitted in partial fulfilment
of the requirements for the degree of
DOCTOR OF PHILOSOPHY

by

SEBA SARA VARGHESE

Under the Supervision of

Prof. Sundaram Swaminathan

&

Prof. K. K. Singh

BIRLA INSTITUTE OF TECHNOLOGY AND SCIENCE, PILANI

2017

BIRLA INSTITUTE OF TECHNOLOGY AND SCIENCE, PILANI

CERTIFICATE

This is to certify that the thesis entitled **Investigation of Doped Graphene Properties using Density Functional Theory and its Applications in Gas Sensing** and submitted by **SEBA SARA VARGHESE** ID No **2012PHXF001U** for award of Ph.D. of the Institute embodies original work done by him/her under my supervision.

Signature of the Supervisor:

Name in capital letters: SUNDARAM SWAMINATHAN

Designation: Pro Vice Chancellor, DIT University, Dehradun, India

Signature of the Co-Supervisor:

Name in capital letters: K K SINGH

Designation: Professor, Department of Physics, BITS, Pilani-Dubai Campus

Date:

ACKNOWLEDGEMENTS

First of all, I would like to thank God Almighty for giving me the opportunity, knowledge, and strength to complete the research work successfully. I take this opportunity to thank all those who have supported me during the pursuit of my Ph.D. degree.

I express my deepest gratitude and sincere thanks to my supervisors, Dr. Sundaram Swaminathan (Pro Vice Chancellor, DIT University, Dehradun, India) and Dr. K. K. Singh (Professor, BITS, Pilani-Dubai Campus) for their heartfelt support, guidance and advice, valuable suggestions and inspiration throughout my Ph.D. work. I also extend my appreciation to my Doctoral Advisory Committee members, Dr. Anand Kumar (Professor, BITS, Pilani-Dubai Campus and Dr. Abdul Razak (Assistant Professor, BITS, Pilani-Dubai Campus) for their great comments. I would also like to thank Dr. Neeru Sood (Associate Dean-Academic Research Division, BITS, Pilani-Dubai Campus) for her constant support and encouragement. I am also grateful to Prof. R. N. Saha (Director, BITS, Pilani-Dubai Campus).

I have great pleasure in acknowledging my gratitude to Dr. Vikas Mittal (Associate Professor, The Petroleum Institute, Abu Dhabi) and Dr. Ahmed Abdala (Senior Scientist, Qatar Environment and Energy Research Institute, Qatar) for their support of the research. I also extend my deep appreciation to Dr. Ortwin Leenaerts (Post-Doc Researcher, Condensed Matter Theory Group, University of Antwerp, Belgium) for clarifying my doubts in ABINIT coding. I greatly appreciate all my former teachers for the help and support that they had given me.

I am also pleased to acknowledge my fellow research scholars at BITS, Pilani-Dubai Campus and my colleagues at the Petroleum Institute for their friendship, and assistance. I am deeply indebted to my family for their spiritual and financial support throughout the Ph.D. program. I have no suitable words to thank my husband, who helped me in software installation, error debugging and in other computer related problems. My special thanks to my father, mother and sister for their love, and support that have given me the courage to face all the challenges that arose in the pursuit of my Ph.D. degree. I express my sincere gratitude to my parents-in-law for their interest in the research that I was doing. I also wish to express heartfelt thanks to my niece who made my leisure time enjoyable.

Seba Sara Varghese

2012PHXF001U

ABSTRACT

Detection of gas molecules has received great attention in various fields and using graphene-based materials for gas sensing applications is one of the hot topics of research in solid state gas sensor technology. Due to its superior properties, such as high surface area, thermo-electric conduction, and mechanical strength, graphene materials have inspired huge interest in sensing of various gaseous species. Previous researches had shown that intrinsic graphene can only physisorb most of the gases. As the low sensitivity of intrinsic graphene prevents its use as gas sensors, studies have centered on approaches for enhancing the sensitivity of graphene by suitable modifications. Many theoretical and several experimental works had demonstrated that the sensitivity of graphene for gases could be remarkably improved by introducing appropriate dopants into the graphene lattice.

The purpose of this work is to gain a deep understanding of the effect of gas molecular adsorbates on the structural and electronic properties of intrinsic and different heteroatom-doped graphene sheets for analyzing the effect of different dopants on the gas sensing properties of graphene and thus for fully exploiting the potential of graphene in making gas sensors. In this thesis, the interactions between the graphene surfaces and adsorbate molecules are simulated using first-principles density functional theory calculations implemented in the ABINIT code using planewave basis and pseudopotentials. The adsorptions of single molecule of gases (*i.e.* the lowest level of target gas species) on the graphene surfaces are studied for evaluating the ultimate sensitivity of the considered graphene sheets. The doping effects on the reactivity of graphene towards several gas molecules are examined by analysing the adsorption energies, charge density distribution, electronic band structure and density of states of graphene-gas molecule adsorption systems. The sensitivity of the doped graphene sheets for gas molecules are predicted from the comparison of the structural and electronic properties of the doped graphene sheets before and after gas adsorption. To validate the work, the obtained results are compared with previously reported theoretical results.

The adsorptions of small gas molecules (CO, NO, NO_2 and H_2O) on group III (B, Al and Ga) doped graphene are simulated for enabling their applications as toxic gas sensing materials in the presence of water vapour. The results show that CO, NO and NO_2 can be electrically detected using Al- and Ga-doped graphene-based sensors, but the presence of water vapour basically limit their practical applications as efficient toxic-gas sensing materials. The structural and electronic properties of Ga-doped graphene are also found to be sensitive to

molecular oxygen present in air and hence strongly affect its sensitivity to other toxic gas molecules. The calculations also indicate that B-doped graphene can be used as an excellent gas sensing platform for detecting NO and NO_2 even in the atmosphere with water vapour.

The adsorption studies of H_2S on intrinsic, P- and S-doped graphene showed physisorption of H_2S on these graphene sheets with small adsorption energies, long binding distances and negligible charge transfers. The structural and electronic properties of intrinsic graphene, P- and S-doped graphene are found to be insensitive to the adsorption of H_2S, which suggests that intrinsic graphene, P- and S-doped graphene are not suitable for the detection of H_2S gas. From the first-principles simulations on the interaction of N_2O with intrinsic, B-, N-, Si-, P-, Ga-, Cr- and Mn-doped graphene sheets, it was found that intrinsic, B-, N-, Si- and P-doped graphene are not sensitive to the presence of N_2O molecule, whereas strong interactions exist between N_2O and Ga-dopant. The chemisorption of N_2O on Cr- and Mn-doped graphene was evident from analysis of structural, energetic and electronic properties of these doped graphenes with and without adsorbed N_2O molecule. The calculations predict the applicability of Cr- and Mn-doped graphene as novel sensors for N_2O detection.

Theoretical investigation of the structural, energetic and electronic properties of graphene doped by boron and nitrogen with different concentrations showed that band gap increases with increase in dopant concentration, whereas the energetic stability of the doped structures decreases with the increase in the dopant concentration. It was also observed that both the band gaps and the cohesive energies also depend on the atomic configurations considered for the substitutional dopant atoms. N-doped graphene structures are considered to be more stable than their B-doped counterparts. The electronic band structures of B- and N-doped graphene structures are also found to be strongly influenced by the positioning of the dopant atoms in the graphene lattice. For all the dopant concentrations considered, the structures with the dopant atoms at alternate sublattices of graphene have been found to have the lowest cohesive energies and therefore form the most stable structures. These results would open up an interesting way for tuning the band gap of graphene using B and N dopants according to the choice of the supercell *i.e.* the dopant density and substitutional dopant sites, which could be useful in the designing future graphene-based nanoelectronic devices.

TABLE OF CONTENTS

LIST OF TABLES

LIST OF FIGURES

LIST OF ABBREVIATIONS

0D	Zero-dimensional
1D	One-dimensional
2D	Two-dimensional
2SG	2Sulphur doped graphene
3D	Three-dimensional
ac-DEP	alternating current dielectrophoresis
AdU	Adsorption units
AG	Aluminium doped graphene
AgG	Silver doped graphene
AGNRs	Armchair graphene nanoribbons
Ag-S-RGO	Silver nanoparticle-decorated-sulfonated reduced-
AuG	Gold doped graphene
B.E.	Binding energy
BFGS	Broyden-Fletcher-Goldfard-Shanno
BG	Boron doped graphene
BVG	Boron doped vacancy-defected graphene
BZ	Brillouin zone
CaG	Calcium doped graphene
CG	Chromium doped graphene
CH	Cysteamine hydrochloride
CNT	Carbon nanotube
CoG	Cobalt doped graphene
Co-SWG	Cobalt doped Stone–Wales defected graphene
C-PANI	Graphene/PANI nanocomposite
Cr-SWG	Chromium doped Stone–Wales defected graphene

CTAB	Cetyltrimethyl ammonium bromide
CVD	Chemical vapour deposition
DB	Dangling bond
det	Determinant
DFT	Density functional theory
DG	Defective graphene
DL	Detection limit
DMMP	Dimethyl methyl phosphonate
DNA	Deoxyribonucleic acid
DNT	2, 4-dinitrotoluene
DOS	Density of states
E_{ad}	Adsorption energy
FeG	Iron doped graphene
FEM	Finite element method
FET	Field-effect transistor
FFT	Fast Fourier transformations
FGS	Functionalized graphene sheets
FLG	Few-layer graphene
GG	Gallium doped graphene
GGA	Generalized gradient approximation
GNR	Graphene nanoribbon
GO	Graphene oxide
G-paper	Graphene-paper
GPL	General public license
	graphene oxide

HCN	Hydrogen cyanide
HEAGNR	Armchair graphene nanoribbons with hydrogenated edges
HK	Hohenberg-Kohn
HOPGr	Highly oriented pyrolytic graphite
IDEs	Interdigitated electrodes
IG	Intrinsic graphene
IL	Ionic liquid
IR	Infrared
K-S	Kohn-Sham
LDA	Local density approximation
LPE	Liquid-phase-exfoliated
LPG	Liquefied petroleum gas
MG	Manganese doped graphene
Mn-SWG	Manganese doped Stone–Wales defected graphene
MP	Monkhorst-Pack
MP2	Second order Møller–Plesset
MWCNT	Multi-walled carbon nanotube
NCPP	Norm-conserving pseudopotential
NCs	Nanocrystals
NFE	Nearly free electron
NG	Nitrogen doped graphene
NNTB	Nearest neighbour tight-binding
NP	Nanoparticle
NVG	Nitrogen doped vacancy-defected graphene
NW	Nanowire

ORR	Oxygen reduction reaction
OTFT	Organic thin film transistor
P3HT	Poly (3-hexylthiophone)
PANI	Polyaniline
PBE	Perdew-Burke-Ernzerhof
PdG	Palladium doped graphene
PDMS	Polydimethylsiloxane
PEDOT	Poly (3, 4-ethylenedioxythiophene)
PEDOT:PSS	Poly(3,4-ethylenedioxythiophene):poly(styrene sulfonate)
PEI	Polyethylenimine
PET	Polyethylene terephthalate
PG	Phosphorus doped graphene
P-GNS	Phosphorus doped graphene nanosheets
PI	Polyimide
PMMA	Polymethyl methacrylate
p-PACA	p-phosphonic acid calix[8]arene
ppb	parts per billion
PPD	p-phenylenediamine
ppq	parts per quadrillion
ppt	parts per trillion
PtG	Platinum doped graphene
QDs	Quantum dots
QM	Quantum mechanical
RGO	Reduced graphene oxide
RGO-A	Reduced graphene oxide reduced from aniline

RGO-H	Reduced graphene oxide reduced from hydrazine
RGO–IDTO	Indium doped tin dioxide-reduced graphene oxide
RGO-PANI	Reduced graphene oxide reduced from polyaniline
RH	Relative humidity
RhB	Rhodamine B
RT	Room temperature
s/n	Signal-to-noise ratio
SAW	Surface acoustic wave
SEM	Scanning electron microscope
SG	Sulphur doped graphene
SiC	Silicon carbide
SiG	Silicon doped graphene
SLG	Single-layer graphene
SPR	Surface plasmon resonance
SVG	Sulphur doped vacancy-defected graphene
SW	Stone–Wales
TA	Tannic acid
TiG	Titanium doped graphene
TM	Transition metal
TNT	Trinitrotoluene
USPP	Ultrasoft pseudopotential
UV	Ultraviolet
VG	Vacancy-defected graphene
VOC	Volatile organic compound
XC	Exchange correlation

XG	Doped graphene
ZnG	Zinc doped graphene
ΔQ	Charge transfer

LIST OF SYMBOLS

b_{BZ}	Side of the Brillouin zone
C_A and C_B	Weights
H_{ij}	Matrix elements of the Hamiltonian
R_{90}	Operator for the clockwise rotation of the vector by 90°
S_{ij}	Overlap matrix elements between Bloch functions
a_1 and a_2	Primitive vectors of the direct lattice
b_1, b_2 and b_3	Primitive vectors of the reciprocal lattice
s_0	Overlap integral
∇	Del operator
A	Area of Brillouin zone
$a_{C\text{-}C}$	Carbon-carbon bond length
d	Equilibrium graphene-gas molecule distance
e	Electron
E_F	Fermi energy
G	Conductance
$\hbar$	Reduced Planck's constant
I	Current
k	Wavevector
m or m_e	Mass of electron
M_I	Mass of the nuclei
R	Position vector
T	Kinetic energy
t	processing time
U or V	Potential Energy

v_F	Fermi velocity
V_g	Gate voltage
V_{pp}	peak-to-peak voltage
V_{th}	Threshold voltage
ψ	Wavefunction
Z	Impedence
Z_I	Nuclear charge (atomic number) of the nuclei
β_g	Material constant
γ	Fitting parameter
δ_{ij}	Kronecker delta function
π	Valence
π^*	Conduction
Ω	Entire space occupied by the lattice
H	Hamiltonian operator
S	Size vector
a	Primitive lattice constant
$g(E)$	Density of states
Φ	Atomic orbitals
ρ	Density

CHAPTER 1

INTRODUCTION

1.1 Overview

Graphene, a one-atom-thick two-dimensional material has grabbed immense research and industrial interest since its first isolation in 2004 [1] due to its extraordinary electronic, chemical, mechanical, thermal and optical properties [2-11]. Graphene-based materials have already demonstrated their applicability in fields like energy storage, electronics, field emission, photovoltaics, catalysis, biomedicine etc. [12-19]. The utilization of graphene as an ultrasensitive sensing element has emerged as one of the most promising applications of graphene [20]. It has extremely high specific surface area (theoretical value close to 2630 m^2/g, about 300 times higher than graphite and two times higher than single-walled carbon nanotubes) and has unique electrical properties such as high electrical conductivity and exceptionally low electronic noise, which makes it ideal for sensing applications [21-29]. Graphene-based nanostructures have proven to possess tremendous potential for fabricating various types of sensors [27]. Wide range of chemicals, biomolecules and gas/vapours has been detected using graphene-based sensors [19, 21-29].

There has been an increasing demand for highly sensitive gas sensors across diverse areas of applications including the agriculture and food industry, biotechnology, medicine, environmental control, industrial production, indoor air quality, homeland security, automobiles etc. The two-dimensional crystal structure of graphene makes it extremely sensitive to gas adsorbates, and thus the electronic properties of graphene are strongly modified by the adsorption of gas species on its surface [30]. Graphene-based gas sensors can detect extremely small concentration of gases present in the environment by measuring the change in graphene's electrical conductivity, caused by the change in carrier concentration of graphene induced by the adsorbed gas molecules, which act as either electron donors or acceptors. The potential of using graphene as an ultrasensitive gas sensor has been experimentally demonstrated by Schedin *et al.* with detection limit of the order of 1 part per billion (ppb) for NO_2, H_2O, NH_3 and CO [30]. The ultimate sensitivity of a single molecule was reported for NO_2 [30].

Graphene-based gas sensors have already demonstrated to have the highest sensitivities and lowest detection limits compared to sensors based on one-dimensional semiconductor nanowires and carbon nanotubes [31]. To use graphene as a super sensitive gas sensing

material, it is very important to understand the interactions between gas molecular adsorbates and graphene surface. Previous theoretical studies on intrinsic graphene (IG) predicted low adsorption energies of gas molecules on the graphene surface [32-34], and hence IG could not meet the essential requirements of gas sensing applications [35]. Graphene could be accidently or deliberately doped with non-carbon elements [36]. It has been shown that the sensitivity of graphene for gases can be enhanced to a higher level by the method of doping [35-59] or by introducing defects into the graphene lattice [36, 41, 60] or by the combination of dopant and defects [61-63].

Many quantum mechanical based simulation studies have investigated the adsorption of gas molecules on intrinsic and heteroatom-doped graphene to analyze the effect of dopant atoms on the interactions between graphene and gas molecules. These works showed that heteroatom doping improves the interactions of gas molecules with graphene and predicted that graphene modified with appropriate dopant atoms can be used as good sensing materials for the detection of various gas species with sensitivity down to single molecule level [35-59]. Still a lot of research needs to be done in this regime, to fully exploit the potential of graphene as highly sensitive gas sensor materials. Continued efforts in identifying suitable doping on graphene for enhanced chemical reactivity to gas molecular adsorbates are beneficial for the realization of highly efficient gas sensors based on graphene in industrial, environmental and medical applications.

Graphene has also attracted the attention of researchers from both experimental and theoretical point of view for electronic applications. The unique physical properties of graphene such as ambipolar electric field effect [1, 5], high charge carrier mobility [64], quantum Hall effect [3, 65] and ballistic electron transport at room temperature [66] derived from its peculiar electronic structure, make it an ideal candidate for future nanoelectronics by overcoming the limitations of silicon-based electronics [67]. The unusual semimetallic nature of graphene with zero band gap at the Dirac point, is unfavourable for its application in various nanoelectronic and energy-related devices [9]. Even though there exist several methods for opening the zero band gap in graphene [68-71], heteroatom doping has proved to be effective in improving the semiconducting properties of graphene as the dopant atom modifies its electronic band structure and opens up an energy band gap between the valence and conduction bands [72-80]. Substitutional doping of graphene with boron (B) and nitrogen (N) atoms has been the subject of many experimental and theoretical researches [72-75, 77-84], since these elements being the nearest neighbours of carbon in the periodic table provide strong probability of entering the graphene lattice and can make *p*-type and *n*-type

semiconducting graphene, which allows for the fabrication of contemporary devices in next generation of graphene-based electronics [77-79, 81]. In order to use graphene vastly in electronics, it is extremely important to understand the electronic structures of graphene doped with B and N atoms.

1.2 Objectives and Scope of the Thesis

The main objective of this thesis is to gain deeper understanding of the effect of gas adsorbates on the structural and electronic properties of different graphenes, and how these effects could be utilized for designing highly sensitive gas sensing devices. Different graphenes considered in the work include intrinsic and heteroatom-doped graphene. The sensitivity of the doped graphene sheets towards several gas molecules are evaluated from the analysis of the structural and electronic properties of graphenes before and after gas molecular adsorption. The effect of doping on the structural and electronic properties of graphene upon interaction with gas molecules are explored by studying the adsorption energies, charge density distribution, band structure and density of states of graphene-gas molecule adsorption systems. The interactions between several gas molecules and intrinsic or heteroatom-doped graphene sheets have been investigated using first-principles approach based on density functional theory. All geometry optimizations, total energy calculations and electronic structure calculations are carried out within the Abinit code using planewave basis and pseudopotentials.

Motivated by the single molecule detection of NO_2 by IG, the interaction of individual gas molecules with various graphene sheets are studied to evaluate their ultimate sensitivity (sensitivity to a single molecule, which corresponds to the lowest level of target gas species). The ultimate sensitivity of various graphene sheets towards several gas species are analyzed using *ab initio* quantum mechanical based theoretical computations.

The most favourable adsorption configurations, adsorption energies, and the distance of the gas molecules from the graphene sheets are calculated to understand the nature of interactions. Understanding the mechanisms involved in adsorption of gas molecules on graphene's surface are of great significance in developing graphene-based gas sensors. The adsorption mechanisms are also discussed from the analysis of charge transfers, electronic band structures and electronic density of states (DOS). The changes in the electronic structures of graphenes caused by the physi- or chemi-sorption of gas molecules on graphene's surface are determined from charge distribution analysis and band structure plots. The effect of the adsorbed gas molecules on the electronic conductivity of graphenes can be

predicted from the DOS of graphene-gas molecule adsorption systems. The properties such as adsorption energies of gas molecules on graphene surfaces, charge transfers between gas molecules and graphenes, band structure and DOS plots are obtained from the simulated gas molecule-graphene adsorption systems.

The effect of various dopant atoms on the gas sensing properties of graphene are analyzed to identify appropriate dopants on graphene that can lead to high sensitivity detection of particular gas species down to single molecule level. The results from these calculations help us to understand the processes involved in the sensing mechanisms, before going for expensive device fabrication. The predictions from quantum mechanical simulations can stimulate interest in experimental works on suitable modification of graphene for achieving improved sensing response towards gas molecules. The results of these studies serve as a basis for designing highly sensitive sensors for practical gas detection applications. These results can provide new insights to support the development of new and improved sensors for gas detection and removal.

Considering the significance of B and N doping in graphene for applications in nanoelectronic devices, the energetic stabilities, structural properties and electronic band structures of B and N substitutional dopants in graphene are also investigated. The dependence of the energetic stability and band gaps in graphene on B- and N- dopant concentrations and dopant configurations has been systematically studied. The results from the calculations provide the opportunity for tailoring the band gap as required and thus could be employed for the design of doped graphene for electronic applications.

To summarize, the objectives of this thesis are as follows:

1. To investigate the structural and electronic properties of various graphene sheets.
2. To understand the interactions of several gas molecules with different graphenes and to explore the effects of the dopant atoms on the interactions between graphene surface and gas molecules
3. To investigate the change in the electronic properties of graphenes caused by the physi- or chemi-sorption of gas molecules.
4. To identify appropriate dopants on graphene that can drastically improve the sensitivity of graphene towards several gas molecules and to predict the applicability of different doped graphenes as sensitive sensing materials for gas detection or removal.

The scope of the thesis involves the investigation of the structural and electronic properties of intrinsic and different heteroatom-doped graphenes such as B-, N-, Al-, Si-, P-, S-, Ga-, Cr- and Mn-doped graphene. The thesis covers the interactions of individual molecules of CO, NO, NO_2, H_2O, O_2, H_2S and N_2O with several doped graphenes.

1.3 Organization of the Thesis

The thesis is organized as follows: Chapter 2 basically discusses the literature review. Chapter 2 is divided into seven sections and starts with a very short introduction to gas sensors and nanotechnology-enabled gas sensors. The first section briefly discusses about the most widely used preparation methods, some properties and exciting applications of graphene-based materials. The second section presents the features of graphene that are useful for its sensing behaviour. The advantages of graphene-based gas sensors over carbon nanotube- and semiconductor-based gas sensors are summarized in the third section. The recent advancements in the field of graphene-based gas sensors with emphasis on the use of modified graphene materials are described in detail in the fourth and fifth sections. The fourth section discusses the applications of intrinsic and modified graphene materials in gas sensing applications. Various graphene modification methods including use of dopants, decoration with metal/metal oxide nanoparticles, and functionalization with polymers are considered. Further, insights of experimental aspects associated with such systems are discussed in fourth section with significance on the sensitivity and selectivity of graphene towards various gas molecules. The fifth section extensively discusses theoretical studies of gas molecule adsorption on intrinsic graphene, graphene nanoribbon, graphene oxide and reduced graphene oxide. The fifth section also focuses on theoretical studies that discuss the structural improvisations of graphene for its effective use as gas sensing materials. The sixth section discusses the identified research gaps from the literature. Chapter 2 concludes with the statement of research problem.

Chapter 3 mainly deals with the physical structure and properties specifically the most important electronic properties of graphene and is divided into three sections. The first section discusses about various allotropes of carbon and then slowly moves onto graphene and its crystal lattice. The second part gives a detailed description of the structural properties of graphene by discussing on the nature of bonding in graphene, direct and reciprocal lattices of graphene. The electronic properties of intrinsic graphene such as its electronic band structure and density of states are described in detail in the third section. Other peculiar features of graphene such as linear energy-momentum dispersion at the Dirac points and the ambipolar electric field effect of intrinsic graphene are also presented briefly.

Chapter 4 describes the computational method employed to perform the calculations discussed in the rest of the chapters. This chapter is divided into three sections, in which the first section discusses about computational material science and the methods used in material science modeling. The second section discusses about the solutions of the Schrödinger equation for many-body systems and the Born-Oppenheimer approximation for enabling practical application. The density functional theory (DFT) formalism used in this work is explained in detail in the third section. The Hohenberg-Kohn theorems underlying the DFT calculation scheme and the Kohn-Sham approach are also discussed. The practical implementation of the DFT formalism is described here. The chapter concludes with a short introduction to the ABINIT software that implements DFT using pseudopotentials and plane wave basis.

Chapters 5-7 are the core of the thesis work, focusing on the gas sensing properties of group III (boron, aluminium and gallium) doped graphene (Chapter 5), the analysis of the sensitivity of different graphenes to H_2S and N_2O (Chapter 6), analysis of energetic stabilities, structural and electronic properties of B and N-doped graphene with varying doping concentrations and doping configurations (Chapter 7). Chapters 5-7 are divided into 4 sections, starting with the first section, the introduction, followed by the computational details, results and discussions section and ends with a summary of the results.

Chapter 5 reports the results of *ab initio* simulations of the interactions of small gas molecules (CO, NO, NO_2 and H_2O) with group III (B, Al and Ga) doped graphene, to understand the effect of group III dopants on the reactivity of graphene towards these gas molecules and to exploit their potential applications as CO, NO and NO_2 toxic gas sensing materials in the presence of water vapour. In the results and discussions section, the influence of the introduction of group III (B, Al and Ga) atoms on the atomic geometry, the electronic band structures and DOS of IG are discussed initially before presenting the adsorption studies. The results of the effect of adsorbed CO, NO and NO_2 molecules on the structural and electronic properties on group III (B, Al and Ga) doped graphene are described in results and discussions. Later, the results of H_2O adsorption behaviour of group III doped graphene are presented, to understand the sensitivity of these doped graphenes to the presence of water vapour in air. This chapter also presents the results of the first-principles investigations on influence of adsorbed O_2 molecule on the sensing properties of gallium doped graphene, and hence to analyze the sensitivity of gallium doped graphene towards molecular oxygen which constitutes more than 20% of the volume of air. The outcome, applications and limitations of this work are discussed in the fourth section.

Chapter 6 focuses on the interactions of H_2S and N_2O gas molecules with intrinsic and doped graphenes. The effects of different dopant atoms such as B, N, Si, P, S, Ga, Cr and Mn on the structural and electronic properties of IG are described in the results and discussions section. Later, the results of the effect of adsorption of H_2S on the structural and electronic properties of IG and heteroatom-doped graphene (such as phosphorus doped graphene and sulfur doped graphene) are presented in order to evaluate the effect of P and S impurities on the reactivity of graphene towards H_2S. This chapter also discusses the results of first-principles simulation of the N_2O adsorption behaviour of intrinsic graphene, heteroatom-doped (B, N, Si, P, Ga, Cr, and Mn) graphene sheets so as to understand the effect of different dopant atoms on the N_2O gas sensing properties of graphene and to exploit their applications as N_2O sensors. The fourth section of chapter 6 discusses the outcome, applications and limitations of this research work.

Chapter 7 discusses the structural, energetic and electronic properties of graphene doped with B and N atoms. The results of the analysis of the dependence of the energetic stability and doping induced energy band gap around the Dirac point of the doped structures on the dopant concentrations and dopant configurations in four different supercell sizes of 8, 18, 32 and 72 host carbon atoms are described in the results and discussions part, which is divided into two sections. The first section on B-doped graphene system discusses the effect of one, two, three, four, five and six boron atoms in different graphene supercell sizes on the atomic structure and electronic band structure, in six subsections respectively. Similarly in the second section, the results of the effect of one, two, three, four, five and six N dopants in different graphene supercell sizes on the atomic geometry and electronic band structure are also presented in this chapter. This chapter concludes with the summary section, which is subdivided into three sections-outcome, applications and limitations.

At the end of the thesis, conclusions of the present research work, specific contributions and the future scope of research in this field are also presented.

CHAPTER 2

LITERATURE REVIEW

Sensors that surround us detect a wide range of parameters and are of great importance for ensuring the safety and quality of our life [20]. Sensors work on the principle that some intrinsic property (e.g. mass, electrical conductivity, capacitance etc.) of the sensing element gets altered by the influence of external stimulus and depending on the transduction mechanism this change gets converted to an appropriate output signal [85].

Gas sensors play a significant role in numerous application areas such as environmental monitoring, industrial chemical processing, public safety, medical diagnosis, military and aerospace [19, 86]. For a long time, metal oxide semiconductor gas sensors have played an inevitable role in environmental contaminant detection and industrial process control [87]. Metal oxide semiconductors are the most widely used gas sensing materials due to their numerous advantages such as high sensitivity towards various gases with ease of fabrication, good compatibility with other processes, low cost, simplicity in measurements along with minimal power consumption [88-90]. The high operating temperatures (200-600 °C) [91], long recovery periods, limited maximum sensitivity (in the range of parts per million), low specificity, and limited measurement accuracy [92] basically limited their applications in rapidly changing environment [20]. Hence new approaches of sensing technology need to be adopted for meeting the increasing demands of industry.

Nanotechnology provides numerous opportunities to develop the next generation gas detectors with enhanced sensor performance metrics such as ultrahigh sensitivity at extremely low concentrations, high specificity, fast response and recovery, low power consumption, room temperature (RT) operation and good reversibility by employing novel nanostructures as sensing elements [19, 93, 94]. Most chemical sensors work on the interactions that occur at the atomic/molecular scale, thus the impact of nanotechnology on sensor world is significant [95]. Nanotechnology primarily involves nanostructures with at least one of its dimensions in nanometres and new properties of matter observed at this scale range due to the laws of quantum physics [96] can be exploited for developing new sensing devices.

The most important parameter that determines the sensitivity of gas sensors is their specific surface-to-volume ratio, which is much higher in nanostructure based sensors than that in conventional micro sensors. The higher detection area of the nanostructured materials leads to greater adsorption of gas species on them and thus increased sensing capability. Hence

they are promising candidates as sensing elements for developing highly efficient gas sensors [19, 97]. So far, several nanostructures have been successfully employed as sensing materials that include one-dimensional (1D) nanowires (NWs) [98] and carbon nanotubes (CNTs) [99]. Detection limit (DL) of as low as few tens of ppb has been achieved using such systems [100]. In addition to increased sensitivity, the use of nanostructure-based devices for chemical detection has also shown other benefits such as low power consumption, lightweight and miniaturized integration[19].

Amongst nanostructured gas sensing systems, nano-carbon based materials proved to be promising due to their intrinsic electrical properties which are very sensitive to the changes in the chemical environments [27, 101-103]. Further, the high surface area, good chemical and thermal stability and functionalization capability of carbon based nanostructures make them suitable for high performance label free chemical sensing [19, 104]. The 1D structure of CNT makes it unsuitable to use with standard semiconductor fabrication techniques. This problem was overcome after the discovery of graphene, which is a two-dimensional (2D) structure of one-atom thickness having superior properties similar to CNTs [24].

2.1 Graphene: Synthesis, Properties and Applications

Graphene sheets were first isolated by Geim and co-workers [1] at the University of Manchester by mechanical exfoliation of highly oriented pyrolytic graphite (HOPGr). For their ground breaking experiments on the 2D material graphene, Geim and Novoselov of the University of Manchester were awarded the Nobel Prize in Physics in 2010 [20]. Since then, graphene has become the topic of extensive research for scientists around the globe due to its fascinating structural, electrical, optical and mechanical properties. The superior properties of graphene make it a suitable replacement for many other materials in existing applications. Its unique characteristics justify its nickname of the “miracle material” [11]. The production of graphene and the implementation of graphene-based devices for various applications had shown great progress since 2004 [19, 105].

Graphene can be synthesized by various methods such as exfoliation-intercalation-expansion of graphite [106], arc-discharge techniques [107], epitaxial growth on silicon carbide (SiC) [108], unzipping CNTs [109]. The mechanical exfoliation method commonly known as the scotch-tape method is not found to be suitable for producing large graphene sheets and hence has low throughput. Chemical Vapour Deposition (CVD) growth [110, 111] is another technique capable of mass producing large areas of single layer graphene sheets. CVD growth provides large detection area, makes sensor device fabrication easier and hence

suitable for sensing applications [11]. The thermal [112] or chemical reduction of graphite oxide [113] is the most commonly employed way to synthesize graphene due to higher cost-effectiveness [114]. Even though various techniques have been developed for graphene synthesis, high yield, economical production is still not widely available and this slow the commercialization of many practical graphene applications[19].

This interesting material has shown great potential for various applications such as solar cells [115], energy storage [116], fuel cells [117], biotechnologies [118], electronics and photonics [119] owing to its extraordinary properties such as high carrier mobility (~10,000 cm^2/Vs at room temperature) [1], high carrier density (10^{13} cm^{-2}) [1], excellent electrical conductivity, great mechanical strength with tensile modulus of ~1.05 TPa [6, 120], high thermal conductivity (from 2000 W/mK to 5000 W/mK at RT) [121] and high optical absorption ($\pi\alpha \approx 2.3\%$ in the infrared limit, where α is the fine structure constant) [7]. Graphene also exhibits many intriguing properties such as [104] anomalous quantum Hall effect at room temperature [3, 65], ambipolar electric field effect [1], high elasticity [6], complete impermeability to any gases [122] and detection of single molecule adsorption events useful for chemical sensing [30]. These properties had led to the implementation of high speed and radio frequency logic devices, transparent electrodes for solar cells and displays, electrically and thermally conductive reinforced composites etc.

2.2 Graphene for gas sensing

The peculiar structural and electronic features of graphene that make it the most promising candidate for gas sensing are:

(1) its 2D structure with only surface and no volume, which maximizes the interactions between surface adsorbates and graphene [32],

(2) its metallic conductivity and hence low Johnson noise,

(3) a little change of charge carrier density can result in detectable changes in electrical conductivity and

(4) few crystal defects which ensures a low level of 1/f noise caused by their thermal switching [2, 3, 5, 30, 123].

All these properties along with the immense mechanical robustness made graphene an excellent candidate for gas sensing applications (Table 2.1) [24]. The target gas species act as dopants to the graphene layer and change the localized charge carrier concentration by

inducing either electrons or holes that can be recorded by change in electrical conductivity [24].

Table 2.1 The properties of graphene useful for gas sensors [1-3, 5, 6, 9, 10, 12, 24, 27, 66, 105, 124].

Property	Reported value
Young modulus	1.05 TPa
Density	0.77 mg/m^2
Carrier density	10^{13}/cm^2
Resistivity	10^{-6} Ωcm
Electron mobility at room temperature	10, 000 cm^2/Vs
Thermal conductivity at 27 °C	2000-5000 W/mK

The interest in graphene for sensing applications is continuously increasing as evident by the exponential growth in number of publications dedicated to graphene-based sensors (Figure 2.1). Based on Scopus search using "graphene" and "graphene and sensors" as keywords, the publications on "graphene and sensors" represent about 5% of the "graphene" publications. More than half of these "graphene and sensors" publications appear in Sensors and Actuators B: Chemical (20%), Biosensors and Bioelectronics (15%), Electrochimica Acta (13%) and Talanta (7%), as shown in the inset of Figure 2.1 [19].

2.3 Advantages of graphene-based gas sensors

Graphene proves to be a good candidate for the development of highly sensitive gas sensors due to its advantageous properties such as:

(a) The extremely high surface-to-volume ratio of graphene with all atoms exposed to surface adsorbates allows this nanomaterial to detect even the lowest concentration of target species i.e. sensitivity down to single atom or molecule [24].
(b) The electronic and mechanical properties of graphene can be easily utilized for sensing signal transduction.
(c) The interaction of graphene with specific molecules can be enabled by its functionalization with polymers, metals or other modifiers [24] thereby improving the selectivity dramatically.
(d) A notable variation in carrier concentration could be recorded even with few charge carriers induced by the target species, due to low intrinsic noise of graphene.
(e) Four-probe devices can be fabricated using graphene monocrystals.
(f) Compared to other graphitic materials like CNTs, graphene and its oxide can be produced economically [24].

The extraordinary material properties such as superior chemical and thermal stability (stable at extremely high temperature *i.e.* > 1500 ºC [125]) and very high electron and hole mobilities (~10,000 cm^2/Vs at RT [1]) enable graphene to outperform both silicon and CNT based sensors [126]. The advantages of graphene that make it highly promising for sensing applications over CNTs include large and planar geometry that provides ease for making electrical contacts, 2D crystal lattice and high electron mobility that leads to low electrical noise (as low as tens of μV [126], nearly one order of magnitude lower than that in standard silicon devices) at RT and atmospheric pressure, and accessibility of both sides of sheet for chemical detection [127] that leads to ultra-high sensitivity. Apart from these, graphene-based chemical sensors are convenient for low cost mass production [128].

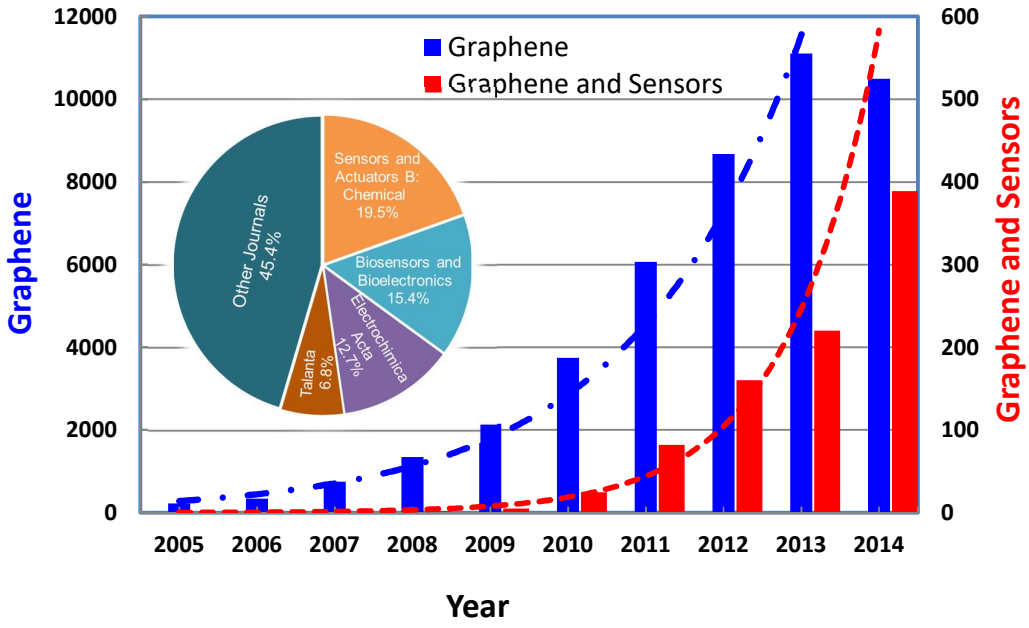

Figure 2.1 Number of annual publications according to Scopus Database using "graphene" and "graphene and sensors" as keywords. Dashed line is exponential fitting of the number of publications. Inset: source of "graphene and sensors" publications [19].

2.4 Experimental Aspects

Based on its structural features, graphene materials such as IG, graphene oxide (GO) and reduced graphene oxides (RGO) have presented distinct gas sensing capabilities. All these materials have different electrical conductivity and surface functional groups, which play important role in gas sensing mechanism. In the following sections, the state of art research work on applications of IG, GO, RGO and functionalized graphene for gas sensing is summarized [19].

2.4.1 IG based gas sensors

IG, the pure and defect free form of graphene, is normally derived from graphite exfoliation or CVD grown methods [19]. Several research groups used IG for sensing gas molecules such as CO_2, NH_3, NO_2, NO, N_2O, O_2, SO_2, H_2O etc. [129-139], since Schedin *et al.* [30] demonstrated the first micrometre-sized sensor made from mechanically exfoliated few-layer graphene that was capable of detecting even a single molecule of NO_2 in high vacuum environment. Absolute sensing resolution down to one particle has been so far beyond the reach of any detection methods due to the limitations caused by intrinsic noise exceeding the sought-after signal from individual molecules by some orders of magnitude [140] due to the fluctuations induced by the thermal motion of charges and defects [141]. The achieved sensitivity down to single molecule is due to the fact that graphene is an exceptionally low-noise material electronically [30]. The operational principle of graphene-based gas sensors is based on the changes in their electrical resistivity due to the change in the local carrier concentration induced by the surface adsorbates which act as electron donors or acceptors (Figure 2.2 (a)) [30]. They found that electron acceptors such as NO_2, H_2O and electron donors such as CO, NH_3 are differentiated by observing their effects on resistivity i.e. a decrease in resistivity due to increased hole concentration by electron acceptors and an increase in resistivity due to increased electron concentration by electron donors as shown in Figure 2.2 (b) [19]. This sensor responded rapidly to the attachment and detachment of a single NO_2 molecule from graphene's surface (Figure 2.3). The change in the local carrier concentration of graphene by one electron due to gas adsorption, led to step-like changes in resistance [142]. Even after stopping the gas flow, a complete recovery of the sensor was achieved within 100-200 s by heating the sensor to 150 ºC in vacuum (as seen in Section IV of Figure 2.2 (b)).

The sensitivity reported for the first graphene sensor was nearly several orders of magnitude greater than that of the previous sensors [20]. The achieved sensitivity down to single molecule level shows that graphene has great potential for gas detection.

Later Dan *et al.* [129] concluded that the experimentally observed high sensitivity of IG towards various gases is attributed to the chemical doping of graphene by the contamination from device fabrication. They determined the impact of the resist residue on the graphene surface left by conventional nanolithographic processing on the sensor characteristics of the IG and measured the intrinsic sensing response of IG by removing the contamination layer through cleaning.

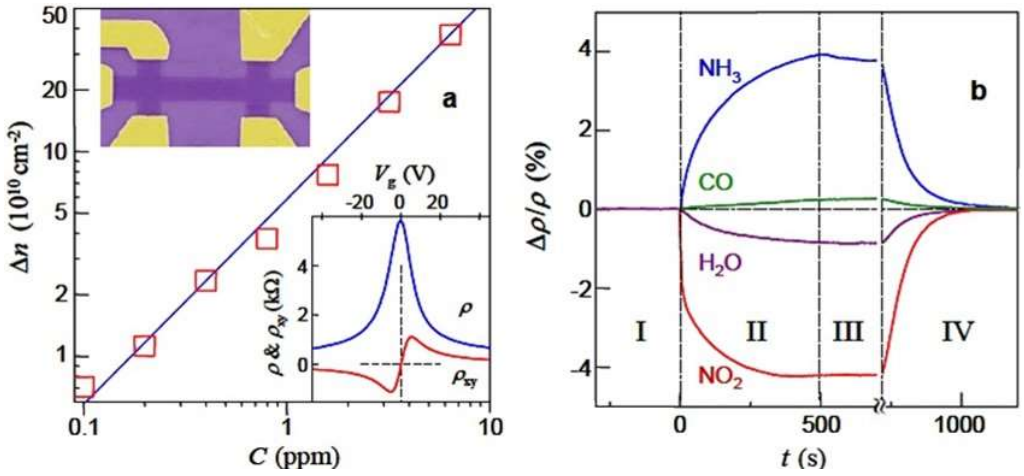

Figure 2.2 Sensitivity of graphene to chemical doping. **(a)** Chemically-induced charge carrier concentration in single-layer graphene (SLG) versus NO_2 concentration; upper inset: Scanning electron micrograph of the device; the width of the Hall bar is 1 μm; Lower inset: Characterisation of the graphene device by the electric field effect. **(b)** Changes in resistivity (ρ) at zero B caused by graphene exposure to 1 ppm of various gases. The positive (negative) sign of changes indicate electron (hole) doping. Region I – the device is in vacuum prior to exposure; II – exposure to a 5-litre volume of a diluted chemical; III – evacuation of the experimental setup; and IV – annealing at 150 ºC. (Figure taken from ref. [30].)

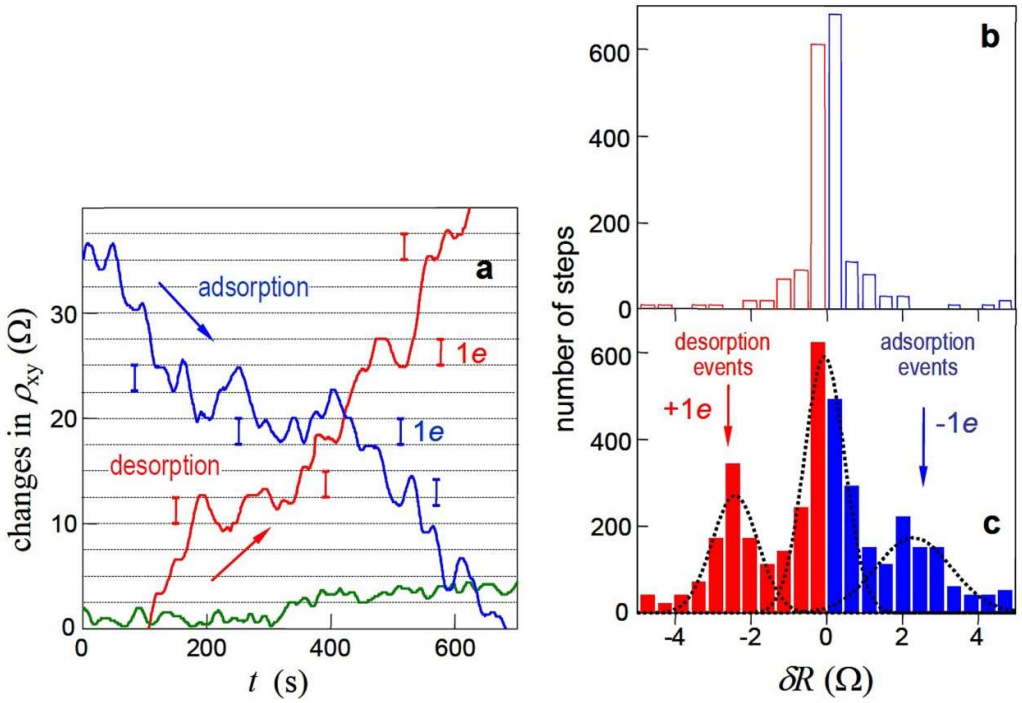

Figure 2.3 Single-molecule detection. **(a)** examples of changes in Hall resistivity observed near the neutrality point ($|n| < 10^{11}$cm^{-2}) during adsorption of strongly diluted NO_2 (blue curve) and its desorption in vacuum at 50 ºC (red). The green curve is a reference – the same device thoroughly annealed and then exposed to pure He. The curves are for a 3-layer device in B =10T. The grid lines correspond to changes in ρ_{xy} caused by adding one electron charge ($\delta R \approx 2.5$ Ohm), as calibrated in independent measurements by varying V_g. For the blue curve, the device was exposed to 1 ppm of NO_2 leaking at a rate of ≈10^{-3} mbar·l/s. (b,c) Statistical distribution of step heights δR in this device without its exposure to NO_2 (in helium) **(b)** and during a slow desorption of NO_2 (c). For this analysis, all changes in ρ_{xy} larger than 0.5 Ohm and quicker than 10 s (lock-in time constant was 1 s making the response time of ≈ 6 s) were recorded as individual steps. The dotted curves are automated Gaussian fits. (Figure taken from ref. [30].)

Similar to CNTs, the intrinsic sensitivity of IG was found to be low even in the presence of strong analytes. This suggests the possibility of tuning the properties and chemical reactivity of graphene towards gas molecules through doping with impurities [129].

Ko *et al.* [131] developed a graphene-based NO_2 gas detector in which mechanically exfoliated graphene layers with thickness in the range of 3.5-5 nm on a SiO_2/Si substrate is connected across two metal contacts defined using electron-beam lithography (Figure 2.4 (a)). This sensor showed fast response (Figure 2.4 (b)), high selectivity, good reproducibility, reversibility and high sensitivity (ratio of change in resistance upon gas exposure to the resistance in air) of ~0.09 in response to the exposure of 100 ppm NO_2 gas at RT.

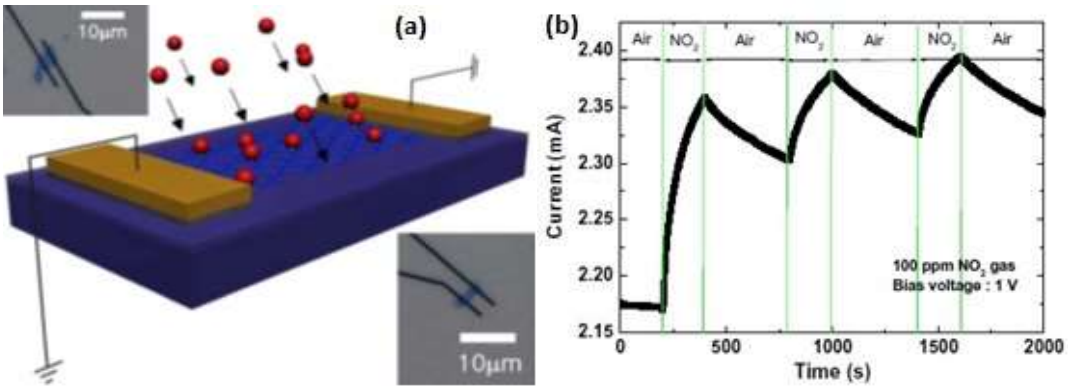

Figure 2.4 (a) Schematic diagram of graphene-based NO_2 gas sensor. **(b)** Response of graphene-based sensor upon 100 ppm NO_2 exposure. (Figure taken from ref. [131].)

In a different approach, Yoon *et al.* [133] employed HOPGr flakes, which were transferred on SiO_2 substrate using cured polydimethylsiloxane (PDMS) stamps for CO_2 gas sensing (Figure 2.5 (a) and (b)). This method allows deposition of graphene flakes at desired locations of the substrate with less residue left behind compared to the traditional scotch-tape method. The recovery time was very short, about 10 s due to physical adsorption of CO_2 on graphene facilitating easy CO_2 gas removal in contrast to other gas molecules such as NO_2 and NH_3, which require high temperature annealing in vacuum for desorption. Thus, CO_2 gas molecules are more easily adsorbed and desorbed on graphene than other gas molecules [19].

A two-terminal CVD grown graphene-based sensor exhibited the capability to detect a wide range of gas molecules at very low concentrations with DL in parts per quadrillion (ppq, 1 part in 10^{12}) range (Figure 2.6) at RT, by continuous *in situ* cleaning of IG with ultraviolet (UV) light and the sensing experiments were conducted in a controlled environment [134]. This ultrahigh sensitivity of IG, which was nearly 300% better than CNT based gas sensors achieved under analog conditions, could be attributed to the recovery of graphene's intrinsic properties by UV light illumination**.** The obtained DLs were lower than the lowest DLs

reported for other nanosensors (Table 2.2). The sensor also showed fast response, good reproducibility and also 80% of recovery within few minutes of exposure to a mixture of 10 parts per trillion (ppt) NO in N_2 (inset of Figure 2.6) [134].

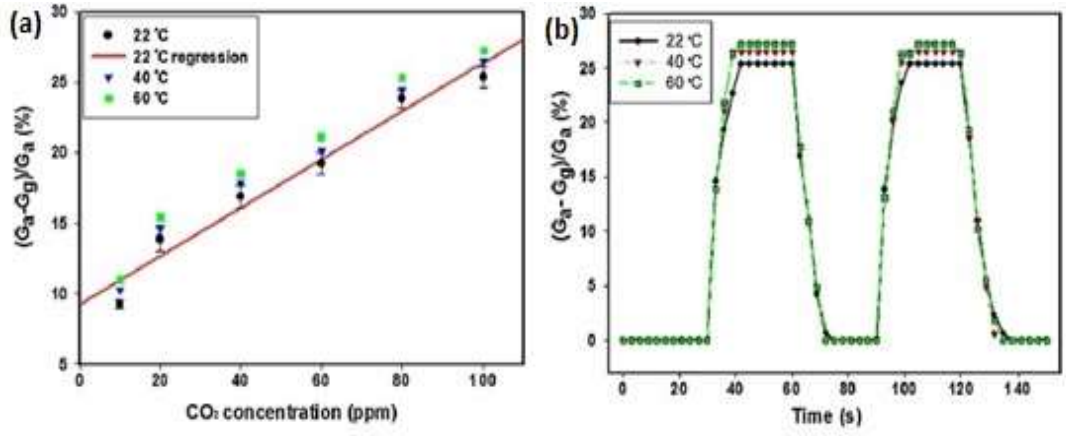

.

Figure 2.5 (a) Conductance changes in response to different CO_2 concentrations. **(b)** Time response of the graphene gas sensor in presence of 100 ppm CO_2 at different temperatures. (Figure taken from ref. [133].)

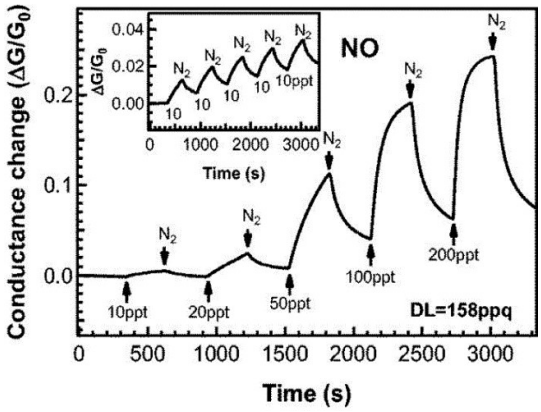

Figure 2.6 Relative change in conductance ($\Delta G/G_0$) versus time after exposure to 10 to 200 ppt NO. The inset shows the reproducibility of the sensor response at 10 ppt NO. The detection limit is estimated as 158 ppq. (Figure taken from ref. [134].)

Table 2.2 Graphene detection limit (DL) of NO, NO_2, NH_3, N_2O, O_2, SO_2, CO_2 and H_2O [134]. C_{min} is the lowest gas concentration used.

Gas	C_{min} (ppt)	Graphene DL (ppt)	CNTs DL (ppt)
NO	10	0.158	0.59
NO_2	40	2.06	1.51
NH_3	200	33.2	27.8
N_2O	200	103	-
O_2	200	38.8	-
SO_2	200	67.4	-
CO_2	200	136	-
H_2O	200	103	-

Recently, Nemade *et al.* [136] investigated the gas sensing properties of electrochemically exfoliated few-layer graphene (FLG, 3-10 layers of graphene) towards CO_2 and liquefied petroleum gas (LPG) gas at RT. The chemiresistor based sensor exhibited sensitivity of 3.83 for CO_2 and 0.92 for LPG with a response time of 11 s for CO_2 and 5 s for LPG, and recovery time of 14 s and 8 s at operating temperatures of 423 K and 398 K for CO_2 and LPG respectively. The DL was found to be 3 ppm for CO_2 and 4 ppm for LPG respectively with excellent stability [136]. The good LPG sensing behaviour of the FLG based chemiresistive gas sensor at relatively low temperatures promise their use for practical LPG detection [20].

One of the main drawbacks of graphene that limits it for practical applications is its poor selectivity i.e. it cannot distinguish between different gases. Rumyantsev and co-workers employed low frequency noise spectrum measurements of IG based devices (Figure 2.7 (a)) for selective detection of vapours of different chemicals [135]. Upon exposure of IG transistor to some gas vapours, distinctive bulges with different characteristic frequencies appear in the low frequency noise spectra of graphene transistors, whereas others introduce only change in resistance with no change in noise spectra. They found that some vapours like ethanol, methanol, tetrahydrofuran, chloroform and acetonitrile induce Lorentzian components with distinct characteristic frequencies in the low frequency noise spectrum (Figure 2.7 (b)), thereby modifying the spectra, which serve as unique gas signatures [19]. They proved that a single IG based device could achieve good selectivity along with high sensitivity by combining low-frequency noise spectrum measurements along with the change in resistance [135].

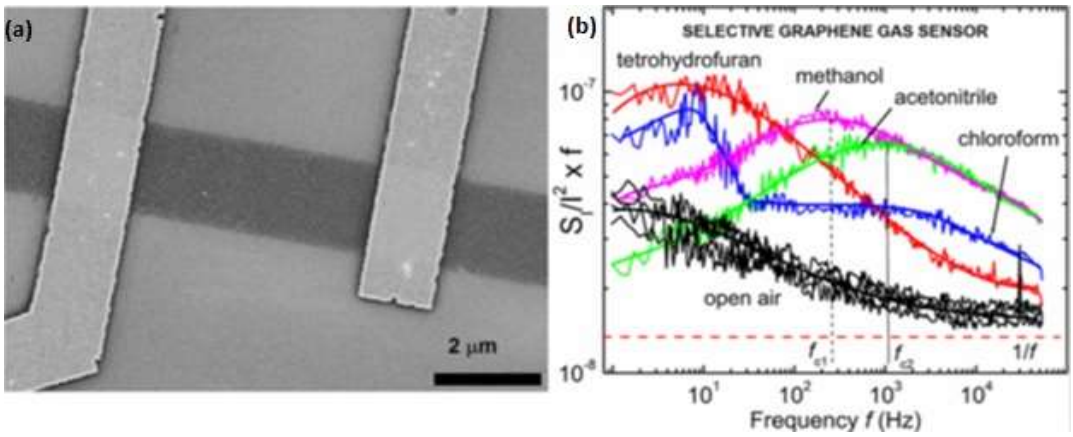

Figure 2.7 (a) Scanning electron microscopy image of back-gated graphene devices with top electrodes **(b)** Noise spectral density multiplied by frequency versus frequency for the device in open air and under the influence of different vapors. (Figure taken from ref. [135].)

Fattah and Khatami reported on a graphene/n-Si Schottky junction and evaluated the H_2S sensing properties [137]. This type of sensor was fabricated by the mechanical deposition of

highly oriented natural graphite on the top of an n-type <100> Si substrate. The sensing capability of the sensor at different temperatures was evident from the variations in the forward bias current-voltage characteristics of the diode. Compared with previously reported H_2S gas sensors, this Schottky diode based sensor had good selectivity, reproducibility, easy adsorption and desorption. The developed H_2S sensor proves the potential of employing graphene-based Schottky diodes for gas detection applications [19].

The huge fabrication cost of graphene-based devices remains as a great obstacle for widespread gas sensing using graphene. Recently, a simple, low power, low cost resistive gas sensor based on graphene-paper (G-paper) prepared by direct transfer of graphene layers on to paper (as shown in Figure 2.8 (a)) without any intermediate layers was demonstrated for the first time by Kumar *et al.* [138]. The G-paper strip showed ~65% increase in conductance in 1400 s to the flow of 2.5 ppm NO_2 gas and the conductance decrease by ~15% in 1500 s on stopping the NO_2 flow (as shown in Figure 2.8 (b)). Cleaning of graphene by UV exposure to remove the adsorbed gas molecules dramatically reduced the recovery time (from hours to 30 s), but the overall response and the characteristic time constant got improved. The achieved resolution limit of ~300 ppt was better than other sensors based on graphitic and semiconducting metal oxides using paper as substrate and these sensors were capable of withstanding minor strain [138].

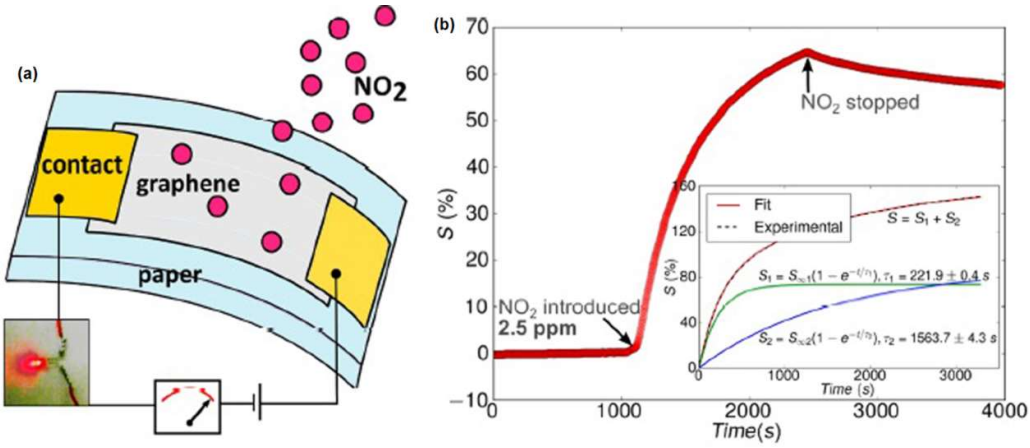

Figure 2.8 (a) Schematic of a G-paper strip based gas sensor; **(b)** Response of a G-paper strip to 2.5 ppm of NO_2. Inset shows a fit of double exponential function to the temporal response for 2.5 ppm of NO_2. The two constituent exponentials are also shown along with the estimates of time-constants. (Figure taken from ref. [138].)

Ricciardella *et al.* [139] demonstrated the potential of inkjet printing technique for manufacturing chemiresistive sensors based on liquid phase exfoliated (LPE) graphene. This technique allows deposition of small ink volumes with a more controlled drying process, which ensures good printed film quality compared to drop casting method. The LPE graphene

being a p-type material, showed a decrease in current on exposure to NH_3 (electron donor) and an increase in current on NO_2 exposure (electron acceptor), thus enabling specific detection of these gases. The fabricated sensor exhibited good repeatability upon exposure to both gases at RT and atmospheric pressure with relative humidity of 50%, which was found to be independent on the number of printed layers. The perennial issue of graphene-based gas sensors operating in environmental conditions such as low reproducibility could be overcome by using inkjet printing technology for sensor fabrication [139].

A cost effective method to produce graphene-based devices in large quantities [143] is to first produce GO (chemically modified graphene) by the oxidative exfoliation of graphite and to subsequently reduce it to graphene by chemical or thermal means using reducing agents or high temperature annealing [144]. Even though GO is electrically insulating due to numerous oxygen functional groups, the conductivity can be restored to several orders of magnitude by the removal of oxygen groups using chemical or thermal reduction which does not produce IG due to the remaining oxygen groups on RGO even after GO reduction [19]. Thus RGO possesses chemically reactive oxygen defect sites and greater conductivity than GO, that makes it highly promising for gas sensing [28].

2.4.2 GO based gas sensors

Chemical oxidation of graphite and simultaneous reduction of resulting graphite oxide is one of the popular approaches used for graphene synthesis [145]. Graphite oxide has a layered structure analogous to graphite, but is heavily decorated with oxygen-containing groups such as hydroxyls, epoxies, carboxyl and lactones. These functional groups not only expand the interlayer spacing but also make the atomic-thick layers more hydrophilic and enable these oxidized layers to exfoliate in water under moderate ultra-sonication or stirring. The single or fewer layers of exfoliated graphite oxide is often termed as GO [146]. Owing to its oxygen rich functional groups, GO is an excellent candidate for gas sensors [19].

Prezioso and co-workers [147] have studied several forms of oxidized graphene to optimize the sensing efficiency. They fabricated sensing device by drop-casting water-dispersed single-layer GO flakes on standard 30 μm spaced interdigitated Pt electrodes. It was observed that the exceptional size of the GO flakes (27 μm mean size and ∼500 μm maximum size) allows single GO flake to bridge adjacent electrodes (Figure 2.9). A typical p-type response is observed by testing the device in both reducing and oxidizing environments. In addition, the specific response to NO_2 is studied by varying the operating temperature and gas concentrations. It was demonstrated that the sensing activity is mainly attributed to the

surface bound oxygen functional groups in GO [19]. A sensing activity with a DL of 20 ppb to NO_2 is measured, which is the lowest value ever reported with other graphene-based gas sensors. Compared to CNTs and RGO based sensors, the large number of active sites on GO lead to highly improved sensitivity and hence suited for applications that require high sensitivity but at the cost of slow response [20]. Hence, this underlines versatility of GO towards gas sensing which is complementary to graphene.

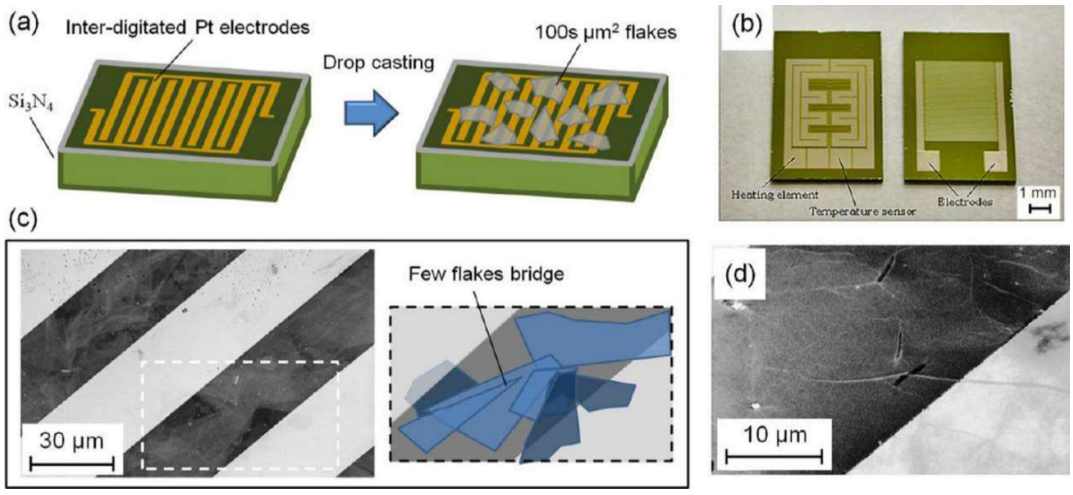

Figure 2.9 (a) Sketch represents the process for fabrication of GO-based H_2 sensor with the electric contacts between prepatterned interdigitated Pt electrodes are realized upon drop-casting deposition of large GO sheets. **(b)** Patterned substrate (front-size) with heating elements and temperature sensors on the backside. **(c)** Scanning electron microscope (SEM) image of few GO sheets bridging two adjacent Pt electrodes. **(d)** SEM image of a GO flake lying over an electrode edge. (Figure taken from ref. [147].)

Wang *et al.* [148] have fabricated hydrogen gas sensors based on GO nanostructures using alternating current dielectrophoresis (ac-DEP) process (Figure 2.10). The GO nanostructures synthesized from Hummers method were assembled into gold electrodes using DEP process by varying parameters such as frequency, peak-to-peak voltage (V_{pp}), and processing time (t). The optimum DEP parameters required for hydrogen gas sensing using GO nanostructures were observed to be $V_{pp} = 10$ V, frequency = 500 kHz, and $t = 30$ s. The optimized device was found more effective and was a better hydrogen sensor compared to a typical drop-dried device. A good sensing response of 5%, fast response time (< 90 s), and fast recovery time (< 60 s) for 100 ppm hydrogen gas concentration at RT was observed [148].

Similarly, GO having SAW (structure with surface acoustic wave propagated) sensing structure has been successfully used to detect low concentration of hydrogen and nitrogen dioxide in the atmosphere of synthetic air [149, 150]. The various concentrations of the analyzed gases at various temperatures of the sensing structure were measured [19].

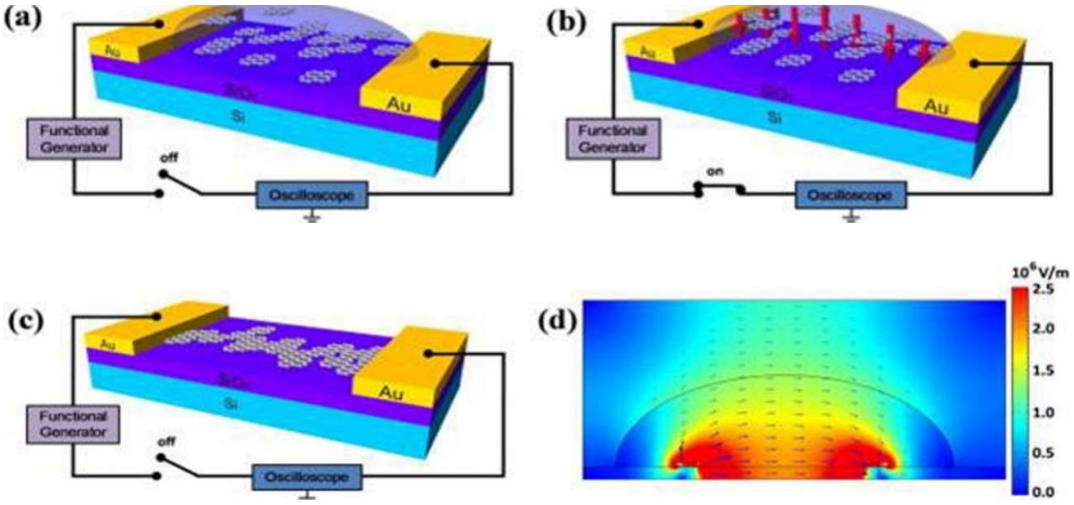

Figure 2.10 Schematic of the setup used for DEP of GO nanostructures in a microgap of Au electrode **(a)** before, **(b)** during, and **(c)** after DEP. The bold red arrows in **(b)** shows the direction of the DEP force acting on the suspended GO, under the influence of which the floating nanostructures are assembled between the electrodes. **(d)** Finite element method (FEM) simulated electric field between a pair of coplanar Au electrodes with a solution drop showing the variation in the electric field intensity. (Figure taken from ref. [148].)

Some *et al.* [151] have demonstrated the high sensitivity of GO under harsh conditions for volatile organic compounds (VOC) such as tetrahydrofuran and chloroform. The high oxygenated functionalities on GO surface was observed to maintain the high sensitivity in highly unfavourable environments (extremely high humidity, strong acidic or basic). Moreover, GO exhibited faster sensing and higher sensitivity when compared to RGO even under extreme environments of over 90% humidity, making it the best choice for an environmentally friendly gas sensor (Figure 2.11). Furthermore, according to the experimental results, the sensitivity of GO to VOCs (mainly nitro and amine containing compounds) is much higher than that of RGO due to the presence of numerous polar functional groups [151].

GO films have also been effectively used in humidity sensing applications. Bi *et al.* [152] have used GO to fabricate a microscale capacitive humidity sensor. It was reported that compared with conventional capacitive humidity sensors, the GO based humidity sensor has a sensitivity of up to 37800%, which is more than 10 times higher than that of the best one among conventional sensors at 15% – 95% relative humidity. The excellent humidity sensing ability of GO is attributed to its hydrophilicity. The mechanism involves, at low relative humidity (RH), water molecules are primarily physisorbed onto the available active sites (hydrophilic groups, vacancies) of the GO surface through double hydrogen bonding, the first-layer physisorption of water (Figure 2.12). In this regime, the water molecules are thus unable to move freely because of the restriction from double hydrogen bonding. The hopping transfer of protons between adjacent hydroxyl groups in the first-layer physical adsorption of

water require much energy, and for this reason, GO films exhibit strong electrical resistance. Hence, GO based materials can be an ideal material for constructing humidity sensors with ultrahigh sensitivity for widespread applications [19].

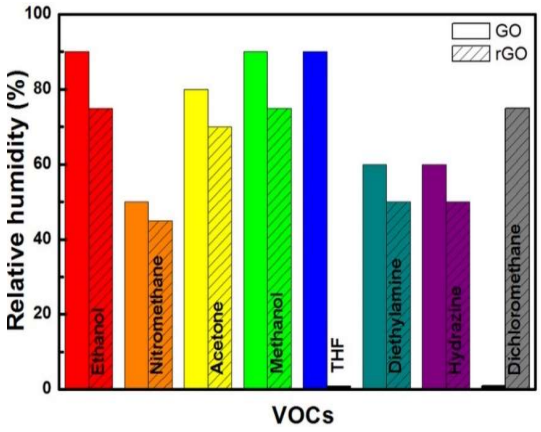

Figure 2.11 A comparative plot for sensing of eight different VOCs with GO and RGO sensors under a maximum amount of humidity. (Figure taken from ref. [151].)

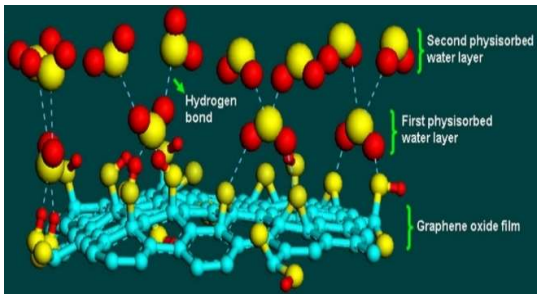

Figure 2.12 A 2-layer process characterizes the adsorption of water molecules on a GO film. The first-layer of water molecules is attached on the GO films through two hydrogen bonds. In contrast, the second layer of water molecules is adsorbed through only one hydrogen bond. (Figure taken from ref. [152].)

Other examples of GO based gas sensor includes use of GO thin film for VOC detection[153], in humidity sensing [154] and other gases etc.

2.4.3 RGO based gas sensors

GO can be partially reduced to graphene-like sheets by removing the oxygen-containing groups with the recovery of a conjugated structure and termed as RGO [155]. The process of GO reduction has significant impact on the quality of the RGO produced, and therefore that determine how close RGO will come, in terms of structure, to IG. Owing to its close structure with graphene and oxygenated functional groups, RGO have been successfully used in various applications including gas sensing [143]. For gas sensing, RGOs proved advantageous over IG considering their low production costs, fine-tuning of structure and properties such as conductivity, dispersibility in water, possibility of further modification etc.

Hence, RGO based sensors have been widely studied in detection of various gaseous species [143, 156-163].

Ganhua *et al.* [143] developed high performance gas sensors based on partial reduction of GO by multi-step, low-temperature thermal treatments (100, 200 and 300 °C). On exposure to 100 ppm NO_2 and 1% NH_3 after either a one-step heating at 200 °C for 1h or a multistep-heating at 100 and 200 °C (for 1h each), the sensor showed a good response. In contrast, non-reduced GO showed no response to these gases. The good response of the partially reduced GO sensor is attributed to the recovery of carbon atoms, vacancies, or small holes created during the thermal treatment that act as active sites for gas adsorption. The 300 °C annealed GO showed high sensitivity (~1.56 to 100 ppm NO_2) and fast response compared to 200 °C annealed GO with sensitivity of ~1.41. This simple, low power GO sensor exhibited ~4.3% increase in conductance for 1 ppm NO_2 compared to the sensor based on mechanically exfoliated graphene [19].

Robinson *et al.* [156] found that sensitivity and 1/f noise get affected by the variation in the exposure time of GO to hydrazine vapour i.e. the level of reduction from GO to graphene. They showed that acetone and chemical toxics such as 2, 4-dinitrotoluene (DNT), hydrogen cyanide (HCN), and dimethyl methyl phosphonate (DMMP) can be detected at ppb concentrations within 10 s by hydrazine-reduced GO based chemical sensor with reduced noise levels as compared to CNT based sensors. They observed both rapid response due to gas adsorption onto aromatic carbon atoms and slow response due to adsorption onto oxygen functionalities, vacancies, and defect sites in RGO sensor response. As the level of reduction increases, the rapid response increases due to the increase in the number of sp^2-bonded carbon sites and recovery time decreases whereas decreased reduction time results in increased slow response and long recovery time [19].

In another approach, Fowler *et al.* [157] developed chemical sensors based on single-layer hydrazine reduced graphene films using spin coating of chemically converted graphene dispersions on interdigitated planar electrode arrays for the detection of NO_2, NH_3 and DNT. The sensor showed a consistent response with charge transfer between graphene and the analyte and a decrease in resistance of ~0.028% for 52 ppb of DNT, a volatile found in trinitrotoluene (TNT) explosive within 10 min exposure. They also observed drop in sensitivity at elevated temperatures to 5 ppm NO_2 by employing a micro hotplate substrate [19].

RGO films synthesized by the reduction of exfoliated GO using ascorbic acid, printed onto flexible polyethylene terephthalate (PET) using inkjet techniques [158] enabled selective and reversible sensing of chemically aggressive vapours of NO_2 and Cl_2 at RT using an air sample with vapour concentrations ranging from 100 ppm to 500 ppb. This high sensitivity could be attributed to the uniform RGO film obtained by controllable inkjet-printing on flexible substrate and also the use of the mild reducing agent (ascorbic acid) which introduces less defects compared to hydrazine, the commonly used reducing agent. They observed long sensor recovery period due to the strong chemisorption of NO_2 on RGO/PET film and complete recovery was achieved by the exposure of the film to 254 nm UV light [158].

Chemically reduced GO based back-gated field-effect transistor (FET)-based gas sensor exhibited a 360% increase in response to 100 ppm NO_2 diluted in dry air at RT and atmospheric pressure, compared to thermally reduced GO sensors [159]. The maximum response (ratio of device resistance in air to that in target gas) of this device to 100 ppm NO_2 was ~9.15 (Figure 2.13 (a)), higher than previously reported thermally reduced-GO sensor (~2.56) [143], due to high oxygen reduction level in chemically reduced-GO with C/O ratio of 11.0 that could lead to more adsorption sites for gas molecules. For NH_3 gas, the resistance increased by ~1.7 fold (Figure 2.13 (b)) but for thermally reduced-GO sensors, the response (ratio of device resistance in target gas to that in air) reported was ~1.3 [19].

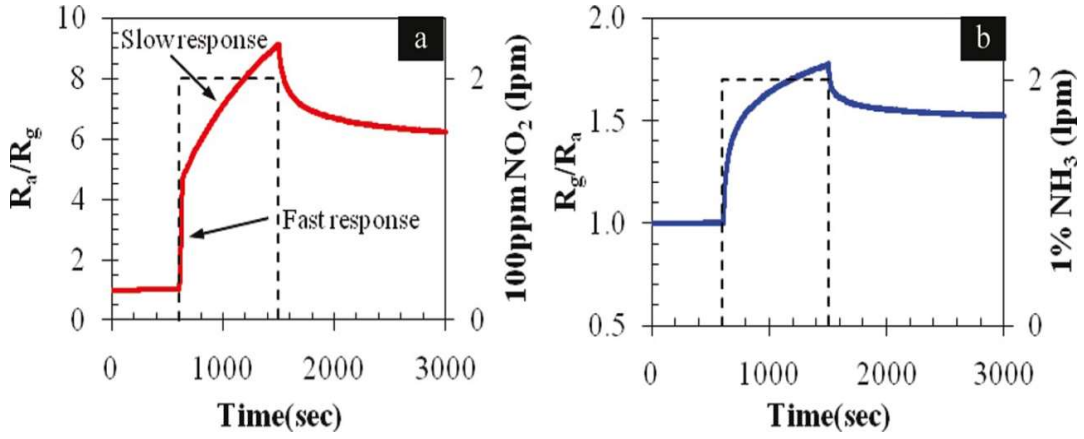

Figure 2.13 Representative dynamic behaviour of RGO sensors for **(a)** 100 ppm NO_2 **(b)** 1% NH_3 detection (Figure taken from ref. [159].)

The molecular adsorption of gases onto RGO with oxygen containing functional groups that act as higher energy binding sites is non-recoverable without any external assistance, due to stronger binding of gases onto these sites. This degrades the sensing performance since the change in conductance during the sensing cycle does not return back to its base value even after removing the target gas supply and this change passes on to the next sensing cycle. The

conventional sensitivity definition i.e. the normalized sensing response varies within a wide range when the response time required for desorption differs from a few minutes for partial recovery to few days for full recovery, making the sensor response non-repeatable even under the same target analyte concentrations [159]. Moreover, the sensitivity of all devices based on graphene/RGO materials produced by same fabrication process and from the same batch may be different. Lu *et al.* [159] proposed a new signal processing method for these devices which suggests that the slope of the difference between the device resistance in air (R_a) and that in target gas (R_g) versus R_a plot is a more reliable indicator of the gas concentration than using the ratio of resistance before and after sensing [19].

An array of thermally reduced GO-based integrated gas sensors (Figure 2.14) developed by Lipatov and co-workers showed definitive identification of chemically similar analytes such as ethanol, methanol and isopropanol by making use of the significant device-to-device variations of RGO based sensors [160]. Each RGO device used in the integrated gas sensing system has a unique sensor response due to the significantly different structural and electronic properties of the RGO flakes produced from the same fabrication process. The characteristic patterns for ethanol, methanol and isopropanol obtained by combining the resistance changes induced by all 20 segments for each analyte (Figure 2.15) were used for selective detection of these gases [19].

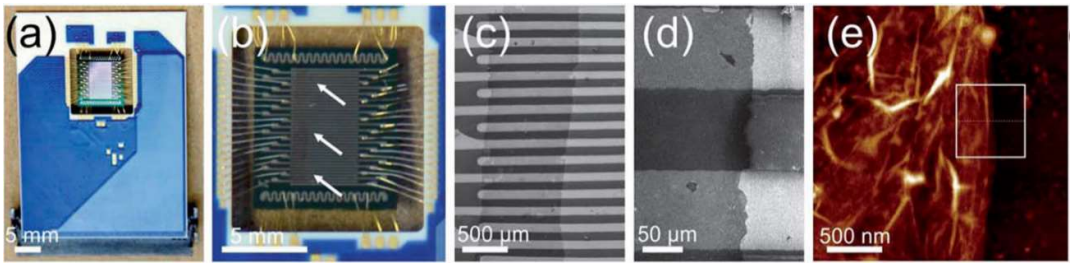

Figure 2.14 RGO-based multisensor array. **(a)** Optical photograph of a multielectrode KAMINA chip. **(b)** Optical photograph of the active part of the KAMINA chip. The white arrows show a dark vertical strip that corresponds to an RGO film. **(c)** SEM image of RGO sensors. Bright horizontal lines correspond to Pt electrodes; darker vertical strip corresponds to RGO. **(d)** SEM image of a fragment of one of the devices shown in **(c)**. **(e)** AFM image of an RGO film on a Si/SiO_2 substrate. (Figure taken from ref. [160].)

A cost-effective method of fabricating RGO based gas sensor on paper substrate was presented by Hassinen and co-workers [161]. The developed sensor exhibited sensitivity to NO_2 in sub-ppm levels. They observed that the size and the thickness of the RGO flakes, use of different reducing agents affected the sensing characteristics of the RGO sensor.

Nantao *et al.* [162] demonstrated highly sensitive and selective RGO sensors prepared by the reduction of GO by using pyrrole as reducing agent for the detection of NH_3 at RT. The observed enhancement in sensing performance is due to the combined effect of the intrinsic

properties of the adsorbed pyrrole molecules and graphene. These low power, low cost RGO sensors, with reported sensitivity of 2.4% to 1 ppb NH_3 within 1.4 s explain the viability of employing these RGO sensors for NH_3 detection in practical applications [19].

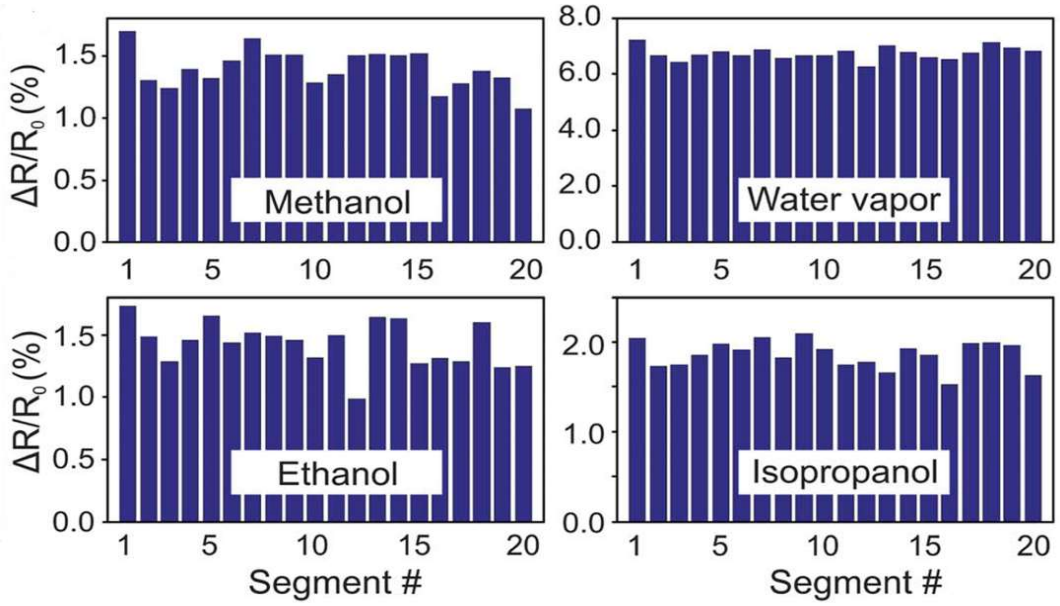

Figure 2.15 Distributions of gas responses of RGO segments to different analytes. (Figure taken from ref. [160].)

Ppb level detection of toxic NO_2 gas was presented by a sensor based on porous RGO synthesized by one-pot hydrothermal method of dilute concentrations of GO at low temperature [163]. The sensing device was fabricated by drop-casting perforated RGO nanosheet suspension onto Si/SiO_2 substrate with Au pre-patterned interdigitated electrodes (IDEs). This enhanced sensitivity was due to the presence of more active sites for gas adsorption, channels for gas diffusion and large surface area of the perforated RGO. Upon exposure to NH_3 gas, the *p*-mode polarity of porous RGO got changed to *n*-mode and this perforated RGO sensor had good reversibility to NH_3. These results prove that structural modification of graphene through perforation is also a promising method for enhancing the gas sensing response [19].

There have also been other reports on the use of RGO for sensing gas molecules such as NO_2 [164], NH_3 [165], H_2 [166-168]. The above-mentioned reports had shown that RGO based gas sensors exhibit high sensor response and reversibility at low concentrations under ambient conditions (RT and atmospheric pressure) with less power requirements compared to IG. RGO with different oxygen-containing functionalities is a highly versatile platform for gas sensing due to its rich chemistry that allows for surface modification with different

functional groups, but at the cost of long recovery periods. Another limitation of RGO for practical gas sensing is its low selectivity, similar to IG [19].

2.4.4 Modified graphene-based gas sensors

Sensitivity is an indispensable parameter for fabricating any high performance gas sensor, since it determines the sensor's capability to verify the minimum value of the target gases' concentration. Hence, considering the moderate sensitivity and stability of graphene-based materials, modified graphene systems with improved performance is critically important to design commercially viable gas sensing systems. In this advent, several approaches are employed to improve the interactions between graphene and the gas. The properties of the graphene materials are often altered when modified with other functional materials such as functional molecules, polymers, nanoparticles (NPs), etc. and such combination often leads to hierarchical multifunctional materials that can combine the advantages of each components. Usually, sensing applications based on graphene require chemical modification to control the physiochemical properties. Hence, various chemical modification methods such as introduction of dopants [169-172], functional molecules, functionalization with metal [173-181], metal oxide NPs [182-194] and polymers [195-206] have been reported. Such alterations allowed the manipulation of the physiochemical properties to suit the required demands and many high performance gas-sensing platforms based on these techniques are reported. In the following sections, various approaches for modification of graphene-based materials to improve their sensing efficiency are discussed [19].

2.4.4.1 Chemically modified graphene-based gas sensors

The excellent gas sensing properties of graphene are attributed to the graphene ability to undergo physicochemical changes under given testing environment. Hence, aforementioned applications not only require the preserved intrinsic electronic properties of graphene, but also demand that they can be easily modified with functional groups sensitive to various gaseous environments. Hence, structural modification that involves atomic doping, molecular impregnation and chemical functionalization of graphene materials is widely studied for gas sensing applications [19].

Doping of graphene with various heteroatoms such as B, N, sulfur (S), silicon (Si), etc. have been widely studied for various applications such as supercapacitors, lithium-ion batteries, high performance FETs, oxygen reduction reaction (ORR), electrochemical and biosensors, photocatalyts, water splitting etc. [207-219]. Insertion of such heteroatom often tunes the electronic properties through band gap alterations [208, 209]. The physical and chemical

properties of graphene are also altered by the introduction of defects in the basal plane [220] that could be extremely useful for enhancing the performance metrics of gas sensors [19].

Several doped graphene-based sensors were experimentally validated. Niu *et al.* prepared highly sensitive NH_3 gas sensors by doping graphene nanosheets with phosphorus (P-GNS) via high temperature annealing of GO and triphenylphosphine mixture (Figure 2.16) [169]. Compared to thermally reduced graphene, the P-GNS based NH_3 sensors (Figure 2.17 (a)) exhibited much improved sensor response, slow response and recovery at RT as shown in Figure 2.17 (b), (c) and (d) due to the adsorption of NH_3 onto the added phosphorus atoms.

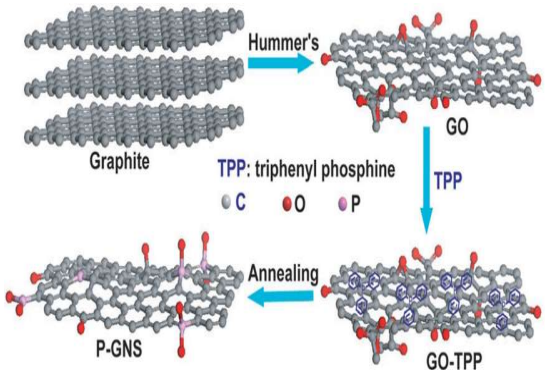

Figure 2.16 Schematic illustration of the synthesis of phosphorus doped graphene nanosheets (P-GNS). (Figure taken from ref. [169].)

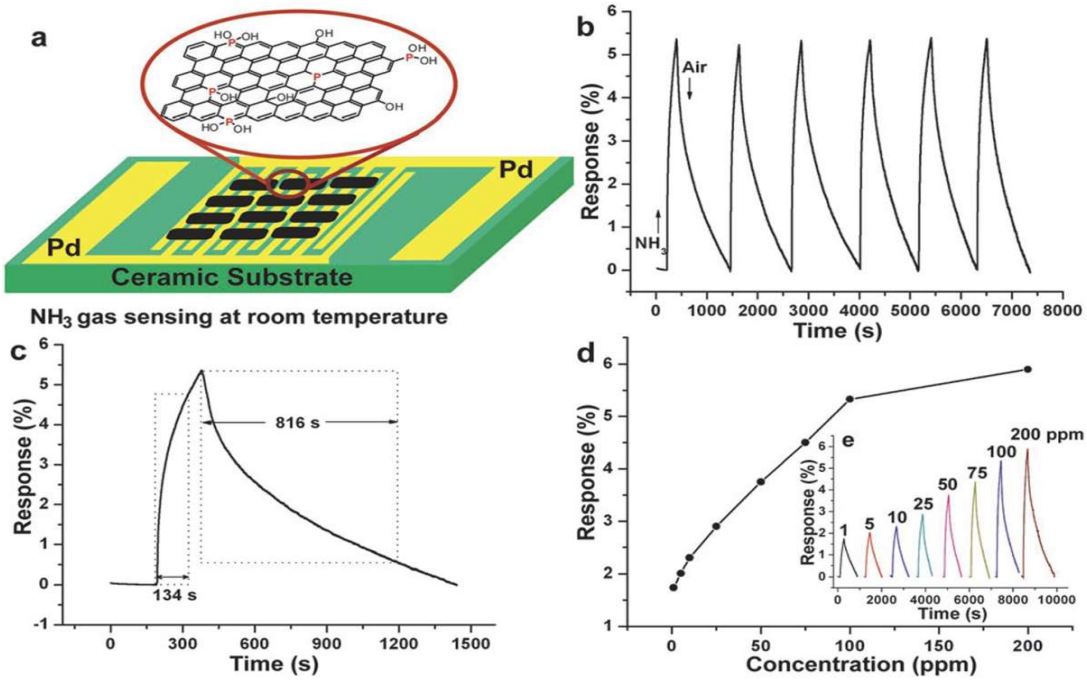

Figure 2.17 (a) NH_3 sensor using P-GNSs as sensing materials, **(b)** the response of P-GNS-400 for 100 ppm of NH_3, **(c)** response and recovery time, **(d)** and the inset **(e)** response values of P-GNSs annealed at 400 °C to NH_3 with various concentrations. (Figure taken from ref. [169].)

Improvement in NO_2 gas sensing properties was achieved by co-doping graphene sheets with nitrogen and silica prepared by high temperature annealing of N and Si-containing GO-ionic liquid (GO-IL) composites [170]. Both N and Si atoms incorporated into the graphene network play significant role in enhancing the NO_2 gas sensing performance. The N atoms introduced into the graphene basal plane act as active adsorption sites for NO_2 whereas Si atoms alter the electronic structure of graphene. NSi-GNS based gas sensor obtained by annealing of GO-IL at 400 °C (NSi-GNS-400) spread on a glass substrate between the silver electrodes (Figure 2.18 (a)), showed high negative sensor response (−26 ± 1%) in 21 ppm of NO_2 and good stability even after five sensing cycles (Figure 2.18 (b)). The response time and the recovery times observed for NSi-GNS-400 were 68 s and 635 s respectively (Figure 2.18 (c). The response of the NSi-GNS-400 upon NO_2 exposure with concentrations varying from 21 to 1 ppm (Figure 2.18 (d)) had a decreasing trend of response with decrease in NO_2 concentration. The high sensitivity of the sensor was evident from the response value of -8.8% at 1 ppm NO_2 [170].

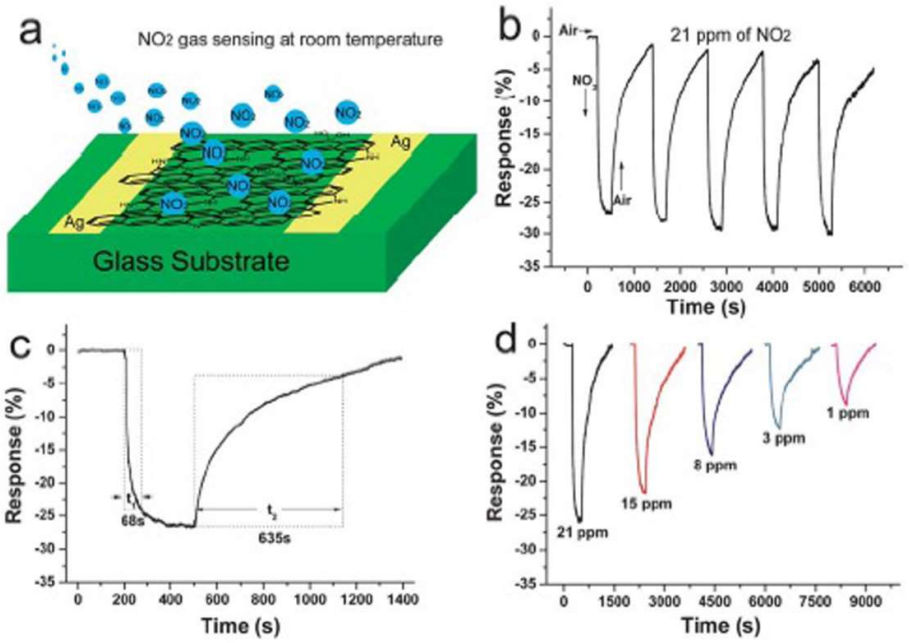

Figure 2.18 (a) NO_2 sensor; **(b)** the response of NSi-GNS-400 to 21 ppm of NO_2; **(c)** response and recovery time; and **(d)** response to NO_2 with varying concentrations. (Figure taken from ref.[170].)

Recently, Liang *et al.* [171] found that the NO_2 adsorption ability of graphene was improved by a simple and effective method of doping graphene with sulfur atoms using hydrogen sulfide gas flow at 1000 °C. The sulfur doped graphene also showed highly selective detection of NO_2 compared with other gases such as NH_3, CH_4, SO_2 and CO [171].

Lv *et al.* [172] demonstrated significantly enhanced sensing behaviour of graphene towards toxic gases such as NO_2 and NH_3 through B-doping. The synthesized large-area and high-quality B-doped graphene (BG) sheets can detect extremely low concentrations (e.g. ppt, ppb) with a clean signal of signal-to-noise ratio (s/n) = 31.5 for 1 ppb NO_2 exposure and s/n of 50.1 for 1 ppm NH_3 exposure. It was observed that upon B doping of graphene, there was significant enhancement in the sensitivity of 27 and 105 times compared with IG and DLs of 95 and 60 ppb, for NO_2 and NH_3 detections respectively [172].

The effects of RGO modifications on its gas sensing capabilities have also been studied. Su and Shieh used RGO films covalently bonded to gold electrodes on a plastic substrate, modified with cysteamine hydrochloride (CH) for fabricating flexible NO_2 gas sensors (Figure 2.19) [221]. These sensors were found to be highly more sensitive to NO_2 compared with graphene-based sensors grown by CVD method at RT and are suitable for practical applications due to their ease of fabrication [221].

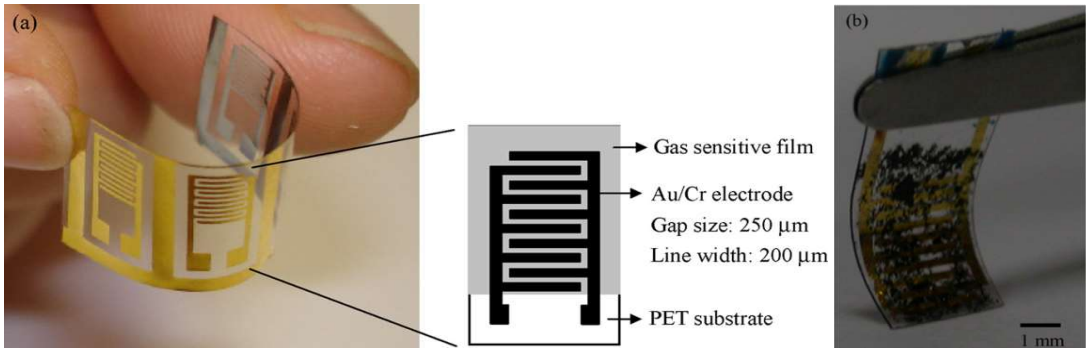

Figure 2.19 (a) Structure of flexible RGO gas sensor; **(b)** Photograph of bent gas sensor based on RGO film anchored on a PET substrate. (Figure taken from ref. [221].)

Selective detection of ammonia was demonstrated by the functionalization and reduction of GO by tannic acid (TA), an effective green reducing agent in place of commonly employed environmentally harmful reducing agents such as hydrazine or sodium borohydride. The observed response (Figure 2.20 (a)) arises from the *n*-type doping of RGO (intrinsically *p*-type) due to the electron donating behaviour of tannic acid [222]. As compared to NH_3, there was negligible resistance change upon exposure to ethanol and acetone, (Figure 2.20 (b)), due to the strong reducing behaviour of NH_3 among other organic vapours. This simple chemiresistor sensor functionalized with environmental friendly reducing agents has also shown wide range detection capability, RT operation, good detection efficiency with excellent response times and recovery times (40 s and 260 s, resp., for 1310–6550 ppm of NH_3). Sensor performance parameters of various chemically modified graphene-based gas sensors are provided in Table 2.3 [19].

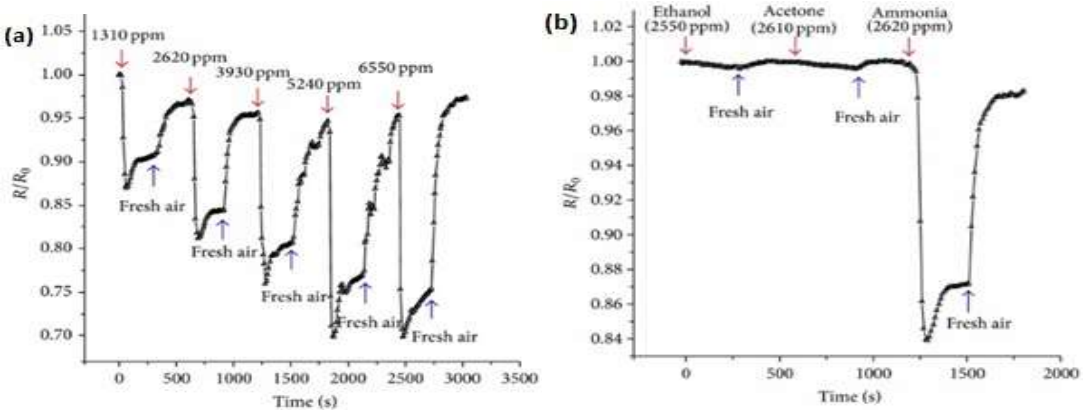

Figure 2.20 (a) Response towards variation of NH_3 concentration **(b)** Selectivity response when exposed to ethanol, acetone, and ammonia (Figure taken from ref. [222].)

Table 2.3 Summary of gas sensor parameters of several chemically modified graphene-based gas sensors.

Type	Modification[1]	Gas[2]	Conc. (ppm)	Sensor response[3]	Response time (min)	Recovery time (min)	Ref.
IG	N and Silica co-doping	NO_2	21	-26% *	1.13	10.5	[170]
	P-doping	NH_3	100	5.4%*	2.23	13.6	[169]
	p-PACA	H_2	10^4	8%**	-	-	[223]
	Ozone	NO_2	200	19.7%*	15	30	[224]
GO	Oleylamine	CH_3OH	-	116%***	10	-	[225]
		$(CH_3)_2CO$	-	45.5%***	10	-	
RGO	PPD	DMMP	20	8%*	18	6	[226]
	Cysteamine	NO_2	5	11.5%*	7	28	[221]
	Tannic acid	NH_3	2620	-87.5%*	0.67	4.33	[222]

[1] p-PACA≡ p-phosphonic acid calix[8]arene, PPD ≡ p-phenylenediamine

[2] RhB≡ Rhodamine B, DMMP≡ Dimethyl methyl phosphate

[3] Sensor response: $*= \frac{R_g - R_a}{R_a}$; $**= \frac{I_g - I_a}{I_a}$; $***= \frac{V_{th_g} - V_{th_a}}{V_{th_a}}$

$R =$ sensor resistance, $I =$ current, V_{th} = threshold voltage, a and g refer to air and gas

2.4.4.2 Graphene/nanoparticle hybrid based gas sensors

Graphene shows high affinity to almost all gases by inducing change in conductance i.e. increase in conductance by electron withdrawing gases and decrease in conductance by electron donating gases. Even though graphene-based devices enable highly sensitive detection of various gas species, they are very unselective. Although graphene and RGO based sensors exhibit excellent sensitivities for detecting various gas species, their performance need to be further improved for meeting the requirements of practical gas sensors such as high selectivity and low detection limit.

Graphene and RGO based hybrid nanostructures have shown promising results for gas sensing applications. Functionalization of graphene/RGO with metal [173-181] and metal oxide NPs [182-194] has proved to be potential approaches for enhancing the gas sensing properties. The hybridization of metal or metal oxide NPs with graphene/RGO has demonstrated a significant synergistic effect towards gas sensing. These hybrids can possess modulated electronic properties, enabling them to enhance the selectivity and sensitivity. The functionalization of graphene/RGO leads to distinct sensor responses to different gases. This improves the selectivity of RGO based devices by enhancing the gas sensing properties of functionalized RGO to specific gas. Review by Gutes and co-workers [175] underlines the efficacy of metal NP decorated graphene in sensing applications [19].

Various graphene–NP nanohybrids such as graphene decorated with noble metal NPs have been studied for gas sensing applications. Kaniyoor *et al.* [173] investigated the sensing performance of H_2 gas sensors based on platinum (Pt)-decorated graphene sheets and Pt-decorated multi-walled CNTs (MWCNTs) fabricated by simple drop casting method. At a detection level of 4 vol% H_2 in air, Pt-decorated graphene exhibited a two fold increase in sensitivity of Pt-decorated MWCNT but with a comparable response time at RT. Li *et al.* [174] developed a highly sensitive graphene-based NO gas sensor (Figure 2.21 (a)) fabricated by ac-DEP in which the sensing channel of RGO is decorated with palladium (Pd) and is connected across electrodes covered with CVD-grown graphene. This sensor was capable of detecting NO gas from 2 to 420 ppb with a response time of several 100 s at RT and a recovery time of ~1000 s at 2 ppb NO concentration (Figure 2.21 (b)) by current annealing [19].

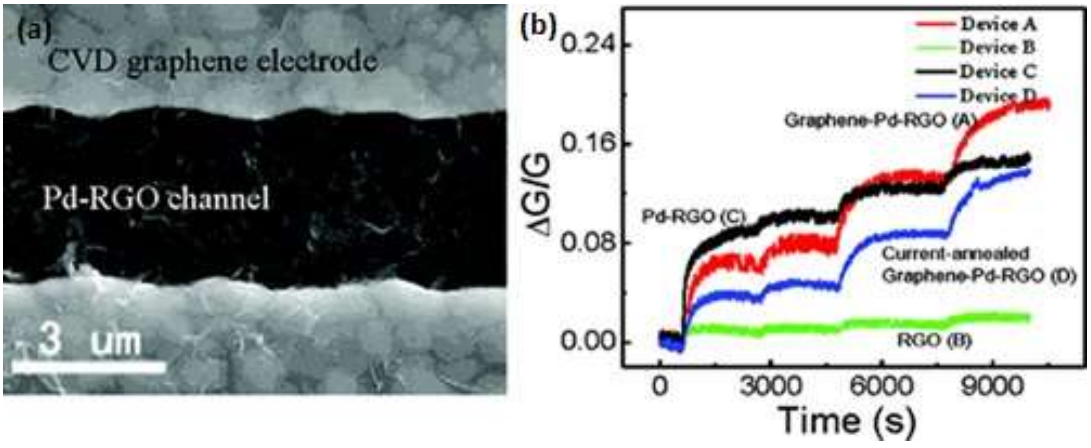

Figure 2.21 (a) Pd-RGO NO sensor and **(b)** sensor response to various concentrations of NO. (Figure taken from ref. [174].)

Gutes *et al.* presented a simple and flexible method to decorate CVD-grown graphene on copper (Cu) substrate with metal NPs, by electroless deposition of the metal using copper as reducing agent [175]. Using this method, Pd, Pt, gold (Au), and silver (Ag) can be easily deposited on Cu-catalyzed graphene since their reduction potential is higher than that of Cu (+0.34 V). This functionalization scheme could be easily integrated into the existing roll-to-roll fabrication methods, which allows the mass production of sensing devices. The decorated graphene is then transferred using polymethyl methacrylate (PMMA) stamping method onto a transducer with two comb-shaped electrodes made of gold. The Au-decorated graphene device demonstrated very fast response, but slow desorption due to strong S–Au bonds.

Chung and co-workers investigated the performance characteristics of H_2 sensing at RT using CVD-grown graphene on Cu foil decorated with Pd NPs [176]. They showed that during H_2 injection, Pd-decorated graphene sensors exhibit significant resistance changes, while no detectable change was observed in the case of IG. The sensing response can be attributed to the change in the composition of the thermally evaporated Pd NPs on graphene surface into palladium hydride with lower work function than pure Pd. The reported increase in resistance is due to the lower work function of palladium hydride that enables transfer of more electrons from Pd NPs to graphene. A sensing response of 33% to 1000 ppm H_2 and a detection limit of 20 ppm H_2 at RT (22 °C) were shown by graphene sensor with thermally evaporated Pd thickness of 3 nm [176]. Pak *et al.* [177] have fabricated Pd NP-functionalized graphene nanoribbon (GNR) array for testing H_2 gas. A rapid response of 90% within 60 s at 1000 ppm and fast recovery of 80% within 90 s in nitrogen environment was achieved using periodically aligned GNR array (Figure 2.22) with no polymer-residue obtained by a chromium interlayer under the polymer residue via laser interference lithography for protection of graphene surface from strains or doping. As compared to the shark-fin sensitivity curve of IG, the GNR sensors had a square response and recovery curve (Figure 2.23 (a), (b)). This low sensing response of Pd-GNR based sensors is due to adsorption of only few gas molecules at the reduced number of Pd NPs deposited on narrow GNRs. Nevertheless, these sensors showed fast response and recovery due to ease of adsorption and desorption of hydrogen gas molecules on Pd NPs [177].

A chemoresistor type sensor fabricated by Gravure printing of Ag NP-decorated-sulfonated RGO (Ag-S-RGO) inks on a polyimide (PI) substrate with Ag pre-patterned IDEs showed sensing response of 74.6% within 12 s to 50 ppm NO_2 at RT and recovery was achieved within 20 s [178]. The chemical modification of RGO with $–SO_3H$ groups and Ag NPs resulted in the superior performance of this hybrid sensor. This Ag-S-RGO based sensor also

showed good flexibility even after 100 bending cycles. This sensor could be deployed for real-time NO_2 detection due to its advantages of mechanical robustness, light weight and easy handling [19].

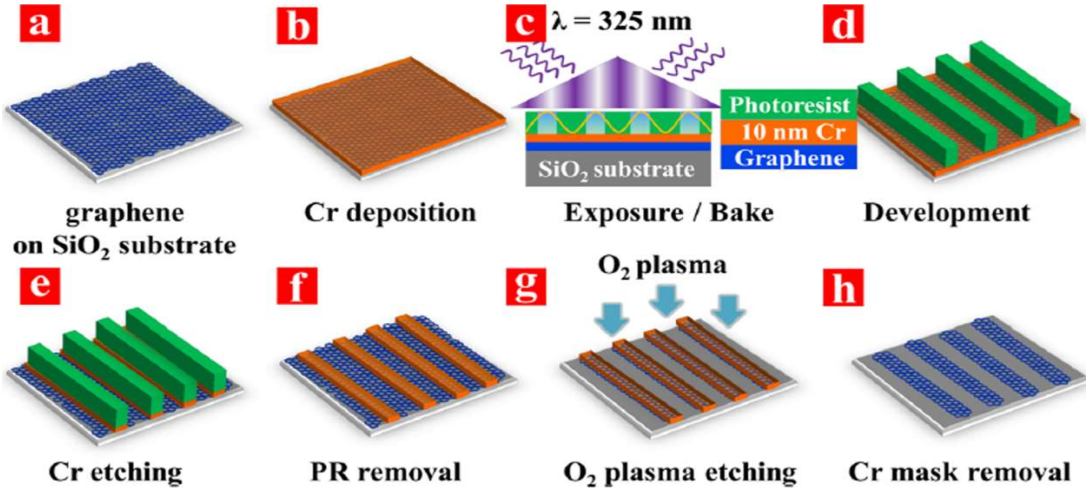

Figure 2.22 Fabrication processes of the GNR array. **(a)** Preparation of monolayer graphene/SiO_2 substrate. **(b)** Deposition of a 10-nm-thick Cr layer by electron-beam evaporation. **(c)** Spin coating of AZ GXR 601 PR on Cr/graphene/SiO_2 substrate followed by exposure to 325 nm interfered laser. **(d)** Development to produce the PR line pattern. **(e)** Wet etching of the underlying Cr layer. **(f)** Removal of the PR with acetone. **(g)** Oxygen plasma treatment to etch the underlying graphene layer with the Cr line-etching mask. **(h)** Removal of the Cr line-etching mask to reveal the GNR array. (Figure taken from ref. [177])

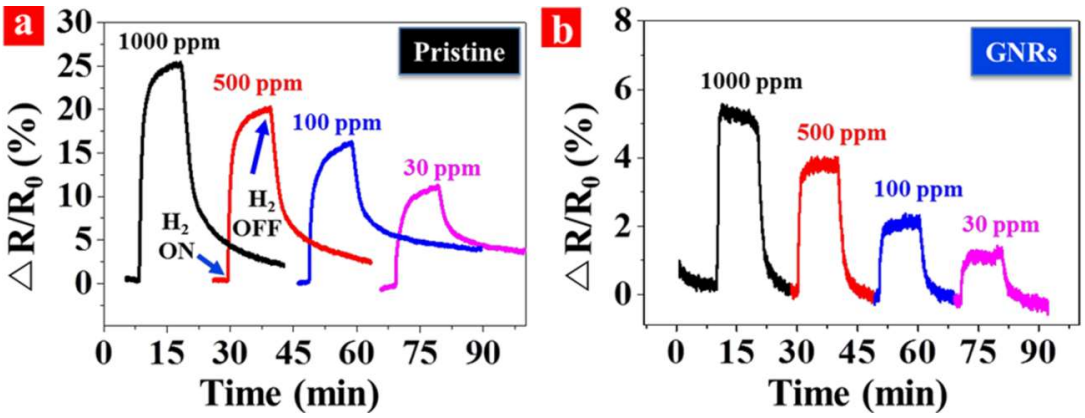

Figure 2.23 Pd-decorated hydrogen-gas-sensor performance: sensitivity change of **(a)** the IG sensor and **(b)** the GNR array sensor at different concentrations. (Figure taken from ref. [177].)

The sensing performance of RGO to NH_3 was found to be greatly improved by the decoration with Ag NPs [179]. The sensitivity was about twice than that of MWCNT/Ag hybrids, but with comparable response and recovery times of 6 s and 10 s respectively. The sensing performance got greatly affected by the loading density of NPs which is controlled by the deposition time during physical vapor deposition. The enhanced performance results from the large surface area of RGO, sufficient active sites for NH_3 adsorption and high charge carrier mobility. The oxidation state of Ag NPs rapidly changes the electronic state of RGO and the

electron transfer between NH_3 and Ag rapidly changes the carrier density of RGO which leads to fast response [179]. Cho and his co-workers [180] proved that the introduction of aluminium (Al) NPs and Pd NPs on graphene lead to improved sensitivity of graphene to NO_2 and NH_3 gases respectively.

Wang *et al.* [181] fabricated gas sensors based on RGO functionalized with Pt NPs by mid-temperature thermal annealing and ac-DEP technique, which allowed for efficient sensing of multiple gases. At RT, the RGO gas sensors with (without) Pt NPs exhibited sensitivities of 14% (7%), 8% (5%), and 10% (8%), for 1000 ppm H_2, NH_3, and NO gases, respectively. An improvement of 100%, 60% and 25%, to H_2, NH_3, and NO gases was observed for Pt functionalized RGO compared to that of RGO sensors without Pt NP decoration. The recovery/response time for H_2 gas was found to decrease with Pt decoration while for NH_3, and NO, it showed the opposite behaviour [20].

Hybrid nanostructures based on graphene and RGO not only provides enhanced sensitivity, but also good selectivity. Recently, there have been reports on the functionalization of graphene/RGO by semiconducting metal oxide NPs such as SnO_2 [182, 185, 189, 190], Cu_2O [183, 188], ZnO [184, 187, 192], WO_3 [191] and their applications as gas sensors [19].

Even though, metal oxide semiconductors exhibit excellent gas sensing properties, the high operating temperature (200-600 °C) and the low selectivity of these gas sensors limit their applications. However, metal oxide NPs functionalized with graphene/RGO are promising as sensitive and selective gas sensing elements. For instance, Mao *et al.* reported a gas-sensing platform with RGO decorated with tin oxide (SnO_2) nanocrystals (NCs), which displayed enhanced NO_2 but weakened NH_3 sensing compared to bare RGO [182]. They observed modification in the sensitivity and selectivity of RGO, by the hybrid formed with SnO_2, n-type NC on p-type RGO sheet. The sensitivity (ratio of device resistance in air to that in target gas) to a 100 ppm NO_2 increased from ~2.16 (for bare RGO) to ~2.87 for SnO_2 NC decoration on RGO sheets whereas for 1% NH_3, the sensitivity decreased from ~1.46 (for bare RGO) to ~1.12 (for SnO_2 NC decorated RGO) (Figure 2.24 (a) and (b)). For SnO_2 NC–RGO sensor, the response time was about 65 s for NO_2 and 30 s for NH_3. The reported results show great promise in tuning the sensitivity and selectivity of RGO-based gas sensors for the realization of high performance RGO-based sensors [19].

Zhou *et al.* [183] designed a RT gas sensor for the detection of H_2S gas using stable cuprous oxide (Cu_2O) NCs uniformly grown on functionalized graphene sheets (FGS), which act as molecular templates (Figure 2.25 (a)). The Cu_2O–FGS nanocomposite based sensor exhibited

fantastic sensitivity of 11% even at very low H_2S concentration of 5 ppb (Figure 2.25 (b)), which can be attributed to the synergistic effect of Cu_2O and FGS. The strong chemisorption of H_2S on Cu_2O due to high surface activity of Cu_2O along with the high electron transfer efficiency of FGS, will lead to a large increase in resistance by large electron transfer from H_2S to Cu_2O. Cu_2O–FGS nanocomposite based sensor is highly sensitive to H_2S compared to various other gases such as H_2S, NH_3, H_2, CH_4, C_2H_5OH (Figure 2.25 (b)) [183].

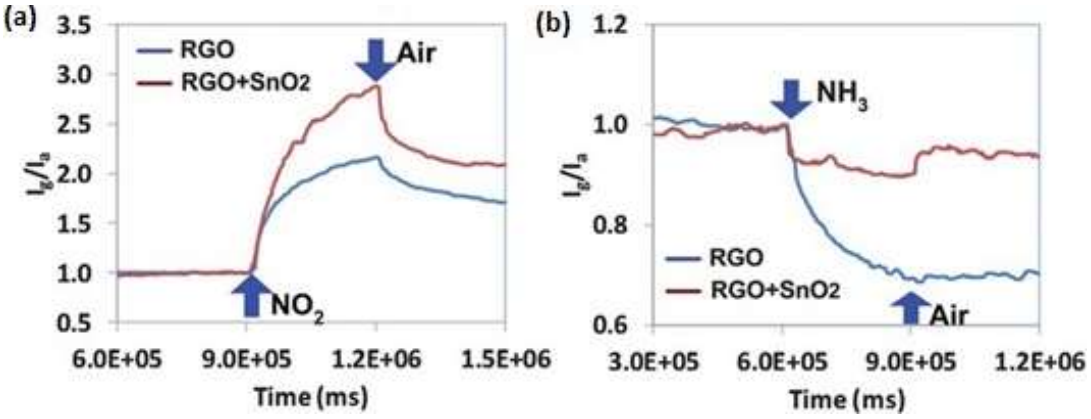

Figure 2.24 Gas sensing signals from RGO sensors with and without SnO_2 NCs to **(a)** NO_2 and **(b)** NH_3. (Figure taken from ref. [182].)

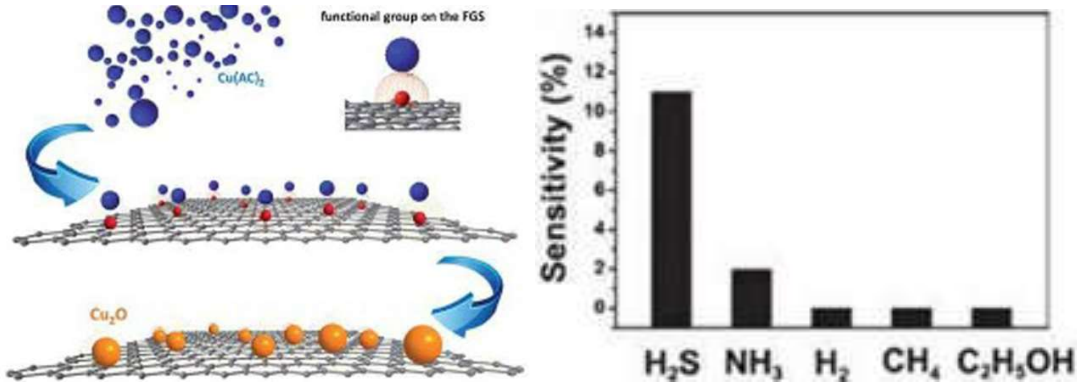

Figure 2.25 (a) Schematic illustration of in situ synthesis of Cu_2O-FGS and **(b)** Sensitivity towards H_2S (5 ppb), NH_3 (25 ppm), H_2 (25 ppm), CH_4 (25 ppm), C_2H_5OH (25 ppm). (Taken from ref. [183].)

Inspired by the good gas sensing properties of zinc oxide (ZnO) and RGO, Liu *et al.* [184] synthesized ZnO-RGO hybrids, using *in situ* production of ZnO NPs on the GO surface followed by the chemical reduction of GO. For the detection of NO_2 gas, they deposited ZnO-RGO dispersion on the microelectrode (Figure 2.26 (a)) and observed high sensitivity detection with fast response, recovery to 5 ppm NO_2 (Figure 2.26 (b) and (c)) and good selectivity [19]. The enhancement in the sensing response than those of sensors based on bare RGO comes from the modification of RGO with ZnO NPs, but still requires further studies on the understanding the gas sensing mechanism of these hybrids. In addition to high

sensitivity, these hybrid based sensors also showed high sensor response (25.6%) to 5 ppm NO_2, much higher than those of the sensor to 5 ppm of other gases such as NO, CO and Cl_2 (Figure 2.26 (d)) [184].

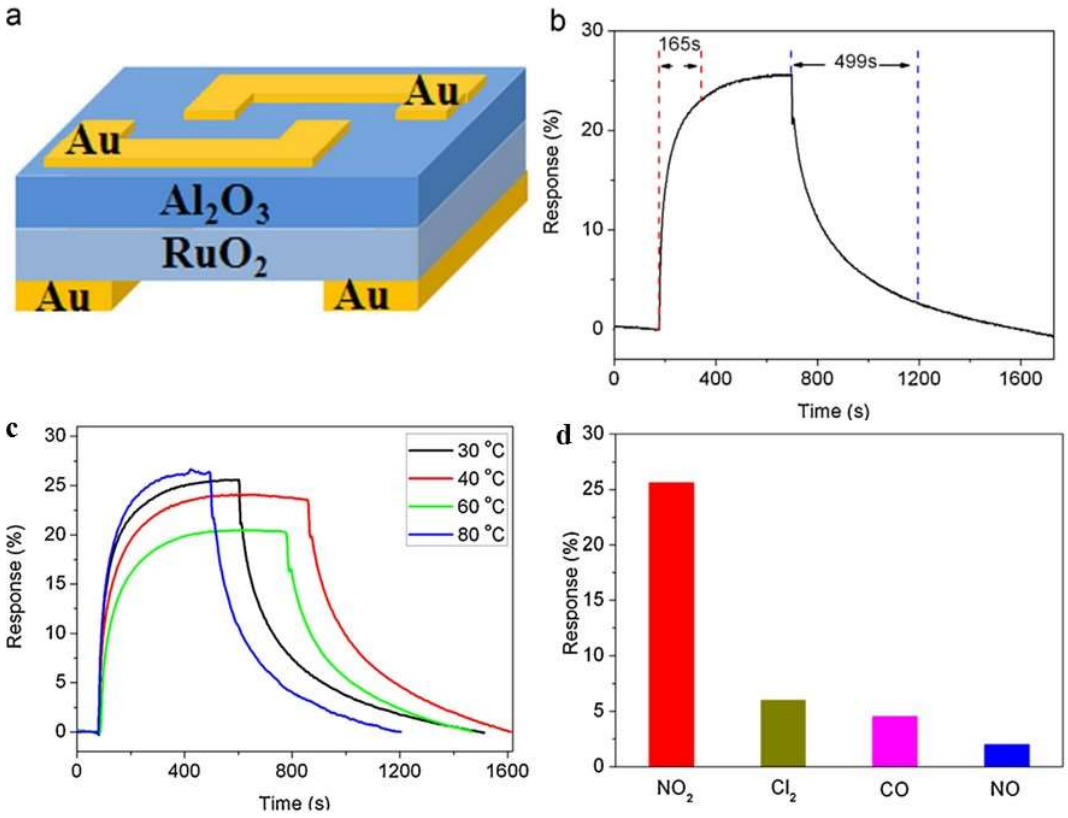

Figure 2.26 (a) Schematic of the microelectrode used for RT detection of NO_2, **(b)**. response and recovery curve of sensor based on ZnO-RGO hybrids towards 5 ppm NO_2, **(c)** response and recovery curves to 5 ppm NO_2 at different temperatures, and **(d)** selectivity toward NO_2, Cl_2, NO and CO at RT and 5 ppm gas concentration. (Figure taken from ref. [184].)

The same group investigated NO_2 gas sensing properties of RGO modified with SnO_2 NPs at low temperature [185]. SnO_2-RGO hybrids were prepared by hydrothermal treatment of GO aqueous dispersion in presence of Sn salts. They reported high sensing response to 5 ppm NO_2 gas of ~3.31 for SnO_2-RGO hybrids compared to bare RGO (Figure 2.27 (a), (b)). Other advantages of this hybrid sensor include fast response, short recovery, good selectivity and reproducibility. The improvement in the gas sensing behaviour is due to the incorporation of SnO_2 NPs into RGO matrix. This leads to optimization of the RGO resistivity, creation of more active sites for gas adsorption, and formation of heterojunction at the RGO-SnO_2 interface. The modification of depletion layer between RGO-SnO_2 interfaces by gas adsorption changes the electrical conductivity of hybrids and thus enables gas detection [185].

RGO modified by Cu_2O nanorods exhibited excellent sensitivity, linear response at RT to NH_3 gas and fast recovery after exposure to fresh air [188]. The Cu_2O/RGO composites were prepared by a two-step synthesis process in which the first step is CuO rod preparation in GO solution using cetyltrimethyl ammonium bromide (CTAB) by microwave-assisted hydrothermal method along with the reduction of GO and the second step is annealing of the complex. The enhanced sensing performance could be attributed to several factors like high surface area, outstanding catalytic activity for ORR, improved conductivity of the composite due to the superior electrical characteristics of RGO and increased gas adsorption in the hybrid composites. Similarly, a SnO_2-RGO hybrid composite synthesized by a facile hydrothermal method showed highly efficient sensing response, fast response, fast recovery and good repeatability [189]. To acetone gas, this hybrid composite had a 2-fold higher gas response than that of pure RGO film due to the three dimensional porous structure and special interactions between SnO_2 NPs and RGO sheets. These hybrid composites also showed ppm-level detection of ethanol, and the detection principle is based on charge transfer between adsorbed gas molecule and p-type semiconducting SnO_2-RGO hybrids [190].

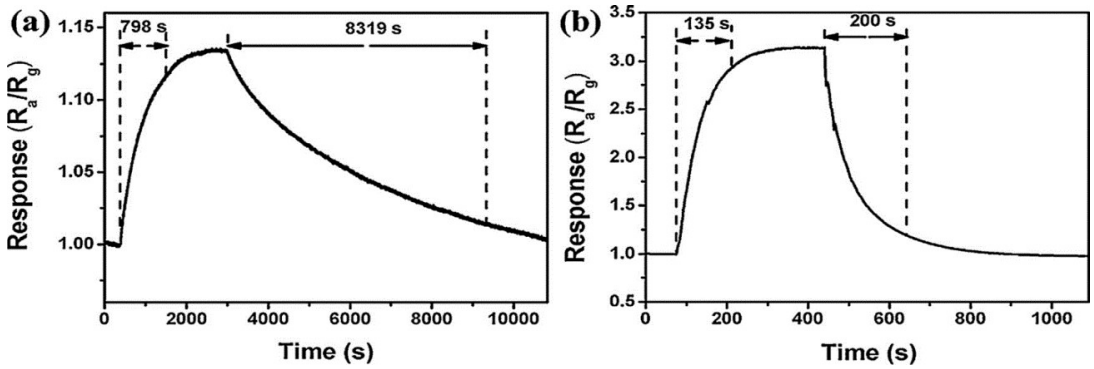

Figure 2.27 (a) The response curve to 5 ppm NO_2 of the sensors based on RGO at 50 °C. **(b)** The response curve to 5 ppm NO_2 of the sensors based on SnO_2-RGO at 50 °C. (Figure taken from ref. [185].)

The combination of one-pot polyol process and metal organic decomposition method was employed to develop a NO_2 gas sensor based on RGO/tungsten trioxide (WO_3) nanocomposite film [191]. By adding few RGO to WO_3 film, a drastic increase in the sensing response of RGO/WO_3 nanocomposite film was seen. On exposure to NO_2, the nanocomposite doped with 3.2% RGO showed the best performance compared to other tested sensors with different degrees of RGO doping [19].

Highly dispersed ZnO NPs on RGO showed acetylene gas sensing capability with a sensing response of 143 at 250 °C for an optimized ZnO and RGO material ratio of 4:1 [192]. In addition to this, high selectivity, prolonged stability, quick response and recovery were also

achieved. The physical properties of the ZnO/RGO composites synthesized by solvothermal method showed that RGO promotes the attachment of ZnO particles and prevents the particle agglomeration without significant changes in morphology and crystal structure.

Recently, gas sensors based on graphene transistors decorated with SnO_2 NPs exhibited high selectivity, fast response and short recovery (~1 s) to 100 ppm H_2 at 50 °C [194] (Figure 2.28 (a-c)). FETs based on graphene decorated with metal oxide NP were employed for developing high performance hydrogen gas sensors. The extremely high surface-to-volume ratio and the abundance of dangling bonds by the decoration of graphene with metal oxide NPs, resulted in strong interactions of gas molecules in the surroundings through the grain boundaries and unsaturated bonds of metal oxide NPs on graphene (Figure 2.29 (b)), which ultimately resulted in excellent H_2 sensitivity of the graphene-metal oxide NP hybrid, compared to IG (Figure 2.29 (a)). Graphene facilitates quick transfer of electrons from metal oxide NPs due to the insignificant Schottky barrier caused by the matching work functions of NPs and graphene. They observed an increase in output current with increase in H_2 concentration from 1 ppm to 100 ppm with good reproducibility (Figure 2.28 (b)). The achieved lowest resolution limit of 1 ppm proves the potential of SnO_2 NP-graphene for high sensitive low level detection of H_2 gas [20].

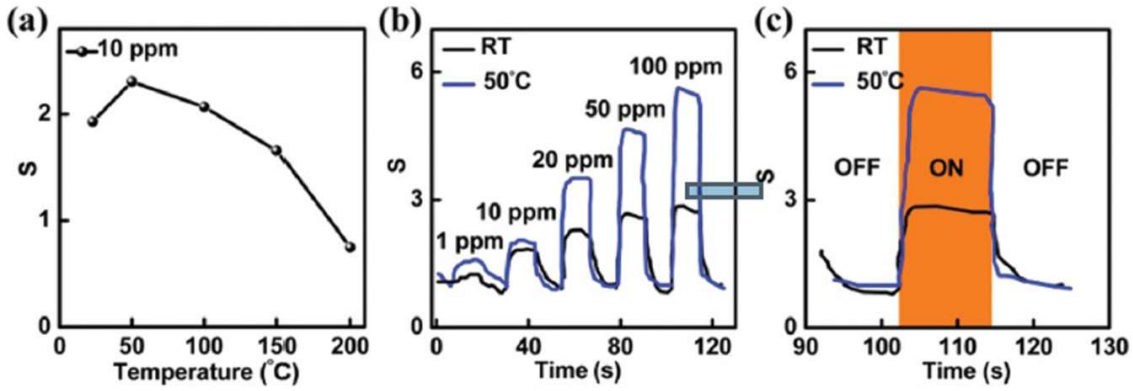

Figure 2.28 (a) The sensitivity of the gas sensor decorated with SnO_2 NPs at various temperatures; **(b)** Real-time dynamic response of gas sensors decorated with SnO_2 NPs exposed to different H_2 concentrations at different operation temperatures; **(c)** The response and recovery times of the sensor exposed to the 100 ppm H_2 concentration. (Figure taken from ref. [194].)

Other graphene-based nanohybrids are also explored as chemical sensors. The gas sensing properties of graphene-based ternary composites have also been analyzed. In this direction, Wang *et al.* [193] prepared CuO-ZnO/RGO composite by one-step hydrothermal method and studied the acetone sensing potential. The obtained sensitivity was about 1.5 and 2 times higher than CuO-ZnO and ZnO/RGO towards acetone and had no response to ethanol, thus exhibiting high selectivity to acetone, about 6-41 times greater than that of other vapors. The

successful anchoring of large number of nanoscale p-n junctions between CuO and ZnO NPs onto RGO sheets promotes the sensing behaviour towards acetone.

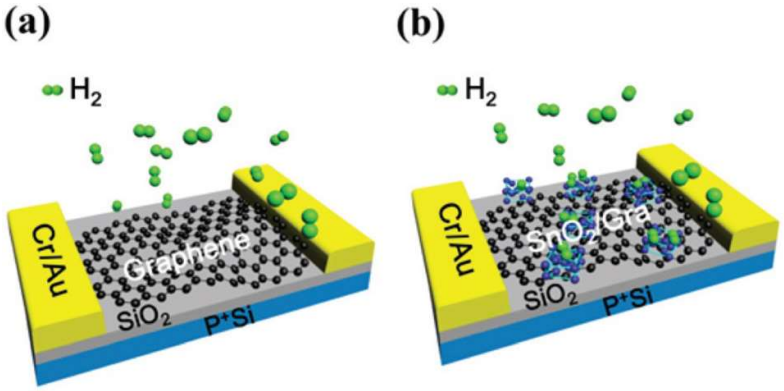

Figure 2.29 (a) The schematic of graphene transistor without obvious sensitivity to hydrogen; **(b)** The schematic of graphene FET decorated by metal oxide NPs with obvious sensitivity to hydrogen. (Figure taken from ref. [194].)

A highly sensitive and selective NO_2 gas sensor based on indium (In)-doped SnO_2 NP decorated RGO was fabricated using a simple one-pot aqueous method at low temperature [227]. The observed much higher sensitivity of In-doped SnO_2-RGO (RGO–IDTO) nanohybrids compared with RGO–SnO_2 (Figure 2.30 (a) and (b)) is due to the increase in the number of surface oxygen ion species in NCs induced by the dopant atom, that are capable of reacting with NO_2 gas molecules. The RGO-IDTO nanohybrid based sensor also demonstrated excellent selectivity to NO_2 in the presence of other common gases such as NH_3, H_2, CO and H_2S (Figure 2.30 (c) and (d)) [227].

Several reports have also shown highly selective gas detection using RGO through functionalization with quantum dots (QDs) [228, 229], NWs [230] and CNTs [231]. Graphene nanohybrids decorated with ZnO QDs fabricated by a facile solution-processed method, showed an enhancement in formaldehyde sensing by 4 times compared to IG at RT due to the synergistic effect of graphene and ZnO QDs [228]. In addition to the improved sensitivity, ZnO QDs/graphene nanocomposite based sensors also exhibited fast response of 30 s and recovery of 40 s, good selectivity and stability. Composites of graphene with Al_2O_3 QDs tested for CO_2 sensing showed higher sensing response, which was linear with the addition of graphene in constant 1 g Al_2O_3 [229]. A high performance ammonia sensor using graphene and Ag NW hybrids with two Ag planar electrode arrays was developed by Trung *et al.* [230]. The sensor showed a sensitivity of 28% at RT (change in resistance to original resistance, $\Delta R/R_0$), which is about eight times the sensitivity ($\Delta R/R_0$ ~3.5%) of IG-based ammonia sensor (Figure 2.31 (a)) with response and recovery time of ~200 and 60 s,

respectively. The reported high sensitivity of RGO-Ag NW composite is due to its improved electrical properties since Ag NWs play the role of small bridges connecting many graphene islands synthesized by chemical methods together (Figure 2.31 (b)) [19].

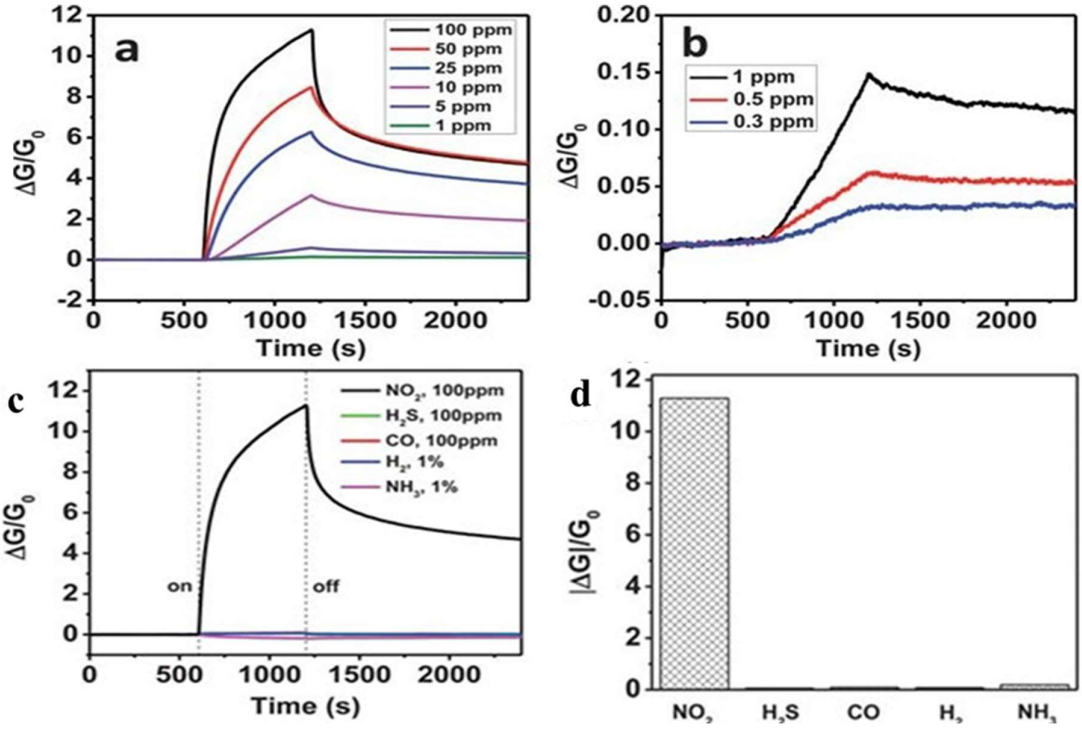

Figure 2.30 (a) and **(b)** Dynamic sensing response of RGO–IDTO towards different NO_2 concentrations, **(c)** sensing responses, and **(d)** sensitivity to various gases. (Figure taken from ref. [227].)

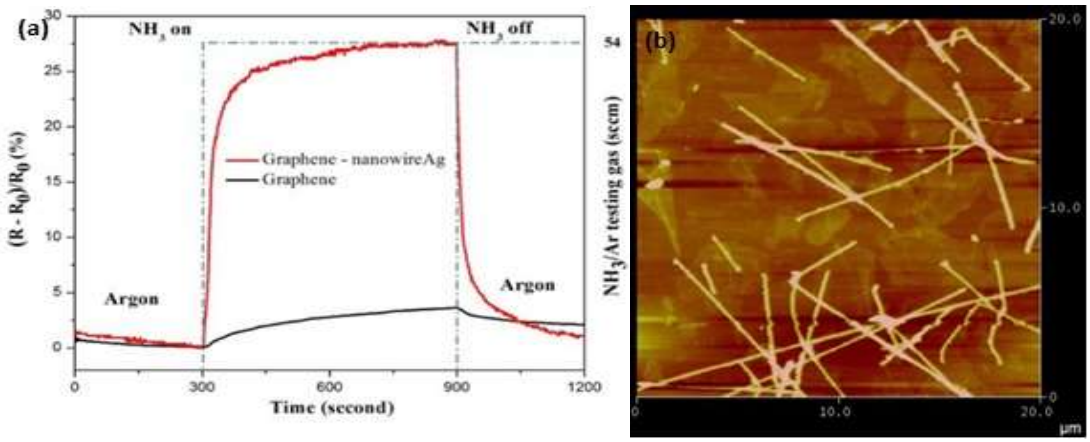

Figure 2.31 (a) Comparison between the response of the RGO and RGO–Ag NWs composite sensors. **(b)** AFM image of RGO–Ag NWs composite expressing the connecting role of Ag NWs between RGO islands. (Figure taken from ref. [230].)

Summary of the sensing characteristics of gas sensors based on NPs hybrids with graphene, GO and RGO are provided in Table 2.4 [19].

Table 2.4 Summary of gas sensor parameters of graphene/NP hybrid based gas sensors.

Type	NP	Gas	Conc. (ppm)	Sensor Response	Response Type[a]	Response time (min)	Recovery time (min)	Ref.
IG	Pd	H_2	1000	5%	ΔR	1.0	1.5	[177]
	Pt	H_2	1000	~33%	ΔR	~1	-	[176]
		H_2	3000	~3%	ΔR	-	-	[232]
		H_2	10^4	66.1 mV	ΔV	1.25	249	[233]
	SnO_2	NO_2	50	-6%	ΔR	3.15	3.75	[234]
	WO_3	NO_2	1	96%	ΔR	0.42-3.3	0.42-3.3	[235]
	Cu(x)O	NO_x	97	95.1%	ΔR	0.16	-	[236]
	Fe_2O_3	H_2S	15	450	AdU	$8.3x10^{-6}$	< 05	[237]
	Sb_2O_3	CO_2	50	< 60%	ΔR	0.26	0.35	[238]
	Bi_2O_3	LPG	30	400%	ΔR	0.26	0.33	[239]
	TiO_2	O_2	100000	20%	ΔR	3.2	2.25	[240]
GO	CNTs	H_2O	-	9.8%	RH	0.2	0.1	[241]
	ZnO	CO	22	~ 243%	ΔG	~ 5	~2-5	[187]
		NH_3	1	~ 24%	ΔG	~ 6	~2-3	
		NO	5	~ - 5 %	ΔG	~1500	-	
RGO	MWCNTs	NO_2	10	20 %	ΔR	60	> 60	[231]
	NiO	NO_2	1	200 %	ΔR	-	-	[242]
	ZnO	NO_2	5	25.6 %	ΔR	2.75	8.3	[184]
	Co_3O_4	H_2	200	250%	ΔR	0.35	1.5	[243]
		CH_3OH	800	8%	ΔR	< 1-2	< 1-2	[244]
		NO_2	60	80%	ΔR	< 1-2	< 1-2	[244]
	$Co(OH)_2$	NO_x	97	70 %	ΔR	-	-	[245]
	$C_{32}H_{16}CuN_8$	NH_3	3200	15.4 %	ΔR	-	-	[246]
	MnO_2	LPG	25	50%	ΔR	0.27	0.32	[247]
	Pd-WO_3	H_2	100	7200%	ΔG	0.59	0.61	[248]
	SnO_2	H_2S	5	2400%	ΔR	< 3.3	<2.6	[249]
		$(CH_3)_2CO$	5	900%	ΔR			
		NO_2	5	231%	ΔR	2.25	3.3	[185]
	WO_3	NO_2	20	102%	ΔR	-	-	[250]
	$ZnFe_2O_4$	$(CH_3)_2CO$	1000	810%		0.012	0.41	[251]
	Pt	H_2	10000	22 mV	ΔV	-	-	[252]
FGS	Cu_2O	H_2S	5	11%		-	-	[183]

[a] $\Delta R = \frac{R_g - R_a}{R_a}$; $\Delta V = V_g - V_a$; $\Delta R = \frac{R_g - R_a}{R_a}$; $\Delta V = V_g - V_a$; $\Delta G = \frac{G_g - G_a}{G_a}$;

AdU≡Adsorption units; V≡ voltage , G≡ conductance, Z ≡impedance. a and g refer to air and gas

2.4.4.3 Graphene/polymer hybrid based gas sensors

Studies on the functionalization of CNTs with an intrinsically conducting polymer, polyaniline (PANI) have demonstrated improved gas sensing performance [253, 254]. Graphene and RGO are also functionalized with polymers to combine the benefits of the two materials, graphene and polymers. The reported graphene/RGO based polymer hybrids have

also shown enhancement in sensing properties compared to bare graphene/RGO [195-206]. For example, RGO functionalized with PANI (RGO-PANI hybrids) exhibited much rapid increase in resistance of 59.2% upon exposure to 50 ppm NH_3 gas as compared to a resistance change of about 5.2% and 13.4% for bare RGO and bare PANI nanofiber based sensor, respectively (Figure 2.32). The sensitivity of RGO-PANI nanofiber hybrid to NH_3 gas is 3.5 times higher than the sensitivity of bare PANI nanofiber sensor and 10.4 times higher than the sensitivity of bare RGO. This much better sensitivity is due to the combined effect of RGO sheets and the decorated PANI NPs [195]. Nevertheless, they observed a long recovery period of ~4 min for sensing device based on RGO-PANI hybrids due to the high surface ratio of RGO sheets and PANI NPs. These hybrids also exhibited good reversibility, stable sensing performance for a long period of time (even after several months) under normal operating conditions and high selectivity to NH_3 gas in the presence of different analysts such as DMMP, methanol, dichloromethane, cyclohexane, and chloroform. Huang *et al.* [195] compared the NH_3 gas sensing performance of RGO–PANI hybrids sensor with other sensors as summarized in Table 2.5 [19].

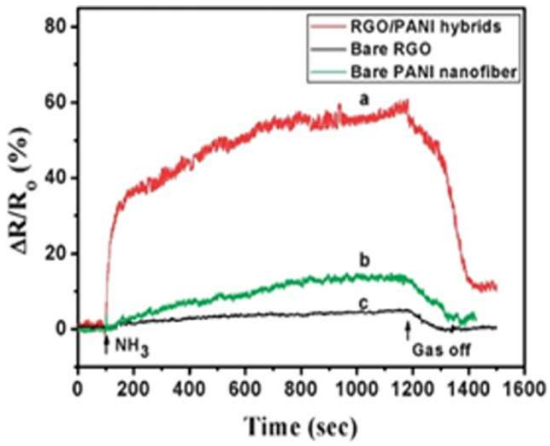

Figure 2.32 The response curve of **(a)** RGO–PANI hybrids, **(b)** bare PANI nanofibers and **(c)** bare RGO to NH_3 gas under the concentration of 50 ppm. (Figure taken from ref. [195].)

A similar comparative study on the toluene sensing behaviour of PANI and graphene/PANI nanocomposite (C-PANI) films at different temperatures (30, 50 and 100 °C) were performed by Parmer *et al.* [196]. They observed an increase in sensor response of both PANI and C-PANI films with increase in the operating temperature. However, the response and recovery time behaviour of both films were quite different. Even though the sensor response of C-PANI films (8.4 at 30 °C, 11.6 at 50 °C, 35.5 at 100 °C) is lower than that of PANI films (12.6 at 30 °C, 18.9 at 50 °C, 38.4 at 100 °C), C-PANI showed better overall sensing

performance in terms of its response and recovery time. Better sensing behaviour in terms of response and recovery time was observed at 50 °C [196].

Table 2.5 Response of sensors based on RGO-PANI hybrid, TiO_2-PANI hybrid, PANI nanofiber, RGO and graphene foam to detection of 50 ppm NH_3.

Sensing Materials	Response (%)	Ref.
RGO–PANI hybrids	59.2	[195]
Bare PANI nanofibers	13.4	[195]
Bare RGO	5.2	[195]
Graphene foam	~6	[255]
TiO_2–PANI hybrids	~35%	[256]

Huang *et al.* [197] compared the NH_3 sensing response of RGO reduced from aniline (RGO-A) with RGO reduced from hydrazine (RGO-H) and polyaniline nanofiber (RGO-PANI). RGO-A based gas sensor, fabricated through drop drying RGO nanosheets suspension between the electrode arrays, exhibited good repeatability and selectivity to NH_3. Upon exposure to 50 ppm NH_3 gas, the achieved sensor response was about 9.2 times and 3.5 times higher than RGO-H and RGO-PANI nanofiber based sensor respectively. The attached oxidized aniline on the surface of the RGO film plays a significant role in the sensing performance of the device [197].

Ye and co-workers [198] have used RGO/Poly (3-hexylthiophone) (P3HT) composite films for fabricating NH_3 gas sensors and the RGO/P3HT films showed better sensitivity than RGO film sensor (Figure 2.33). The superior surface morphology of the composite films and the π-π interactions between the P3HT and RGO films resulted in this increased sensor response.

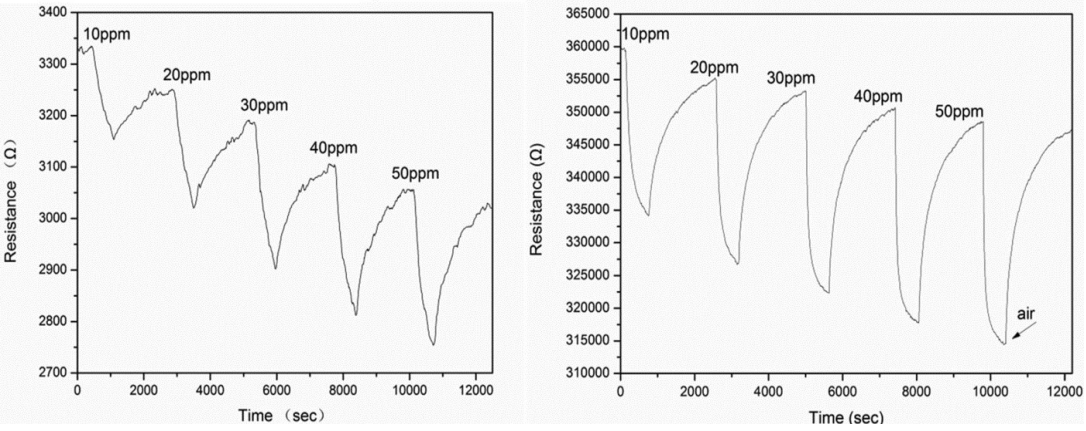

Figure 2.33 Real time response curve of (a) RGO and (b) RGO/ P3HT sensor exposed to NH_3. (Figure taken from ref. [198].)

The reported sensing parameters include sensitivity (7.15 for RGO/P3HT films; 5.37 for RGO), response time (141 s for RGO/P3HT films; 637 s for RGO films), and recovery time (488 s for RGO/P3HT films; 609 s for RGO films).

Mishra and co-workers tested the detection of NH_3, H_2S, Cl_2, H_2 and N_2 with surface plasmon resonance (SPR) based fibre optic gas sensors using nanocomposite films of PMMA, RGO, PMMA/RGO [199]. The sensing probes were fabricated by coating copper film onto the unclad portion of the optical fibre using thermal evaporation followed by a coating of PMMA, PMMA/RGO nanocomposite film over layer. The SPR spectra of the transmitted light recorded a red shift in the resonance wavelength with NH_3 in the chamber (Figure 2.34). The probes with PMMA/RGO over layer showed higher sensitivity. The sensor had wide operating range, reproducibility, reusability, with added advantages of low cost, remote operation, probe miniaturization due to sensor fabrication of optical fibre [199].

The NO_2 detection behaviour of organic thin film transistor (OTFT) based gas sensors employing pure P3HT film and RGO/P3HT bilayer films were compared and the results demonstrated an 80% improvement in the sensing response of OTFT gas sensor based on RGO/P3HT bilayer film due to the deposited RGO as the bottom layer of the bilayer film [200]. The peculiar features of RGO such as large surface area and availability of many graphitic carbon atoms as active sites for NO_2 adsorption resulted in larger sensitivity of RGO/P3HT based OTFT gas sensor. On exposure to other gases such as NH_3, SO_2, CO, CO_2 and H_2S, the sensing response of RGO/P3HT based sensor was two orders of magnitude lower than that of NO_2, owing to the presence of P3HT layer that prevents the interference gases from contacting RGO.

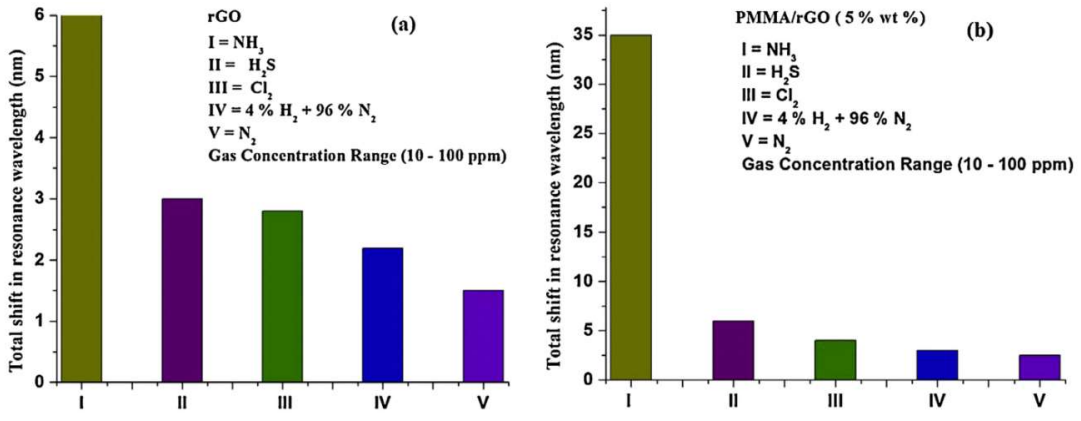

Figure 2.34 Total shift in the resonance wavelength for the concentration range 10–100 ppm of different gases with **(a)** RGO as a sensing layer, and **(b)** PMMA/RGO nanocomposite as a sensing layer. (Figure taken from ref. [199].)

An efficient chemiresistive sensing platform using RGO based nanocomposite with porous conducting polymer poly (3, 4-ethylenedioxythiophene) (PEDOT) showed great promise for high performance gas sensing due to the enhanced sensitivity and selectivity of the gas sensor to NH_3 gas at ppb-level [201]. The enhanced sensing behaviour compared to bare RGO and common PEDOT is due to the large surface area and very open structure of the nanocomposite. Due to the uniform distribution of the porous PEDOT network on RGO, high selectivity to NH_3 gas was also observed. Seekaew and his co-workers developed a gas sensor in which graphene–poly(3,4-ethylenedioxythiophene):poly(styrene sulfonate) (PEDOT:PSS) composite film was employed as the sensing film and the NH_3 sensing properties at RT were investigated [202]. The sensor was fabricated by a simple, low-cost and practical inkjet-printing technique in which electronic ink of graphene dispersion in PEDOT: PSS conducting polymer solution is printed on a transparency substrate with prefabricated electrodes. High sensitivity and selectivity of the ink-jet printed graphene-PEDOT: PSS to NH_3 was observed at RT owing to the increased specific surface area of graphene and enhanced interactions between the nanocomposite film and NH_3 molecules through the π-electrons network [202].

Recently, a highly sensitive and selective hydrogen gas sensor based on PMMA membrane-coated Pd NP/SLG hybrid was fabricated by the spin coating of PMMA membrane layer on a Pd NP deposited CVD graphene by employing a graphene-buffered galvanic displacement reaction between Cu and Pd ions [257]. The sensor did not show any response to CO, NO_2 or CH_4 gas due to the selective filtration of H_2 by the polymer membrane coating on the Pd NP/SLG hybrid. Upon exposure to 2% H_2, this hybrid sensor showed sensing response of 66.37% within 1.81 min and a recovery within 5.52 min [257]. These works suggest that the low selectivity issue of graphene/RGO could get benefit from the functionalization of graphene with polymers.

Graphene modified with other polymers such as polyethylenimine (PEI) [203], nylon-6 [204], polypyrrole [205, 206] etc., have also been tested for evaluating the sensitivity of these graphene composite films towards different gases. All these reports show that graphene/polymer nanohybrids are more suitable for gas detection than bare graphene and polymer films. The sensing performance of these graphene-polymer hybrids towards different gas molecules is provided in Table 2.6 [19].

Table 2.6 Summary of gas sensor parameters of graphene/polymer hybrid based gas sensors

Type	Polymer	Gas	Conc. (ppm)	Response ΔR	Response time (min)	Recovery time (min)	Ref.
IG	Polyethylenimine	CO_2	3667	2.1%	10	10	[203]
	Polypyrrole	H_2O		138	0.25	0.33	[205]
	Polyaniline	NH_3	20	3.65	0.83	0.35	[258, 259]
	PMMA membrane-coated Pd NP	H_2	2 %	66.67%	1.81	5.52	[257]
RGO	Nylon-6	$(CH_3)_3N$	45	7.38%	1.67	-	[204]
	Polymethyl methacrylate	HCHO	2	13.7%	-	Slow	[260]
	Poly(3- hexylthiophene)	NH_3	10	7.15%	1.34	8.1	[198]
	Polyaniline	NH_3	50	31.7%	18	~ 2	[197]
		NH_3	50	59.2%	~ 15	~ 4	[195]
		$C_6H_5CH_3$	100	35.5%	~ 11	~54	[196]
		H_2	10000	16.57 %	-	-	[261]

2.5 Theoretical Aspects

Theoretical studies based on first-principles have drawn the attention of scientists because they enable the study and analysis of the interactions of various gas molecules with new materials and the results provide insights into new and improved sensor designs before going for expensive experimental analysis. Moreover, these theoretical studies can improve our understanding and analysis of the existing experimental results [19]. The excellent gas sensing properties of graphene have inspired theoreticians to investigate the interactions between the graphene surface and the adsorbate molecules. In the first-principles or *ab initio* studies on the gas sensing capability of graphene, the most stable adsorption position and orientation of gas molecules on graphene are determined by considering different positions and orientations of the molecules above the graphene sheet. The adsorption energies, direction of charge transfer (from gas molecules to graphene or vice versa) are calculated based on the most favourable adsorption configuration. The total DOS of graphene-gas molecule adsorption system provides further insights into the effect of gas molecule adsorption on the electronic structure of graphene. There have been many reports on theoretical studies of gas molecular adsorption on graphene. The theoretical aspects of the sensing performance of graphene-based materials [19] are summarized in the following sections.

2.5.1 Gas adsorption on IG, GNR, GO and RGO

Even though the detection of NH_3, CO, NO_2 and H_2O diluted in concentrations of 1 ppm had been demonstrated experimentally using graphene [30], understanding of physical mechanism behind chemical doping and related excellent chemical sensor properties of graphene had been lacking [262]. The first work in this direction was by Wehling *et al.* [262], who conducted both theoretical and experimental investigation on doping of graphene induced by gas adsorbates. They proved that DOS of graphene is suitable for chemical sensing and they also explained the experimentally observed single molecule NO_2 detection by graphene [30]. In this way, the presence of strong acceptor level due to individual NO_2 in graphene had been predicted [262].

Leenaerts *et al.* [32] studied the interactions between IG and different gas molecules such as H_2O, NH_3, CO, NO_2 and NO using first-principles simulations based on DFT calculations. Their results showed that H_2O, NH_3, CO, NO_2 and NO are only physically adsorbed on IG. Molecular doping was discussed in the light of DOS and molecular orbitals of the adsorbates. Moreover, the charge transfer analysis indicated that NO_2 and H_2O serve as electron acceptors whereas CO and NH_3 serve as electron donors, in agreement with the previous experimental findings [30].

The adsorption of NH_3 molecule onto IG has been investigated using molecular mechanics and DFT based calculations [263]. The energetically stable position for the adsorption of NH_3 on graphene surface was the top of the center of the carbon hexagon (H) from both DFT (Figure 2.35 (a)) and molecular mechanics based studies (Figure 2.35 (b)).

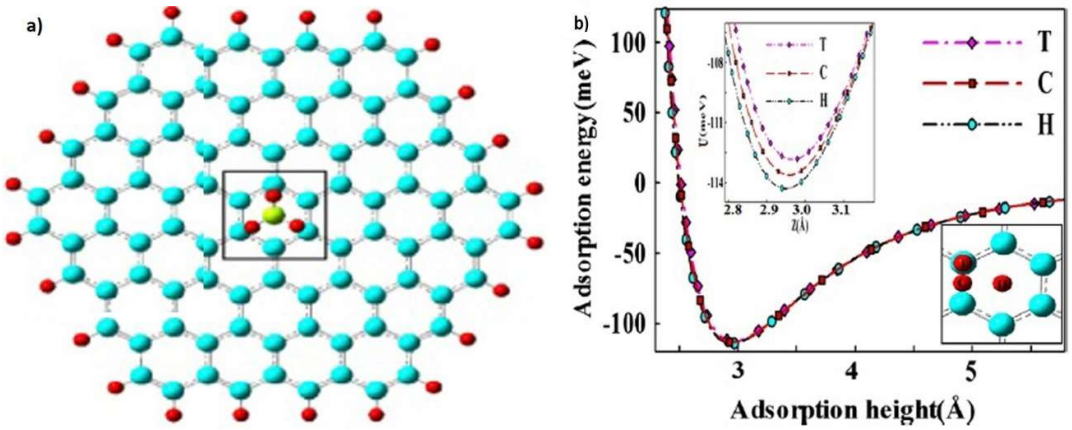

Figure 2.35 (a) Optimized structure of NH_3 adsorbed graphene from DFT, (**b)** The molecular mechanics result for NH_3 adsorption onto graphene sheet in three possible positions of NH_3 on graphene surface, T (top of a carbon atom); C (top of the center of the C–C bond) and H (top of the center of carbon hexagon) (Figure taken from ref. [263].)

The calculated adsorption energy (E_{ad}) of ammonia molecule on the hydrogen terminated graphene flake was 0.01 eV, which indicates weak physisorption. The DOS plots of graphene flake with and without NH_3 molecule revealed that the interactions between NH_3 and graphene flake does not change the electronic structure of graphene flake significantly (Figure 2.36) [263].

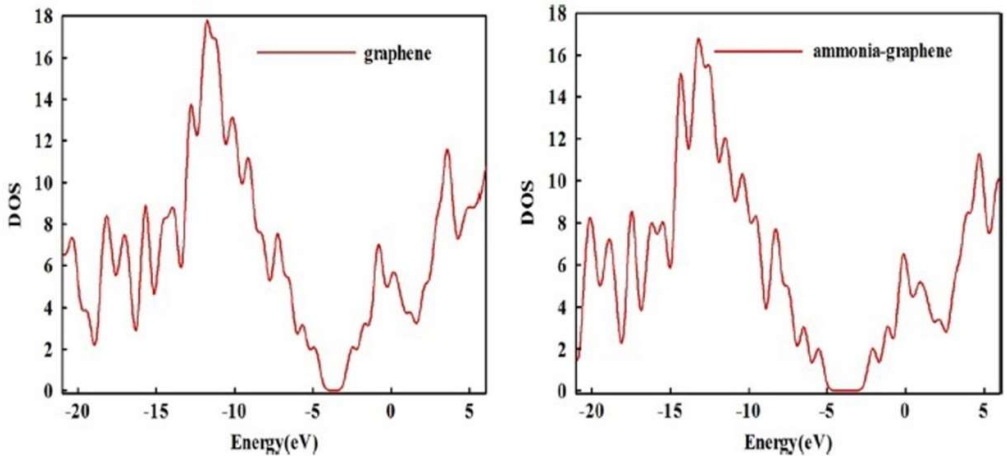

Figure 2.36 DOS spectrum of graphene and ammonia–graphene (Figure taken from ref. [263].)

Several studies focused on the use of GNR, a quasi-one-dimensional material with chemically active dangling bond (DB) defects obtained by patterning graphene through standard lithographic techniques for the detection of NH_3 [264, 265], NO_2 [264, 265], CO [264-266], O_2 [264, 265], N_2 [264], CO_2 [264-267], and NO [264]. DFT investigation of the adsorption of various gas molecules around the sites of DB defects on semiconducting GNRs with armchair-shaped edges (AGNRs) indicated energetically favourable adsorption of CO, NO, NO_2, O_2, CO_2, and NH_3 on AGNR, except that the N_2 adsorption is endothermic in nature [264]. The adsorption energies of CO, NO, NO_2, and O_2 on AGNR are larger than 1 eV, which indicates strong chemisorption. For CO_2 and NH_3 adsorption, the adsorption energies are -0.31 eV and -0.18 eV respectively which indicate that the adsorptions lie between strong physisorption and weak chemisorption. They also showed that all gas molecules influence the electronic structure of AGNRs. Quantum transport calculations indicated that semiconducting AGNRs can be employed for selective detection of NH_3 out of the other gas molecules due to the modification of the conductance of AGNR by NH_3 adsorption, while all others have little effect on conductance. The charge transfer analysis on the adsorbed configurations showed that CO, NO, NO_2, O_2, and CO_2 act as electron acceptors whereas NH_3 act as electron donor (Table 2.7). From these results, it could be concluded that the interactions of gas molecules with GNR edges are much stronger than that with graphene or GNR surface [264].

Table 2.7 summarizes the results obtained from first-principles simulations of IG and AGNR-gas molecule systems, which shows large adsorption energies and large charge transfer of gas molecules on GNR edges as compared to that observed on the surface of IG. This is due to the chemically reactive edges of AGNR as compared to IG having highly stable sp^2-bonded carbon atoms [19].

Paulla and Farajian used second order Møller–Plesset calculations (MP2) calculations and DFT to examine the detection capability of AGNR having ~1 nm width for CO and CO_2 gas molecules [266]. These gas molecules undergo physisorption on AGNR with binding energies of -0.35 eV for CO_2 and -0.252 eV for CO with low charge transfer values ranging from -0.005 e^- to +0.005 e^- respectively. Quantum conductance calculations on AGNR based nanosensor showed shift in the conductance characteristics on the order of few meV, compared to pure AGNR for the adsorption of one and two molecules per two unit cells of AGNR.

Table 2.7 E_{ad} and charge transfer (ΔQ) for IG and AGNR-gas molecules.

Type	Gas	E_{ad} (eV)	ΔQ (e)	Ref.
IG	NH_3	0.031	0.027	[32]
	H_2O	0.047	-0.025	
	NO_2	0.067	-0.099	
	CO	0.014	0.012	
	NO	0.029	0.018	
AGNR	NH_3	-0.18	0.27	[264]
	CO	-1.34	-0.30	
	NO_2	-2.7	-0.53	
	NO	-2.29	-0.55	
	O_2	-1.88	-0.78	
	CO_2	-0.31	-0.41	
	N_2	0.24	-	

The effect of concentration of O_2 molecule adsorption on the electronic properties of semiconducting AGNRs with hydrogenated edges (HEAGNR) has been investigated *via* DFT [268]. The adsorption energy calculations for different positions of gas molecule on HEAGNRs indicated that the carbon atoms at the edges are the most favourable centres for adsorption. The results showed decrease in the energy gap with increase in the concentration of O_2 molecule and the energy gap disappears at gas concentration of 0.02. This dependence of the electronic properties of HEAGNR on gas concentration could be used for sensing O_2 gas [268].

IG undergoes weak interactions with gases due to the absence of DBs on its surface along with its high stability arising from the strong sp^2 carbon-carbon bonds [19]. The structural

properties and electronic structures of gas molecule-adsorbed IG systems do not show any significant change after gas adsorption, which implies that IG is not sensitive to most of gas molecules and hence not suitable for practical use [32, 36].

Few reports on theoretical understanding of molecular adsorption on GO and its comparison with graphene also exist. Peng *et al.* [269] proved that GO could be used as a good sensor for the detection of ammonia in comparison with graphene, since the surface epoxy and hydroxyl groups of GO promote the interactions between ammonia and GO. The calculated adsorption energy and the charge transfer for NH_3 on IG's surface were small. The simulation results proved that adsorption energy and charge transfer of ammonia for the hydroxyl groups is greater than that of epoxy groups of GO. The results have shown that doping of graphene with -O and -OH species could increase the adsorption energy and the charge transfer of the NH_3 adsorbate (Table 2.8). Adsorption of NH_3 on epoxy or hydroxyl groups that exist on the basal plane of graphene does not show an appreciable increase in the adsorption energy (Table 2.8).

Table 2.8 E_{ad} and ΔQ of NH_3 adsorbed on IG and GO [269]

Type	E_{ad}	ΔQ (e)
IG	0.112	0.004
GO with one epoxy group	0.143	0.128
GO with two epoxy groups	0.219	0.009
GO with one hydroxyl group	0.175	0.018
GO with two hydroxyl groups	0.840	0.136
GO with both epoxy and hydroxyl groups on the basal plane	0.270	0.050

First-principles calculations of the interactions between nitrogen oxides NO_x (x = 1, 2, 3) and N_2O_4 with graphene and GO [270] demonstrated that the presence of active defect sites on GO such as hydroxyl, carbonyl and their nearby carbon atoms lead to stronger adsorption of nitrogen oxides on GO than graphene. The sufficient active sites on GO increases the adsorption energy and enhances the charge transfer from NO_2 to GO which result in chemisorption of gas molecules on GO. The DOS graphs of gas molecule-adsorbed GO showed strong hybridization of frontier orbitals of NO_2 and NO_3 with the electronic states around the Fermi level of GO, which resulted in strong acceptor doping of GO by these gas molecules [270].

Mattson *et al.* [271] reported *in situ* infrared (IR) microspectroscopy investigation of NH_3 adsorption on RGO to study the dynamics of adsorption under various realistic working conditions (i.e. ambient pressure) along with DFT results. The interactions between NH_3 and RGO with chemically reactive sites such as the epoxide groups and carbon vacancies result in

the formation of different surface species such as physisorbed NH_3, wide variety of chemisorbed fragments such as NH_2, OH, and CH due to the dissociation of NH_3 by the carbon vacancies and epoxide groups. The calculations have shown that the chemisorbed fragments such as NH_2, OH, and CH can produce small electron donor effect [271].

2.5.2 Gas adsorption on modified graphene

Theoretical studies have proved that introduction of dopants and defects on graphene drastically improved the sensitivity of graphene-based gas sensors by stronger adsorption of gas molecules on doped and defective graphene, as compared to IG [19].

Doping and functionalization of graphene with other atoms or molecules is an important approach for tailoring its electrical properties, which had been successfully proved for other nanostructures such as CNTs. Upon heteroatom doping, the carbon atoms in the crystal lattice are substituted with other atoms such as N, B, S, Si, etc. and their introduction into the lattice would disturb the sp^2 hybridization of C atoms that lead to changes in graphene's electronic properties [220]. Heteroatom substitutional doping not only tunes the electrical characteristics [74, 83] but also the surface and local chemical features [219] of graphene, thus opening avenues for developing highly improved gas sensors. Apart from heteroatom doping, there are other methods for graphene functionalization such as molecular grafting, hydrogen passivation or modification with different functional groups etc. The attachable functional groups provide graphene with tailor-made characteristics such as sensing, electron mobility and customizable solubility [220]. The symmetric band structure of graphene makes it an appropriate choice for physical and chemical modification.

Zhang *et al.* [36] reported results of first-principles simulation of interactions between small gas molecules such as NO_2, CO, NO, NH_3 and different types of graphene such as IG, B- and N-doped graphene, and defective graphene (hereafter abbreviated as BG, NG and DG respectively). The gas molecules exhibited stronger adsorption on doped and defective graphenes than that on IG. The adsorption energies of gas molecules on modified graphene are higher than that on IG and the charge transfer between gas molecules and modified graphenes are also larger as shown in Table 2.9 [19]. NG had weak interactions with CO, NO and NH_3, but had strong binding with NO_2. B-doping of graphene had improved its adsorption properties for NO, NO_2 and NH_3. The adsorption energy, charge transfer and the electronic total charge density plots for CO, NO and NO_2 molecules on DG indicate that vacancy on DG acts as strong chemisorption binding site for these gas molecules and hence DG can be used as suitable sensing material for detecting these gas molecules compared to

other graphenes. It was seen from the calculations that strong interactions between the adsorbed molecules and the modified graphenes induce dramatic changes to the electronic properties of modified graphenes. The DOS plots of the adsorbed systems have shown that DG, BG and NG are best suitable for sensing CO, NO and NO_2, respectively. The current-voltage curve of gas sensor based on BG show dramatic increase of current on NO_2 adsorption and sensitivity of nearly two orders of magnitude higher than that of IG was observed at an optimum bias voltage of 1.0 V. BG was found to be more sensitive to NO_2 than NH_3 as the observed sensitivity to NH_3 was only one order of magnitude than the IG, when the bias voltage is greater than 1.0 V. Their work revealed that the sensitivity of graphene-based chemical gas sensors could be drastically improved by introducing appropriate dopant or defect [36].

Table 2.9 E_{ad} and Mulliken charge (Q) of NO_2, CO, NO, NH_3, SO_2, and H_2S adsorbed on different graphene materials.

Type	E_{ad}, (eV)						ΔQ (e)					
	NO_2	CO	NO	NH_3	SO_2	H_2S	NO_2	CO	NO	NH_3	SO_2	H_2S
IG	-0.48	-0.12	-0.30	-0.11	0.012	-0.17	-0.19	-0.01	0.04	0.02	-0.077	0
BG	-1.37	-0.14	-1.07	-0.50	0.205	-0.91	-0.34	-0.02	0.15	0.40	-0.110	0.74
NG	-0.98	-0.14	-0.40	-0.12	0.172	-0.11	-0.55	0	0.01	0.04	-0.263	0.01
DG	-3.04	-2.33	-3.04	-0.24		-0.14	-0.38	0.26	-0.29	0.02		0.01
Ref.		[36]			[40]	[41]			[36]		[40]	[41]

Ao *et al.* [37] investigated the adsorption of CO molecule on IG and Al-doped graphene (hereafter abbreviated as AG) theoretically and proved the enhanced sensitivity of AG to CO. DFT based computations have shown strong chemisorption of CO molecule on AG through the formation of a tight Al-CO bond (Figure 2.37 (d)) with significant electron transfer from AG to CO. But CO molecules are only weakly adsorbed onto IG (Figure 2.37 (c)) with small adsorption energy value and large distance between the CO molecule and graphene. The charge difference caused by CO adsorption in AG (Q = 0.027 e^-) was almost one order larger than that in IG (Q = 0.003 e^-), due to the modified electronic properties of graphene by Al doping. The noticeable increase in the DOS value of AG around the Fermi energy and the closure of energy band gap after CO adsorption (Figure 2.38) indicated the introduction of extra number of shallow acceptor states in AG through CO interaction. As a result, the chemisorbed CO on AG will give rise to a large increase in the electrical conductivity of AG [37].

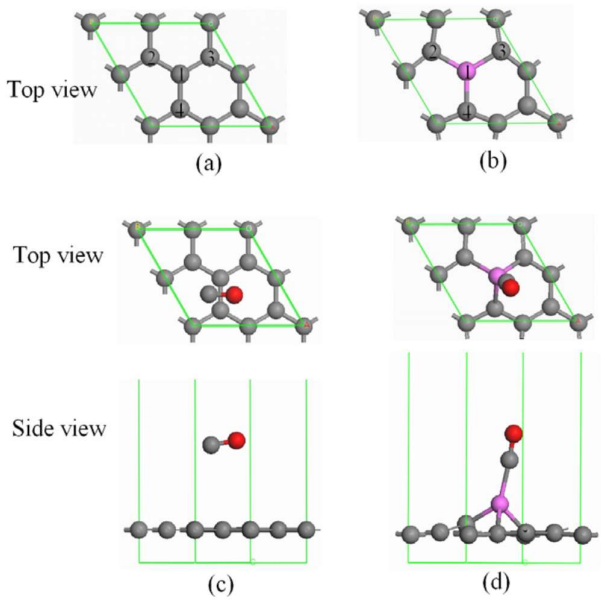

Figure 2.37 Atomic configurations of IG and AG before and after adsorption of CO gas molecule where one Al atom dopes in site 1. **(a)** and **(b)** are the relaxed configurations IG and AG before CO adsorption. **(c)** and **(d)** are the preferred configurations of IG and AG after CO adsorption, respectively. The carbon atoms are shown in grey, aluminium and oxygen atom in pink and red respectively. (Figure taken from ref. [37].)

Another similar study on the adsorption of H_2CO molecule on IG and AG showed the potential of using AG as a promising sensing material for the detection of H_2CO molecule [38]. Large adsorption energies, short binding distance and the observed orbital hybridization between H_2CO and AG, compared to that obtained for IG indicates chemisorption of H_2CO molecule on the surface of AG. The Mulliken charge analysis of H_2CO-adsorbed IG and AG systems showed a charge transfer of 0.085 e^- from AG to H_2CO molecule, which was about 4 times more than the charge transfer of 0.019 e^- from IG to H_2CO molecule [38].

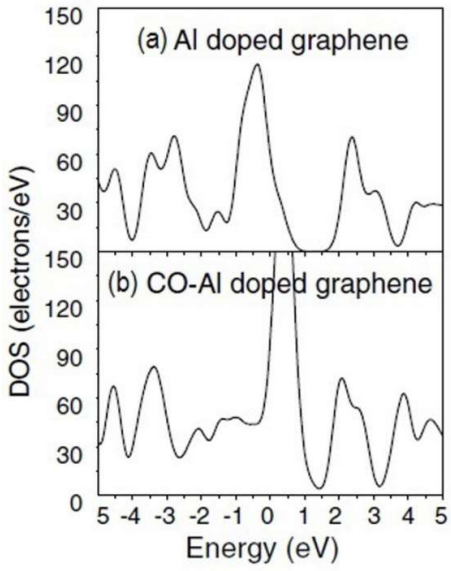

Figure 2.38 Electronic DOS of AG **(a)**, CO–AG system with preferred configuration **(b).** (Figure taken from ref. [37].)

Dai *et al.* [39] examined the adsorption property of many common or polluting gases such as H_2, H_2O, O_2, CO_2, CO, NO_2, NO, SO_2, NH_3, and N_2 on graphene doped with impurities such as B, N, Al, and S using DFT. The results from the first-principles calculations have been summarized in Table 2.10. It was found that BG can chemically bind NO and NO_2, whereas S-doped graphene (hereafter abbreviated as SG) can only bind NO_2 molecule. The Löwdin charge analysis showed a charge transfer of about 0.35 e^- from BG to NO_2, and of about 0.76 e^- from SG to NO_2, which could produce large changes in the conductivity of these doped graphenes. From the results, they predicted that BG and SG can be used as good sensors for the detection of polluting gases such as NO and NO_2. AG was found to be strongly reactive and binds all gas molecules such as NO, NO_2, NH_3, CO, CO_2, H_2O, SO_2, O_2, and N_2 except H_2 through tight Al−X (X = O, N, C) bonds. The large local curvature induced by the Al atom in the graphene lattice tends to make AG more chemically reactive [39].

Table 2.10 E_{ad} in eV and equilibrium graphene-molecule distance (d) in Å (defined as the shortest atom-to-atom distance) for the most stable configurations of gas molecules on different doped graphenes [39].

		NO	NO_2	NH_3	CO	CO_2	H_2O	SO_2	O_2	H_2	N_2
BG	E_{ad}	-0.341	-0.325	-0.016	-0.019	-0.007	-0.040	-0.030	-0.01	-0.014	-0.004
	d	2.38	1.56	3.37	3.81	3.57	3.73	3.63	3.45	3.22	4.11
NG	E_{ad}	-0.093	-0.260	-0.015	-0.013	-0.025	-0.060	-0.189	-0.149	-0.008	0.017
	d	3.56	3.03	3.49	3.89	3.27	3.47	3.21	3.30	3.22	4.02
AG	E_{ad}	-1.351	-2.476	-1.374	-0.662	-0.218	-0.809	-1.538	-1.661	-0.013	-0.202
	d	1.90	1.79	2.03	2.05	2.10	1.99	1.79	1.81	2.92	1.98
SG	E_{ad}	-0.122	-0.831	-0.003	-0.006	-0.004	-0.019	-0.092	-0.034	-0.006	-0.0001
	d	2.89	1.47	4.03	4.15	3.60	3.88	3.224	3.45	3.60	4.20

Dai and Yuan [272] evaluated the effect of O_2 on doped graphene for enabling practical applications of gas sensors, electronic and spintronic devices by simulating the adsorption of molecular oxygen on BG, NG, AG, Si-, P-, Cr- and Mn-doped graphene (hereafter abbreviated as SiG, PG, CG and MG respectively) using DFT. Physisorption was observed for O_2 adsorption on BG and NG due to the weak interactions of O_2 molecule with the dopant atom (B and N). O_2 molecule was found to be chemisorbed on AG, SiG, PG, CG and MG with induced obvious changes in the electronic structures due to the enhanced reactivity of these doped graphenes towards O_2. The results from the simulations indicate that the presence of O_2 molecule in air greatly affects the sensitivity of the gas sensors based on AG, SiG, PG, CG and MG, which limit their usage as efficient gas sensors [272]. Similar studies on the adsorption of gas molecules such as H_2, H_2O, CO_2, CO, NO, NO_2, SO_2, N_2, O_2, and NH_3 on PG concluded that PG has weak binding with H_2, H_2O, CO_2, CO, N_2 and NH_3. The calculated large binding energies, short distances of gas molecules from the graphene plane for the

interactions of NO, NO_2, SO_2 and O_2 with PG showed that these gas molecules are strongly adsorbed on the surface of PG [273].

Lv *et al*. [54] carried out first-principles study of N_2O interaction with IG, AG and gallium (Ga)-doped graphene (abbreviated as GG). N_2O was found to be chemisorbed on the surface of AG and GG by the stronger covalent bond formed between the dopant atom and the N_2O molecule via the *p* orbitals coupling. They observed that the N_2O molecule adsorbed on the surface of AG and GG can be easily decomposed to N_2 and O_2 with the application of a perpendicular electric field. Therefore both AG and GG can be used as excellent candidates for the detection and the dissociation of N_2O, thus protecting the ozone layer and controlling the global warming effects [54].

The adsorption properties of gas molecules such as CO, O_2, NO_2 and H_2O on IG and SiG had been investigated using *ab initio* calculations [35]. The electronic properties of IG are observed to be sensitive to the adsorption of O_2 and NO_2 molecules, but not changed by the adsorption of CO and H_2O molecules. The electronic structures of O_2 and NO_2 adsorbed on IG showed large peaks just above E_F, thereby modifying the shape of the DOS of IG by the adsorption of O_2 and NO_2. Compared to IG, SiG has strong affinity towards CO, O_2, NO_2 and H_2O molecules and hence SiG could be used as a good sensor for detecting CO, O_2, NO_2 and H_2O. In the case of SiG, the strong interactions between SiG and the adsorbed molecules result in significant change in the electronic properties of SiG [35]. Another DFT investigation of the adsorption of NO, N_2O and NO_2 on IG and SiG predicted the possibility of using SiG as an excellent candidate for the detection of NO and NO_2, as well as a catalyst for N_2O reduction [55]. The results indicated significant enhancement in the interactions of these gas molecules with graphene sheet upon Si doping. It was found that the adsorption of NO and NO_2 result in large changes in the electronic properties of SiG [55].

From the first-principles investigation of the adsorption of SO_2 on IG and heteroatom (B, N, Si, Al, Cr, Ag, Au, Mn and Pt)-doped graphene, Shao *et al.* [40] proved that the introduction of appropriate dopants such as Cr and Mn makes graphene more reactive to the adsorption of SO_2 compared to other dopants (Table 2.9 and 2.11) [40]. SO_2 is found to be chemically adsorbed on the surfaces of AG, SiG, CG, MG, AgG, AuG and PtG from the computed large binding energies, short SO_2-graphene distances, and large charge transfers. On the other hand, weak physisorption of SO_2 molecule on IG, BG and NG was inferred from the analysis of structural and electronic properties of SO_2 adsorbed graphene systems [40].

In another study, graphene modified with single vacancy defect and transition metal (TM) dopants such as Ca, Co, Fe exhibited much higher affinity to H_2S gas compared to IG, BG and NG (Table 2.9 and 2.11) [41]. The enhanced interactions between TMs and H_2S lead to dramatic changes in the electronic and magnetic properties of graphene. The electron transport properties of gas sensors using Fe-doped graphene (abbreviated as FeG) sheets as sensing materials exhibited much higher sensitivity than that of the devices made with IG. Similar study on the effect of doped Fe atom on the H_2S sensing behaviour of graphene also showed significantly improved interactions between H_2S and FeG sheet from the results of adsorption energy, electron density difference, and DOS plots [56]. Different H_2S adsorbed FeG systems with distinct binding distances (2.5-7.0 Å) were simulated to investigate the influence of the distance between H_2S and the FeG sheet on their interactions. The adsorption energies approach to zero for binding distances larger than 5.0 Å, which is similar to that of H_2S on IG. The DFT calculations proved that the adsorbed H_2S on FeG finally dissociates into S and H_2 [56].

Table 2.11 Sensing characteristics for the adsorption of SO_2 and H_2S on metal doped graphene.

Type	SO_2 [40]		H_2S [41]	
	E_{ad}, eV	Q, e	E_{ad}, eV	Q, e
AG	1.262	-0.744	-	-
PtG	1.018	-0.550	-	-
MG	1.729	-0.599	-	-
CG	1.675	-0.672	-	-
AgG	0.968	-0.454	-	-
AuG	1.284	-0.479	-	-
SiG	0.902	-0.959	-0.94	0.26
CaG	-	-	-0.66	0.04
CoG	-	-	-1.80	1.16
FeG	-	-	-1.92	1.23

In an effort to verify the effect of different dopant atoms such as N, Al, Zn, Ti, Zr on the interactions between hydrogen molecules and graphene sheets, Zhang *et al.* [57] performed DFT based calculations on the hydrogen molecule-intrinsic and doped graphene adsorbed systems. The interaction energy with the hydrogen molecule was found to be the largest for Ti-doped graphene (abbreviated as TiG), followed by the Zn-doped graphene (abbreviated as ZnG) and then AG. N-doping did not enhance the interactions between graphene sheet and H_2 molecule [57]. The same group showed improved gas sensing properties of TiG towards gas molecules such as CO, NO, SO_2 and HCHO compared to IG and NG [42]. TiG also exhibited selective gas adsorption, whereas NG did not exhibit selective adsorption

behaviour. The results suggested the possibility of using TiG sheet as an efficient sensing material than IG and NG sheets for the detection and removal of these harmful gases [42].

DFT based study on the adsorption potential of IG, group III (B, Al and Ga)-doped graphene for H_2S molecule also reported weak binding of H_2S molecule to IG and BG with small adsorption energy values, while strong binding of H_2S molecule to AG and GG was observed with large adsorption energies, which correspond to chemisorption [43]. DFT study of phenol adsorption on IG and group III (B, Al and Ga)-doped graphene by Avila *et al.* [44] showed weak physical interactions of phenol molecule with IG and BG. The structural and electronic properties of IG and graphene doped with B atom remain unaffected by phenol adsorption. Much stronger interaction was seen between the phenol molecule and graphene doped with Al and Ga, which corresponds to chemical adsorption [44].

The investigation of the adsorption of H_2CO on BG, NG, SiG, AG, CG, MG, and AuG suggested that BG and NG are not sensitive to H_2CO, whereas SiG, AG, CG, MG, and AuG are sensitive to H_2CO as they can strongly adsorb H_2CO molecule [45]. Al and Mn were found to be the most appropriate dopants on graphene for the detection of H_2CO molecule because of their relatively large adsorption energies, large charge transfers and significant changes of DOS before and after adsorption [45].

The analyses of the adsorption energies of molecular halogens, CH_3OH, CH_3SH, H_2O, and H_2S on graphene, SG and 2S-doped graphene (2SG) showed that the SG is the best adsorbent, fluorine is the best adsorbate, and all molecular halogens adsorb on graphene better than other molecules. The enhancement in the electrical conductivity of SG after the interactions with molecular halogens was predicted from the molecular orbital results and DOS graphs [274].

DFT based study of the adsorption of CO on intrinsic and VIIIB TM (Fe, Ru, Os, Co, Rh, Ir, Ni, Pd, and Pt)-doped graphene sheets revealed enhanced sensitivity of graphene doped with group VIIIB TMs to the presence of CO molecule [46]. Among the considered VIIIB TM-doped graphene sheets, Os- and Fe-doped graphenes displayed strong chemical interactions with C and O atoms of CO molecule respectively. Later Nasehnia and Seifi considered the effect of O_2 molecule on VIIIB TM-doped graphene structures to evaluate the suitability of these TM-doped graphenes as toxic gas sensing materials in air [275]. O_2 molecule was found to be chemisorbed on these doped graphene sheets with large adsorption energies (−0.653 eV to −1.851 eV) and appreciable amounts of charge transfers (0.375 e^- to 0.650 e^-) from doped graphene sheets to O_2 molecule. The enhanced reactivity of VIIIB TM-doped graphene

structures to O_2 could be attributed to the metallic doping and the pyramidalization of the doped graphene sheets. The adsorption energies for both O_2 and CO molecules on VIIIB TM-doped graphene sheets were found to be similar. Hence these materials may not be considered as a good choice for toxic gas sensing application [275].

Ma *et al.* [47] analyzed the sensitivity of IG and Pd-doped graphene (abbreviated as PdG) toward small gas molecules such as CO, NH_3, O_2 and NO_2 using first-principles. They found weak adsorption of these gases on IG and significant increase in the interactions of graphene with gas molecules by the introduction of Pd dopants. They proposed that PdG is more appropriate for the detection of CO, NH_3, O_2 and NO_2 compared to IG owing to the dramatically increased adsorption energy and elevated charge transfers of gas molecule-Pd doped graphene systems [47].

Recent theoretical studies of gas molecular adsorption on AG sheets have shown improvement in the interactions of several gas molecules with AG, as compared to IG. For example, AG has shown to be sensitive to NO_2 and N_2O [48]. Another DFT study revealed increased adsorption strength of CO, CO_2 and H_2O on AG [49]. The weak physisorption of these gas molecules on IG and the strong chemisorption on AG was confirmed from natural bond orbital analysis and DOS plots apart from the analysis of adsorption energies and charge transfers. The enhancement in the adsorption of the gases on graphene through Al-doping could be attributed to the modification in the electronic properties of graphene with increased electron density on carbon atoms surrounding the Al-dopant and decreased electron density on Al-dopant. This charge relocation makes the dopant atom as the reactive site for gas molecules [49]. The application of AG as an adsorbent for halomethane gases was also reported [50].

Another work on the adsorption properties of O_3, SO_2 and SO_3 on BG reported strong chemisorption for O_3 with dissociation on the surface of BG [51]. The very low adsorption energies of SO_2 and SO_3 on BG indicated weak interactions of these molecules with BG. Rad *et al.* pointed out that the n-type semiconducting property of BG is responsible for the improved sensitivity of BG to O_3 molecule. The observed high sensitivity of BG to O_3 can be exploited for developing highly selective O_3 sensors [51].

Recently, Rad and co-workers used DFT calculations to investigate the adsorption of SO_x ($x = 2, 3$) molecules on the surface of IG and NG [52]. This report showed that the binding energy and the net charge transfer of the molecules on graphene got increased by doping with N. The DOS plots displayed major orbital hybridization between SO_x and NG, while there

was no hybridization between SO_x molecules and IG. Physical and chemical adsorption of SO_2 and SO_3 molecules were observed on the surface of NG with binding energies of −27.5 and 65.2 $kJmol^{-1}$, respectively. From the results, they concluded that NG can be used as sensitive sensor for the detection of SO_2 and SO_3 [52].

Wang *et al.* [53] recently studied the adsorption of CO on IG, NG and AG and they found very low adsorption energies of CO molecule on IG and NG. Large adsorption energy and large charge transfer were observed for CO molecule adsorption on AG. Although N-doping enhances the interactions of CO molecule with graphene, the adsorption still remained to be weak. The calculated band structures, DOS, and the charge density difference for the doped graphene sheets with and without adsorbed CO molecule showed significantly different adsorption on AG compared to that on IG and NG. Their work concluded that AG is much more sensitive than IG and NG to the adsorption of CO [53].

DFT based study of the adsorption of H_2S molecules onto DG as a function of vacancy concentration showed stronger interactions of the molecule with the carbon atoms surrounding the vacancy than with the carbon atoms in a perfect arrangement, which corresponds to chemisorption process followed by the release of H_2 molecule [60]. The DOS plots of IG, DG and DG with chemisorbed sulfur demonstrated that the systems change the electrical conductivity. The most stable adsorption configuration of H_2S molecule on DG facilitates covalent binding of the sulfur atom with three carbon atoms through unsaturated bonds [60].

Inspired by the enhanced gas sensing behaviour of graphene modified with dopants and defects, some theoretical works have also concentrated on modifying graphene with both dopants and defects. Zhou and co-workers [61] showed that vacancy-defected graphene (VG) is more sensitive to the presence of H_2CO molecule that IG. But H_2CO molecule had physisorption on VG with small adsorption energy. The adsorption studies of H_2CO on graphene modified with a combination of vacancy and dopants such as B, N and S have shown chemisorption of H_2CO on B-doped, N-doped and S-doped vacancy-defected graphene (abbreviated as BVG, NVG and SVG respectively) for which the adsorption energies and net charge transfer are larger than that of VG without dopants. The enhanced adsorption of H_2CO molecule on the dopant-defect combination due to the strong orbital interaction between the *p* orbitals of dopant atoms and carbon atoms around the vacancy was also evident from the results of partial DOS [61]. Using first-principles calculations, Ma and his coworkers showed that VG firmly adsorb gas molecules such as NO, CO and O_2 [62]. The analysis of binding energies and charge transfer calculations on the adsorption of NO, CO, N_2

and O_2 molecules on pyridinic-like N-doped graphene have shown high selectivity of pyridinic-like N-doped graphene to CO in the presence of N_2, O_2 and NO due to the observed chemisorption along with large charge transfer for CO, as compared to the weak adsorption of N_2, O_2 and NO on the surface of pyridinic-like N-doped graphene (Table 2.12) [62].

TM-doped Stone–Wales (SW) defected graphene has also been verified as a promising sensing material for H_2CO detection due to the enhanced adsorption on its surface [63]. H_2CO molecule undergoes chemisorption on TM atoms (Cr, Mn and Co) doped graphene and SW defective graphene structures. The larger binding energy and shorter binding distance of H_2CO molecule on TM-doped defected graphene (Cr-SWG, Mn-SWG and Co-SWG) than that on TM-doped perfect graphene structures showed that the presence of SW-defect improved the adsorption of H_2CO. It was found that the adsorption of H_2CO affect the electronic conductance of the Cr-doped and Mn-doped defective graphene, and hence by measuring the change in electronic conductance, the presence of H_2CO molecule can be detected sensitively. These works theoretically revealed the combined effect of defect and doping on the sensitivity of graphene towards H_2CO gas, which could be exploited for developing future H_2CO sensing devices [63].

Hussain *et al.* [276] investigated the adsorption capability of hydrogenated graphene (graphane) sheet for H_2S and NH_3 gases using DFT. Both pure graphane sheet and defected graphane sheet (obtained by removing a few surface H atoms from the graphane sheet) have been found to have low affinity for both H_2S and NH_3 gas molecules. The sensing affinity of graphane sheet to these gas molecules was found to be stronger on doping the graphane sheet with Li adatoms. Li-doped graphane sheet showed higher affinity for NH_3 gas compared to H_2S gas due to the stronger hybridization of *s* orbitals of Li adatom with *p* orbitals of nitrogen atom of NH_3 compared to that of with the *p* orbitals of sulfur atom of H_2S. The adsorption energy calculations indicated that Li-doped graphane sheet is suitable for the detection of H_2S and NH_3 gases [276].

In another work by Tanveer *et al.* [277], pure graphane sheet showed less affinity towards CO, H_2O and NO_2 gas molecules. Defected graphane sheet had strong affinity towards these gas molecules. But CO and H_2O were found to be weakly physisorbed to the defected graphane sheet. Defected graphane sheet chemically binds NO_2 molecule due to the strong hybridization of the N (*p*) and O (*p*) states with the most active C (*p*) states which lie at the defected site of the graphane sheet. The observed increase in the trend of the work function of the defected graphane sheet on the adsorption of CO, H_2O and NO_2 gas molecules opens up possibilities for next generation gas sensors [277].

Table 2.12 The binding energy (B.E.) and the charge transfer of different gases adsorbed on VG and NG [62].

System	B.E.	ΔQ (e)
N_2 on VG	0.15	0.07
N_2 on NG	0.03	0.01
O_2 on VG	6.24	1.27
O_2 on NG	0.69	0.11
CO on VG	6.05	-2.00
CO on NG	3.43	-0.36
NO on VG	6.64	0.98
NO on NG	0.07	0.06

2.6 Research Gaps

It is clear from the literature described above that gas sensors based on graphene, its derivatives such as GO, RGO and modified graphene present a promising platform for detecting various gas species at room temperature. GO and RGO have shown highly sensitive sensing response compared to IG, by virtue of the surface rich oxygen functional groups. In further advancement, the modification of graphene surface was found to be highly successful in achieving high sensitivity and providing good selectivity for gases [19].

Among different modified graphenes, doped graphenes have been widely studied as highly sensitive toxic gas sensing materials. Apart from these studies, the investigation of the sensitivity of doped graphenes to constituents of air such as N_2, O_2 and traces of water vapour is also of great importance in realizing potential applications of doped graphene-based gas sensors. Only limited studies on the effect of atmospheric constituents on doped graphene-based structures have been reported [272, 275]. The usage of doped graphenes as gas sensors strongly depend on their sensitivity towards various components of air. The application of doped graphenes as toxic gas sensors under normal working conditions necessitate insensitivity of the doped graphene structures to the presence of atmospheric constituents. The chemisorption of the atmospheric constituents on doped graphene would lead to false alarm and affects the sensitivity to the toxic gas to be detected, which thus prevent their usage as gas sensing materials in air.

Molecular oxygen that constitutes more than 20% of the volume of air is a highly reactive gas [275]. Water vapour which represents only a small volume of the air is also an environmentally significant constituent of atmosphere. Hence, the effect of these atmospheric constituents on doped graphenes that have already demonstrated their applicability as novel toxic gas sensors, need to be analyzed. The results from the analysis of the effects of the

adsorbed atmospheric constituents on doped graphene structures can only indicate the suitability of using doped graphenes as toxic gas sensors in air.

Even though gas sensors based on several doped graphene have shown high sensitivity detection of various gases, the processes involved in the gas sensing mechanism of different doped graphene are still unclear. Further studies on the understanding of the interactions between doped graphene and gas molecules are required for fully exploiting the potential of doped graphene as gas sensors.

Even if high resolution in the order from ppm to ppb level had been demonstrated by graphene-based gas sensors, they were not able to identify individual gases [28]. The real drawback that has limited this type of sensors for practical applications is the lack of selectivity and hence they cannot determine the type of the gas and its concentration [158, 278]. Graphene gets strongly influenced by a range of different gas species and mixtures [28]. For example, exposure of graphene to oxidizing gases such as O_2 and NO_2 results in an increase in graphene conductance that makes graphene difficult to distinguish between these oxidizing gases. Also, combination of different oxidizing and reducing gases in equal amounts will not create any change in conductivity [28]. This gap can be addressed by a systematic study on the nature of various gas molecules and how they affect the sensor response. Thus, future work needs to concentrate on functionalization of graphene with appropriate capture agents that specifically bind the target gas to graphene's surface. Another approach that can be employed for addressing the selectivity problem is to use multiple transduction mechanisms beyond electrical transduction so that the collective information can be used for target gas identification.

The electrical conductivity of graphene is also sensitive to other environmental changes such as temperature, contamination, moisture etc. and this creates problems for reliable and reproducible sensing [28]. The low selectivity problem of graphene-based conductometric nanosensors limited their application for high performance multiple analyte detection in a gas mixture. This problem can be addressed by employing an array of graphene sheets that may be less influenced by other external factors.

2.7 Problem Statement

To fully exploit the potential of doped graphene as toxic gas (CO, NO, NO_2, H_2S and N_2O) sensors, it is extremely important to understand the interactions between different doped graphene and toxic gas molecules such as CO, NO, NO_2, H_2S and N_2O. The effect of important atmospheric constituents such as O_2 and H_2O on doped graphenes that have already

demonstrated their applicability as novel toxic gas sensors need to be analyzed, as the results from these investigations can only predict the application of doped graphenes as toxic gas sensors under normal working conditions.

In the next chapter, the geometry and electronic structure of graphene are discussed in detail. Chapter 3 also describes the structural and electronic properties that are relevant for gas sensing applications of graphene.

CHAPTER 3

GRAPHENE: STRUCTURAL AND ELECTRONIC PROPERTIES

3.1 Carbon and its allotropes

Carbon, which belongs to Group IV of the periodic table, forms the basis for all organic life on earth. It is present in almost 95% of all known chemical compounds [279]. Compared to the other elements in the periodic table, carbon atom possesses the capability to bind with a variety of atoms and form molecular compounds or crystalline solids [280, 281]. Carbon atom is made up of 6 protons, 6 electrons and x neutrons in which x can be 6, 7 or 8 that yield stable isotopes such as ^{12}C (most common isotope in nature), ^{13}C and radioactive isotope ^{14}C. Its ground state atomic configuration is $1s^2\ 2s^2\ 2p^2$. In the elemental form, two electrons fill the innermost atomic orbital, 1*s* and the remaining four electrons fill the outermost shell of 2*s* and 2*p* ($2p_x$ and $2p_y$) orbitals each with 2 electrons (Figure 3.1). The interaction of four valence electrons with each other forms various types of carbon allotropes (Figure 3.2). It is favourable to excite one electron from 2*s* orbital to the third 2*p* orbital [282], $2p_z$ orbital in the presence of other carbon atoms so as to make covalent bonds with them. Since the 2*s* and 2*p* orbitals of carbon have very similar energies, these orbitals can mix together to form hybrid orbitals. The bonding or interaction between 2*s* and 2*p* orbitals of neighbouring carbon atoms is termed as hybridization and the newly formed orbitals are called hybrid orbitals [280].

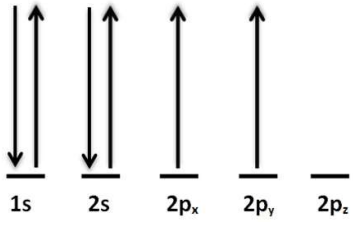

Figure 3.1 Electronic arrangement in elemental carbon

Depending on the type of hybridization of the atomic orbitals (usually either sp^2 or sp^3), the carbon allotropes are divided into three classes such as diamond with all the carbon atoms having sp^3-hybridization, graphitic with all sp^2-hybridized carbon atoms and the third class, amorphous carbon, which consist of both sp^2- and sp^3-hybridized carbon atoms [281].

Even though carbon has been known for centuries dating back to the period before middle ages, several new crystalline forms of carbon such as fullerenes, CNTs and graphene have only been experimentally discovered in the last few decades [280]. A schematic overview of various carbon allotropes is shown in Figure 3.2. Even though all forms of carbon have the

same hexagonal arrangement of carbon atoms, the newer forms exhibit contrasting properties as compared to older allotropes such as diamond and graphite. CNTs and graphene are often referred to as reduced dimensional or low dimensional solids or nanomaterials (CNTs are 1D and graphene is 2D) since they occupy only less space compared to graphite and diamond. Graphene is about 300,000 times thinner than a sheet of paper whereas CNTs are about 10,000 times smaller than the average width of a human hair. Graphene, a single atomic layer of graphite is only 0.34 nm thick, whereas the diameter of CNTs ranges from about 1 to 100 nm. The exotic properties unique to CNTs and graphene arise from the reduced dimensions and the distinct lattice structures [280].

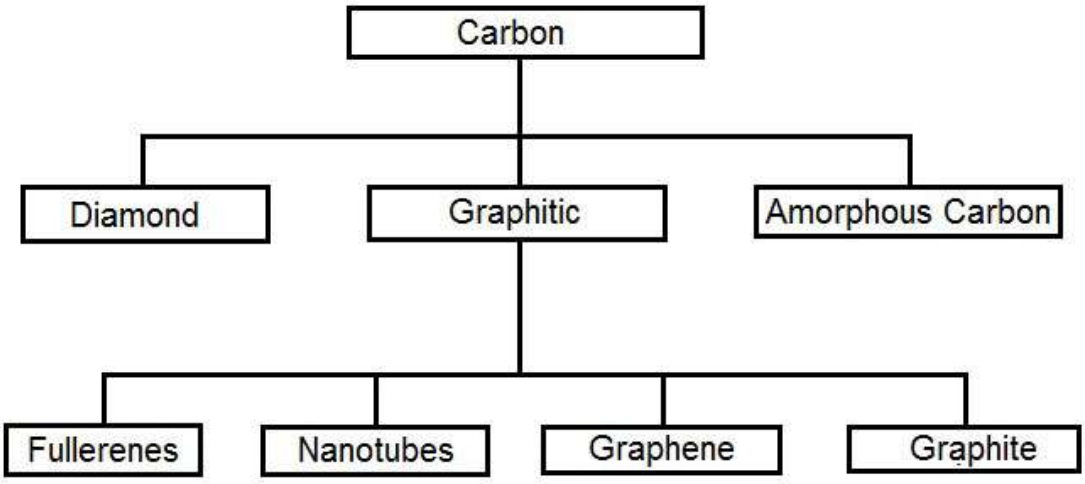

Figure 3.2 Different carbon allotropes

The last carbon allotrope discovered, graphene is the basic building block of other carbon allotropes [1, 5] such as graphite (stacked graphene sheets, three-dimensional (3D)), discovered before 1565, CNTs (rolled up graphene sheets, 1D), discovered by Iijima in 1991 [283], and fullerenes (wrapped up graphene spheres, zero-dimensional (0D)), discovered by Smalley in 1985 [284] as shown in Figure 3.3. It was not until 2004 that a single graphene sheet could be isolated [1], since 2D crystals were believed to be thermodynamically unstable and hence could not exist [285, 286]. This flat fullerene molecule was the first 2D crystal ever observed in nature [11].

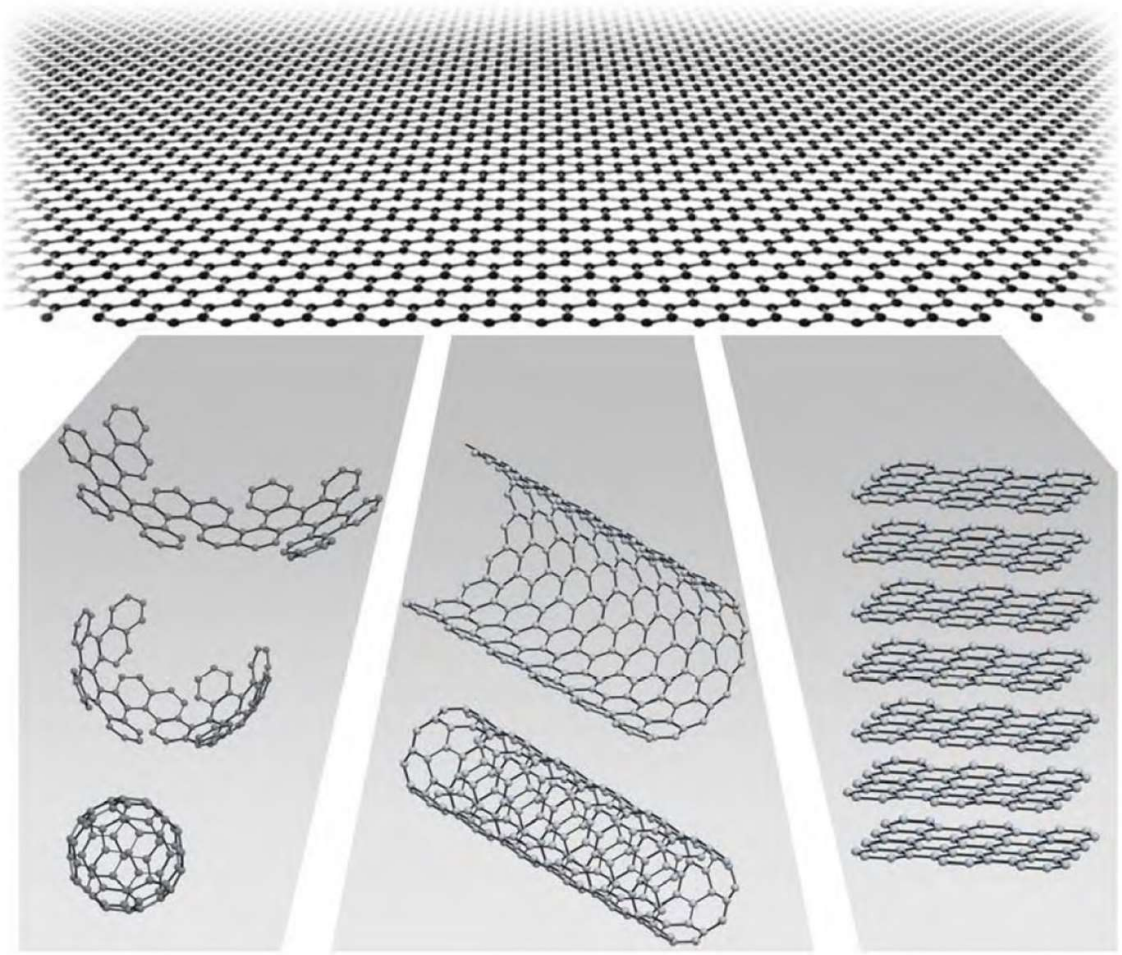

Figure 3.3 Mother of all graphitic forms. (Figure taken from ref. [5].)

3.2 Structural properties of graphene

Graphene is a single, one-atom-thick sheet of carbon atoms arranged in a honeycomb lattice. A stack of large number of graphene sheets with 3.35 Å interplanar spacing forms graphite; 1-mm thick graphite flake contains ~3 million layers of stacked graphene sheets [19]. It is the thinnest material imaginable in the universe [142] (one-atom-thick), lightest material known (density of 0.77 mg/m^2) and yet the strongest material measured (strength nearly 100-300 times higher than steel) [9]. Graphene can also be considered as an indefinitely large aromatic molecule, the limiting case of the family of flat polycyclic aromatic hydrocarbons.

3.2.1 Bonding in graphene

Graphene is a planar allotrope of carbon in which all the carbon atoms are covalently bonded to each other in a single plane. Within graphene, one 2*s* and two in-plane 2*p* orbitals ($2p_x$ and $2p_y$) of carbon are associated with planar sp^2-hybridization and form three sp^2-hybrid orbitals. Figure 3.4 shows the electron arrangement in graphene. The sp^2-hybridized orbitals lie in the

xy-plane and are 120° apart (Figure 3.5 (a)). The remaining unhybridized $2p_z$ orbital is oriented perpendicular to the xy plane.

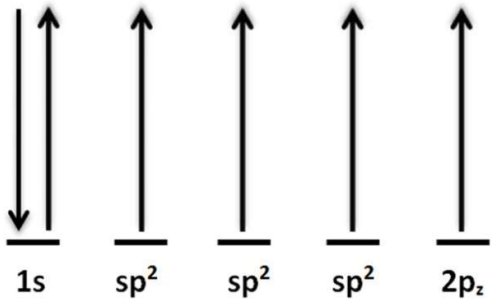

Figure 3.4 Electron arrangement in graphene.

A famous chemical example of sp^2-hybridization is benzene molecule [282]. The chemical structure of benzene proposed by August Kekul´e in 1865 [287] consists of a hexagon with carbon atoms arranged at the corners and are linked by σ-bonds (Figure 3.5 (b)). Each carbon atom also form covalent bonds with hydrogen atoms that stick out from the hexagon in a star like manner. The remaining $2p_z$ orbitals form three π-bonds, represented as double bonds, alternate with single σ-bonds around the hexagon. The measured carbon-carbon distance in benzene is 0.142 nm for all bonds [282], which is nearly the average of a single σ-bond (with a C-C distance of 0.147 nm) and a double π-bond (with a C-C distance is 0.135 nm). Linus Pauling explained the structure of benzene based on quantum mechanical analysis of the ring [288]. The quantum mechanical ground state of benzene molecule shown schematically in Figure 3.5 (c) is obtained by the superposition of the two configurations of benzene ring which differ by the position of the double π-bonds. Thus, the π electrons are delocalised over the benzene ring. Graphene can be viewed as a tiling of benzene hexagons (Figure 3.6) in which the hydrogen atoms are replaced by carbon atoms to form a neighbouring carbon hexagon. The carbon atoms in graphene arrange themselves in a honeycomb crystal lattice due to their sp^2-hybridization [282]. The hexagonal arrangement of carbon atoms of SLG has been experimentally observed [289] (Figure 3.7).

The sp^2 interactions result in three σ-bonds/atom which are the strongest type of covalent bonds and these bonds in graphene lead to great mechanical strength. σ-bonds have electrons localized along the plane connecting the carbon atoms (Figure 3.8) and hence these electrons do not take part in electrical conductivity. The $2p_z$ electrons that are weakly bound to the nuclei also form covalent bonds called π-bonds and are relatively delocalized (Figure 3.8). These electrons are accountable for the electronic properties of graphene [280]. The in-plane

σ-bonds act as the rigid backbone of the graphene structure, whereas the out-of-plane π-bonds control interaction between adjacent graphene layers [290].

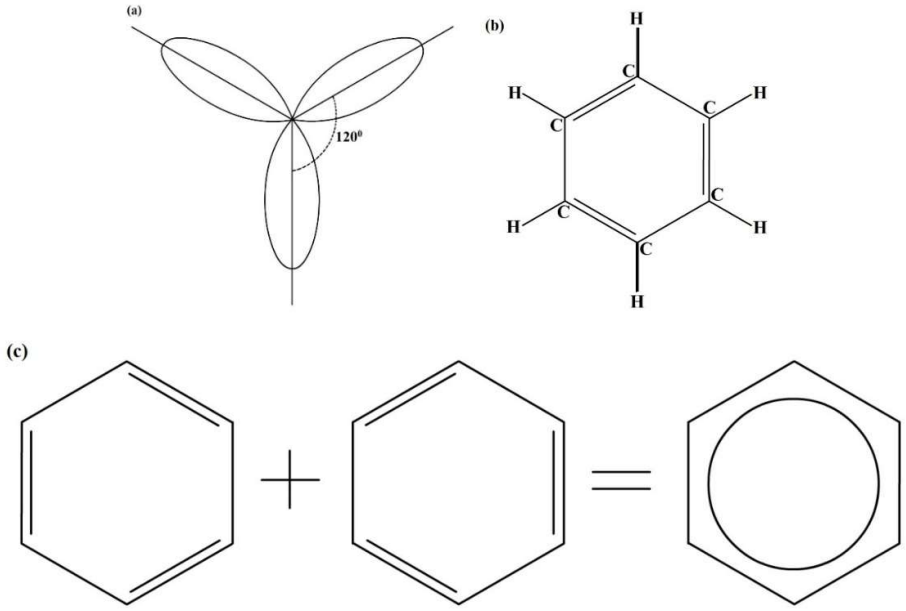

Figure 3.5 (a) Illustration of orbitals, **(b)** Benzene-ring and **(c)** The quantum-mechanical ground state of the benzene ring.

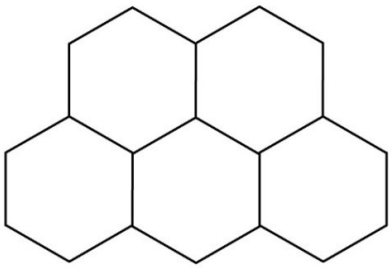

Figure 3.6 Graphene viewed as tiling of benzene hexagons.

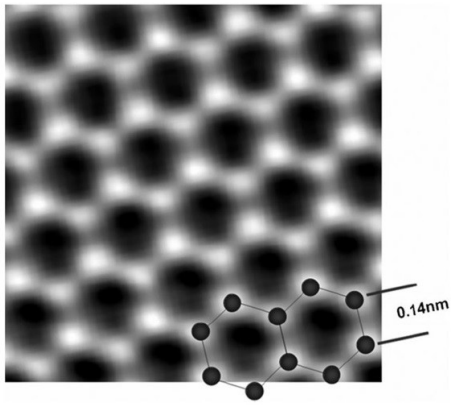

Figure 3.7 Atomic-resolution image of a clean and structurally perfect synthesized graphene which clearly shows individual carbon atoms and bonds in the structure. (Figure taken from ref. [289].)

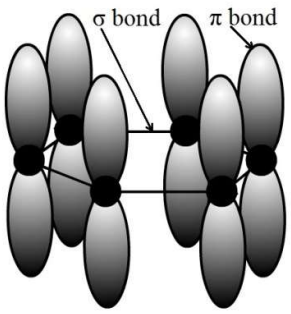

Figure 3.8 Schematic of the in-plane σ bonds and the π orbitals perpendicular to the plane of graphene sheets.

3.2.2 The graphene lattice

Graphene made of carbon atoms arranged in a honeycomb lattice is represented using the ball and stick model in Figure 3.9, where the balls represent the carbon atoms and sticks symbolize the σ-bonds between the carbon atoms. The carbon-carbon bond length (nearest-neighbour distance) represented by $a_{C\text{-}C}$ is approximately 1.42 Å. As the lattice sites of the honeycomb structure are not identical, it is not a Bravais or fundamental lattice (in which lattice sites are indistinguishable). This non-fundamental lattice can be transformed into Bravais lattice by starting at a lengthy lattice and identifying a collection of lattice points that when grouped together result in a Bravais lattice. For the honeycomb lattice, consider grouping together A and B atoms and all repeating instances of A and B, the resulting lattice is now a Bravais lattice in which every Bravais lattice point represent two crystal lattice points and thus the basis of graphene is two. The Bravais lattice, which is usually measured in terms of a position vector is also known as the direct lattice [280].

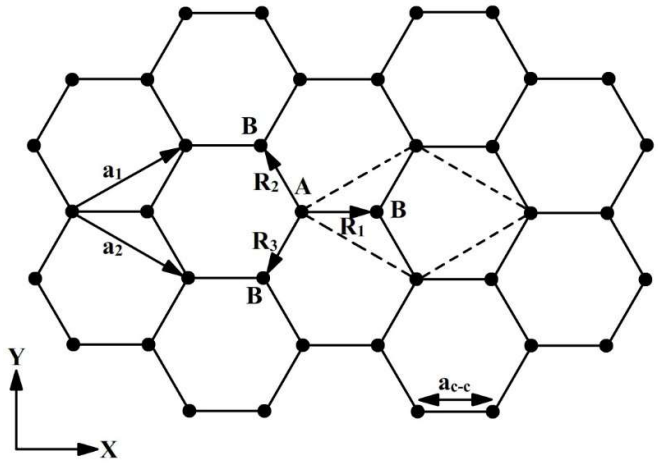

Figure 3.9 The honeycomb lattice of graphene

The honeycomb lattice can be characterized as a Bravais lattice (Figure 3.10) with a basis of two atoms denoted by A and B as shown in Figure 3.9. These two atoms contribute 2 π

electrons per unit cell to the electronic properties of graphene. The underlying Bravais lattice is a hexagonal lattice (Figure 3.10) and the primitive unit cell can be considered as an equilateral parallelogram (shown in dashed lines in Figure 3.9) with a side of $a = \sqrt{3}a_{C-C} = 2.46$Å [280].

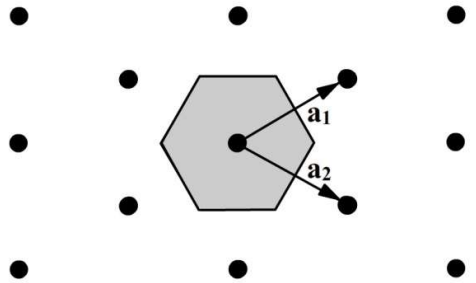

Figure 3.10 The hexagonal lattice

For a Bravais lattice, any vectors connecting to lattice sites are lattice vectors. The primitive unit vectors, a_1 and a_2 defined in Figure 3.9 and Figure 3.10 are

$$a_1 = a\left(\frac{\sqrt{3}}{2}, \frac{1}{2}\right),\ a_2 = a\left(\frac{\sqrt{3}}{2}, -\frac{1}{2}\right), \tag{3.1}$$

For the hexagonal lattice, $a = |a_1| = |a_2|$ and a is the lattice constant. It is clear from Figure 3.9 that in graphene, the carbon atoms form covalent bonds with its three nearest neighbouring carbon atoms in a single plane. The vectors that describe the separation between a type A atom and nearest type B atoms in Figure 3.9 are,

$$R_1 = \left(\frac{a}{\sqrt{3}}, 0\right), \quad R_2 = -a_2 + R_1 = \left(\frac{-a}{2\sqrt{3}}, -\frac{a}{2}\right), \quad R_3 = -a_1 + R_1 = \left(\frac{-a}{2\sqrt{3}}, \frac{a}{2}\right), \tag{3.2}$$

with $|R_1| = |R_2| = |R_3| = a_{C-C}$.

To visualize and sketch Bravais lattice in 3D, a primitive unit cell known as Wigner-Seitz cell constructed from simple geometric rules has been broadly utilized. This unit cell has a boundary about a Bravais lattice point that contains only that point. The Wigner-Seitz cell is constructed using the following steps [280]:

i) Draw connection lines from a lattice point to adjacent lattice points, upto the second nearest neighbours,

ii) Bisect the connection lines with perpendicular lines,

iii) Connect the bisecting lines at common intersections to form a closed polygon.

The grey hexagon in Figure 3.10 shows the Wigner-Seitz cell for hexagonal lattice. This cell is extremely useful in understanding the properties of reciprocal lattice and the band structure [280].

3.2.3 The reciprocal lattice of graphene

The reciprocal lattice is of supreme importance since it provides fundamental insight into the behaviour of electrons in crystalline solids. The discrete Fourier transform of the direct lattice is termed as the reciprocal lattice [291]. The reciprocal equivalent of direct lattice [292] is reciprocal lattice. The reciprocal lattice satisfies the following basic relation that comes from the Fourier analysis of the direct lattice as

$$e^{ik\cdot R} = 1, \tag{3.3}$$

where R is the Bravais lattice primitive vector and k is the set of wavevectors that determine the sites of the reciprocal lattice. In three dimensions, the primitive vectors of the reciprocal lattice, b_1, b_2 and b_3 are determined from the primitive vectors of the direct lattice as:

$$b_1 = 2\pi \frac{a_2 * a_3}{a_1 \cdot (a_2 * a_3)}, b_2 = 2\pi \frac{a_3 * a_1}{a_1 \cdot (a_2 * a_3)},\ b_3 = 2\pi \frac{a_1 * a_2}{a_1 \cdot (a_2 * a_3)}, \tag{3.4}$$

For deriving the reciprocal lattice in two dimensions, the 2D space defined by primitive vectors a_1 and a_2 and the corresponding reciprocal lattice vector, $b_1$and b_2 is considered. The result will become meaningless if we set a_3 as zero (the denominator of Eq. (3.4) vanishes). For graphene (2D material), the lattice is limited to a plane with vanishing thickness, where the vanishing thickness is an approximation for the relatively small thickness of graphene (~0.34 nm thick for single layer graphene) relative to its width and length. The vanishing thickness approximation demands that both a_1 and a_2 have zero components in the third dimension and the vector a_3 exists only in the third dimension as it vanishes in other dimensions. Hence the reciprocal vectors in two dimensions can be written as [280]:

$$b_1 = 2\pi \frac{R_{90}(a_2)}{\det(a_1, a_2)},\quad b_2 = 2\pi \frac{R_{90}(-a_1)}{\det(a_1, a_2)} \tag{3.5}$$

R_{90} is the operator for the clockwise rotation of the vector by 90° and determinant (det) represents area of a parallelogram formed by vectors a_1 and a_2. The rotation operation indicates that the reciprocal lattice vectors are either normal or parallel to the direct lattice primitive vectors corresponding to $b_i a_j = 2\pi\delta_{ij}$, where δ_{ij} is the Kronecker delta function and δ_{ij}= 1 if and only if i = j [280].

Some of the properties of reciprocal lattice are described below:

i) Since the direct lattice is always a Bravais lattice, reciprocal lattice is also a Bravais lattice. Reciprocal lattice is a slightly different Bravais lattice as compared to the original Bravais lattice in real space.

ii) The direct lattice exists in the real space and reciprocal lattice exists in the reciprocal space also called as k-space, momentum space or Fourier space.

iii) The reciprocal of the reciprocal lattice is the direct lattice

iv) The direct lattice can be observed through a high-resolution electron microscope but the reciprocal lattice is often characterized by X-ray diffraction patterns.

v) The direct lattice is always described in terms of the position vector R with units of length whereas reciprocal lattice is measured in terms of the wavevector K with units of 1/length.

vi) If s is the area of the primitive cell of the direct lattice, then $(2\pi)^2/s$ is the area of the reciprocal lattice primitive cell.

The reciprocal lattice of graphene is also a hexagonal lattice as shown in Figure 3.11, but is rotated 90° with respect to the direct lattice.

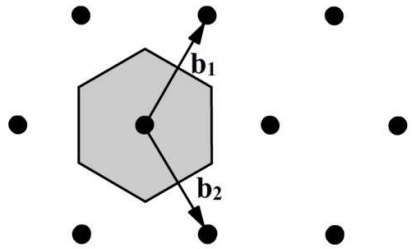

Figure 3.11 The reciprocal lattice, primitive vectors and the first Brillouin zone of graphene (grey hexagon)

The reciprocal lattice primitive vectors computed from Eq. (3.5) are as follows:

$$b_1 = \left(\frac{2\pi}{\sqrt{3}a}, \frac{2\pi}{a}\right), \quad b_2 = \left(\frac{2\pi}{\sqrt{3}a}, -\frac{2\pi}{a}\right), \tag{3.6}$$

with $|b_1| = |b_2| = \frac{4\pi}{\sqrt{3}a}$.

The resulting reciprocal lattice generated by sweeping b_1 and b_2 by integer multiples is shown in Figure 3.11. The first Brillouin zone (BZ) is the key concept in defining the band structure of electrons within the solids. Higher BZs also exist, but they duplicate the information present in the first BZ and thus the common usage of the term BZ referees to the first BZ in particular. The Wigner-Seitz primitive cell of the reciprocal lattice is the first BZ. The obtained BZ is a grey hexagon as shown in Figure 3.11 with sides of length $\mathrm{b_{BZ}} = \frac{|b_1|}{\sqrt{3}} = \frac{4\pi}{3a}$ and area equal to $A = \frac{3\sqrt{3}}{2}\ {b_{BZ}}^2 = \frac{8\pi^2}{\sqrt{3}a^2}$. Figure 3.11 shows that both the reciprocal lattice and first BZ are rotated 90° with respect to direct lattice. There are three locations of high symmetry in the BZ labelled as the Γ-point, K-point and M-point [293]. The Γ-point is at the centre of the BZ, M-point is at the midpoint of the side and K-point is at the corner of the BZ. The K-point which is also a hexagonal corner is equivalent to the K-point. There are 6 K-points and 6 M-points in the BZ. The unique solutions for the energy bands of crystalline

solids are found within the BZ and the dispersion is usually described along the high symmetry points of the BZ. Reciprocal lattice is also termed as k-space and the vector that locates any point within the BZ is the wavevector k. Every allowed point within the BZ can be reached by k [280].

3.3 Electronic properties of graphene

The electronic properties of graphene are described by the electronic band structure of a perfect, flat, free standing and infinite graphene crystal in vacuum [294].

3.3.1 The electronic band structure of graphene

The electronic band structure of graphene is of great significance as it is the starting point for the understanding of graphene's properties and investigation of graphene-based devices such as sensors, diodes, transistors etc. The electronic band structures of both graphene and graphite were studied experimentally and theoretically for decades. The analytical description of the band structure of graphene can be developed by solving the time-independent Schrodinger's equation in the 3D space [280].

$$H\psi(k,r) = E(k)\psi(k,r), \tag{3.7}$$

The Hamiltonian operator (H) acts on the wavefunction to obtain the permitted energies (E). The Hamiltonian for an independent electron in a periodic solid is given by

$$H = -\frac{\hbar^2}{2m}\nabla^2 + \sum_i^N U(r - R_i), \tag{3.8}$$

in which the first term in H is the kinetic energy operator and latter term is the potential energy operator. R_i is the i^{th} Bravais lattice vector, N is the number of primitive unit cells and $U\ (r - R_i)$ is the potential energy contribution from the atom centered in the i^{th} primitive unit cell. The potential energy is the sum of single-atom potentials and, hence is periodic and Columbic in nature. Substitution of the Hamiltonian (Eq. (3.8)) into the Schrodinger equation (Eq. (3.7)) results in a second order partial differential equation. Constructing a wavefunction that satisfies the partial differential equation is non-trivial and may consist of iterating over several trial wavefunctions until a suitable wavefunction is determined. Acceptable wavefunctions in a crystalline solid must satisfy Bloch's theorem that states that valid travelling waves in a lattice have the property:

$$\psi(r + R) = e^{ik\cdot R}\psi(r)\ , \tag{3.9}$$

Periodic boundary conditions are imposed on the wavefunction to obtain allowed values of wavevector that leads to running waves:

$$\psi(r) = \psi(r + S) = e^{ik\cdot S}\psi(r), \therefore\ e^{ik\cdot S} = 1, \tag{3.10}$$

where S is the size vector whose lengths in all co-ordinates of space are the spatial dimensions of the lattice [280].

For obtaining the wavefunction and associated band structure, there are two limiting techniques called the nearly free electron (NFE) model and the tight-binding model. In NFE model, the outermost valence electrons are considered free and are weakly bound to the nucleus by Columbic attraction. The full periodic potential is thus replaced by a weak perturbing potential and by employing standard techniques in quantum mechanics, Schrodinger's equation can be solved. NFE model gives solutions in the form of modulated plane waves ($\psi \sim u(r)e^{ik\cdot R}$) and associated energy bands have a parabolic structure. This model has shown to be useful in predicting the band structure of metals.

In another limiting technique, called as tight-binging model assumes that the outermost electrons are tightly bound (localized) to their respective atomic cores and these electrons are described by atomic orbitals with discrete energy levels. Since these electrons are not isolated but they exist in an ordered solid, the atomic orbitals of identical electrons in neighbouring atoms in a solid with N unit cells will overlap and result in the broadening of N discrete energy levels into quasi-continuous energy bands with N states/bands according to Pauli's exclusion principle. The use of atomic orbitals for describing the electrons in a solid is inaccurate due to the overlap of wavefunctions. But for the special case of a very small overlap, tight-binding model can be used to obtain an approximate analytical band structure that shows good agreement with more sophisticated numerical *ab initio* band structure calculations or experimental measurements [280].

In order to develop an analytical expression for the electronic band structure of graphene, one model need to be chosen out of the above mentioned models. The band structure of graphene computed numerically from *ab initio* calculations is presented in Figure 3.12. The obtained band structure (Figure 3.12) show linear energy-momentum dispersion around the Fermi energy (E_F, the energy at 0 eV) and hence the tight-binding model is an attractive choice. Graphene can be considered as a large carbon molecule from point of view of chemistry and the initial guess is to employ standard quantum chemistry techniques such as linear combination of atomic orbitals also called as tight-binding for deriving the molecular band structures [280].

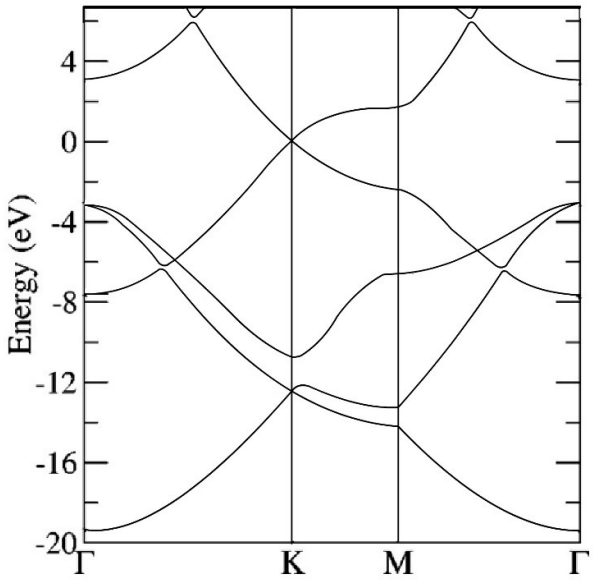

Figure 3.12 The *ab initio* band structure of graphene. (Figure taken from ref. [295].)

3.3.1.1 Tight-binding model of graphene

The tight-binding band structure of graphene is described here. The challenge in the tight-binding model is to construct a wavefunction that satisfies the Bloch's theorem while retaining the atomic character. A general tight-binding *ansatz* for the wavefunction has been constructed in terms of linear combination of atomic orbitals originally proposed by Bloch in 1928. For graphene with a basis of two, the tight-binding wavefunction is the weighted sum of 2 sublattice Bloch functions [280]:

$$\psi(k,r) = C_A\Phi_A(k,r) + C_B\Phi_B(k,r), \tag{3.11}$$

where C_A and C_B are the weights that are functions of k and are independent of r. Subscripts A and B denote two different atoms in a unit cell. The *ansatz* expresses the Bloch functions as linear combination of atomic orbitals that are assumed to be known:

$$\Phi_A(k,r) = \frac{1}{\sqrt{N}}\sum_j^N e^{ik\cdot R_{Aj}}\,\Phi\left(r - R_{Aj}\right) \tag{3.12}$$

$$\Phi_B(k,r) = \frac{1}{\sqrt{N}}\sum_j^N e^{ik\cdot R_{Bj}}\,\Phi\left(r - R_{Bj}\right), \tag{3.13}$$

where N is the number of unit cells in the lattice and $R_A(R_B)$ are the Bravais lattice vectors identifying the locations of all type A (B) atoms in the lattice. The atomic orbitals Φ belong to a class of functions known as Wannier functions, that are orthonormal functions sufficiently localized such that at distances increasingly removed from the center point R_j, the functions decay to zero very rapidly. The sum is over all the lattice vectors and $\frac{1}{\sqrt{N}}$ serves as the normalization vector for the Bloch functions in the limit when the Wannier function in

cell j has zero overlap with neighbouring Wannier functions. The Bloch functions must satisfy Bloch's theorem stated in Eq. (3.9):

$$\Phi_A(r + R_{Al}) = \frac{e^{ik\cdot R_{Aj}}}{\sqrt{N}} \sum_j^N e^{ik\cdot(R_{Aj} - R_{Al})}\, \Phi\big(r - (R_{Aj} - R_{Al})\big). \tag{3.14}$$

As the difference between two Bravais lattice vectors is another Bravais lattice vector,

$$(R_{Aj} - R_{Al}) = R_{Am} \tag{3.15}$$

Substituting (3.15) into (3.14) results in:

$$\Phi_A(r + R_{Al}) = \frac{e^{ik\cdot R_{Aj}}}{\sqrt{N}} \sum_m^N e^{ik\cdot R_{Am}}\, \Phi(r - R_{Am}) = e^{ik.R_{Al}} \Phi_A(r). \tag{3.16}$$

The Bloch functions must also satisfy the periodic boundary conditions stated in Eq. (3.10). The reciprocal lattice variable k is expressed in terms of the coordinate components as $k = k_x x + k_y y$ and let the size vector of the graphene Bravais lattice be $S = aNox + aNoy$ where $No = \sqrt{N}$. By imposing the periodic boundary condition of $e^{ik\cdot S} = 1$,

$$\textit{i.e. } Cos\left(ak_x No + ak_y No\right) + iSin\big(ak_x No + ak_y No\big) = 1, \tag{3.17}$$

Eq. (3.17) is satisfied only when $Cos\left(ak_x No + ak_y No\right) = Cos\, 2\pi p = 1$.

$$k_x = \frac{2\pi p}{aNo}, k_y = \frac{2\pi p}{aNo}\ , p = 0,1,2, \ldots . (No - 1), \tag{3.18}$$

where the allowed set of wavevectors those yield unique solutions for the energy bands are limited to the first BZ. The maximum number of k-states in the BZ is $No^2 = N$. Inserting Eq. (3.11) in Schrodinger equation (Eq. (3.7)) results in

$$HC_A\Phi_A(k,r) + HC_B\Phi_B(k,r) = E(k)C_A\Phi_A(k,r) + E(k)C_B\Phi_B(k,r). \tag{3.19}$$

Multiplying by the complex conjugate of Φ_A and Φ_B separately, two equations are obtained as follows:

$$\begin{aligned} HC_A\Phi_A\Phi_A^* + HC_B\Phi_B\Phi_A^* &= E(k)C_A\Phi_A\Phi_A^* + E(k)C_B\Phi_B\Phi_A^* \\ HC_A\Phi_A\Phi_B^* + HC_B\Phi_B\Phi_B^* &= E(k)C_A\Phi_A\Phi_B^* + E(k)C_B\Phi_B\Phi_B^* \end{aligned} \tag{3.20}$$

Integrating the above equations over the entire space occupied by the lattice (denoted by **Ω**) produces:

$$\begin{aligned} C_A\int H\Phi_A\Phi_A^* dr + C_B\int H\Phi_B\Phi_A^* dr &= E(k)C_A\int \Phi_A\Phi_A^* dr + E(k)C_B\int \Phi_B\Phi_A^* dr \\ C_A\int H\Phi_A\Phi_B^* dr + C_B\int H\Phi_B\Phi_B^*\, dr &= E(k)C_A\int \Phi_A\Phi_B^* dr + E(k)C_B\int \Phi_B\Phi_B^* dr \end{aligned} \tag{3.21}$$

To make the equations more manageable, the following symbolic definitions are used:

$$H_{ij} = \int \Phi_i^* H\Phi_j dr\,, \quad S_{ij} = \int \Phi_i^*\Phi_j dr \tag{3.22}$$

Hence $\int \Phi_A^* H\Phi_A dr = H_{AA}$, $\int \Phi_A^* H\Phi_B dr = H_{AB}, \int \Phi_B^* H\Phi_A dr = H_{BA}, \int \Phi_B^* H\Phi_B dr = H_{BB}$,

$$\int \Phi_A^*\Phi_A dr = S_{AA}\,, \quad \int \Phi_A^*\Phi_B dr = S_{AB}\,, \quad \int \Phi_B^*\Phi_A dr = S_{BA}\,, \quad \int \Phi_B^*\Phi_B dr = S_{BB}\,,$$

H_{ij} are the matrix elements of the Hamiltonian and have units of energy. S_{ij} are the overlap matrix elements between Bloch functions and are unitless. Since the two atoms in the unit

cell are identical, the overlap between the types of atoms are the same and thus $S_{AA} = S_{BB}$ and $H_{AA} = H_{BB}$. Also H_{ij} and S_{ij} correspond to physical observables and hence are Hermitian that leads to the condition $H_{BA} = H_{AB}^*$ and $S_{BA} = S_{AB}^*$. Thus

$$C_A H_{AA} + C_B H_{AB} = E C_A S_{AA} + E C_B S_{AB}$$
$$C_A H_{BA} + C_B H_{BB} = E C_A S_{BA} + E C_B S_{BB}\,. \quad (3.23)$$

By combining C_A and C_B terms,

$$C_A(H_{AA} - E S_{AA}) = C_B(E S_{AB} - H_{AB}) \quad (3.24)$$
$$C_A(H_{AB}^* - E S_{AB}^*) = C_B(E S_{AA} - H_{AA}). \quad (3.25)$$

This system of two linear equations can be solved easily by the method of substitution. Solving for C_B in Eq. (3.25), $C_B = C_A \frac{(H_{AB}^* - E S_{AB}^*)}{(E S_{AA} - H_{AA})}$ and then substituting C_B in Eq. (3.24) results in $C_A(H_{AA} - E S_{AA}) = C_A \frac{(H_{AB}^* - E S_{AB}^*)}{(E S_{AA} - H_{AA})}(E S_{AB} - H_{AB})$.

This procedure results in a quadratic equation that is readily solved for energy.

$$E(k)^{+}_{-} = -\frac{E_0(k) + \sqrt{E_0(k)^2 - 4(S_{AA}(k)^2 - |S_{AB}(k)|^2)(H_{AA}(k)^2 - |H_{AB}(k)|^2)}}{2(S_{AA}(k)^2 - |S_{AB}(k)|^2)} \quad (3.26)$$

$$E_0(k) = (2H_{AA}(k)S_{AA}(k) - S_{AB}(k)H_{AB}^*(k) - H_{AB}(k)S_{AB}^*(k)). \quad (3.27)$$

The positive and negative energy branches in Eq. (3.26) represent conduction (π^*) and valence (π) bands that are used to describe the bonding and anti-bonding interactions or energies respectively [280]. For further mathematical development of energy bands, the assumptions belonging to the tight-binding formalism are incorporated into the analysis. The assumptions and mathematical consequences are [280]:

1. *Nearest neighbour tight-binding (NNTB) model*: The wavefunction of an electron in any primitive cell overlaps with the wavefunction of its *nearest neighbours*. The nearest neighbours of a type-A atom in graphene lattice are three equivalent type-B atoms. NNTB model stipulates that the p_z wavefunction of a type-A atom overlaps with the p_z wavefunctions of its three nearest neighbours and zero overlap with wavefunctions from farther atoms. This simplifies Eq. (3.26) as the Hamiltonian matrix element reduces to

   $$H_{AA}(k) = \int \Phi_A^* H \Phi_A dr = \frac{1}{N}\sum_j^N \sum_l^N e^{-ik.R_{Aj}} e^{ik\cdot R_{Al}} \int \Phi^*\left(r - R_{Aj}\right) H\Phi(r - R_{Al})dr$$
   $$H_{AA} = \frac{1}{N}\sum_j^N \sum_l^N e^{-ik.R_{Aj}} e^{ik\cdot R_{Al}} E_{2p}\delta_{ij} = E_{2p}, \quad (3.28)$$

   The constant term, E_{2p} is nominally close to the energy of the *2p* orbital in isolated carbon, but not exactly the same, because the Hamiltonian of the lattice given by Eq.

(3.8) has a periodic potential, in contrast to the single Columbic potential of the isolated atom [280]. The overlap matrix reduces to

$$S_{AA} = \int \Phi_A^* \Phi_A dr = \frac{1}{N} \sum_j^N \sum_l^N e^{-ik.R_{Aj}} e^{ik\cdot R_{Al}} \int \Phi^*\left(r - R_{Aj}\right) \Phi(r - R_{Al}) dr \quad (3.29)$$

By applying the below feature of Wannier functions,

$\int \Phi^*(r - R_j)\, \Phi\left(r - R_j\right) dr = 1$ in Eq. (3.29):

$$S_{AA} = \frac{1}{N} \sum_j^N \sum_j^N e^{-ik.R_{Aj}} e^{ik\cdot R_{Al}} \delta_{ij} = 1, \quad (3.30)$$

2. Electron-hole symmetry: In the *ab initio* band structure of graphene (Figure 3.12), at energies very close to E_F (E = 0 at the K-point), π and π* branches have similar structure. These energy branches are mirror images of each other in the neighbourhood of E_F. Since electrons are the mobile charges in the π* band and holes are the mobile charges in the π band, this approximation is termed as electron-hole symmetry. The physical outcome of this symmetry is that both electrons and holes will have identical equilibrium properties such as DOS, group velocity, and carrier density. But this symmetry does not hold over a wide range of energies. Since the electron dynamics in practical devices occur over a small range of energies close to E_F this approximation is useful. A key physical outcome of this symmetry is that electrons and holes will have identical equilibrium properties such as DOS, group velocity and carrier density. The only part of Eq. (3.26) that possesses symmetry about some number is the plus/minus square root argument i.e. $-\sqrt{f(k)}$ is a mirror image of $+\sqrt{f(k)}$. In order for Eq. (3.26) to retain this symmetry, $S_{AB}(k)$ must vanish to zero. Mathematically, electron-hole symmetry forces $S_{AB}(k) = 0$. Therefore Eq. (3.26) becomes:

$$E(k) \pm = E_{2p} \pm \sqrt{H_{AB}(k) H_{AB}^*(k)}, \quad (3.31)$$

This is the energy dispersion originally proposed by P. R. Wallace in 1947 [296].

For graphene, the reference potential is the E_F, which is independent of k, and is customarily set to zero. Since $E_{2p}$is independent of k, it is convenient to employ it as the reference and hence $E_{2p} = E_F = 0\ eV$. Thus Eq. (3.31) reduces to

$$E(k) \pm = \pm\sqrt{H_{AB}(k) H_{AB}^*(k)}, \quad (3.32)$$

The Hamiltonian matrix element $H_{AB}(k)$ can be calculated as:

$$H_{AB}(k) = \int \Phi_A^* H \Phi_B dr = \frac{1}{N} \sum_j^N \sum_l^N e^{-ik.R_{Aj}} e^{ik\cdot R_{Bl}} \int \Phi^*\left(r - R_{Aj}\right) H\Phi(r - R_{Bl}) dr \quad (3.33)$$

Let the nearest neighbours of type-A atom (as represented in Figure 3.9) be

$R_1 = R_{Aj} - R_{Bj}, R_2 = R_{Aj} - R_{Bj+1}, \quad R_3 = R_{Aj} - R_{Bj-1}$

where j, j+1 and j-1 are the indices of the primitive unit cells where the type B-nearest neighbours are located w.r.t. type-A atom in cell j. Thus

$$H_{AB}(k) = \frac{1}{N}\sum_{j}^{N}\sum_{1}^{3} e^{-ik.R_m}E_m \tag{3.34}$$

E_m is the finite value of integration of the nearest neighbour Wannier functions. As the integrals are radially dependent and the nearest neighbor distances are radially symmetric, $E_1 = E_2 = E_3$. For convenience, it is set as $E_m = \gamma$, which can be viewed as a fitting parameter of positive value, often called as nearest neighbour overlap energy, the carbon-carbon interaction energy, the hopping or transfer energy. The Hamiltonian matrix element reduces to a sum of three terms:

$$H_{AB} = \gamma\left(e^{-ik.R_1} + e^{-i\ .R_2} + e^{-ik.R_3}\right) \tag{3.35}$$

and

$$H_{AB}(k)\, H_{AB}^{*}(k) = \gamma^2\left(e^{-ik.R_1} + e^{-ik.R_2} + e^{-ik.R_3}\right)\left(e^{ik.R_1} + e^{ik.R_2} + e^{ik.R_3}\right), \tag{3.36}$$

By simplifying Eq. (3.36) becomes:

$$H_{AB}(k){H_{AB}}^{*}(k) = \gamma^2\{3 + 2Cos[k.(R_1 - R_2)] + 2Cos[k.(R_1 - R_3)] + 2Cos[k.(R_2 - R_3)]\} \tag{3.37}$$

Since the nearest neighbours, R_1, R_2 and R_3 are given by Eq. (3.2), thus

$$H_{AB}(k)H_{AB}^{*}(k) = \gamma^2\left(1 + 4Cos\frac{\sqrt{3}a}{2}k_x Cos\frac{a}{2}k_y + 4Cos^2\frac{a}{2}k_y\right) \tag{3.38}$$

By inserting Eq. (3.38) in Eq. (3.32),

$$E(k)\pm = \pm\gamma\left(\sqrt{1 + 4Cos\frac{\sqrt{3}a}{2}k_x Cos\frac{a}{2}k_y + 4Cos^2\frac{a}{2}k_y}\right). \tag{3.39}$$

This formula is the most widely used NNTB approximation in which γ is used as a fitting parameter that matches with *ab initio* computations or experimental data. The commonly used values for γ range from 2.7 eV to 3.3 eV. The extracted value of γ ~ 3.1 eV from experimental measurements of the Fermi (group) velocity ($v_F \sim 10^6$ m/s) in graphene is used for routine measurements. The highest energy state within the valence band and the lowest energy state within the conduction band occur at the K-point corresponding to 0 eV. The NNTB dispersion given by Eq. (3.39) shows good agreement with *ab initio* computations for the π bands (Figure 3.13) with the strongest agreement at low energies i.e. energies close to the E_F (a range within $\pm 1\ eV$ of E_F) [297]. By relaxing the electron-hole symmetry, great agreement at higher energies can be achieved that leads to nonzero S_{AB} (k). For this case, the energy dispersion is given by [280]:

$$E(k)\pm=\frac{\pm\gamma\left(\sqrt{1+4Co\ \frac{\sqrt{3}a}{2}k_xCos\frac{a}{2}k_y+4Cos^2\frac{a}{2}k_y}\right)}{1\mp s_0\sqrt{1+4Co\ \frac{\sqrt{3}a}{2}k_xCos\frac{a}{2}k_y+4Cos^2\frac{a}{2}k_y}} \tag{3.40}$$

where s_0 is the overlap integral, often employed as a fitting parameter with positive value and nominally close to zero. The use of these two fitting parameters (γ,s_0) leads to a better overall agreement [280].

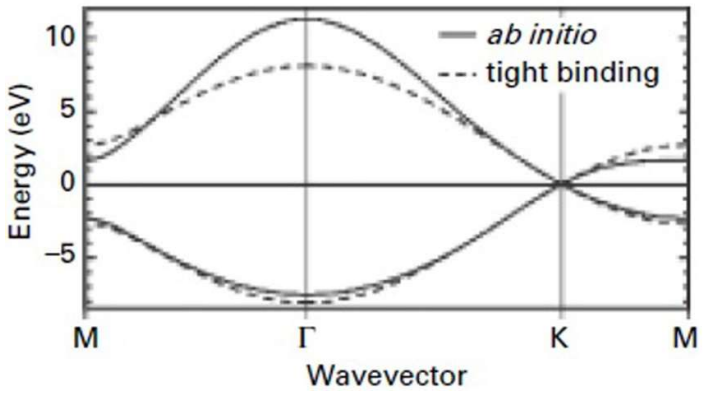

Figure 3.13 *Ab initio* and nearest-neighbor tight-binding dispersions of graphene. (Figure taken from ref. [297].)

The electronic properties of graphene differ from the usual three-dimensional structures as its Fermi surface is characterized by six double cones [24] (Figure 3.14). The upper-half of the dispersion is the conduction band and the lower-half is the valence band. The valence and conduction band look like conical valleys [142] and touches at the high-symmetry K and K' points of the BZ [10]. The 6 k points in the band structure of graphene where valence and conduction bands meet are called Dirac points where the energy is E_F.

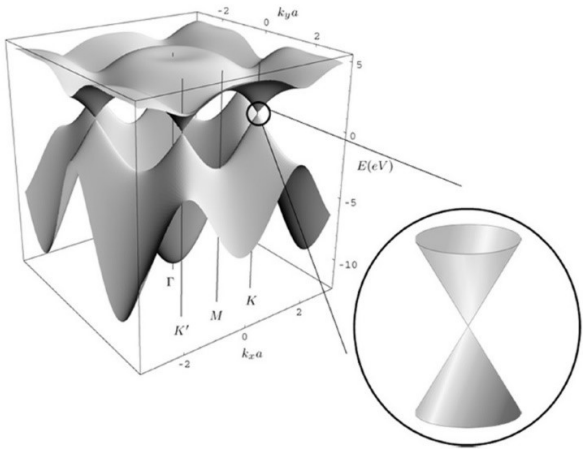

Figure 3.14 Band structure of single layer graphene showing the linear dispersion at the Dirac point (Figure taken from ref. [27].)

Owing to the absence of the band gap at E_F and the fact that valence and conduction bands meet at E_F, graphene is considered as a semi-metal or zero-gap semiconductor in contrast to a

regular metal in which E_F is located in the conduction band and a regular semiconductor, where E_F is located inside the band gap [280].

3.3.2 The electronic density of states

A central property of electronic materials is the DOS, $g(E)$, that defines the density of mobile electrons or holes present in a solid at a given temperature. For two dimensions, the total number of states between energy E and an interval dE is given by a differential area in k-space, dA divided by the area of one k-state is

$$g(E)dE = 2g_z \frac{dA}{(2\pi)^2 \Omega} \tag{3.41}$$

where the factor of two in the numerator represents the spin degeneracy, g_z is the zone degeneracy. For graphene, the six equivalent k-points are shared by three hexagons and hence, g_z = 2. For determining dA, consider a circle of constant energy in k-space and the perimeter of this circle is $2\pi k$. The differential area obtained by an incremental increase of the radius by dk is $2\pi k dk$.

$$\therefore g(E) = \frac{2}{\pi}\left|k\frac{dk}{dE}\right| = \frac{2}{\pi}\left|k\left(\frac{dE}{dk}\right)^{-1}\right| \tag{3.42}$$

Substituting from Eq. (3.41) results in linear DOS suitable for low energies:

$$g(E) = \frac{2}{\pi(\hbar v_F)^2}|E| = \beta_g|E|, \tag{3.43}$$

where β_g is a material constant $\beta_g \approx 1.5\times10^{14} eV^{-2}cm^{-2}$. At E_F (E_F = 0 eV), $g(E) = 0$, i.e. the DOS vanishes to zero even though there is no band gap. This is the reason why graphene is considered as a semimetal in contrast to normal metals that have a large DOS at the E_F [280].

Even though the carrier density is zero at the Dirac points, the conductivity of pure graphene does not vanish at all. The reason behind this is not yet known, but the theory suggests that this observed high conductivity is due the unique nature of graphene's electrons. The electron state might be present or absent in a particular region in space implies that the electron has been localized and it behaves as a particle rather than as a wave [24]. The unusually strong interactions among electrons near the Dirac points suppress localization and hence the electron behaves as a wave which allows conduction to occur even with zero charge carrier state. But the electrical conductivity of doped graphene is very high, which is higher than that of copper at room temperature [24].

3.3.3 Linear energy dispersion

At Dirac points and energies close-by, the dispersion centred at k-point can be expressed as a linear equation as follows:

$$E(k)^{\pm}_{linear} = \pm\hbar v_F|k| = \pm\hbar v_F\sqrt{{k_x}^2 + {k_y}^2} = \pm\hbar v_F k, \quad (3.44)$$

v_F is defined as $\left(\frac{1}{\hbar}\right)\left(\frac{\partial E}{\partial k}\right)$ evaluated at E_F, k is in spherical co-ordinates, $\hbar$ is the reduced Planck's constant and $\hbar v_F$ is the gradient of dispersion. The 3D plot of the linear dispersion (*Dirac cone)* is shown in Figure 3.15. Angle-resolved photoemission spectroscopic measurements have confirmed the linear dispersion of pure graphene up to approximately ±0.6 eV [298].

As the energy varies linearly with the magnitude of momentum [142]near the Fermi level, the charge carriers in graphene obey linear energy momentum dispersion relation. As the effective mass depends on the second derivative of energy with respect to electron's momentum vector [24] and since the energy-momentum relation is linear, the second derivative of this linear function is zero, which implies that effective mass of the electrons in graphene is zero near the Fermi level. Thus they behave like massless relativistic particles and Einstein's special relativity comes into play in the form of Dirac's relativistic quantum mechanical wave equation for describing particle dynamics [2, 8, 10].

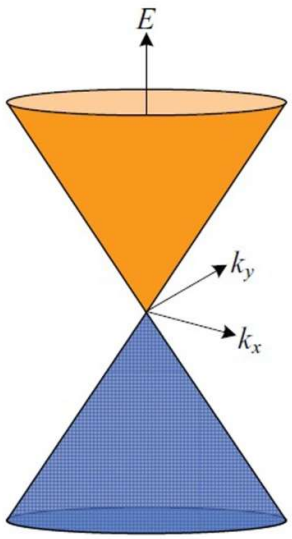

Figure 3.15 Linear energy dispersion of graphene at the K-point known as Dirac cone. (Figure taken from ref. [280].)

3.3.4 Fermi energy

The equilibrium Fermi energy is the energy of the highest occupied *k*-state when the solid is in ground state (temperature of 0 K). Determining E_F involves populating the *k*-states in the BZ with all the π electrons in the solid according to Pauli's exclusion principle. Each carbon atom provides one p_z electron, resulting in two electrons/unit cell. Since there are N unit cells in the solid that can hold 2N electrons, there are N *k*-states in the valence band. The highest state occupying the most energetic electrons are at the K-points and the corresponding energy is formally defined as Fermi energy (E_F = 0 eV).

The properties of electrons around E_F determine the characteristics of practical electronic devices [280]. The behaviour of graphene electrons at E_F is a matter of great importance in condensed matter physics due to the linear energy dispersion relation. Since the electrons moving through the perfect honeycomb lattice have smooth sailing [24] due to their mass-less behaviour, the electrons within graphene travel at the speed of ~10^6 m/s, which is about 300 times slower than the speed of light [2, 10, 27].

The Fermi level in pure graphene is located at the converging point [24] of six double cones in the energy spectrum where the DOS is zero and there is no gap in the band structure [294]. The Fermi level departs from its equilibrium value of 0 eV, under non-equilibrium conditions (applied electric or magnetic field) or extrinsic conditions (presence of impurity atoms). This deviation from the equilibrium value is very valuable in determining the strength of the field and concentration of impurity atoms [280]. The application of electric field may change the position of the Fermi level and the material becomes either *n*-doped (with electrons) or *p*-doped (with holes). Graphene gets also doped by the adsorption of ammonia or water or other target gas species on graphene's surface [30, 262], which forms the basis of gas sensing property [24].

3.3.5 Ambipolar electric field effect

The peculiar electronic spectrum of graphene opens up the possibility to tune the type (electron or hole) and density of the charge carriers in graphene through the application of an external electric field [281]. The position of the Fermi level may get shifted up or down with positive or negative gate voltages by inducing electrons or holes in graphene [5]. Since the charge carriers in graphene can be changed continuously between holes and electrons through the application of a homogenous electric field perpendicular to graphene plane [5, 281], graphene exhibits ambipolar electric field effect. The measurements of resistivity under changing gate voltages [5] (Figure 3.16) experimentally confirmed the ambipolar electric

field effect in SLG. The insets of Figure 3.16 show the conical low-energy spectrum with different positions of E_F, corresponding to negative, zero, and positive gate voltages, V_g, respectively. Such an ambipolar electric field effect is the key for extensive research on graphene studying its transport behaviour, sensing properties and other related device applications. The finite resistivity of graphene at vanishing gate voltage is also evident from Figure 3.16.

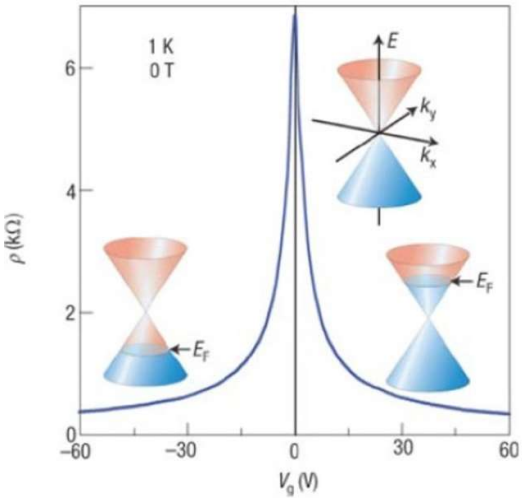

Figure 3.16 Ambipolar electric field effect in SLG on a SiO_2 substrate (Figure taken from ref. [5].)

The subsequent chapter presents the computational methodology used to perform the calculations discussed in the rest of the chapters. The *ab initio* DFT method employed in the thesis is described in detail. The approximations used for the implementation of DFT in practical situations are also presented in this chapter. This chapter also briefly discusses the DFT implementation using ABINIT simulation package.

CHAPTER 4

COMPUTATIONAL METHODOLOGY

4.1 Computational materials science methods

Modern society is largely dependent on materials, as they form the basis of our health, energy sources, clothing, transportation, buildings, food supplies and our modern technologies. Successful new applications of materials come from the complex interactions occurring within the material on different time and length scales. The properties of materials can be derived by understanding the interactions at the atomic scale [299]. The interdisciplinary field of materials science focus on the study of the relationships between the properties, microstructure of materials, processing and performance of materials that enable an engineering function for various applications which include energy, electronics, environment, transportation, medicine, manufacturing, communications, etc. Material scientists study the relationships between the structure and properties of a material. By understanding and modifying the microstructure, material scientists tune the properties of materials to develop materials with desired properties for specific uses.

Computers have become an important research tool in materials science and simulations based on computers are a connecting link between analytical theory and experiment, as they allow to carefully examine analytical theories and also to explore situations that are not probable in real laboratory experiments and this interdisciplinary research area is often referred to as “Computational Materials Science” [300]. This rapidly growing area within materials science has great potential to manage multi-disciplinary simulations in realistic conditions across physics, chemistry and engineering. Today, fast and extremely powerful computer systems assist in solving complex, many body problems without using mathematical approximations as in analytical theory, which were not possible to solve few years ago. Computational methods in materials science helps researchers to gain fundamental understanding of the structural, magnetic, optical, electrical properties of materials, or phenomena associated with their design, characterization, and utilization by numerically solving the quantum mechanical equations.

Scientists can now solve theoretical material science problems, predict future or unobserved situations by combining advanced computing technologies and quantum mechanical theories. Quantum mechanical based theoretical computation allows analysing the properties of systems which are difficult to characterize experimentally or predicting the physical

properties of materials which have not yet been made. This method can be successfully employed for studying the structure-property relationship of nanoscale materials and thus enabling the identification and design of these materials for specific applications.

Computational methods in materials science can be divided into three, namely molecular mechanics, semi empirical, and *ab initio*, which differ in the use of approximations and hence produce results with different levels of accuracy. Molecular mechanics utilize classical physics to model the behaviour of molecular systems, instead of solving Schrödinger equation and hence the results from this method are less accurate. All constants appearing in the classical equations must be obtained either from *ab initio* calculations or from experiments. As this method totally avoids quantum mechanics, large molecules such as deoxyribonucleic acid (DNA) segments, proteins etc. can be modelled successfully, which makes it a suitable tool of computational biochemists. Semi empirical methods use quantum physics and experimentally derived empirical parameters in the mathematical model. As these methods use extremely simplified Schrödinger equation, the results are less accurate, but are much faster. These methods can be successfully employed for calculations in organic chemistry, where there are only a few elements which are of moderate size.

Ab initio (first-principles) methods do not take any input from experiments and consider only fundamental physical constants. "*Ab Initio*" is a Latin word which means "from the beginning". As the computations are derived directly from fundamental principles, they are computationally expensive, but they can give good qualitative results. These calculations do not use empirical parameters other than fundamental constants and the atomic numbers of the atoms present. These methods calculate the molecular properties of the systems using quantum mechanical theory.

4.2 The Schrödinger equation

A good theoretical model is extremely useful to understand the reactivity of modified graphene towards gas molecules. Quantum mechanical based modeling methods assist in modeling, interpreting and predicting the interactions at the atomic and molecular level. As this thesis investigates the interactions of individual gas molecules with different graphene surfaces, the theoretical model employed should be quantum mechanical in nature.

The properties of any system (atoms, molecules or solids) can be obtained from its total energy by solving the non-relativistic, time-independent Schrödinger wave equation, referred to as the Schrödinger equation. Any physical property that can be related to the total energy

of the system can be described by using *ab initio* based computations. For a system with N electrons and M nuclei, the Schrödinger equation can be written as

$$\hat{H}_{tot}\psi(x_1, \ldots\ldots, x_N, R_1, \ldots, R_M) = E(k)\psi(x_1, \ldots\ldots, x_N, R_1, \ldots, R_M), \quad (4.1)$$

where R_i represent the position coordinates of the M atomic nuclei in the system and x_i represent the coordinates of the N electrons. The non-relativistic Hamiltonian operator $\hat{H}_{tot}$ for a many-particle system can be written as the sum of electronic, nuclear and mixed terms as follows:

$$\begin{aligned}\hat{H}_{tot} &= \hat{T}_e + \hat{T}_N + \hat{V}_{Ne} + \hat{V}_{ee} + \hat{V}_{NN} \\ &= -\frac{\hbar^2}{2m_e}\sum_i^N \nabla_i{}^2 - \sum_I^M \frac{\hbar^2}{2m_I}\nabla_I{}^2 - \sum_i^N \sum_I^M \frac{Z_I e^2}{|r_i - R_I|} + \frac{1}{2}\sum_{i=j}^N \frac{e^2}{|r_i - r_j|} + \frac{1}{2}\sum_{I\neq J}^M \frac{Z_I Z_J e^2}{|R_I - R_J|}\end{aligned} \quad (4.2)$$

where T is the kinetic energy, V the potential energy and e and N represent electrons and nucleus respectively. In Eqn. (4.2), m_e is the mass of an electron, M_I and Z_I are the mass and the nuclear charge of the nuclei, r and R are the coordinates of the electron and nucleus respectively. The first and second term of Eqn. (4.2) correspond to the kinetic energies of the electrons and nuclei, while the other terms represent the electron-nucleus, electron-electron, and nucleus-nucleus Coulomb interaction terms respectively. As the Hamiltonian $\hat{H}_{tot}$ includes all the interactions of the system, the Schrödinger equation could solve these interactions by calculating the total energy of many-body systems. Unlike a single-electron system, it is difficult or impossible to analytically solve the Schrödinger equation for many-body systems, as these systems include Coulomb interactions among the nuclei and electrons and their mutual interactions. Several types of approximations are widely employed for practical application.

The first approximation, termed as Born-Oppenheimer approximation, can be made by considering the fact that the mass of proton (lightest nucleus) is approximately 1800 times greater than that of an electron and hence nuclei travel at much slower speed compared to electrons. For carbon atoms, the ratio of the mass of the nuclei to the mass of electrons is about 22000. Thus the kinetic energy of the nuclei (the second term in Eqn. (4.2)), which is inversely proportional with the nuclear mass M_I, is comparatively small and hence can be neglected. This approximation considers the nuclei to be stationary with respect to electrons, and also the nucleus-nucleus repulsion term becomes merely a constant. Thus the Hamiltonian can be rewritten as

$$\hat{H}_{tot} \simeq \hat{H}_e + \hat{V}_{NN}, \quad (4.3)$$

$$\text{with } \hat{H}_e = -\frac{\hbar^2}{2m_e}\sum_i^N \nabla_i{}^2 + \frac{1}{2}\sum_{i=j}^N \frac{e^2}{|r_i - r_j|} - \sum_i^N \sum_I^M \frac{Z_I e^2}{|r_i - R_I|} \quad (4.4)$$

and $\hat{V}_{NN} = \frac{1}{2}\sum_{I\neq J}^{M} \frac{Z_I Z_J e^2}{|R_I - R_J|}$ (4.5)

$\hat{H}_e$ which represents the electronic part can be solved by using the nuclear coordinates as parameters (Eqn. (4.4)) and by adding $\hat{V}_{NN}$ (the nuclear repulsion energy), total energy of the system can be calculated. $\hat{V}_{NN}$ can be calculated easily and hence Eqn. (4.4) is of interest now. let $\hat{H}_e$ be $\hat{H}$ for convenience and for removing all the constants in Eqn. (4.4), it is defined as $\hbar = e = m_e = 1$. Thus Eqn. (4.4) becomes

$$\hat{H} = -\frac{1}{2}\sum_i^N \nabla_i{}^2 + \frac{1}{2}\sum_{i=j}^N \frac{1}{|r_i - r_j|} - \sum_i^N \sum_I^M \frac{Z_I}{|r_i - R_I|} \quad (4.6)$$

$$\hat{H} = \hat{T} + \hat{V}_{ee} + \hat{V}_{Ne} \quad (4.7)$$

Thus, the hamiltonian in Eqn. (4.6) is entirely determined by the positions R_I and charges Z_I of the nuclei and the number of electrons (N). Out of the three terms in Eqn. (4.6), the first two terms can be considered universal and thus the Hamiltonian is entirely specified through the third term i.e. the term originating from the nuclear potentials. The electron-nuclei interaction energy, $\hat{V}_{Ne}$ is included as an interaction with an external potential as $V_{ext}(r) = \sum_I \frac{Z_I}{r - R_I}$. Thus, this approximation results in energy values that are dependent on the relative nuclear coordinates. Thus, the total energy can be rewritten as:

$$E_{tot} = \langle \hat{H}_{tot} \rangle \simeq \langle \hat{H} \rangle + \hat{V}_{NN} = \langle T \rangle + \langle \hat{V}_{ee} \rangle + \langle \hat{V}_{ext} \rangle + \hat{V}_{NN} \quad (4.8)$$

where the expectation values are taken with respect to $\psi(x_1, \ldots\ldots, x_N)$.

4.3 Density Functional Theory

One of the most commonly used approximations that *ab initio* methods used to reduce the complexity of many body systems is DFT. Hohenberg and Kohn proposed this method to solve the many body Schrödinger equation by expressing the total energy of the system in terms of the total electron density [301]. Hence properties of a many-body system can be determined by using functional of the electron density, from where DFT got its name.

This quantum mechanical (QM) modeling method is used in materials science, physics and chemistry to predict ground state properties (e.g. the total energy, the atomic and electronic structure etc.) of many-body systems [302]. It has been very popular for computational solid-state physics calculations since 1970s. Until 1990s, this method was not found to be accurate for quantum-chemical calculations. By refining the approximations used in DFT to include the exchange and correlation interactions, this method has been acceptable for quantum-chemical applications. Due to the favorable price/performance ratio of DFT compared with electron-correlated wave function-based methods such as Møller–Plesset perturbation theory

or coupled cluster [302], larger molecular systems can be analyzed using DFT as it offers sufficient level of accuracy and great predictive power. Apart from these, comparatively low computational costs of DFT than that of traditional methods and its descendants based on the complex many-electron wavefunction, made DFT one of the most popular approaches to investigate the electronic structures of many body systems. Thus DFT has emerged as one of the most versatile methods in condensed-matter physics and computational chemistry [303].

DFT was proposed in 1964–65 by Hohenberg, and Kohn [301] and Kohn and Sham [304]. Both significantly reduce the complexity of the "first-principles" approach, at the expense of some approximations.

4.3.1 The Hohenberg-Kohn theorems

DFT is based on two theorems stated by Hohenberg and Kohn in 1964, commonly called as Hohenberg-Kohn (HK) theorems [301]. Walter Kohn was awarded with the Nobel Prize in Chemistry in 1998 'for his development of the density-functional theory'. The first theorem states that the wavefunction can be replaced by the electron ground state density without any loss of information and the second theorem is the equivalent of the variation principle in standard quantum mechanics.

4.3.1.1 The first Hohenberg-Kohn theorem

The first Hohenberg-Kohn theorem can be stated as follows:
The external potential, $V_{ext}(r)$, of any system of interacting particles is uniquely determined, except for a constant, by the ground state particle density $\rho_0(r)$.

Hence the Hamiltonian stated in Eqn. (4.7), which is completely specified by the external potential, is also uniquely determined by the ground state electron density. Therefore, all the ground state properties of a system can be faithfully determined by its ground state density, $\rho_0(r)$. In this way, the system properties can be obtained without knowing the exact numerical form of the external potential $Vext\ (r)$.

4.3.1.2 The second Hohenberg-Kohn theorem

The second Hohenberg-Kohn theorem can be stated as follows:
For any external potential, $V_{ext}(r)$, the exact ground state energy of a system is given by the minimum value of the energy functional, $E_{HK}[\rho]$ and the density for which this minimum is reached corresponds with the ground state particle density $\rho_0(r)$. Hence $E_{HK}[\rho_0]$ alone is sufficient to determine the exact ground state energy and density.

Hence the ground state energy of the system with Hamiltonian (4.7) can be written as:

$$E_{HK}[\rho_0] = T[\rho_0] + V_{ee}[\rho_0] + V_{ext}[\rho_0] = F_{HK}[\rho_0] + \int \rho_0(r)V_{ext}(r)dr \quad (4.9)$$

where $F_{HK}[\rho_0]$ is a universal functional of density and the functional $E_{HK}[\rho]$ in the Eqn. (4.9) depends on the external potential $V_{ext}(r)$.

Thus, DFT can determine any ground state or excited state property of a system given a functional that maps the ground state density to that property.

4.3.2 The Kohn-Sham approach

The energy functional, $E_{HK}[\rho]$ contains the kinetic energy, $T[\rho]$, the electron-electron Coulomb interactions $V_{ee}[\rho]$, and the interaction with the external potential, $V_{ext}(r)$ as

$$E_{HK}[\rho] = T[\rho] + V_{ee}[\rho] + \int \rho(r)V_{ext}(r)dr \quad (4.10)$$

The main problem in finding the approximate expression for the energy functional directly from the ground state density is with calculation of the kinetic energy term. To get a specific expression for the kinetic energy term, $T[\rho]$, Kohn and Sham constructed a set of one-electron orbitals (K-S orbitals), which are eigen vectors of the Kohn-Sham equation,

$$-\left(\frac{1}{2}\nabla^2 + V_{eff}(r)\right)\phi_i(r) = \varepsilon_i\phi_i(r) \quad (4.11)$$

Where ε_i is the energy of the corresponding K-S orbital, ϕ_i. The electron density, $\rho(r)$, can be defined as : $\rho(r) = \sum_i^N |\phi_i(r)|^2$ (4.12)

They introduced an imaginary many-body non-interacting system having the same electron density as that of the real many-body system [304]. Based on the Kohn-Sham ansatz, $T[\rho]$ can be approximated by the N-electron non-interacting system as:

$$T_s[\rho] = -\frac{1}{2}\sum_i^N \langle\phi_i|\nabla^2|\phi_i\rangle \quad (4.13)$$

Therefore, the total energy can be re-written as:

$$E[\rho] = T_s[\rho] + \int \rho(r)V_{ext}(r)dr + E_H[\rho] + E_{XC}[\rho] \quad (4.14)$$

where $E_H[\rho]$ is the Hartree energy, and is expressed as $E_H[\rho] = \frac{1}{2}\int \rho(r)\rho(r')drdr'$ (4.15)

In Eqn. (4.14), $E_{XC}[\rho]$ is the exchange correlation energy, which includes all the many-body interactions. The expression of $E_{XC}[\rho]$ is as follows:

$$E_{XC}[\rho] = (T[\rho] - T_s[\rho]) + (V_{ee}[\rho] - E_H[\rho]), \quad (4.16)$$

Eqn. (4.16) states that the exchange correlation energy is the energy difference of the kinetic energy terms and internal interactions between the real interacting system and the imaginary non-interacting system. Thus, this term includes the errors from the consideration of non-interacting kinetic energy and the treatment of electron-electron Coulomb interactions.

The Kohn-Sham potential obtained by varying the total energy functional with respect to K-S orbitals is as follows:

$$V_{eff} = V_{ext}(r) + \int \frac{\rho(r')}{|r-r'|} dr' + \frac{\delta E_{XC}(\rho)}{\delta \rho(r)} \quad (4.17)$$

In Eqn. (4.17), $V_{ext}(r)$ is the external potential representing interactions of valence electrons with core electrons, the second term represents the electron-electron Coulomb interaction potential and $\frac{\delta E_{XC}(\rho)}{\delta \rho(r)}$ is the exchange correlation potential representing the many body interactions of electrons. V_{eff} depends on electron density, while electron density is defined by the eigenfunction, ϕ as in Eqn. (4.12), hence a self-consistent field (SCF) method is used to find the solutions of the Kohn-Sham equations [281].

4.3.3 Implementation of DFT calculation scheme

Even though DFT is exact in principle [302], its practical implementation for real solids necessitates some approximations.

4.3.3.1 Exchange correlation functional

The main problem with the Kohn-Sham approach of the DFT is the introduction of the unknown exchange-correlation functional energy, $E_{XC}(\rho)$. As there is no specific expression for this term, it is not easy to solve the Kohn-Sham equations. Hence different approaches have been developed for approximating this term [305]. The success of DFT depends on the use of efficient exchange correlation (XC) energy functionals, which are separated into an exchange and a correlation part. The most frequently used approximation methods in solid state physics for calculating the exchange correlation energy and corresponding potential are local density approximation (LDA) and generalized gradient approximation (GGA). These approximations do not involve the use of experimentally derived empirical parameters. LDA functional assumes uniform density for a homogeneous electron gas and the XC functional is defined as:

$$E_{xc}^{LDA}[\rho] = \int \rho(r)\epsilon_{xc}\big(\rho(r)\big)dr \quad (4.18)$$

$\epsilon_{xc}\big(\rho(r)\big)$ is a function that gives the exchange-correlation energy per particle of an electron gas of uniform density ρ(r). The exchange part of the LDA XC functional can be found precisely, whereas for the correlation part, very accurate data, based on quantum Monte-Carlo simulations, is available [306]. At first sight, it would seem that LDA is not very accurate since the density of any real system is far from homogeneous, LDA functional gives reasonably good estimation of real systems. LDA is used to calculate the ground state properties of materials and for successfully calculating physical quantities such as bond

lengths and lattice parameters. But in some cases, LDA overestimates the ground state energies and the adsorption energies, and underestimates the band gap of semiconductors and insulators to experimental values [307]. In the GGA approximation, the gradient of density is used to describe the exchange correlation energy and the GGA based XC functional can be expressed as follows:

$$E_{xc}^{GGA}[\rho] = \int \epsilon_{xc}(\rho(r), |\nabla\rho(r)|, \dots)dr \quad (4.19)$$

There are a lot of different GGA exchange-correlation functionals based on both physical insights and empirical data, and the most popular ones include the Perdew and Wang (PW91) [308], Becke (B88) [309]and Perdew-Burke-Ernzerhof (PBE) [310]. In this work, both LDA and GGA-PBE based methods have been used.

4.3.3.2 Bloch states

The independent particle reference system introduced by the Kohn-Sham approach of DFT described by Eqn. (4.11) can be solved by making use of the Bloch theorem and writing the single particle wavefunctions from Eqn. (4.11) as:

$$\phi_k(r) = e^{ik.r}u_k(r) \quad (4.20)$$

In large systems, calculation of properties such as energy or density requires integration over k, as the spectrum of k-points is quasi continuous in these systems. Due to symmetry, the integration can be restricted to the irreducible Brillouin zone. But these integrals need to be approximated by discretized versions on a finite, well chosen, grid of k-points, since there is no trivial functional dependence between k and ϕ_k. Monkhorst and Pack proposed the use of uniform-point grids defined by:

$$k_{m_1,m_2,m_3} = \sum_{i=1}^{3} \frac{2m_i - q_i - 1}{2q} b_i \text{ with } m_i = 1, 2, \dots, q_i \quad (4.21)$$

Where b_i represents the reciprocal lattice vector, q_i denotes the number of discretization steps in the direction of b_i. In total, there are $q_1q_2q_3$ k-points and by restricting the k-points to the first BZ, the number of k-points can be further reduced. The number of required k-points depends upon the size, nature of the system under study and the property of interest. Hence convergence with respect to the k-point grid needs to be checked for all calculations.

4.3.3.3 Basis sets

A basis set is a set of functions used to project the molecular orbitals. The molecular orbitals are expanded as a linear combination of these functions, for which the weight need to be calculated. The K-S orbitals can be more effectively represented by using basis set rather than representing them on a finite grid. Different basis sets have been suggested and are selected based on the system under study, the computational resources and the desired accuracy. For

periodic boundary conditions, which include bulk materials and surfaces, plane wave basis set is used.

Only the cell periodic part of the Bloch states (4.20), $u_k(r)$ is expressed in plane wave basis. $u_k(r)$ in Eqn. (4.20) is periodic in nature and is of the form:

$$u_k(r) = \sum_G c_{k,G} e^{iG.r} \quad (4.22)$$

with summation over all the reciprocal lattice vectors, G of the system. Hence $u_k(r)$ can be expressed using a discrete spectrum of plane waves *i.e.* with a simple Fourier series. For practical implementation, the discrete, but infinite plane wave basis set need to be shortened. Thus, plane wave basis sets with G smaller than G_{max} are always adopted:

$$|G| < G_{max} \quad (4.23)$$

This is roughly the same as stating that details in the structure of the wavefunction smaller than $\lambda = \frac{2\pi}{G_{max}}$ are ignored.

Plane wave basis set has several advantages and also disadvantages as compared to other basis sets. It allows easy switching between the real space and the reciprocal space by fast Fourier transformations (FFT). Another advantage of the pane wave basis set is that the basis remains fixed during geometry relaxation, in contrast to local basis sets where the basis changes when the atoms change their positions. One can get artificial effects as the space in not uniformly described by the basis set of plane waves. The plane wave basis set can be easily improved by adding more plane waves corresponding to increasingly small wavelengths. The huge size of the basis is the major disadvantage of using plane wave basis set. As compared to other basis sets, it needs a large number of basis functions to precisely represent realistic wavefunctions.

4.3.3.4 Pseudopotential

The electronic wavefunctions of the valence states of atoms strongly oscillate to satisfy the orthogonality condition with respect to the core states. These oscillations are confined to the core region and hence require a lot of plane waves to accurately describe the core electron wavefunction. The need for large number of plane waves increases the computational effort significantly and hence it would be useful to remove the oscillations. Different methods have been implemented to reduce the computational effort, and the most frequently used one is the pseudopotential method.

Pseudopotentials replace the strong Coulomb potential of the nucleus and the effects of the tightly bound core electrons by an effective ionic potential acting on the valence electrons. As the first step, the core electrons are removed and then, the wavefunctions of valence electrons

are replaced by smooth pseudowavefunctions that require less plane waves for their description. When atoms interact with other atoms to form molecules or solids, the core states of individual atoms remain unchanged due to the tight binding of core electrons to the nucleus. Hence the core states can be removed from the calculation and the properties of matter are dictated by the valence electrons. The core electrons can be incorporated into the potential acting on the valence electrons, but due to the orthogonality condition with respect to the core states, the valence wavefunctions with different angular momentum will feel a different potential. The modified potential is called pseudopotential. The second step in the pseudopotential method is to replace the full ionic core interaction potential by a softer pseudopotential, which results in smoother wavefunctions.

There are different types of pseudopotential and the most commonly used ones include *ab inito* norm-conserving (NCPP) [311], and ultrasoft pseudopotentials (USPP) [312]. In this work, the Troullier-Martins NCPP scheme within plane wave basis [313] is adopted to investigate the properties of considered systems.

4.3.3.5 DFT Implementation in ABINIT simulation package

DFT has gained great popularity in solid state physics and in now widely used in many fields due to the availability of high performance computers that can perform the iterations at a very high rate. DFT based theoretical analysis have been used as powerful technique for studying the properties of bulk, surfaces and nanostructures of various materials. DFT is supported by many simulation packages, along with other computational material modeling methods. Many codes based on pseudopotentials or projected-augmented waves and planewaves are available today, which include ABINIT [314], CASTEP [315], DMol [316], Quantum ESPRESSO [317], VASP [318] etc.

In this thesis, *ab initio* quantum mechanical based calculations have been implemented in the ABINIT simulation package. This code has been applied by many users on different geometries and processes and hence it is well tested. The main program of the ABINIT software application allows one to compute the total energy, the electronic charge density, the electronic structure and many other properties of systems composed of electrons and nuclei (molecules, periodic solids, nanostructures etc.) [314, 319-321] using first-principles approach, *i.e.*, without any adjustable parameters. It implements DFT, using a planewave or wavelet basis set and pseudopotentials or the projector augmented-wave method [322]. The ground state properties are calculated based on DFT in the Kohn-Sham scheme. It gives access to cohesive, vibrational, elastic, magnetic, mechanical, optical, dielectric,

thermodynamical, thermoelectric properties, geometry predictions, electronic structures, spectroscopic responses etc. of solids and nanostructured systems.

The ABINIT software project was started in 1997, but the first publicly available version of ABINIT was released, under GNU GENERAL PUBLIC LICENSE (GPL) in December 2000. It has already been described in papers published in 2002 [314], 2005 [319], 2009 [320] and 2016 [321]. The code is developed collaboratively by researchers (around fifty people) and it is used by more than a thousand researchers throughout the world.

The thesis work based on the first-principles density functional method as implemented in the ABINIT code is explained in detail in the subsequent chapters (Chapters 5-7). Chapter 5 describes the results from the DFT calculations on the adsorption of toxic gases (such as CO, NO, NO_2) and water vapour on Group III (B, Al and Ga) doped graphene by determining the optimized adsorption geometries, adsorption energies, electronic band structures and DOS and by performing the charge distribution analysis of the doped graphene systems before and after gas adsorption. In chapter 5, the effect of the adsorbed CO, NO, NO_2 and H_2O on the structural and electronic properties of BG, AG and GG are investigated to evaluate the potential use of group III (B, Al, Ga) doped graphene as toxic gas sensors in the presence of water vapour. As the application of GG as toxic gas sensor strongly depends on its reactivity towards O_2 in air, this chapter also analyzes the effect of adsorbed O_2 molecule on the structural and electronic properties of GG.

CHAPTER 5

GAS SENSING PROPERTIES OF GROUP III (B, Al, Ga) DOPED GRAPHENE

5.1 Introduction

For improving the sensitivity of IG towards gas molecules, the method of doping has proved to be very efficient [35-58]. Doping of graphene with group III atoms such as B, Al and Ga has shown significant improvement in the sensing capability of graphene due to the strong adsorption of gas molecules on the doped graphene surface compared to IG [36-40, 43, 44, 48, 49, 53, 54, 58, 59, 323, 324].

Zhang *et al.* [36] observed that B-doping in graphene enhances the interactions between small gas molecules (CO, NO, NO_2 and NH_3) and graphene. They found that only weak physisorption takes place between CO and BG, whereas the B-dopant act as strong chemisorption site for NO, NO_2 and NH_3. Dai *et al.* [39] also suggested that BG can be used as a good sensing material for the detection of important polluting gases such as NO and NO_2 based on theoretical study on the adsorption capability of graphene doped with boron, nitrogen, aluminium and sulfur towards common gases such as H_2, H_2O, O_2, CO_2, CO, NO_2, NO, SO_2, NH_3 and N_2. Among these doped graphenes, AG has been found to be highly sensitive to most of the gases [39]. Using first-principles calculations, Ao *et al.* proved that AG shows high sensitivity to CO molecules [37]. Chi *et al.* reported strong adsorption of H_2CO molecule on AG with much higher charge transfer from AG to H_2CO compared to that of IG [38]. In addition to these, there have been many theoretical reports on the adsorption property of various other gas molecules on AG, which indicate the suitability of using AG based nanostructures as a novel platform for the detection of toxic gases such HF [58], N_2O [48, 54], H_2S [43], NO_2 [48], CO [49, 53], CO_2 [49] etc. Ga-doped graphene (GG) has also proved to be a strong adsorbent for N_2O [54], H_2S [43] and phenol [44] from simulation based studies. AG and GG showed significantly enhanced interactions with N_2O through the formation of strong chemical bonds between the dopant atom and the N_2O molecule [54]. Another study showed increase in the sensitivity of graphene to H_2S molecule when doped with Al and Ga, whereas weak physisorption was observed in the case of B-doped graphene [43]. In the study by Avila *et al.*, it was found that Al and Ga doping induces strong interaction between the phenol molecule and the doped layer, that corresponds to chemical adsorption [44].

The adsorptions of several small gas molecules (CO, NO and NO_2) on GG have been investigated using first-principles approach based on DFT calculations, to analyse the effect of Ga-dopant on the sensitivity of graphene towards these gas molecules and to exploit the possibilities of graphene as toxic gas sensors. This chapter also reports the first-principles simulation of the adsorption of these gas molecules on other group III (B and Al) doped graphenes, to understand the effects of doping graphene with B and Al on the structural and electronic properties of graphene upon interaction with these small molecules.

In order to use the above mentioned group III doped graphenes as good toxic gas sensing materials in air, it should not get affected by the constituents of air such as N_2, O_2 and traces of water vapour. As molecular oxygen constitutes more than 20% of the volume of air, the effect of O_2 on gas sensors based on group III doped graphene need to be studied. Dai and Yuan theoretically investigated the adsorption of O_2 on BG and AG [272] and they observed that O_2 is only physisorbed on BG with small adsorption energy and long molecule-graphene distance, which shows that BG is inert. On the other hand, chemisorption was observed on AG with large adsorption energy and short molecule-graphene distance, indicating that Al-doped graphene is strongly reactive to molecular oxygen [39, 272]. The interaction of O_2 molecule on GG sheets has not been investigated. Considering the importance of the study in practical situations, the effect of adsorption of O_2 on GG sheet is also investigated using DFT calculations.

For enabling the detection of harmful gases in air using group III doped graphene, the effect of the presence of water vapour on the structural and electronic properties of group III doped graphene need to be analyzed. The adsorption energy and binding distance calculations from ref. [39] indicate physisorption of H_2O on BG. The results from the DFT analysis of the adsorption of H_2O on the surface of AG showed high adsorption energies with short binding distance and large charge transfer, which indicate chemisorption H_2O on the surface of AG [49]. From these studies, it can be concluded that O_2 and H_2O present in the air get strongly adsorbed on the surface of AG which leads to false alarm on employing AG for the detection of other toxic gases. To the best of our knowledge, there are no systematic theoretical studies towards the adsorption of H_2O on the surface of BG and GG and also on the investigation of structural and electronic properties of BG and GG before and after H_2O adsorption. Therefore, in this chapter, the adsorption of H_2O on graphene doped with B, Al and Ga are also studied using DFT calculations [325].

5.2 Computational Details

The XC functional of LDA, which has shown to be successful for studying weakly interacting systems and has given binding energies close to the experimental results [326] was adopted for the study. LDA was also proven to be effective in accurately describing the interactions of graphene, doped or defective graphene with various gas molecules [36, 41]. The Teter and Pade (fitting of PW92 data) parameterization have been used for LDA [327]. A plane wave basis set with a kinetic energy cutoff value of 30 Ha was used for the calculations after doing convergence of the desired properties. The interactions of the valence electrons with atomic core were represented using norm-conserving Troullier-Martins pseudopotentials [313]. The Brillouin zone was sampled using a 7 × 7 × 1 Monkhorst-Pack (MP) k-point [328], after performing convergence with respect to the k-point grid. A denser MP grid of 15 × 15 × 1 was used for the calculation of DOS. Structural optimization have been performed for all considered systems employing Broyden-Fletcher-Goldfard-Shanno (BFGS) minimization [329] until the residual forces on each atom were smaller than 0.05 eV/ Å. The charge transfer analysis is based on the Hirshfeld method [330]. The structural and electronic properties of group III doped graphenes before and after exposure to gas molecules are studied using the above mentioned DFT method.

5.2.1 Model building

5.2.1.1 Model of IG sheet

An IG sheet was built by cleaving a crystal cell of graphite [42]. The IG sheet was modelled using a 4 × 4 graphene supercell containing 32 carbon (C) atoms with a single gas molecule adsorbed to it. A space width of 16 Å is taken in the direction normal to the graphene plane to minimize the interactions between graphene sheets of bordering supercells. The optimized structural model of 4 × 4 graphene sheet is shown in Figure 5.1.

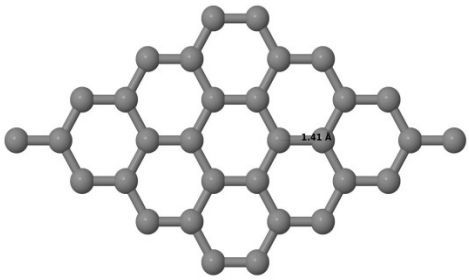

Figure 5.1 Optimized structure of IG sheet

5.2.1.2 Model of B-, Al- and Ga-doped graphene sheets

The model of doped graphene sheets was built based on the model of IG sheet. BG, AG and GG sheets were constructed by replacing the C atom with B, Al or Ga atom respectively. The geometries of these doped graphene sheets were then allowed to optimize and the optimized structural models are shown in Figure 5.2 (a)-(c).

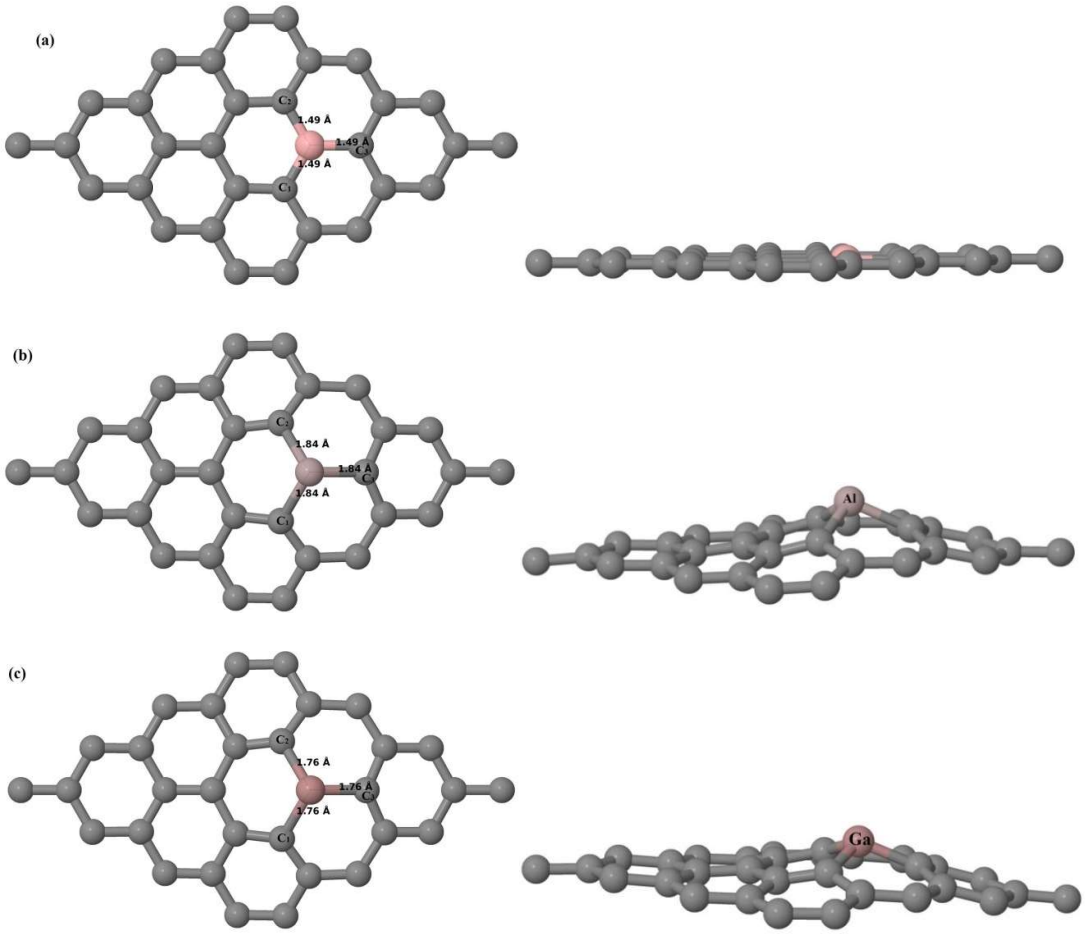

Figure 5.2 Top (left) and side (right) views of optimized structures of **(a)** BG, **(b)** AG and **(c)** GG sheets.

5.2.1.3 Model of Gas-adsorbed B- or Al- or Ga- doped graphene system

To determine the most stable adsorption structure of gas molecules on doped graphene sheets, different initial configurations of the gas molecules were considered. The adsorption energies of the optimized geometries obtained from the considered initial states of gas molecules on graphene sheets are compared to identify the energetically stable adsorption structure.

E_{ad} is defined as the difference between the total energy of the relaxed doped graphene system with the adsorbed gas molecule ($E_{(molecule+XG)}$), and the sum of the total energies of isolated doped graphene (E_{XG}) and gas molecule ($E_{molecule}$) in which X denotes the considered

dopant atom (can be either B, Al or Ga), as represented in Eqn. (5.1). The total energies of all the above mentioned atomic structures were calculated after full relaxation.

$$E_{ad} = E_{(molecule+XG)} - (E_{XG} + E_{molecule}) \quad (5.1)$$

E_{ad} indicates the intensity of interaction between doped graphene sheets and the gaseous molecules. A negative E_{ad} value indicates that the adsorption is energetically favourable *i.e.* stable adsorption. The more negative the E_{ad} value, the more stable the adsorbed systems.

5.3 Results and Discussions

5.3.1 Structural and Electronic Properties of IG

The two atoms unit cell of the hexagonal graphene structure was considered initially. The structure was fully relaxed and the calculated C-C bond length is 1.41 Å, which is in agreement with previously reported values of 1.40-1.42 Å [8, 289]. The unit cell of graphene was extended to 4 × 4 to construct a supercell which consists of 32 C atoms. The supercell was also allowed to relax fully (Figure 5.1) and the calculated C-C bond length of 1.41 Å was again found to be consistent with that reported in literature [8, 289, 331]. The calculated lattice constant of IG of 2.45 Å is slightly less than the experimental value of 2.46 Å [331].

Hirshfeld charge distribution analysis performed on IG sheet shows that all the carbon atoms are neutral and they have a homogeneous charge state of zero (Table 5.1). As the electronic structure of graphene is of great importance in this study, the electronic structure and the DOS of graphene were calculated. Figure 5.3 (a) presents the band structure of graphene along the high symmetry points (Γ-K-M-Γ) of the hexagonal Brillouin zone of graphene. In IG, the valence and conduction bands cross at the K-point with zero energy band gap and the linear dispersion of valence and conduction bands around the Fermi level seen in Figure 5.3 (a)) is in accordance with the reported results [5, 296, 298, 332]. The DOS plotted in Figure 5.3 (b) shows that the band gap of graphene is 0 eV, which agrees well with the experimental value of 0 eV. Since the DOS plot shows zero charge carrier density at E_F, the electrical conductivity of IG is quite low [2, 5, 333]. Hence the adopted theoretical model is good enough for further study.

5.3.2 Effect of doped atoms on the structural and electronic properties of IG

The obtained optimized structures of BG, AG and GG are shown in Figure 5.2. BG retains the planar geometry of IG as seen in Figure 5.2 (a) due to the comparable atomic sizes of C and the B atom dopant, which is in accordance with previous results [39, 43].

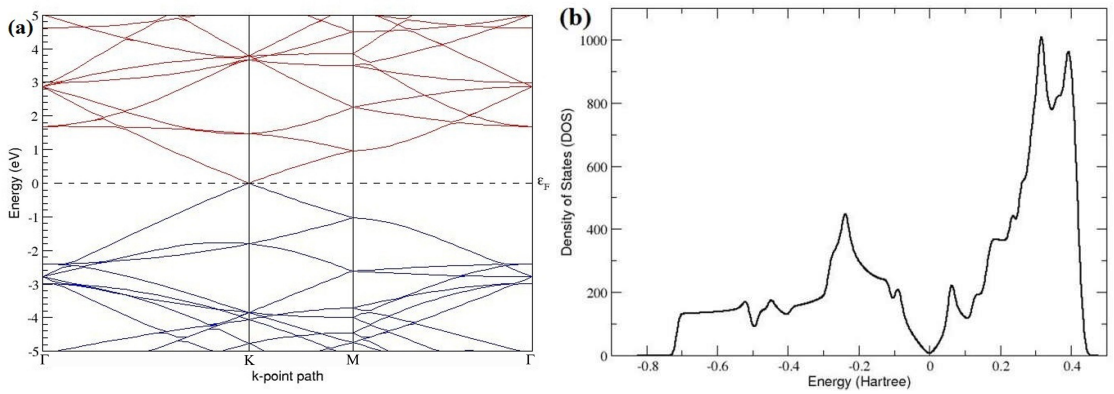

Figure 5.3 The band structure **(a)** and DOS **(b)** of IG sheet

In AG and GG, the planar geometry of IG is found to be distorted due to the stress introduced by Al or Ga atom having a larger size compared to the C atom. In both AG and GG, the dopant atom protrudes out of the graphene layer at a distance *d* from the graphene plane of *d* = 1.302 Å for Al, and d = 1.049 Å for Ga. The dopant atom-carbon distance is found to be $d_{(B\text{-}C)}$ = 1.49 Å in BG (Figure 5.2 (a)), $d_{(Al\text{-}C)}$ = 1.84 Å in AG (Figure 5.2 (b)) and $d_{(Ga\text{-}C)}$ = 1.76 Å in GG (Figure 5.2 (c)), which are also in agreement with previous theoretical studies [39, 43].

Table 5.1 presents the results of Hirshfeld charge distribution analysis performed on BG, AG, and GG sheets. The electronic charge state of the dopant atoms and that of the three nearest C atoms surrounding the dopant are also illustrated in Table 5.1. Upon replacing C atom with B, Al or Ga atom, the three C atoms around the dopant strongly attract electrons from the dopant atom and attain a charge state of -0.059, -0.107 and -0.027 in BG, AG and GG respectively, due to the fact that electronegativity of C atom is much higher that of these group III atoms. Thus the dopant atoms lose electronic charge [54, 75] and attain charge state of +0.014 for B in BG, +0.274 for Al in AG. But in GG, Ga shows a charge state of -0.027 due to the partial overlapping of its density with the neighbouring C atoms due to the larger size of Ga, compared to B and Al, than the host C atoms.

Table 5.1 Hirshfeld charge distribution analysis of the dopant atom, three nearest C atoms around the dopant atom of BG, AG and GG sheets[a]

System	C_1	C_2	C_3	B	Al	Ga
IG	0	0	0	-	-	-
BG	- 0.059	-0.059	-0.059	0.014	-	-
AG	- 0.107	-0.107	-0.107	-	0.274	-
GG	-0.027	-0.027	-0.027	-	-	-0.027

[a] A negative sign indicates electrons gained, whereas positive sign implies electron lost by the atom (the unit of charge is electron)

Figure 5.4 (a)-(c) present the band structures of BG, AG and GG along the high symmetry points (Γ-K-M-Γ) of the hexagonal Brillouin zone of graphene. Upon doping with group III atoms, (having one electron less than that of C atom), it was found that the Dirac point shifts above E_F of the doped systems (Figure 5.4 (a)-(c)), due to the hole doping behaviour of group III atoms and hence the doped graphene systems behave as p-type semiconductors [75]. In addition to this, doping with group III (B, Al and Ga) atoms introduce band gaps of 0.184 eV (Figure 5.4 (a)), 0.109 eV (Figure 5.4 (b)) and 0.238 eV (Figure 5.4 (c)) respectively in graphene. The observed increase in the electronic states with high electron density near E_F in the band structures of BG, AG and GG (Figure 5.4 (a)-(c)), compared to that of IG are in agreement with reported literature [43].

Figure 5.5 (a)-(c) show the DOS of BG, AG and GG respectively, in which the Dirac point is seen shifted towards the conduction band. This shifting of the Dirac point into unoccupied states indicates enhancement in the electrical conductivity of graphene after doping with B, Al or Ga [43].

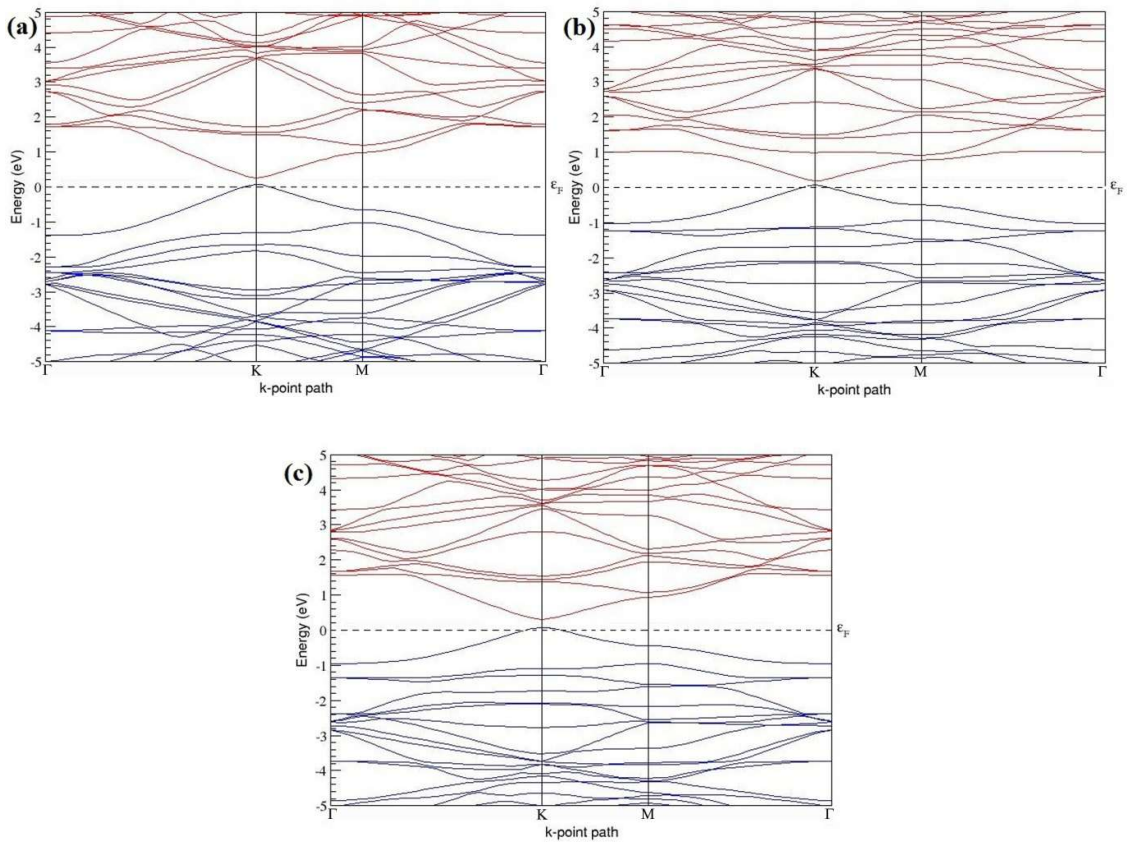

Figure 5.4 Electronic band structures of **(a)** BG **(b)** AG and **(c)** GG sheets, where E_F is set to zero

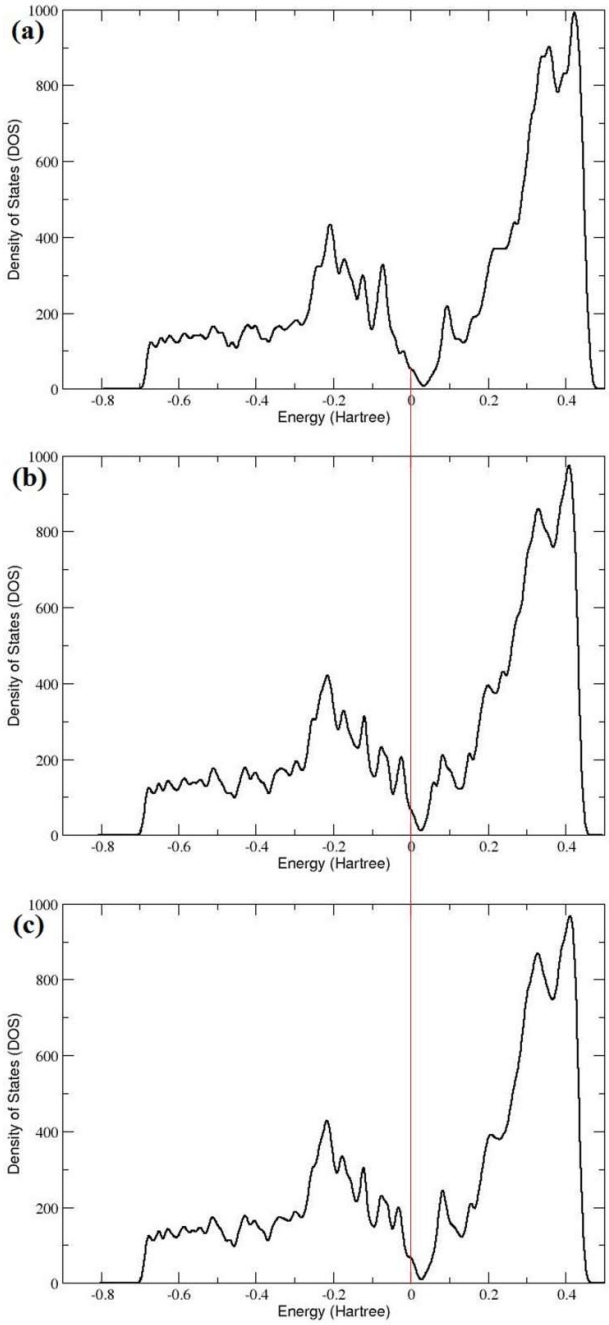

Figure 5.5 The DOS of **(a)** BG **(b)** AG and **(c)** GG. The red vertical line represents the E_F of all the systems, set to zero.

5.3.3 Structural Properties of gas-adsorbed B- or Al- or Ga-doped graphene systems

As the first step, the atomic geometries of isolated CO, NO, NO_2, and H_2O molecules were optimized. The calculated bond lengths of 1.14 Å in CO and 1.17 Å in NO are slightly greater than the experimental bond lengths of CO (1.13 Å) and NO (1.15 Å) [334]. In NO_2, the optimized bond length and bond angle are observed to be 1.22 Å and 133.1^0 respectively (experimental bond length is 1.20 Å and O-N-O bond angle is 134.3^0) [334]. The optimized

bond length and bond angle of H_2O molecule are calculated to be 0.990 Å and 104.7^0, which are found to be slightly larger than the experimental values of 0.958 Å and 104.5^0 [335]. The bond length of O_2 molecule in the ground state is 1.24 Å (experimental value is 1.207 Å) [272] in the calculations.

After determining the relaxed geometry of the XG sheets and gas molecules, as the next step, their adsorption properties with considered gas molecules are examined by first relaxing different adsorption configurations of gas molecules with respect to the XG sheet.

5.3.3.1 CO on graphene

To find the most favourable adsorption configuration of CO molecule on XG sheets, three different orientations were tested. One in which the CO molecule is placed parallel to the graphene plane, the other two with the CO molecule perpendicular to the graphene plane with the O atom above the C atom and the other way around. The most energetically stable adsorption configuration of CO on XG sheets are identified by comparing the adsorption energies of the optimized geometries obtained from the considered initial states of CO molecule on doped graphenes. The favourable adsorption geometry of CO on BG, AG and GG are found to be the same in which the molecule is oriented perpendicular to the graphene plane with the C atom close to the graphene plane (Figure 5.6 (a)-(c)). We also observe that there is no notable change in the atomic structure of BG upon CO adsorption and the minimum atom-to-atom distance between CO and the BG is 3.12 Å (Figure 5.6 (a)). The structure of AG and GG are found to be dramatically changed by the adsorption of CO (Figure 5.6 (b), (c)). The observed structural change in AG by the adsorption of CO is similar to that reported in Ref. [37, 53]. The carbon-dopant atom length elongates to 1.86 Å (Al–C) and 1.8 Å (Ga-C) in AG and GG respectively, upon interaction with CO molecule (Figure 5.6 (b), (c)). After CO adsorption, the dopant atoms protrude more outwards, with d = 1.39 Å for Al and d = 1.18 Å for Ga respectively. The molecule-sheet distance is found to be 2 Å and 1.94 Å in CO-adsorbed AG and GG respectively (Figure 5.6 (b), (c)).

The bond lengths before and after CO adsorption are compared to investigate for possible dissociation of the gas molecule upon adsorption. The bond length in isolated CO molecule is 1.14 Å, and even after adsorption on XG sheets, the bond lengths are found to be almost the same (1.13 Å, 1.14 Å and 1.14 Å in CO adsorbed BG, AG and GG systems respectively) (Figure 5.6 (a)-(c)). These observations make it clear that there is no dissociative adsorption of CO on XG sheets [325].

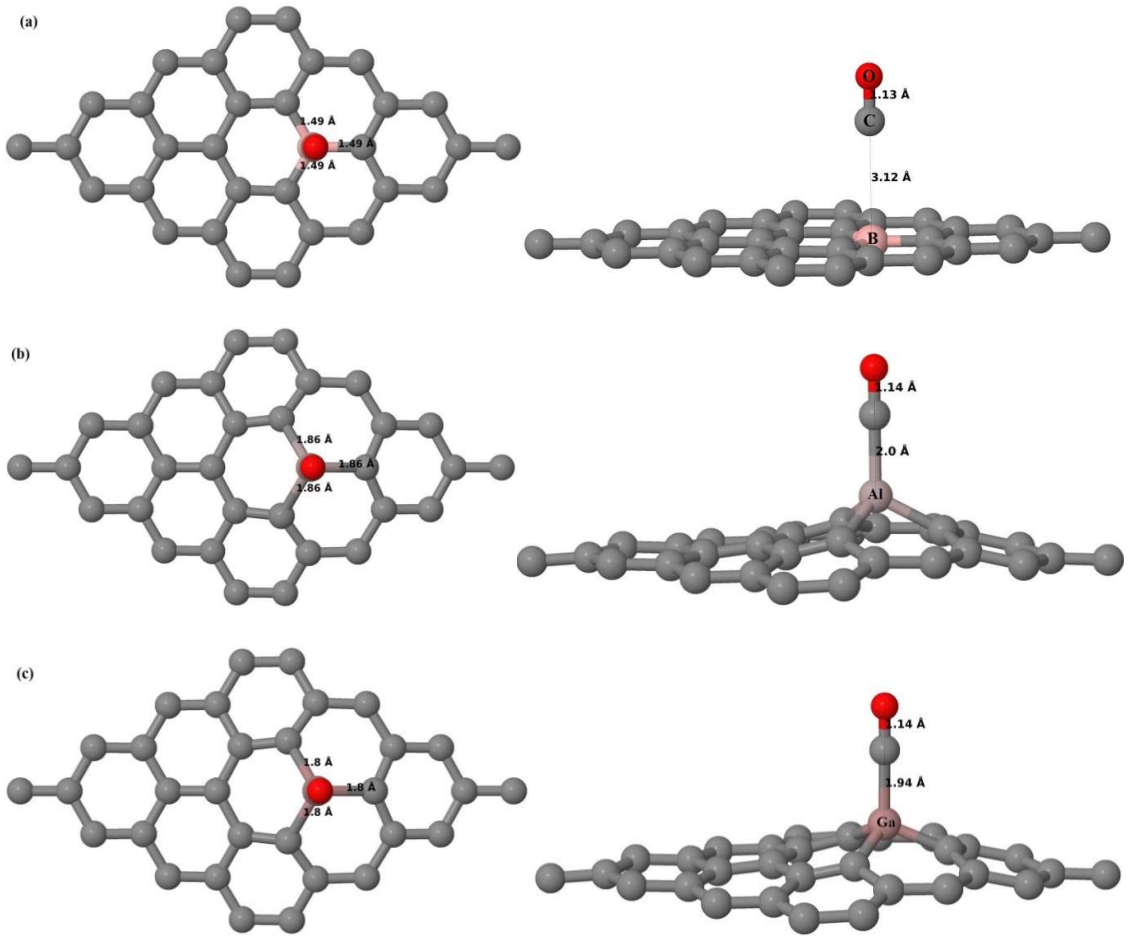

Figure 5.6 Top (left) and side (right) views of optimized structures of CO molecule on **(a)** BG, **(b)** AG and **(c)** GG sheets, where the O atom is shown in red colour.

5.3.3.2 NO on graphene

The most favourable adsorption configurations of NO molecule on different doped graphenes are determined by considering three different initial orientations of NO molecule, one in which the NO molecule is parallel to the graphene plane, and the other two with the NO molecule oriented perpendicular to graphene plane with the O atom above the N atom and the other way around, similar to that considered for CO molecule. The energetically stable geometry of NO molecule on XG sheets are observed to be the same in which the molecule is oriented perpendicular to the graphene plane with the N atom close to the graphene plane (Figure 5.7 (a)-(c)), similar to the relaxed geometries of CO on XG (with C replaced by N). Figure 5.7 (a)-(c) show that the adsorption of NO leads to structural changes in XG sheets. The bonds around the dopant atoms elongate to 1.89 Å (Al–C) and 1.82 Å (Ga-C) in AG and GG (Figure 5.7 (b), (c)), whereas in BG, it shortens to 1.48 Å (B-C) respectively, upon interaction with NO molecule (Figure 5.7 (a)). The elevation of the dopant atoms increases to 1.45 Å in AG and 1.24 Å in GG respectively after NO adsorption due to the strong attraction

between the adsorbed NO molecule and the Al or Ga dopant. After full relaxation of the NO adsorbed XG systems, the NO molecule is found to located be at a distance *d* above the XG sheets of $d_{(B\text{-}N)} = 2.65$ Å (Figure 5.7 (a)), $d_{(Al\text{-}N)} = 1.82$ Å (Figure 5.7 (b)) and $d_{(Ga\text{-}N)} = 1.79$ Å (Figure 5.7 (c)) respectively.

The calculated N-O bond length is found to be 1.17 Å before adsorption and after adsorption on AG and GG sheets, the bond length got slightly extended to 1.2 Å and 1.19 Å, respectively (Figure 5.7 (b),(c)), whereas it reduced to 1.16 Å after adsorption on BG sheet (Figure 5.7 (a)). The low differences between the bond length value of NO before and after adsorption on XG sheets indicate that there is no dissociative adsorption of NO on BG, AG and GG sheets.

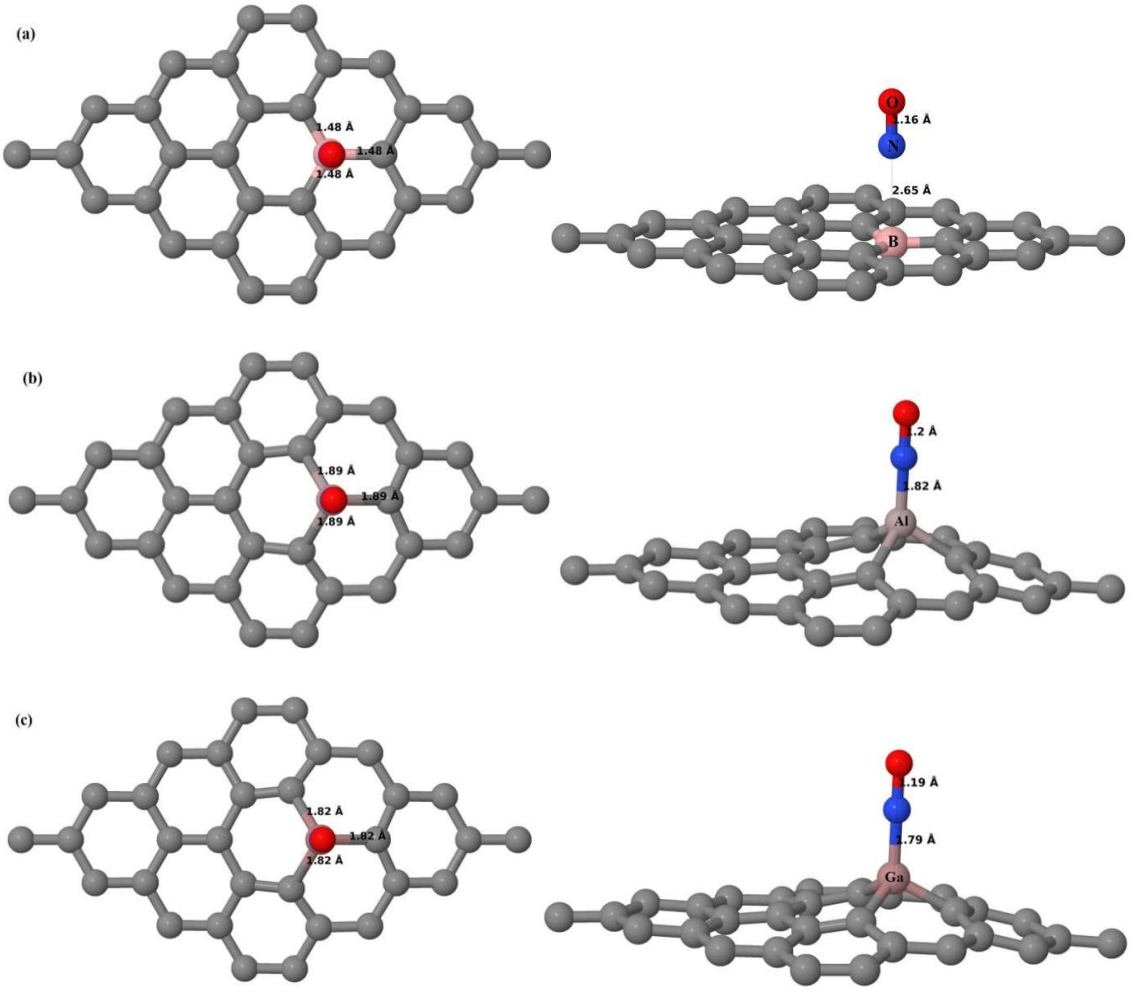

Figure 5.7 Top (left) and side (right) views of optimized structures of NO molecule on **(a)** BG, **(b)** AG and **(c)** GG sheets, where the N and O atoms are shown in blue and red colour respectively.

5.3.3.3 NO_2 on graphene

The most stable adsorption configurations of NO_2 on XG sheets are determined by examining different initial orientations with either the N or O atom nearest to the graphene surface. Figure 5.8 (a)-(c) show the energetically stable adsorption geometries of NO_2 adsorbed on BG, AG and GG sheets respectively. NO_2 is favourably adsorbed on the surface of BG *via* the N atom with the N-O bonds oriented upwards (Figure 5.8 (a)). The B atom protrudes out of the graphene plane with a distance of 0.49 Å and the formed B-N bond has a short length of 1.69 Å. The B-C bonds extend to 1.53/1.54 Å after NO_2 adsorption (Figure 5.8 (a)). In the case of AG and GG, the energetically stable geometry of NO_2 molecule is the one with the O atom close to the graphene plane and with the N-O bonds pointing down (Figure 5.8 (b), (c)). The bonds around the dopant atoms elongate to 1.9/1.91 Å (Al–C) and 1.83 Å (Ga-C) in AG and GG, upon interaction with NO_2 molecule (Figure 5.8 (b), (c)). The elevation of the dopant atoms increases to 1.53 Å in AG and 1.36 Å in GG respectively after NO_2 adsorption.

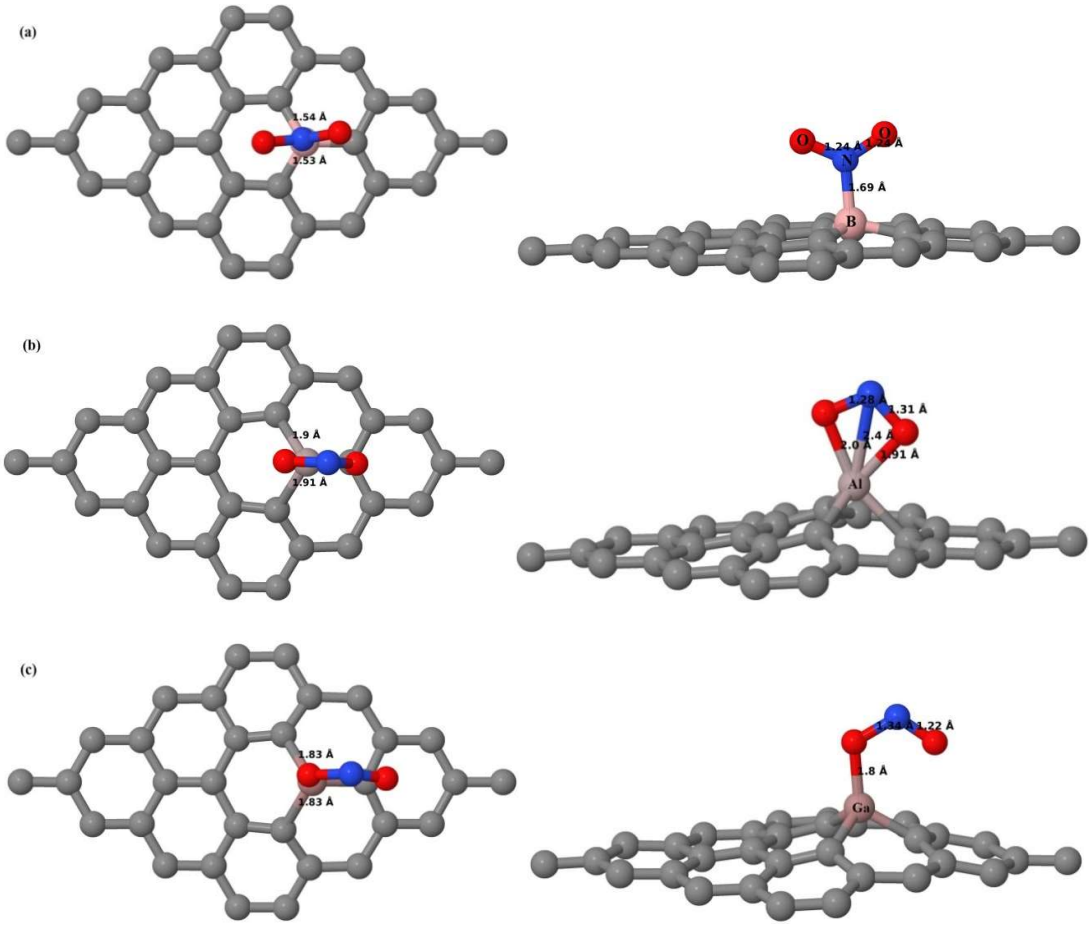

Figure 5.8 Top (left) and side (right) views of optimized structures of NO_2 molecule on **(a)** BG, **(b)** AG and **(c)** GG sheets.

After full relaxation of the NO_2 adsorbed XG systems, the NO_2 molecule is found to located be at a distance *d* above the XG sheets of $d_{(B-N)}$ = 1.69 Å (Figure 5.8 (a)), $d_{(Al-O)}$ = ~2 Å (Figure 5.8 (b)) and $d_{(Ga-O)}$ = 1.8 Å (Figure 5.8 (c)) respectively.

The N-O bond length in isolated NO_2 molecule is 1.22 Å and the interaction of NO_2 with XG sheets extend the bond length to 1.24 Å in BG, ~1.3 Å in AG and 1.34 Å in GG (Figure 5.8 (a)-(c)). These results indicate NO_2 adsorption on BG, AG and GG sheets is non-dissociative in nature [325].

5.3.3.4 H_2O on graphene

For obtaining the most stable adsorption configuration of H_2O on different doped graphenes, the adsorption site considered is the one in which oxygen atom is placed on top on the dopant atom. The following orientations of H_2O with respect to the doped graphene sheet are examined: starting from the oxygen atom with O-H bonds parallel to the graphene surface (p), O-H bonds pointing up (u) and O-H bonds pointing down (d).

The adsorption energy and the binding distance are calculated for all adsorption configurations of H_2O on BG, AG and GG sheets. We observe that the planar geometry of BG remains undisturbed after H_2O adsorption, which is evident from Figure 5.9 (a). For BG, the stable H_2O adsorption geometry is the one in which the O atom of H_2O is located on the top of the B-dopant with the O-H bond oriented downwards (Figure 5.9 (a)). In both AG and GG, H_2O adsorption results in elongation of the X-C bond of $d_{(Al-C)}$ = 1.85 Å (Figure 5.9 (b)) and $d_{(Ga-C)}$ = 1.79 Å (Figure 5.9 (c)) as compared to the BG with the same $d_{(B-C)}$ = 1.49 Å (Figure 5.9 (a)). The elevation of Al and Ga atoms increases to 1.331 Å and 1.220 Å respectively upon H_2O adsorption. After structural relaxation of the H_2O-adsorbed XG systems, the H_2O molecule is found to located be at a distance *d* above the XG sheets of $d_{(B-O)}$ = 2.86 Å (Figure 5.9 (a)), $d_{(Al-O)}$ = 1.94 Å (Figure 5.9 (b)) and $d_{(Ga-O)}$ = 1.93 Å (Figure 5.9 (c)) respectively. The energetically most stable adsorption geometry of H_2O on both AG (Figure 5.9 (b)) and GG (Figure 5.9 (c)) are found to be the one in which the dopant atom is facing towards the O atom of the H_2O molecule with the O-H bonds oriented upwards i.e. away from the graphene sheet.

The O-H bond lengths of the H_2O adsorbate before and after adsorption on XG are also calculated to investigate for possible dissociation of H_2O upon adsorption. The isolated H_2O molecule has a bond length of 0.990 Å, whereas after adsorption on BG, AG and GG, the bond lengths are found to be 1.0 Å, 1.01/1.0 Å and 1.0 Å (Figure 5.9 (a)-(c)) respectively. Hence, we could conclude that there is no dissociative adsorption of H_2O on the considered

XG sheets. This is in agreement with the report of non-dissociative adsorption of H_2O on AG surface [49].

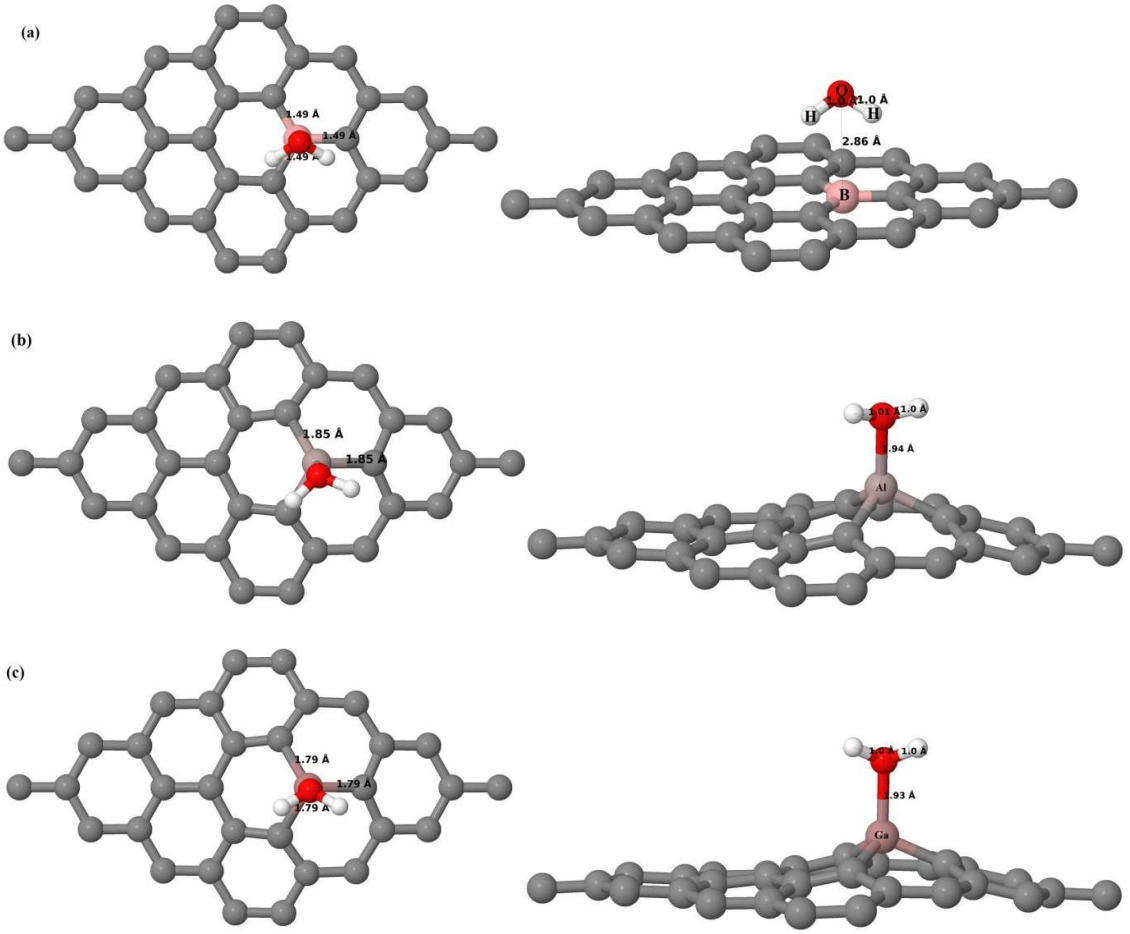

Figure 5.9 Top (left) and side (right) views of optimized structures of H_2O molecule on the top of **(a)** BG, **(b)** AG and **(c)** GG, where the H atom is shown in white colour.

5.3.3.5 O_2 on graphene

The adsorption of O_2 on GG sheet is discussed in this section. O_2 molecule is initially placed at the top of the dopant atom and oriented parallel to the graphene plane [272]. The system is then allowed to relax. Figure 5.10 shows the optimized structure of O_2 adsorbed on GG sheet and the structure of GG is found to be dramatically changed after O_2 adsorption. The elevation of Ga atom above graphene plane is extended to 1.461 Å and the Ga-C bond is elongated to 1.85 Å (Figure 5.10), upon O_2 adsorption. Ga-O bonds are formed with short length of around 1.8 Å as seen in Figure 5.10. The adsorption results in the extension of O-O bond length to 1.45 Å (Figure 5.10). The strong adsorption of O_2 on the surface could be attributed to the observed local curvature in GG [336].

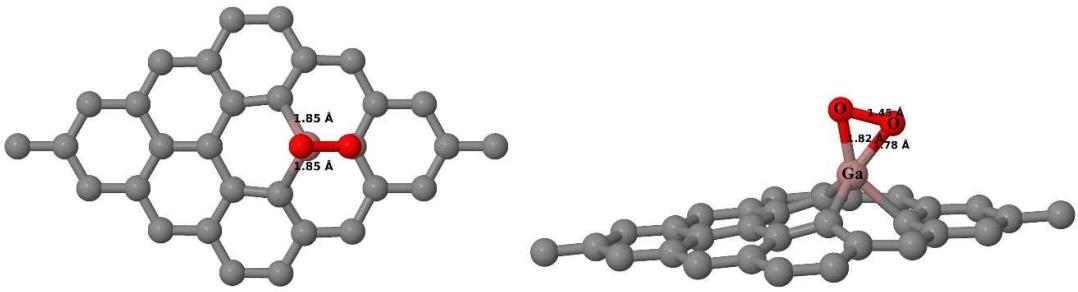

Figure 5.10 Top (left) and side (right) views of optimized structures of O_2 molecule on GG sheet, where the O atoms are shown in red colour.

5.3.4 Energetic Properties of gas-adsorbed B- or Al- or Ga-doped graphene systems

The energetic properties of the adsorption of CO, NO, NO_2, H_2O and O_2 on XG sheets are studied by calculating the adsorption energies and are presented in Table 5.2. The negative E_{ad} values of the considered gas molecules on XG sheets show exothermic reactions which are thermodynamically stable. The adsorption energy and the binding distance (equilibrium graphene-gas molecule distance) are calculated.

5.3.4.1 CO on graphene

The adsorption energy of CO on BG is -0.153 eV, and the molecule-sheet distance is 3.12 Å, which are in good agreement with the reported values of -0.14 eV and 2.97 Å [36]. The low adsorption energy and long binding distance observed for CO on BG indicate weak interactions and thus corresponds to physisorption process. The observed weak interactions between CO and BG are consistent with other reports [36, 39]. On the other hand, large adsorption energies (-0.929 on AG and -0.960 eV on GG) and short binding distances (2.0 Å on AG and 1.94 Å on GG) (Table 5.2) suggest strong interaction of CO molecule with AG and GG, corresponding to chemisorption mechanism. This high sensitivity of AG and GG towards CO molecule could be attributed to the local curvature in graphene introduced by the dopant atoms (Al and Ga). The observed strong reactivity of AG to the adsorption of CO is consistent with other similar studies [37, 49, 53]. The interactions are found to be stronger in the case of GG.

5.3.4.2 NO on graphene

The adsorption energy of -0.375 eV and the binding distance of 2.65 Å for NO on BG are close to the values (-0.341 eV and 2.38 Å) reported in Ref. [39]. These results indicate strong interactions between BG and NO and are consistent with earlier theoretical reports [36, 39]. NO is chemisorbed on AG and GG with large adsorption energies (-1.610 eV and -1.401 eV on AG and GG) and short molecule-sheet distances (1.82 Å and 1.79 Å for AG and GG),

respectively (Table 5.2). The calculated E_{ad} and binding distance values of NO on AG are close to the values reported in Ref. [39]. The interaction of NO with AG is found to be much stronger than that with BG and GG.

5.3.4.3 NO_2 on graphene

The results presented in Table 5.2 show that NO_2 undergoes chemisorption on the surfaces of BG, AG and GG sheets with large adsorption energies of -1.450 eV, -3.474 eV and -3.050 eV on XG sheets respectively and binding distances less than 2 Å. The calculated E_{ad} and molecule-sheet distance for NO_2 adsorption on BG, matches well with the reported values of -1.37 eV and 1.67 Å [36]. Hence BG, AG and GG are strongly reactive towards NO_2. The observed reactivity of BG and AG to NO_2 agrees well with previous theoretical predictions [36, 39, 48]. As E_{ad} of AG is greater than that of BG and GG, the adsorption is found to be much stronger on AG surface, than that on BG and GG sheets.

5.3.4.4 H_2O on graphene

For H_2O adsorption on BG, low adsorption energy and long binding distance suggest weak physical adsorption of H_2O on BG surface, whereas in AG and GG, large adsorption energies and short binding distances (Table 5.2) indicate strong interactions and thus correspond to chemisorption of H_2O on both AG and GG surfaces. The obtained adsorption energy (-1.323 eV) and the AG-H_2O distance (1.94 Å) are found to be close to the values reported in ref. [49]. This high reactivity of AG and GG to H_2O is due to the local curvature induced by the Al- and Ga-dopants, being larger in size compared to the host carbon atoms [325].

5.3.4.5 O_2 on graphene

The large adsorption energy of -2.557 eV and short binding distance of around 1.8 Å for O_2 adsorbed on GG, indicates that the interactions between O_2 and GG are strong. The observed chemisorption of O_2 on GG sheet shows that GG is highly reactive towards O_2 molecule.

Table 5.2 Values of adsorption energy and molecule-sheet distance of CO, NO, NO_2, H_2O and O_2 above BG, AG and GG sheets

		CO	NO	NO_2	H_2O	O_2
BG	E_{ad} in eV	-0.153	-0.375	-1.450	-0.170	-
	d in Å	3.12	2.65	1.69	2.86	-
AG	E_{ad} in eV	-0.929	-1.610	-3.474	-1.323	-
	d in Å	2.00	1.82	~ 2	1.94	-
GG	E_{ad} in eV	-0.960	-1.401	-3.050	-1.284	-2.557
	d in Å	1.94	1.79	1.80	1.93	1.8

5.3.5 Electronic Properties of gas-adsorbed B- or Al- or Ga-doped graphene systems

The electronic band structures of XG before and after H_2O adsorption are calculated to analyse the effect of H_2O adsorption on the electronic properties of XG.

5.3.5.1 CO on graphene

After the adsorption of CO on BG sheet, there is only a slight increase and decrease in the electronic charge states of the C neighbours and the B-dopant atom respectively with a charge state of 0.047 for the adsorbed CO molecule, as presented in Table 5.3. These results show that there is no charge transfer between CO and BG, similar to that reported in Ref. [36]. When CO is adsorbed on AG *via* the C atom, Al atom loses electronic charge of 0.181, and the adsorbed CO molecule gets a charge state of 0.166. In CO-adsorbed GG system, Ga atom gains more electronic charge of -0.145 and the adsorbed CO molecule attains a charge state of 0.238. The carbon atoms around the Al- and Ga-dopant experience slight decrease and increase in charge state of around -0.106 and -0.032 respectively. Thus, the adsorption of CO on AG and GG result in significant change in the charge state of Al- and Ga-dopant atom due to the charge transfer between AG or GG and the CO molecule. These results are in agreement with their adsorption energies. These results show that a chemical bond is formed between the Al or Ga dopant and the gas molecule in CO-adsorbed AG and GG systems.

The band structures of CO adsorbed on BG, AG and GG systems are presented in Figure 5.11 (a)-(c). There is almost no change in the band structure of BG upon CO adsorption and the observed band gap in CO adsorbed BG system is 0.198 eV (Figure 5.11 (a)). On comparing this band gap with that in BG, there is only a negligible increase of ~0.014 eV, which indicate that the electronic structure of BG is not sensitive to the presence of CO. Significant changes are found near E_F in the band structures of CO adsorbed on AG and GG systems. The band structures of CO adsorbed on AG and GG have indirect band gaps of 0.030 eV (Figure 5.11 (b)) and 0.185 eV (Figure 5.11 (c)), in which the top of the valence band is located at the K-point and the bottom of the conductive band is at the Γ-point. Thus, the adsorptions of CO on AG and GG have resulted in a large decrease in the band gaps of AG and GG. These band structure plots indicate that the electronic properties of AG and GG are highly sensitive to the adsorption of CO. The observed change in the band structure of AG after CO adsorption and that reported in Ref. [53] are in good agreement.

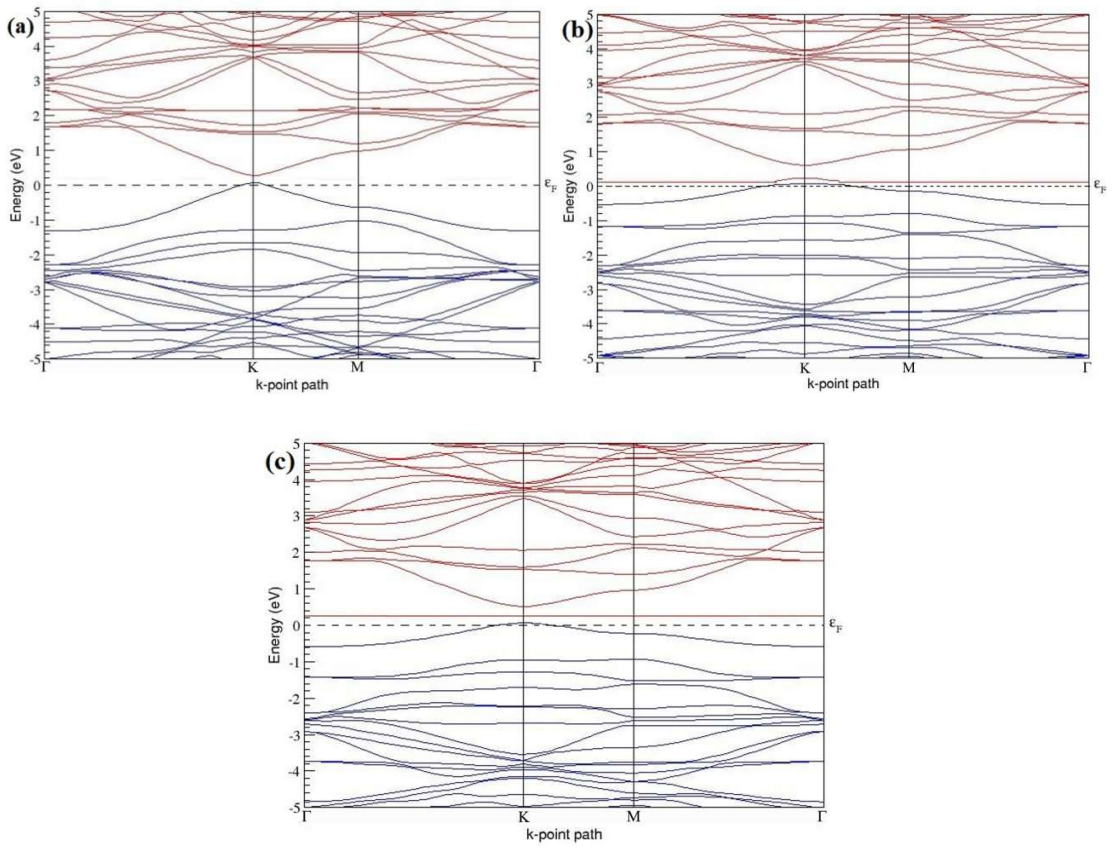

Figure 5.11 Electronic band structures of **(a)** CO adsorbed BG **(b)** CO adsorbed AG and **(c)** CO adsorbed GG.

Figure 5.12 (a)–(c) present the DOS of BG, AG and GG before and after CO adsorption. There are no distinct changes in the DOS of BG near E_F after the adsorption of CO (Figure 5.12 (a)) and hence it would not result in a notable change of electrical conductivity of BG, which is consistent with that reported in Ref. [36]. Therefore, we could conclude that BG is not sensitive for the presence of CO molecule. After CO adsorption, the DOS of CO adsorbed AG and GG systems have changed considerably, due to strong CO-Al or Ga interactions (Figure 5.12 (b), (c)). The large peaks that appear above E_F indicate clear increase of DOS in the region above E_F and are expected to increase the conductivities of CO on AG and GG. These results suggest that AG and GG can be used as good candidates for sensing CO. The obtained DOS of CO on AG are consistent with those reported in other studies [37, 49, 53].

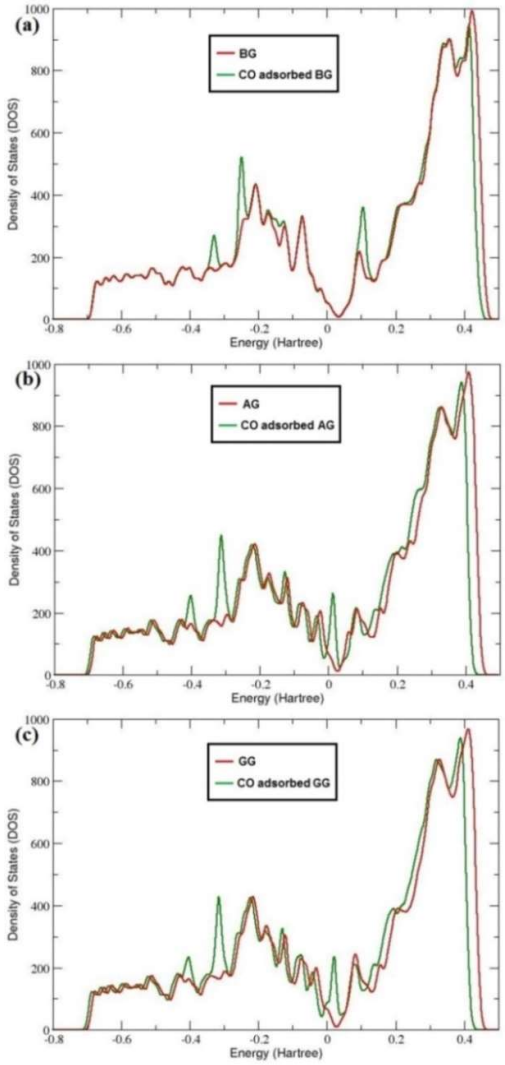

Figure 5.12 The DOS of **(a)** BG and CO adsorbed BG **(b)** AG and CO adsorbed AG **(c)** GG and CO adsorbed GG.

5.3.5.2 NO on graphene

Upon adsorption of NO on BG, B atom gains electronic charge of -0.011 along with increase in the electronic charge states of the C neighbours to -0.069 and NO gets a charge state of 0.163, indicating obvious charge transfer between NO molecule and BG sheet, in agreement with that reported by Zhang *et al.* [36]. When NO is adsorbed on AG, Al atom loses electronic charge of 0.205, C atoms surrounding the Al-dopant attain lower charge state of -0.087 and the adsorbed NO molecule gets a charge state of -0.034. In the case of GG, Ga atom gains more electronic charge of -0.119 and the adsorbed NO molecule attains a charge state of -0.062. The carbon atoms around the Ga-dopant experience a slight decrease in the charge state. The observed variations in the charge state of the group III dopants after NO adsorption (Table 5.3) indicate notable charge transfer between NO and BG, AG or GG and

is consistent with the calculated adsorption energies. This charge transfer between NO and XG sheets result in strong bond formation between the dopant atoms and the adsorbed NO molecule.

The band structures of BG, AG and GG with adsorbed NO molecule show indirect band gaps of 0.035 eV, 0.007 eV and 0.010 eV respectively as seen in Figure 5.13 (a)-(c). The valence band maximum of NO adsorbed BG, AG and GG systems are located at the K-point, and the conduction band minimum at Γ-point. On comparing the band gap of BG before NO adsorption (0.184 eV) and after NO adsorption (0.035 eV), it was observed that the band gap has reduced significantly. These results show that the electronic properties of BG are strongly influenced by the adsorption of NO molecule on its surface. Even though, there exists a small band gap in BG, the band gaps in AG and GG are found to be almost closed after NO adsorption (Figure 5.13 (b), (c)), which clearly show that the interactions of NO with AG and GG are expected to bring about notable variation in their electronic properties.

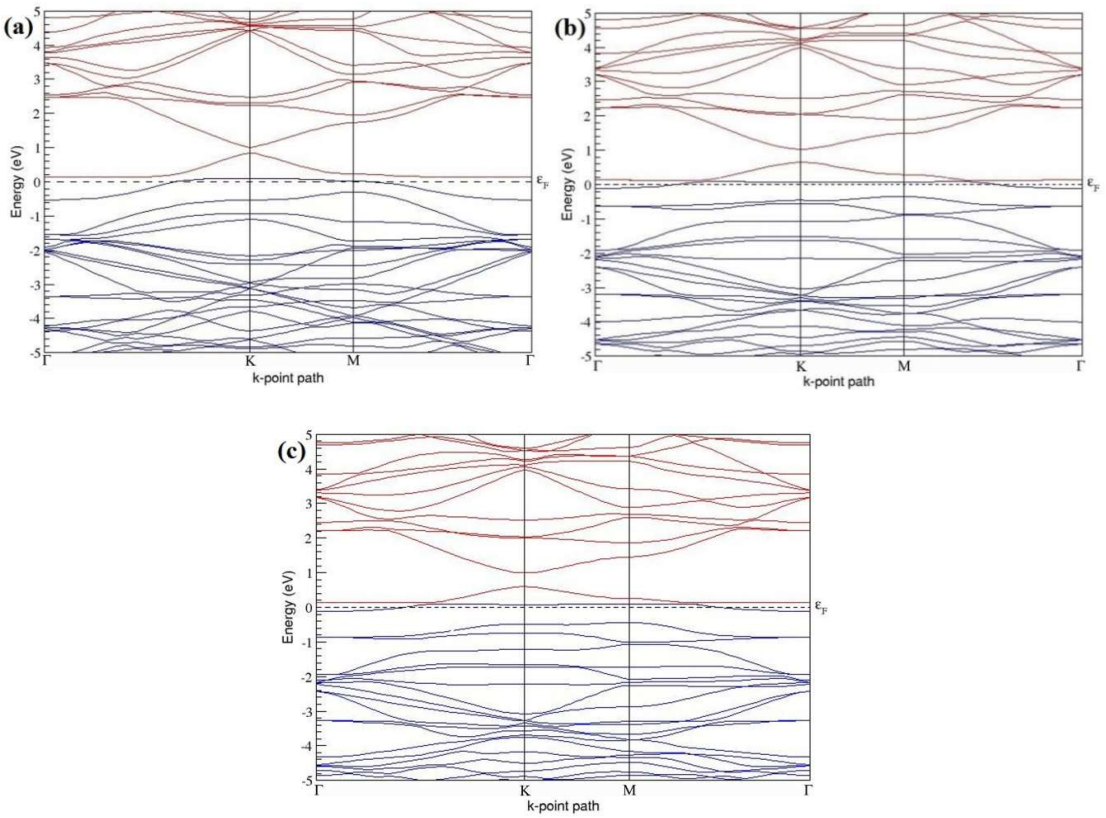

Figure 5.13 Electronic band structures of **(a)** NO adsorbed BG **(b)** NO adsorbed AG and **(c)** NO adsorbed GG.

The DOS of BG, AG and GG with and without adsorbed NO molecule are presented in Figure 5.14 (a)-(c).

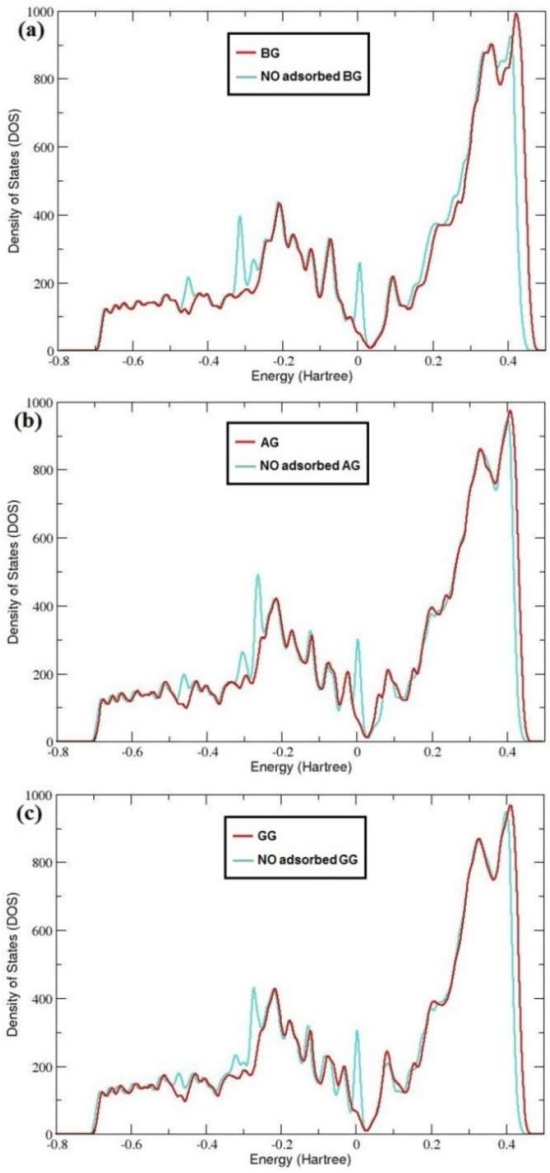

Figure 5.14 The DOS of **(a)** BG and NO adsorbed BG **(b)** AG and NO adsorbed AG **(c)** GG and NO adsorbed GG.

Figure 5.14 (a) shows that the DOS of BG has changed slightly upon adsorption of NO, compared with the DOS of BG, and a large peak appears just above E_F after exposure to NO. Thus, the adsorption of NO causes a clear increase in DOS above E_F and significant increase in the electrical conductivity of BG is expected. This is in close agreement with that reported by Zhang *et al.* [36]. The adsorption of NO has dramatically changed the DOS of AG and GG systems and a larger peak appear just above E_F as shown in Figure 5.14 (b) and (c). Thus, the chemisorption of NO on AG and GG will give rise to a large increase in the electrical conductivities of AG and GG due to strong graphene-molecule interactions. The observed high sensitivity of BG, AG and GG to NO makes it possible their usage as efficient NO gas

sensors. Our suggestion on the applicability of BG as NO gas sensors are in agreement with previous theoretical predictions [36, 39].

5.3.5.3 NO_2 on graphene

B-dopant gains significant charge of -0.033, whereas the C atoms surrounding the B-dopant exhibit significantly reduced charge state upon NO_2 adsorption on BG. The adsorbed NO_2 molecule attains a charge state of -0.123. When NO_2 is adsorbed on AG, Al atom loses electronic charge of 0.230, and the adsorbed NO_2 molecule gets a charge state of -0.203. In the case of NO_2 adsorbed on GG, Ga atom gains more electronic charge of -0.087 and the adsorbed NO_2 molecule attains a charge state of -0.128. The charge state of carbon atoms surrounding the Al or Ga-dopant also reduce significantly after NO_2 adsorption (Table 5.3). The significant change in the charge state of B-, Al- and Ga-dopant after NO_2 adsorption is due to the charge transfer between BG, AG or GG and the NO_2 molecule. The large charge transfers between NO_2 and BG or AG are consistent with other similar studies [36, 48]. Consistent with the adsorption energies, the results of charge distribution analysis of NO_2 adsorbed on BG, AG and GG systems indicate strong bond formation between the dopant atoms (B, Al or Ga) and the adsorbed atom.

The band structures of BG, AG and GG with adsorbed NO_2 molecule shown in Figure 5.15 (a)-(c)), exhibit indirect band gaps of 0.568 eV, 0.421 eV and 0.445 eV respectively. The interactions of BG, AG and GG with NO_2 has led to large increase in the band gap widths of about 0.370 eV, 0.312 eV and 0.207 eV respectively, compared to that of BG, AG and GG before adsorption. The observed band gap width of 0.568 eV in BG adsorbed NO_2 (Figure 5.15 (a)) is very close to the reported value of ~0.6 eV [39]. These results indicate that the electronic properties of BG, AG and GG are highly sensitive to the adsorption of NO_2.

The DOS of BG, AG and GG has changed drastically after NO_2 adsorption as seen in Figure 5.16 (a)-(c) due to strong NO_2-BG, AG or GG interactions. The DOS plot of NO_2 adsorbed on BG (Figure 5.16 (a)) is consistent with that reported in literature [39]. These results imply that the chemisorption of NO_2 on BG, AG and GG induce significant change in electrical conductivities of BG, AG and GG, which suggests that the BG, AG and GG are sensitive to the adsorption of NO_2 and therefore can be used as novel gas sensors for detecting NO_2. Our prediction of the suitability of BG as gas sensing material for the detection of NO_2 agree very well with previous simulation based studies [36, 39] and recent experimental findings [172].

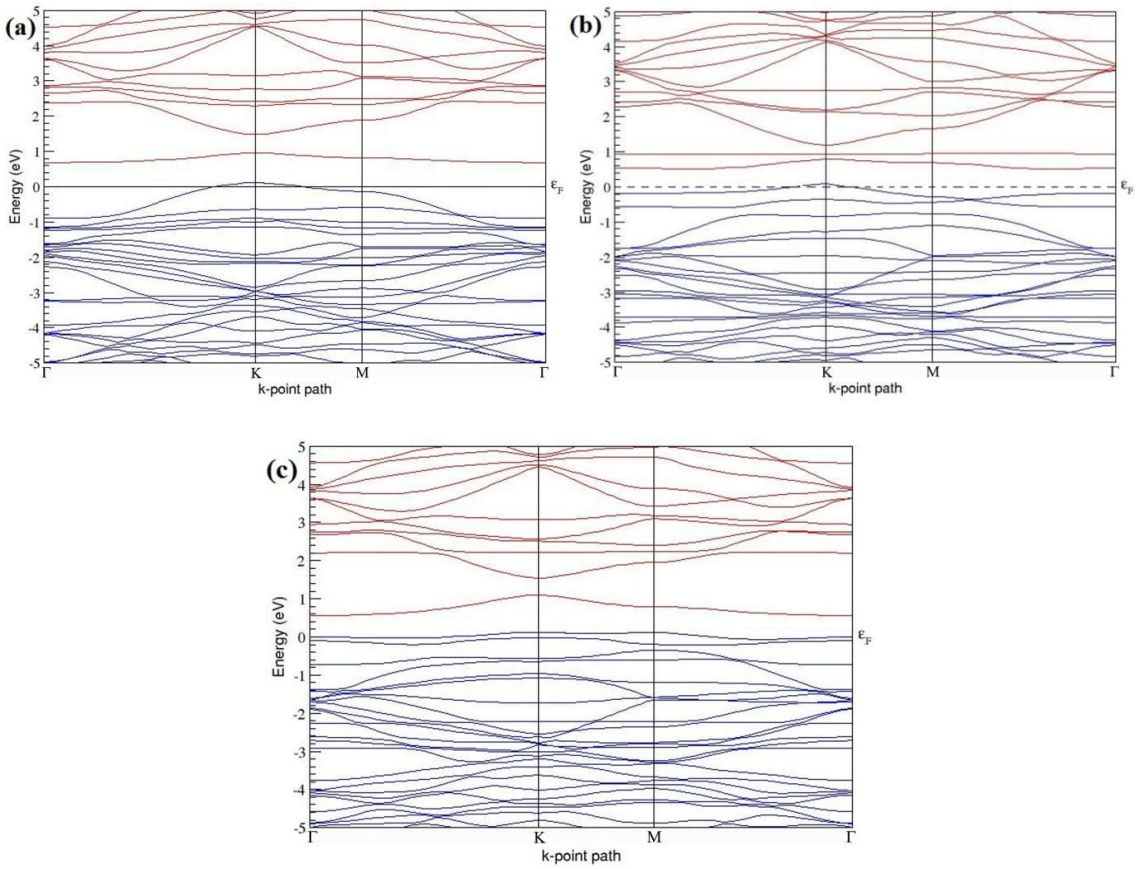

Figure 5.15 Electronic band structures of **(a)** NO_2 adsorbed BG **(b)** NO_2 adsorbed AG and **(c)** NO_2 adsorbed GG.

5.3.5.4 H_2O on graphene

Upon H_2O adsorption on BG, it was observed that there is only a slight increase and decrease in the electronic charge states of the three neighbouring C atoms and the B atom respectively, along with a charge state of 0.007 for the adsorbed H_2O molecule which shows negligible charge transfer between BG and H_2O. But when H_2O is adsorbed on the top site of AG, Al atom loses electronic charge of 0.216, and the adsorbed H_2O molecule gets a charge state of 0.300. In the case of H_2O adsorption on GG, Ga atom gains more electronic charge of -0.102 and the adsorbed H_2O molecule attains a charge state of 0.334. These results show that a chemical bond is formed between Al or Ga atom and the adsorbed H_2O molecule, which is in good accordance with their large adsorption energy values. The carbon atoms around the Al and Ga-dopant attain more electrons with a charge state of around -0.12 and -0.04 respectively. Thus the adsorption of H_2O on AG and GG result in significant change in the charge state of Al- and Ga-dopant atom due to the charge transfer between AG or GG and the H_2O molecule (Table 5.3) and are consistent with recent similar studies [49]. The carbon atoms surrounding the dopant atom experience an increase in the charged state after

adsorption of H_2O. The enhanced reactivity of AG and GG towards H_2O adsorption could be attributed to the large change in the electron density around these dopants [49].

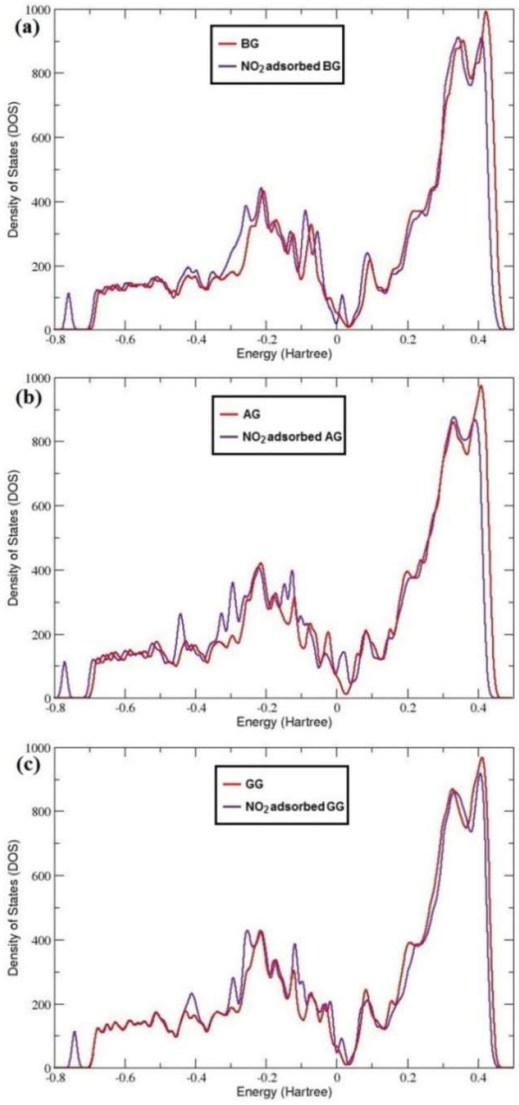

Figure 5.16 The DOS of **(a)** BG and NO_2 adsorbed BG **(b)** AG and NO_2 adsorbed AG **(c)** GG and NO_2 adsorbed GG.

The band structures of H_2O adsorbed on BG, AG and GG systems are presented in Figure 5.17 (a)-(c). The band structure of H_2O adsorbed BG system remains similar to that of BG with a negligible increase in band gap of ~0.020 eV, which indicates weak interactions between H_2O and BG. H_2O adsorbed on AG and GG systems exhibit band gaps of 0.297 eV and 0.346 eV respectively (Figure 5.17 (b), (c)), which shows significant increase in the energy band gaps in AG and GG after H_2O adsorption compared to BG. Rad *et al.* [49] also reported increase in band gap in H_2O adsorbed AG compared to that in AG. The observed large difference in band gaps in AG (0.188 eV) and GG (0.108 eV) before and after H_2O

adsorption indicates that interactions of AG or GG with H_2O are much stronger than those with BG. The results imply that the exposure of AG and GG to a single H_2O molecule alters their electronic structures [325].

Table 5.3 Hirshfeld charge distribution analysis of the dopant atom, three nearest C atoms around dopant atom and the adsorbed gas molecules on the surface of BG, AG and GG [a]

System	C_1	C_2	C_3	B	Al	Ga	CO	NO	NO_2	H_2O	O_2
IG	0	0	0	-	-	-	-	-	-	-	-
BG	-0.059	-0.059	-0.059	0.014	-	-	-	-	-	-	-
AG	-0.107	-0.107	-0.107	-	0.274	-	-	-	-	-	-
GG	-0.027	-0.027	-0.027	-	-	-0.027	-	-	-	-	-
CO-BG	-0.062	-0.062	-0.062	0.005	-	-	0.047	-	-	-	-
CO-AG	-0.106	-0.106	-0.106	-	0.181	-	0.166	-	-	-	-
CO-GG	-0.032	-0.032	-0.032	-	-	-0.145	0.238	-	-	-	-
NO-BG	-0.069	-0.069	-0.069	-0.011	-	-	-	0.163	-	-	-
NO-AG	-0.087	-0.087	-0.087	-	0.205	-	-	-0.034	-	-	-
NO-GG	-0.020	-0.020	-0.020	-	-	-0.119	-	-0.062	-	-	-
NO_2-BG	-0.038	-0.037	-0.039	-0.033	-	-	-	-	-0.123	-	-
NO_2-AG	-0.077	-0.078	-0.060	-	0.230	-	-	-	-0.203	-	-
NO_2-GG	-0.012	-0.014	-0.010	-	-	-0.087	-	-	-0.128	-	-
H_2O-BG	-0.064	-0.056	-0.061	0.009	-	-	-	-	-	0.007	-
H_2O-AG	-0.125	-0.115	-0.123	-	0.216	-	-	-	-	0.300	-
H_2O-GG	-0.047	-0.039	-0.045	-	-	-0.102	-	-	-	0.334	-
O_2-GG	-0.005	-0.005	-0.007	-	-	-0.078	-	-	-	-	-0.176

[a] A negative sign indicates electrons gained, whereas positive sign implies electron lost by the atom (the unit of charge is electron)

To further determine the effect of H_2O adsorption on the electrical conductivities of XG, the electronic DOS of XG before and after H_2O adsorption are calculated. The DOS of BG, AG and GG before and after H_2O adsorption are presented in Figure 5.18 (a)-(c). The DOS of the H_2O adsorbed BG has no significant changes near E_F, on comparing with that of BG as seen in Figure 5.18 (a), and hence this would not lead to a dramatic change in the electrical conductivity of BG upon H_2O adsorption. This fact suggests that BG is not sensitive to the presence of H_2O. The DOS of AG and GG after H_2O adsorption have changed slightly compared to that of AG (Figure 5.18 (b)) and GG (Figure 5.18 (c)) due to the interactions between AG or GG and H_2O. The DOS of H_2O adsorbed AG and GG show a small drop at E_F (Figure 5.18 (b) and (c)), which implies that the 2*p* orbitals of H_2O also take part in the formation of O-X (X= Al or Ga) bond. Thus the DOS of AG and GG at E_F got reduced by the adsorption of H_2O, which is expected to reduce the electrical conductivities of AG and GG. The expected reduction in the conductivity of H_2O adsorbed AG system is consistent with

that reported in recent literature [49]. Therefore, both AG and GG are sensitive to H_2O molecule.

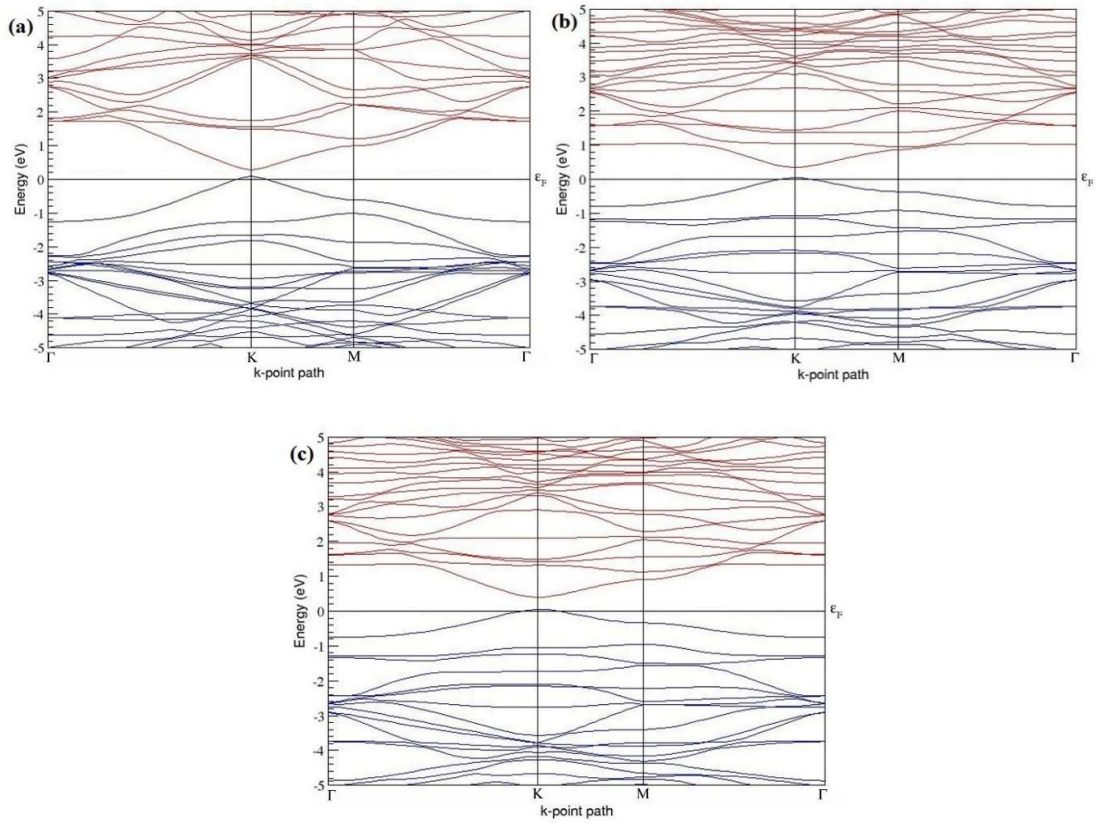

Figure 5.17 Electronic band structures of **(a)** H_2O adsorbed BG **(b)** H_2O adsorbed AG and **(c)** H_2O adsorbed GG.

5.3.5.5 O_2 on graphene

When O_2 is adsorbed on GG, Ga atom gains more electronic charge of -0.078, and the adsorbed O_2 molecule gets a charge state of -0.176. The large change in the charge state of Ga-dopant after O_2 adsorption indicates obvious charge transfer between GG and adsorbed O_2 molecule, which will give rise to strong bond formation between Ga atom and the adsorbed O_2 molecule, consistent with the calculated adsorption energy. The carbon atoms around the Ga-dopant lose electrons with a charge state of around -0.005 (Table 5.3).

The influence of adsorbed O_2 on the electronic properties of GG is also determined by comparing the electronic band structure of GG with and without O_2 adsorption (Figure 5.19). The band structure of GG has changed significantly, after O_2 adsorption, and exhibits an indirect band gap of 0.366 eV (Figure 5.19), compared to the band gap of 0.238 eV in GG before O_2 adsorption. The increase in the band gap induced by the adsorption of O_2 indicates that the strong interactions between O_2 and GG modify the electronic properties of GG.

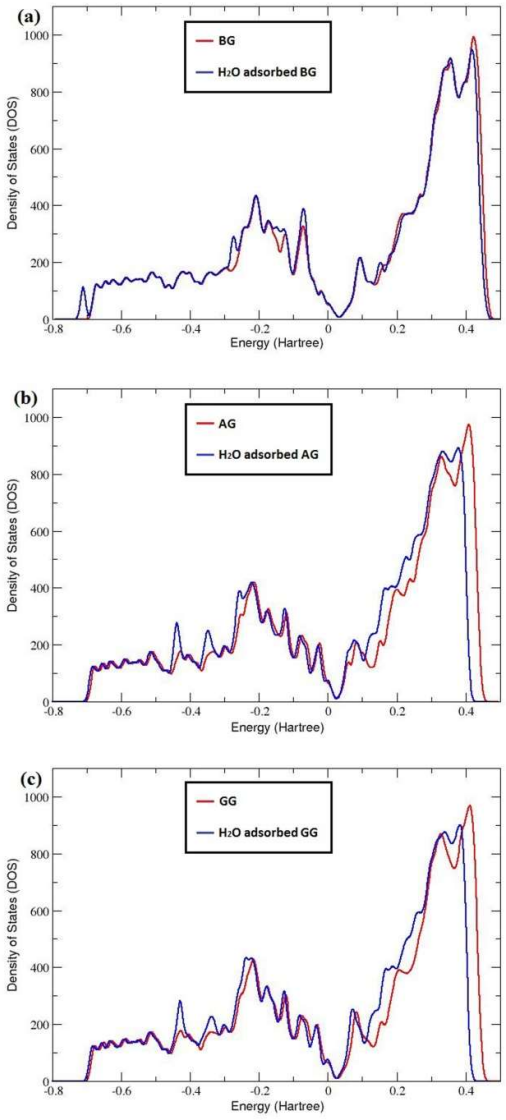

Figure 5.18 The DOS of **(a)** BG and H_2O adsorbed BG **(b)** AG and H_2O adsorbed AG **(c)** GG and H_2O adsorbed GG.

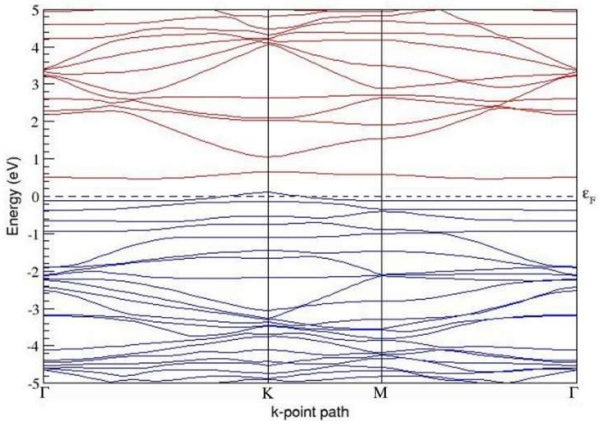

Figure 5.19 Electronic band structure of O_2 adsorbed GG

Figure 5.20 presents the electronic DOS of GG with and without adsorbed O_2 molecule. The DOS of O_2 adsorbed GG system has changed dramatically around the Fermi level and show large peaks just above the Fermi level (Figure 5.20) due to strong interactions between O_2 and Ga-doped graphene. The changes in the DOS in the region around E_F are expected to bring about significant changes in the corresponding electronic properties. Thus, it can be concluded that GG is sensitive to the presence of molecular oxygen.

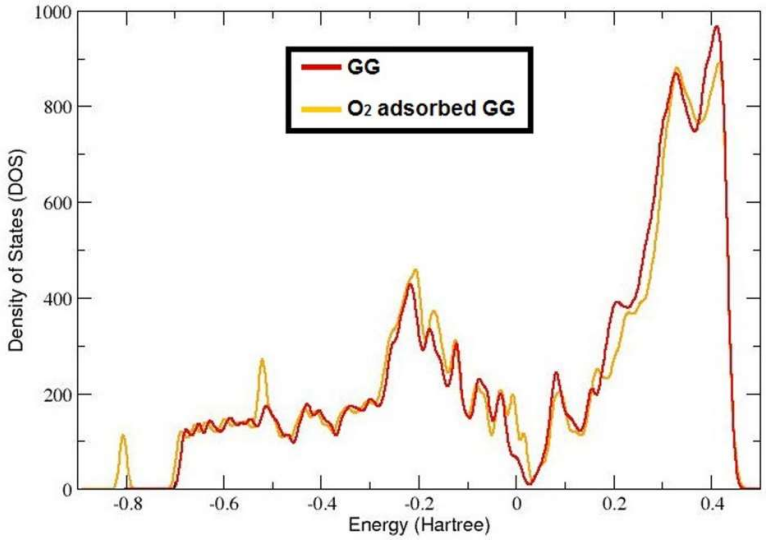

Figure 5.20 The DOS of O_2 adsorbed GG and GG

5.4 Summary

The adsorptions of small gas molecules (CO, NO, NO_2 and H_2O) on graphene doped with group III (B, Al and Ga) atoms have been studied using DFT calculations for enabling their application as toxic gas sensing materials in the presence of water vapour. First-principles calculations on the adsorption of O_2 on GG have also been performed to understand the influence of adsorbed oxygen molecule on the structural and electronic properties of GG.

5.4.1 Outcome

It was observed that BG exhibits similar structural and electronic properties before and after CO and H_2O adsorption, suggesting weak physical adsorption of CO and H_2O on its surface. The structural and electronic properties of BG are found to be sensitive to the adsorption of NO and NO_2, due to strong molecule-graphene interactions. Hence BG can be used as good sensors for the detection of toxic gases such as NO and NO_2 in the atmosphere with water vapour, as it is not sensitive for the presence of H_2O molecule. Both AG and GG have large adsorption energies and short binding distances towards CO, NO, NO_2 and H_2O adsorption, which suggests that the interactions of AG or GG with CO, NO, NO_2 and H_2O involve

chemisorption. The Hirshfeld charge distribution analysis, electronic band structures and DOS of these doped graphene and CO-, NO-, NO_2- and H_2O-adsorbed-doped graphene systems prove that the electronic properties of AG and GG are sensitive to CO, NO, NO_2 and H_2O molecules, which would result in notable changes in their electrical conductivities. The local curvature in the ground state configuration of graphene doped with Al and Ga due to the large dopant atom-carbon bond length results in high reactivity of AG and GG to these gas molecules. Our results suggest that both AG and GG can be used as promising candidates as gas sensing materials for toxic gases such as CO, NO and NO_2. But the presence of water vapour basically limits the practical applications of AG and GG structures as efficient toxic-gas sensing materials. The chemisorption of O_2 on GG induces dramatic changes of atomic structures and electronic structures of GG, which reveals that GG is sensitive to O_2 molecule. The chemisorption of O_2 on the surface of GG significantly affects its sensitivity to other gas molecules and thus prevents the potential usage of GG as toxic gas sensors.

5.4.2 Applications

Detection and monitoring of CO, NO and NO_2 released during industrial processes are of critical importance in industrial workplaces, residential areas and healthcare sector for ensuring public safety. The high sensitivity of BG towards NO and NO_2 and the insensitivity of BG towards O_2 and H_2O makes it the most promising gas sensors for the detection of NO and NO_2 in environmental monitoring and control, industrial processing and medical industry. Gas sensors using AG- and GG-based materials could be employed for the detection of CO, NO and NO_2 in industrial, environmental, medical applications etc., in the absence of water vapour.

5.4.3 Limitations

The work is limited to graphene doped with group III atoms such as B, Al and Ga. The work covers only the interactions between group III (B, Al and Ga) doped graphene and several toxic gas molecules such as CO, NO and NO_2. Out of the constituents of the air, only O_2 and H_2O has been selected for investigating the effect of atmospheric constituents on group III (B, Al and Ga) doped graphene. The study can be extended to other constituents of air for analysing the operation of group III doped graphene based gas sensors in ambient conditions. The sensitivity of other experimentally demonstrated doped graphenes to gases present in normal working conditions has not been covered and need to be explored for enabling practical gas sensing applications in future.

Out of the various sensor performance parameters, only sensitivity has been considered. This work only predicted the sensitivity of group III (B, Al and Ga) doped graphenes towards the considered gas molecules and has identified suitable dopants on graphene out of the considered group III dopants (B, Al and Ga) that can lead to single molecule sensing of CO, NO and NO_2 in the presence of water vapour. The sensing materials were not optimized in terms of selectivity.

In the next chapter, the adsorption of harmful gases such as H_2S and N_2O on intrinsic and several doped graphenes have been studied to evaluate the suitability of using doped graphenes as H_2S and N_2O gas sensors. The effect of dopant atoms such as P and S on the interactions between graphene and H_2S are analyzed in chapter 6 to determine the H_2S gas sensing properties of P- and S-doped graphene. Chapter 6 also investigates the effects of substitutional doping of graphene with B, N, Si, P, Ga, Cr and Mn atoms on the reactivity of graphene towards N_2O molecule to identify the best suitable dopants on graphene that could sense the presence of a single molecule of N_2O for environmental safety applications.

CHAPTER 6

H_2S AND N_2O ADSORPTION ON INTRINSIC AND HETEROATOM-DOPED GRAPHENE

6.1 Introduction

Hydrogen sulphide (H_2S), a colourless gas with distinct odour of rotten eggs is an important environmental and industrial pollutant. H_2S is easily found in raw natural gas, in swamps and sewers, in waste gas streams from paper and petrochemical industry [337]. H_2S can cause a wide range of health effects [338, 339]. Prolonged low-level H_2S exposure (20 ppm) may result in loss of appetite, poor memory, fatigue, headache, dizziness and irritability. H_2S in micro-amounts of 50-300 ppm can cause various respiratory difficulties ranging from rhinitis to acute respiratory failure. H_2S concentrations of 500 ppm can cause loss of consciousness and concentrations above 700 ppm can result in instant death [43, 340]. Being toxic, corrosive, flammable and explosive in nature, H_2S detection and control is inevitable in laboratories and for various processes such as coal or natural gas manufacturing.

DFT based calculations have shown weak binding of H_2S to IG [41]. Doping of graphene with B and N atoms were also not found to be promising routes for improving the adsorption of H_2S on graphene surface [41]. Zhang and co-workers found that graphene doped with Si can strongly adsorb H_2S molecule on graphene surface through the formation of Si-S bond [41], compared to the weak physisorption of H_2S molecule onto IG, BG and NG. Another DFT study revealed increase in the sensitivity of IG to H_2S molecule through Al and Ga doping, as H_2S got chemisorbed on these doped graphenes with relatively large adsorption energies and small binding distances [43]. It was also found that graphene modified with transition metals such as calcium (Ca), cobalt (Co) and iron (Fe) show much higher sensing affinities towards H_2S [41, 56]. PtG has also been studied as a promising adsorbent for H_2S detection, owing to the significantly enhanced interactions between graphene and H_2S through Pt doping [56]. Theoretical calculations have predicted the applicability of graphene modified with Al, Si, Ga, Fe, Ca, Co, and Pt dopants as good sensors for the detection of H_2S.

Until now, it has been reported that N, B, and Si atoms can be successfully doped into graphene [72, 215, 341-350]. Experimental works on doping of graphene with P and S atoms have also been performed [351-353]. DFT based calculations on the adsorption of several gas molecules on PG have reported strong chemisorptions of O_2, NO, NO_2 and SO_2 onto PG through the formation of P-X (X = O, N, S) bonds, while weak physisorption was observed

for H_2, H_2O, CO_2, CO, N_2 and NH_3 [273]. Liang *et al.* have demonstrated high selectivity gas sensing of SG to NO_2 in the presence of other gases such as NH_3, CO, SO_2, CH_4 [171]. SG showed strong binding to NO_2 among other gas molecules such as NH_3, SO_2, H_2O, CO, CO_2, NO, H_2, O_2, according to DFT based analysis [39]. Faye *et al.* studied H_2S adsorption on SG and concluded that H_2S exhibits a long range interaction with SG with no sign of any new bond formation [354], from the analysis of adsorption energy and charge transfer calculations. However, the effect of the P dopant on the reactivity of graphene towards H_2S has not been investigated. In this chapter, the adsorption of H_2S on graphene sheets doped with P and S impurities are studied.

The detection of nitrous oxide (N_2O), commonly known as laughing gas is also very important since increasing N_2O concentrations lead to global warming and stratospheric ozone-layer destruction [355-357]. N_2O is considered as the single greatest ozone-depleting substance and is expected to remain the dominant ozone-depleting substance throughout the 21st century [358]. The global warming potential of N_2O is 298 times higher than that of CO_2, with an atmospheric lifetime of about 120 years [359]. N_2O is estimated to contribute about 6% of the global warming effect due to green-house gases [360]. Significant efforts have been made to find an effective method for detecting N_2O gas. The sensing affinity of graphene or doped graphene to N_2O may provide new insights into the development of future N_2O gas sensors for environmental monitoring and control. Therefore, the adsorptions of N_2O on heteroatom-doped graphene such as BG, NG, SiG, PG, GG, CG and MG sheets have been investigated here. The adsorption of N_2O on IG is also studied for comparison. The energetically favourable adsorption configurations, adsorption energies, charge distribution analysis, band structures and DOS of the graphene-N_2O adsorbed systems were calculated and analyzed to understand the effect of different dopants on the N_2O gas sensing properties of graphene and to exploit the application of graphene as N_2O gas sensors.

6.2 Computational Details

DFT calculations are performed using the GGA-PBE XC functional [361]. A plane wave basis set with a kinetic energy cutoff of 30 Ha is chosen in all simulations. The pseudopotentials were constructed using the Troullier and Martins scheme [313] to approximate the electron-ion interactions. The Brillouin zone is sampled using a 5 × 5 × 1 MP k-point [328]. A denser MP grid of 15 × 15 × 1 is used for the calculation of DOS. BFGS minimization [329] was employed to optimize the atomic coordinates and all atoms were allowed to relax until the forces were smaller than 0.0257 eV/Å. The charge transfer analysis is based on the Hirshfeld method [330].

6.2.1 Model building

Based on the model of IG sheet described in Chapter 5, different doped graphene sheets (BG, NG, SiG, PG, SG, GG, CG and MG) were built by replacing the C atom with corresponding dopant atom (B, N, Si, P, S, Ga, Cr or Mn). The geometries of the doped graphene sheets were optimized for further calculations.

E_{ad} of H_2S and N_2O on different graphenes can be calculated as the difference between the energy of the fully relaxed graphene sheet with the adsorbed gas molecule (E_{tot}) and the sum of the energies of the isolated intrinsic or doped graphene sheet (E_{sheet}) and the isolated gas molecule ($E_{molecule}$). Thus, the expression of E_{ad} is as follows:

$$E_{ad} = E_{tot} - (E_{sheet} + E_{molecule}) \quad (6.1)$$

The energies of all the atomic structures were calculated after full relaxation.

6.3 Results and Discussions

The optimized lattice constant and C-C bond length of IG are found to be 2.46 Å and 1.42 Å, which are in agreement with that reported in literature [8, 289, 331].

6.3.1 Effect of doped atoms on the structural and electronic properties of IG

As the first step, different doped graphene sheets were allowed to relax. Figure 6.1 (a)-(h) show the optimized structures of various heteroatom-doped graphene sheets such as BG, NG, SiG, PG, SG, GG, CG and MG respectively. After relaxation, both BG and NG retain the planar form of undoped graphene as seen in Figure 6.1 (a) and (b). The carbon-dopant atom distance is found to be 1.49 Å (B-C bond) for BG and 1.41 Å (N-C bond) for NG. The substitution of a single C atom by other dopant atoms (such as Si, P, S, Ga, Cr and Mn in SiG, PG, SG, GG, CG and MG respectively) results in a distorted geometry, compared to IG, due to the stress induced by the bigger sized dopant atoms compared to the host carbon atoms (Figure 6.1 (c)-(h)). The dopant atom protrudes out of the plane, at a distance *d* from the plane of *d*=0.989 Å for Si, *d*=1.107 Å for P, *d*=1.005 Å for S, *d*=1.220 Å for Ga. The bond around the dopant atom elongates to 1.74 Å (Si-C bond) in SiG and 1.76 Å (P-C bond) in PG, 1.74 Å (S-C bond) in SG and 1.83 Å (Ga-C bond) in GG from the ideal C–C bond length of 1.42 Å (Figure 6.1 (c)-(f)). These results are in good agreement with previously reported theoretical works [35, 39, 43, 273]. In CG and MG, the dopant atom is displaced more outwards forming a bump (Figure 6.1 (g), (h)) with an elevation of 1.318 Å and 1.304 Å respectively. The carbon-dopant atom distances of 1.85 Å (Cr-C bond) (Figure 6.1 (g)) and 1.82 Å (Mn-C bond) (Figure 6.1 (h)), are consistent with the results reported in ref. [272].

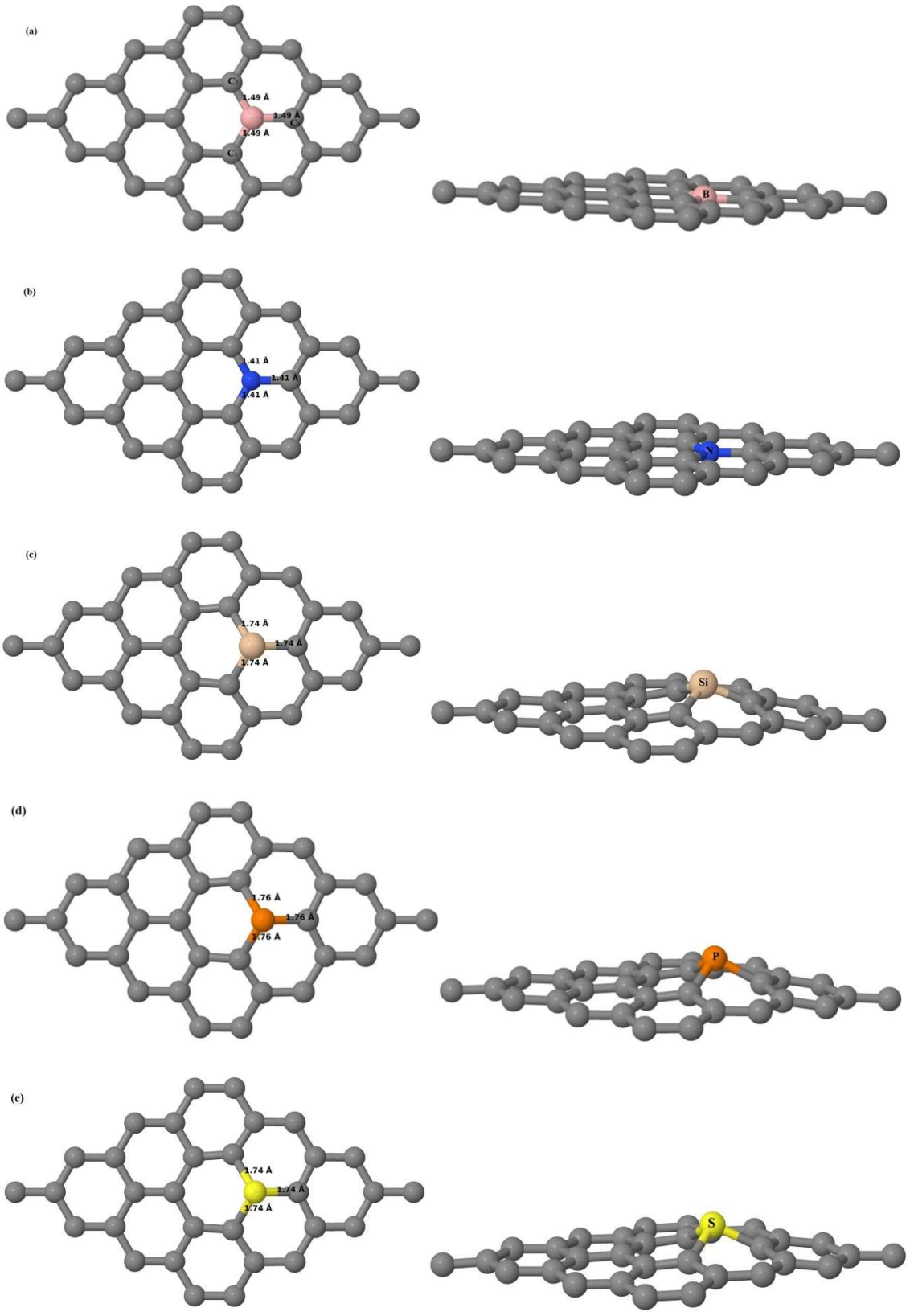

Figure 6.1 (a)-(e) Top (left) and side (right) views of optimized structures of **(a)** BG, **(b)** NG, **(c)** SiG **(d)** PG **(e)** SG.

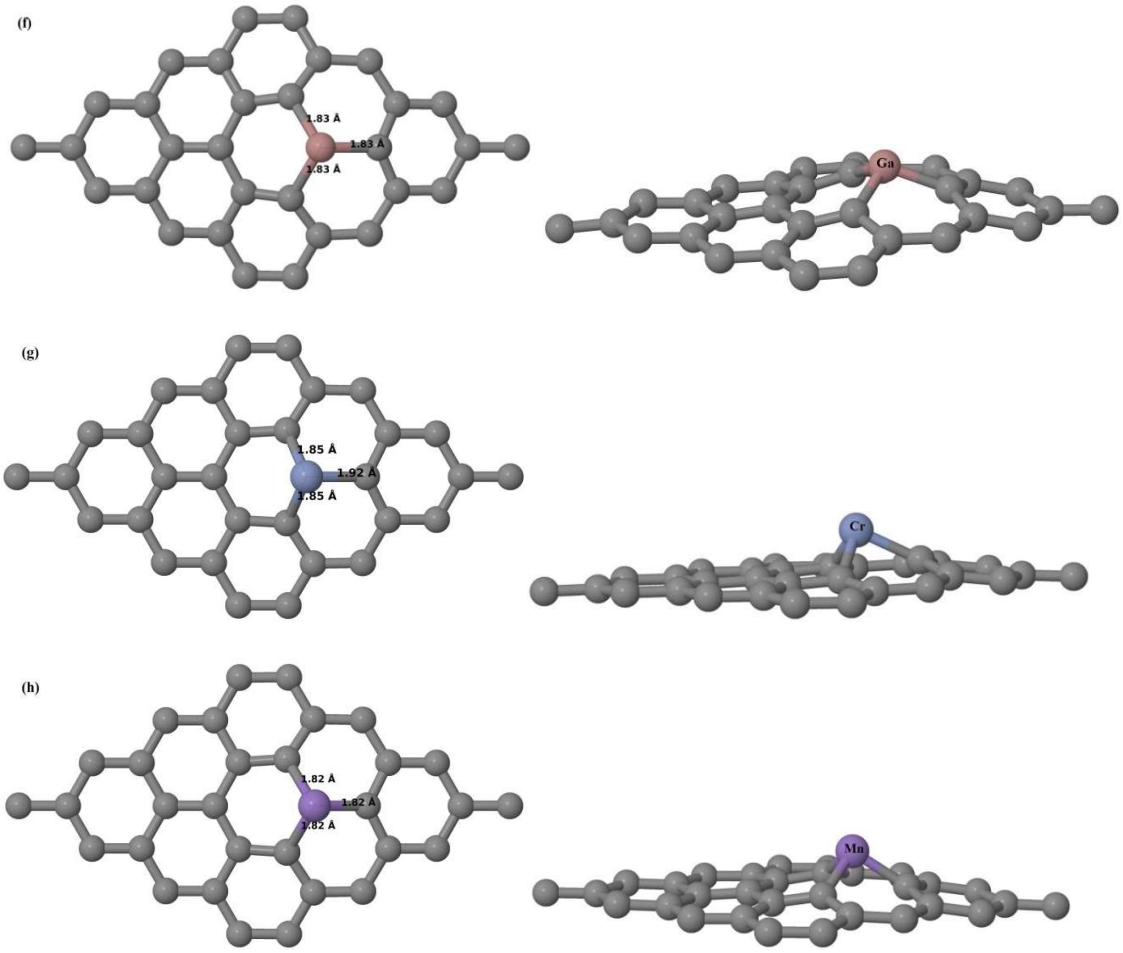

Figure 6.1 (f)-(h) Top (left) and side (right) views of optimized structures of **(f)** GG, **(g)** CG and **(h)** MG sheets.

Table 6.1 present the results of the charge distribution analysis of IG, BG, NG, SiG, PG, SG, GG, CG and MG sheets. In IG, all the carbon atoms are neutral and hence they possess zero charge state. In BG, the three neighbouring C atoms have a charge state of -0.061 and the B-dopant has a charge state of +0.023, since the neighbouring C atoms attract electrons from the B atom. As N atom is more electronegative than C atom, the neighbouring C atoms possess a charge state of +0.045 and the N-dopant has a charge state of +0.030 in NG. In SiG, the C neighbours attain a charge state of -0.084 and the Si-dopant lose electronic charge of +0.205. Upon replacing C atom with P atom, the neighbouring C atoms gain a charge state of -0.046 in PG and the P-dopant lose electronic charge of 0.172. Even though both carbon and sulfur atoms have almost the same electronegativity, the smaller size of C makes it more electronegative than S. Hence the nearest C neighbours attract electrons from S and gain a charge state of -0.037, whereas S-dopant loses electrons with a charge state of 0.300. In GG, the Ga-dopant loses electronic charge of 0.020 and the C neighbours gain electronic charge of -0.028. As the C atoms around the dopant atom attract electrons from the dopant atom, the C neighbours attain a charge state of -0.067 and -0.037 in CG and MG, whereas the dopant

atoms lose electronic charge and attain a charge state of +0.327 and +0.151 in CG and MG respectively. Similar behaviour of the charge state of C neighbours and the dopant atom in BG, SiG, PG, GG, CG and MG is due to the fact that the electronegativity of C atom is higher than B, Si, P, Ga, Cr and Mn atoms and thus the C atoms surrounding the dopant atom catch electrons from the dopant atom and a decrease in electron density is observed on the dopant atom.

Figure 6.2 (a)-(f) present the electronic band structures of some representative systems such as IG, PG, SG, GG, CG and MG sheets along the high symmetry points (Γ-K-M-Γ) of the hexagonal Brillouin zone of graphene. The DOS of IG, PG and SG are shown in Figure 6.3 (a)-(c) and the DOS of GG, CG and MG are shown in Figure 6.4 (a)-(c) respectively. Although the electronic properties of IG and GG have already explained in Chapter 5, the band structure and DOS figures of IG and GG are presented here for completeness. Since both P (Group V) and S (Group VI) atoms have one and two valence electrons more than the host C atoms, these elements act as donors of electrons in graphene [336] and thus modify the electronic structure of graphene. Substitutional doping with P and S atoms in graphene lattice results in band gap opening in graphene. The calculated band structure plots of PG and SG agree well with those in previous reports [73]. Doping with P and S introduce band gaps of 0.658 eV (Figure 6.2 (b)) and 0.583 eV (Figure 6.2 (c)) respectively in graphene. The observed band gap values are very close to the previously reported band gap values of 0.67 and 0.57 eV [73]. The band structure plot (Figure 6.2 (e)) and the DOS profile (Figure 6.2 (b)) of CG show that CG is metallic or half metallic in nature with finite DOS at E_F, as similar to previous reports [272, 362]. The band structure of MG has an indirect band gap of 0.385 eV as seen in Figure 6.2 (f).

Table 6.1 Hirshfeld charge distribution analysis of the dopant atom, three nearest C atoms around the dopant atom of BG, NG, SiG, PG, SG, GG, CG and MG sheets[a]

System	C_1	C_2	C_3	B	N	Si	P	S	Ga	Cr	Mn
IG	0	0	0	-	-	-	-	-	-	-	-
BG	-0.061	-0.061	-0.061	0.023	-	-	-	-	-	-	-
NG	0.045	0.045	0.045	-	0.030	-	-	-	-	-	-
SiG	-0.084	-0.084	-0.084	-	-	0.205	-	-	-	-	-
PG	-0.046	-0.046	-0.046	-	-	-	0.172	-	-	-	-
SG	-0.037	-0.037	-0.037	-	-	-	-	0.300	-	-	-
GG	-0.028	-0.028	-0.028	-	-	-	-	-	0.020	-	-
CG	-0.067	-0.067	-0.076	-	-	-	-	-	-	0.327	-
MG	-0.037	-0.037	-0.037	-	-	-	-	-	-	-	0.151

[a] A negative sign indicates electrons gained, whereas positive sign implies electron lost by the atom (the unit of charge is electron)

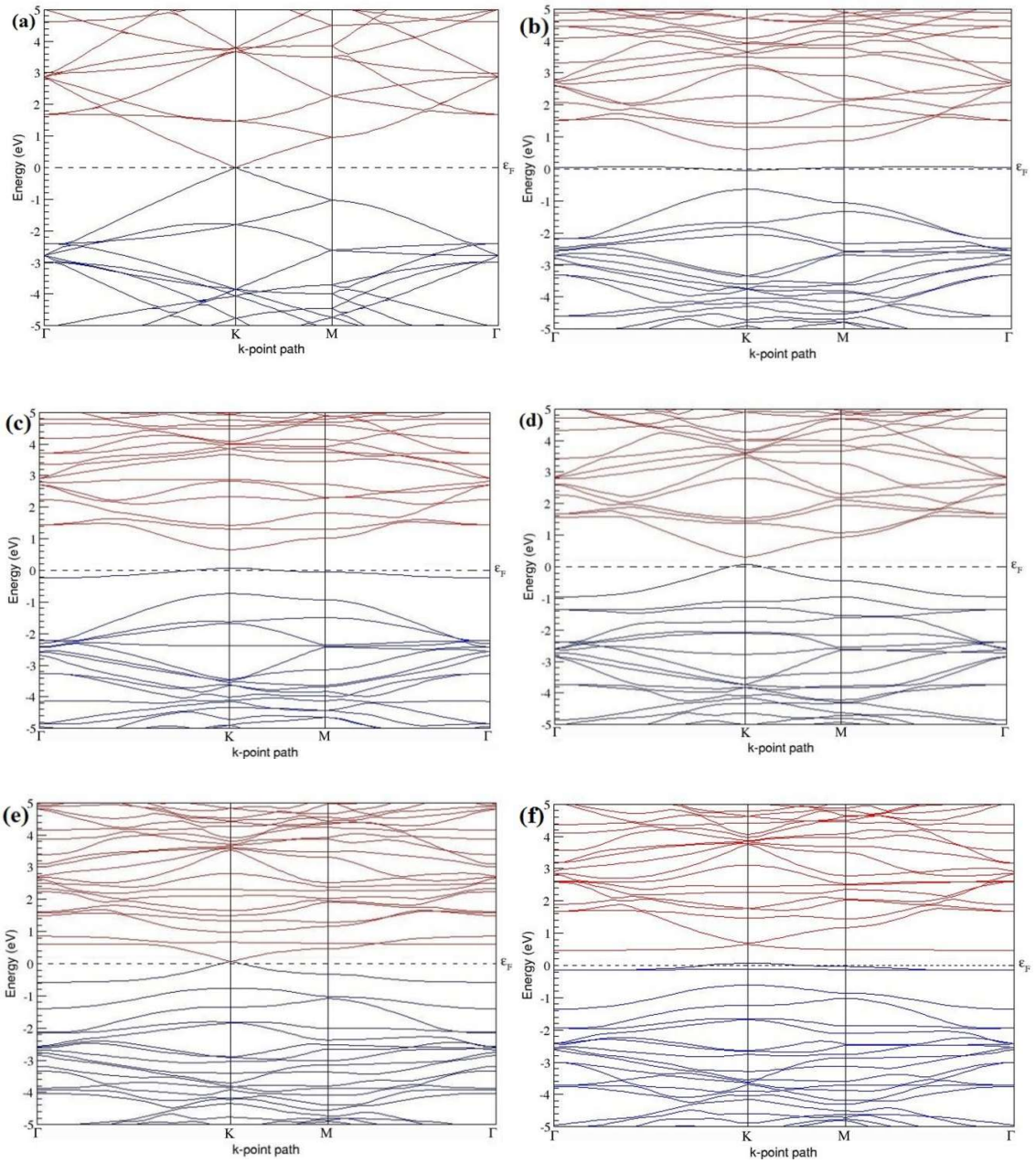

Figure 6.2 Electronic band structures of **(a)** IG, **(b)** PG, **(c)** SG **(d)** GG **(e)** CG, and **(f)** MG sheets

6.3.2 Structural Properties of gas-adsorbed intrinsic, and doped graphene systems

The atomic geometries of isolated H_2S and N_2O molecules were first optimized. The optimized H-S bond length and the H–S–H bond angle of H_2S are calculated to be 1.35 Å and 91.6^0, which are close to the experimental values of 1.336 Å and 92.11^0. In N_2O molecule, the optimized N-N bond length of 1.13 Å, N-O bond length of 1.19 Å and the N–N–O angle of 180^0 are in good agreement with experimental values (N-N bond length of 1.1282 Å, N-O bond length of 1.1842 Å and N–N–O angle of 180^0 respectively).

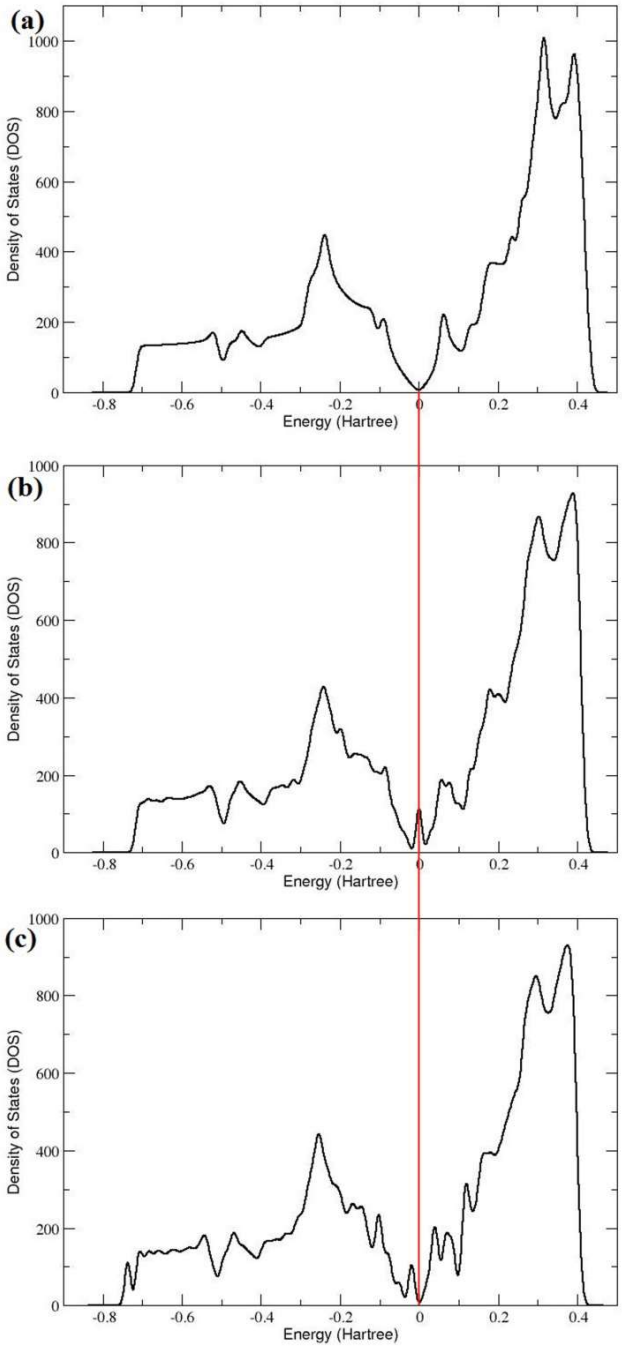

Figure 6.3 The DOS of **(a)** IG, **(b)** PG, **(c)** SG sheets

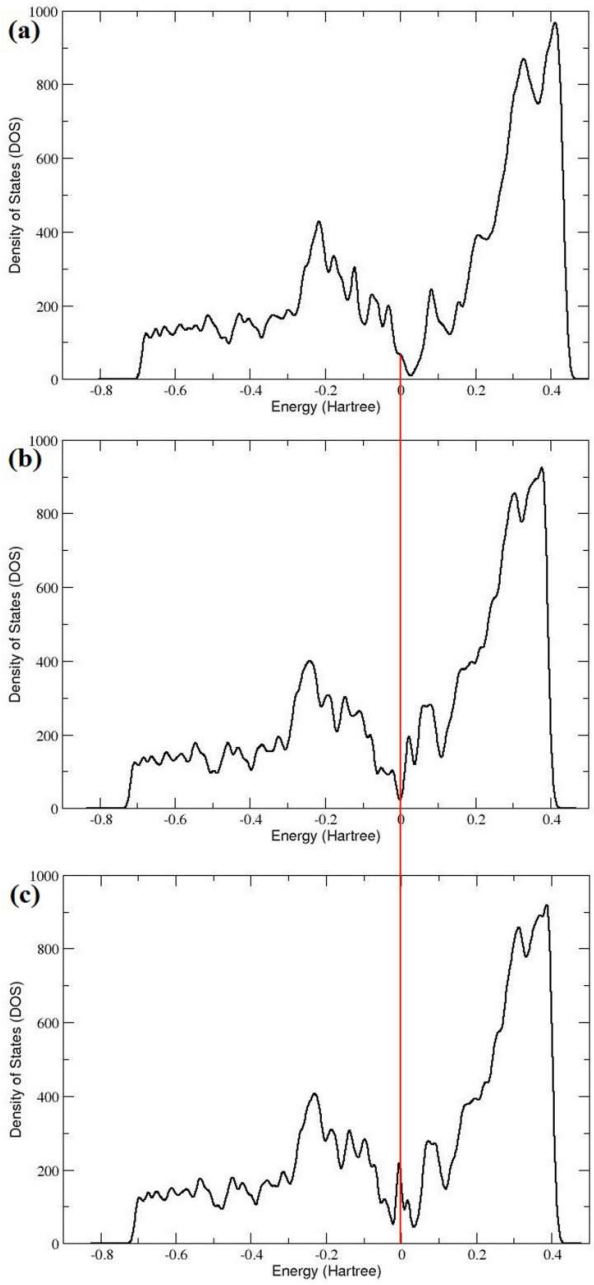

Figure 6.4 The DOS of **(a)** GG, **(b)** CG, and **(c)** MG sheets

6.3.2.1 H_2S on graphene

After determining the most stable structures of intrinsic and heteroatom-doped graphene sheets, the adsorption of H_2S on IG, PG and SG are discussed in this section by testing different adsorption configurations of H_2S on graphene surfaces. Various orientations of H_2S with respect to graphene sheet are considered by starting from S atom with H–S bonds parallel, pointing up and down. The system is optimized for all the considered adsorption configurations. Then the adsorption energy and the binding distance are calculated for these configurations. The most energetically stable adsorption configurations of H_2S on considered

graphene sheets determined by comparing the adsorption energies of the optimized geometries obtained from the initial states of H_2S are shown in Figure 6.5 (a)-(c). It was observed that there is no remarkable change in the geometry of IG, PG and SG sheets after H_2S adsorption. The energetically favourable adsorption configuration of H_2S on IG, PG and SG sheets are found to be the same in which is H_2S is oriented downwards with both H-atoms close to the graphene plane than the S-atom, according to the calculations (Figure 6.5 (a)-(c)). The minimum atom-to-atom distance between H_2S and IG sheet is 3.33 Å (Figure 6.5 (a)).

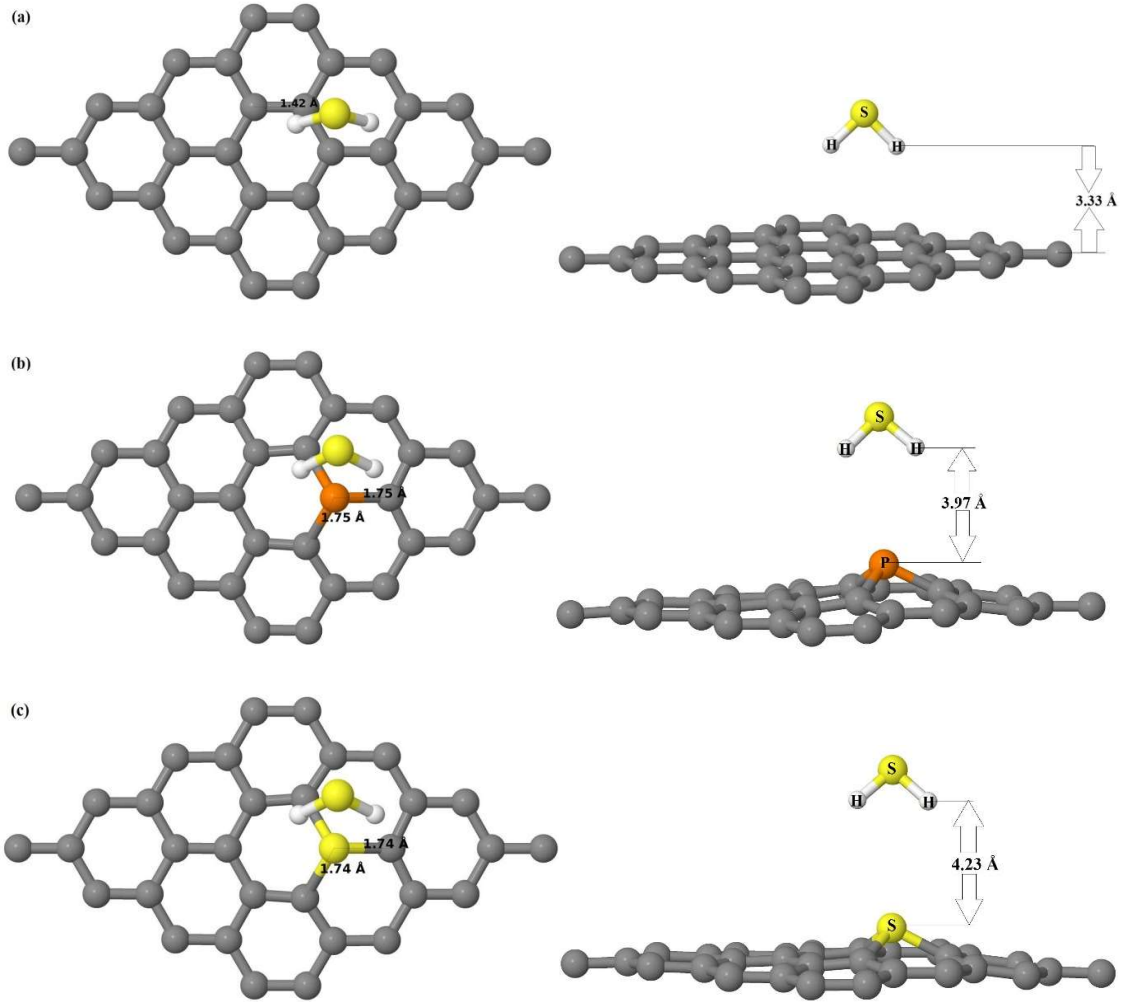

Figure 6.5 Top (left) and side (right) views of optimized structures of H_2S molecule on **(a)** IG, **(b)** PG and **(c)** SG sheets.

After structural relaxation of the H_2S-PG and SG systems, the H_2S molecule is located at a distance larger than 3.5 Å above the doped graphene sheets (Figure 6.5 (b), (c)). The elevation of P atom decreases to 1.025 Å with decreased P–C bond length of 1.75 Å on H_2S adsorption (Figure 6.5 (b)). In SG, the elevation of S atom decreases to 0.901 Å with the same S-C bond length of 1.74 Å (Figure 6.5 (b)) upon H_2S adsorption. Thus both the dopant

atoms are slightly pushed downwards by the adsorbed H_2S, which indicates the repulsive force between the dopant atoms and the H_2S molecule.

6.3.2.2 N_2O on graphene

The adsorptions of N_2O on different graphene sheets are investigated by considering three different orientations of N_2O with respect to graphene plane, one in which the N_2O molecule is parallel to the graphene plane and the other two with the molecule oriented perpendicular to the surface. The perpendicular orientation was investigated *via* two modes based on the binding atom of N_2O, labelled as N-end and O-end. In N-end binding mode, the N atom of N_2O is close to the graphene sheet, whereas in O-end binding mode, the O atom is close to the graphene sheet. The nature of interactions of N_2O molecule with IG, BG, NG, SiG, PG, GG, CG and MG sheets are studied in this section.

Figure 6.6 (a) and (b) show the optimized structures of N_2O adsorbed on IG through the N-end and O-end binding mode respectively. After N_2O adsorption, the atomic geometry of IG remains unchanged (Figure 6.6 (a), (b)). Having determined the relaxed structures of different heteroatom-doped graphene sheets, the next step is to investigate the N_2O adsorption process. N_2O molecule is initially placed on the top site of the dopant atom in the considered doped graphene sheets. Figure 6.6 (c) and (d) present the relaxed structures of N_2O-adsorbed BG and NG system and there is no notable variation in the structures of BG and NG upon N_2O adsorption. For both N_2O adsorbed on BG and NG, the energetically favourable geometry is the one in which the O-end binding mode is tilted with the oxygen atom of N_2O facing towards the dopant atom (Figure 6.6 (c), (d)). The carbon-dopant atom distance remains unchanged in both BG and NG even after N_2O interaction. The molecule-graphene binding distance in BG and NG are observed to be 3.72 Å and 3.58 Å respectively (Figure 6.6 (c), (d)).

In N_2O adsorbed SiG and PG systems, N_2O molecule is far away from the doped graphene sheets with distances of 3.41 Å in SiG and 4.28 Å in PG (Figure 6.6 (e), (f)). After N_2O adsorption, the elevation of Si atom decreases to 0.863 Å with decreased Si–C bond length of 1.73 Å (Figure 6.6 (e)). In the case of PG, the elevation of P atom decreases to 1.010 Å with the same P-C bond length of 1.76 Å (Figure 6.6 (f)). These structural parameters indicate the repulsive force between the N_2O molecule and the Si (or P) atom. Figure 6.6 (g) and (h) depict the optimized structures of N_2O adsorbed on GG *via* the N-end and O-end respectively. A strong chemical bond is formed between Ga atom and the adsorbed N atom in the scheme of N_2O adsorbed on GG *via* N-end. The elevation of Ga atom and the Ga–C bond

length increase to 1.245 Å and 1.84 Å on N_2O adsorption *via* N-end (Figure 6.6 (g)). In the case of N_2O adsorbed on GG *via* O-end, there is no change in the atomic structure of GG (Figure 6.6 (h)). After N_2O adsorption, the structures of CG and MG are changed dramatically. The stable configurations of N_2O molecule adsorbed on CG and MG *via* N-end and O-end are presented in Figure 6.6 (i)-(l) respectively. Figures 6.6 (i)-(l) show that N_2O molecule can strongly bond to CG and MG sheets by the O atom or by the two N atoms with dopant atom-gas molecule distance of around 2 Å. The partial dissociation of N_2O into N_2 and O-species on the Cr-dopant can be seen In Figure 6.6 (j). The resulting NNCrO species remains bonded to the doped graphene sheet through the Cr dopant. In N_2O adsorbed on CG, the carbon-dopant atom distance got extended to 1.89 Å (Figure 6.6 (j)) and the elevation of Cr above the graphene sheet has extended significantly to 1.550 Å after N_2O adsorption. In N_2O adsorbed on MG, the Mn-C bond length remains the same, whereas the elevation of Mn has got slightly extended to 1.396 Å, upon N_2O interaction (Figure 6.6 (k), (l)).

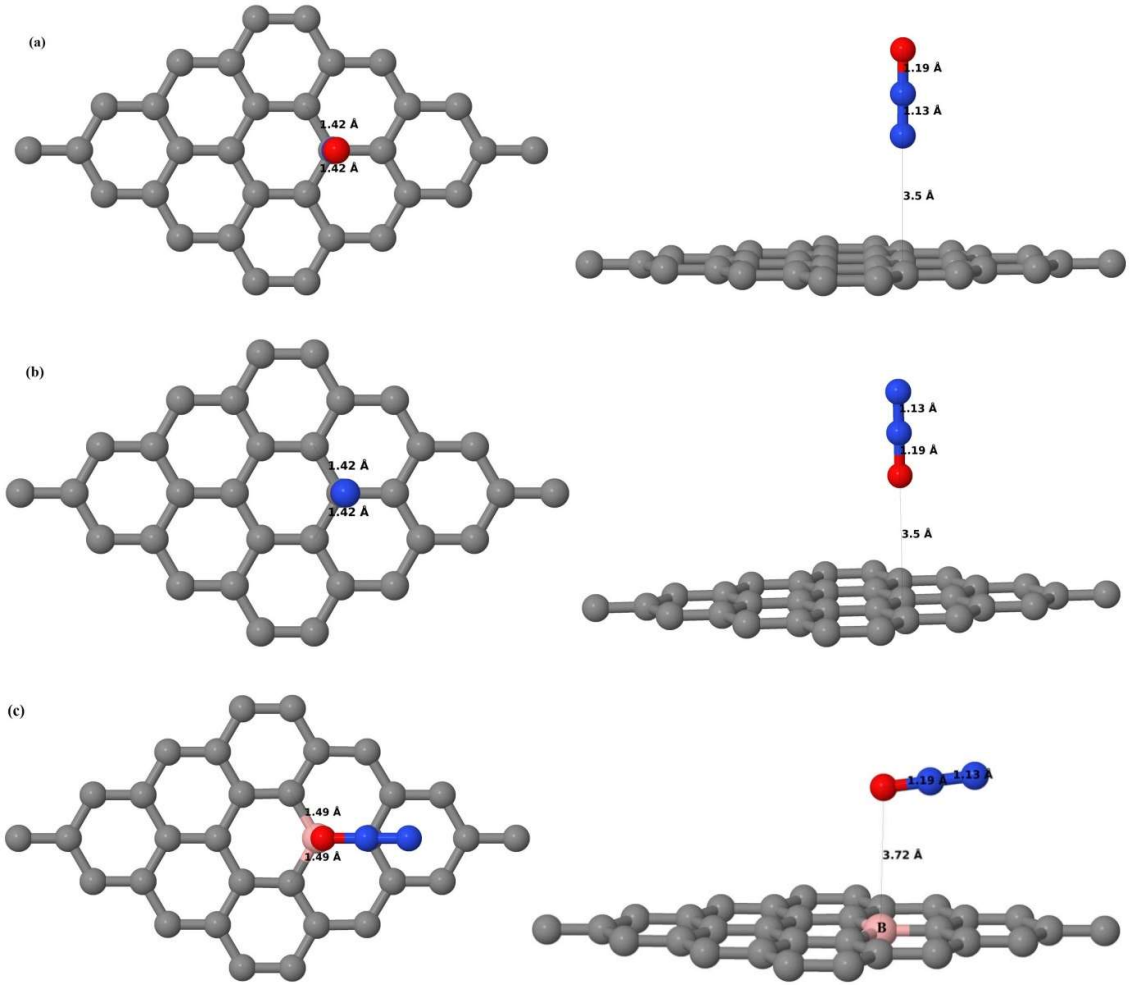

Figure 6.6 Top (left) and side (right) views of the optimized adsorption structures of N_2O on **(a)** IG via N-end **(b)** IG via O-end, **(c)** BG

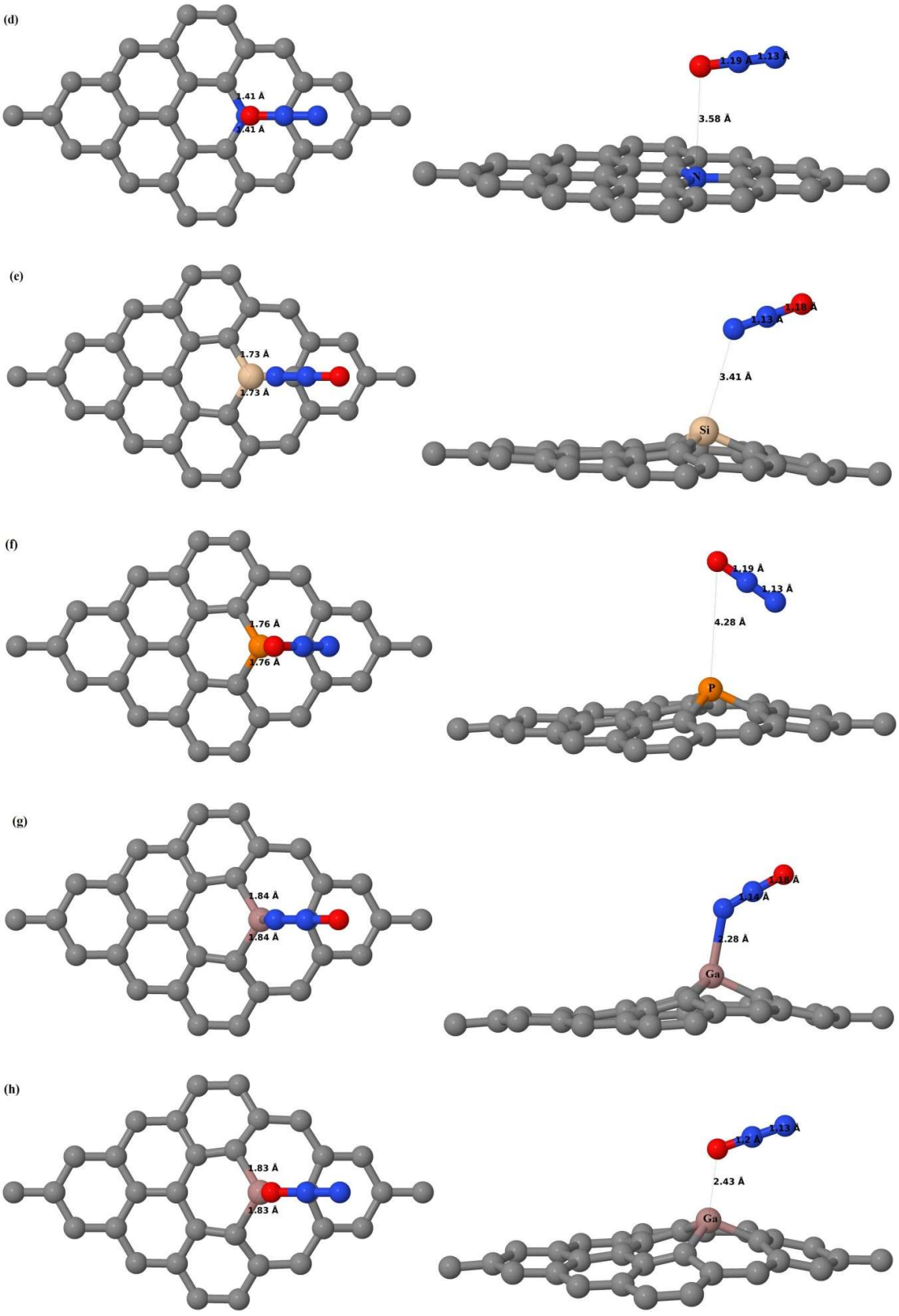

Figure 6.6 Top (left) and side (right) views of the optimized adsorption structures of N_2O on **(d)** NG, **(e)** SiG **(f)** PG, **(g)** GG via N-end and **(h)** GG via O-end.

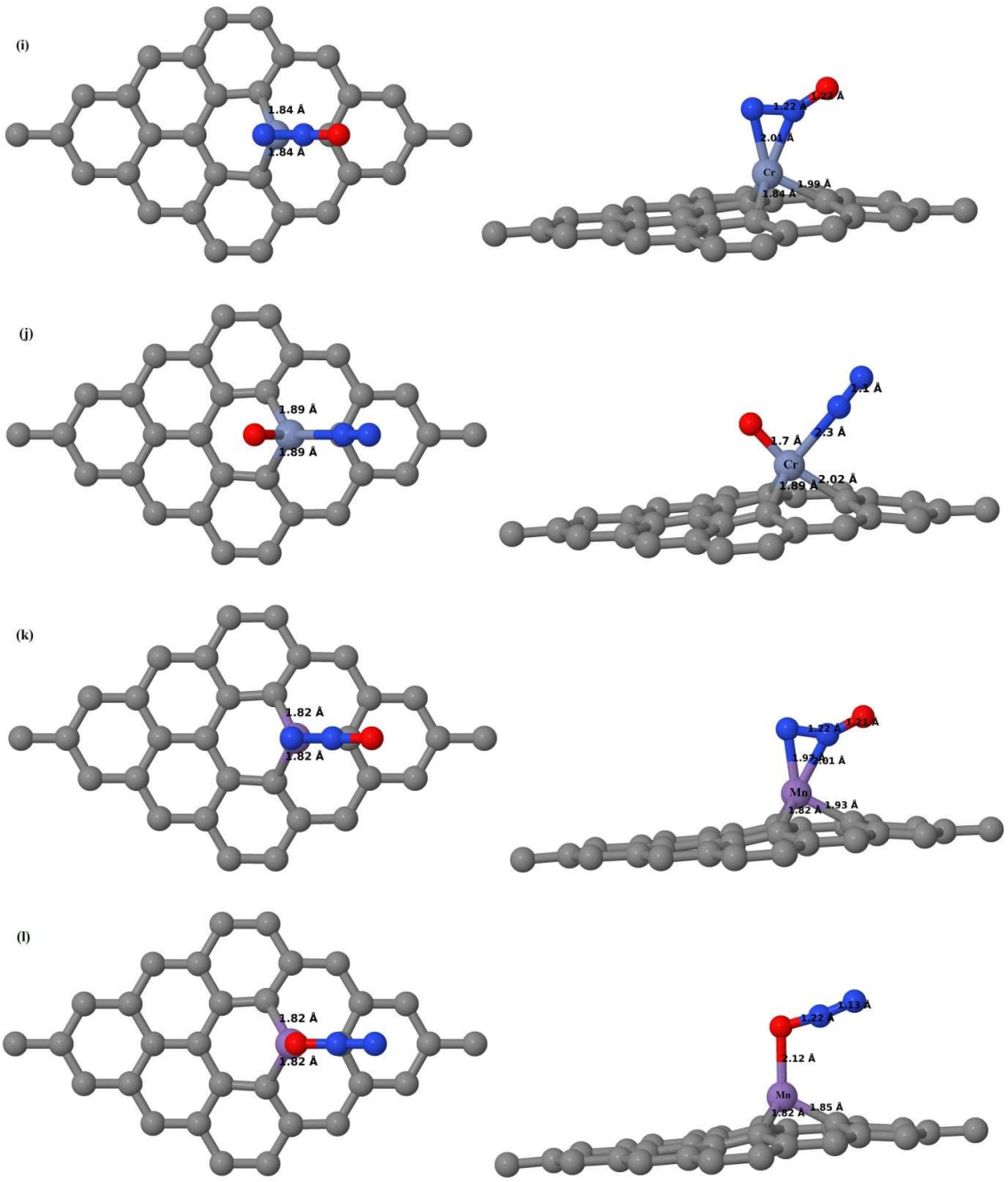

Figure 6.6 Top (left) and side (right) views of the optimized adsorption structures of N_2O on **(i)** CG via N-end **(j)** CG via O-end **(k)** MG via N-end, and **(l)** MG via O-end.

6.3.3 Energetic Properties of gas-adsorbed intrinsic, and doped graphene systems

6.3.3.1 H_2S on graphene

The energetic behaviour of H_2S adsorptions on IG, PG and SG sheets are studied by calculating the adsorption energies and are presented in Table 6.2. The negative E_{ad} values in all cases indicate that H_2S adsorption is energetically favourable. The relatively low values of adsorption energies (-0.023 eV for IG, -0.037 eV for PG and -0.011 eV for SG) and large

binding distances show that the interactions of H_2S with IG, PG and SG are weak and H_2S-adsorbed IG, PG and SG systems are in the very weak physisorption region. The observed physisorption of H_2S on SG agrees well with the recent findings by Faye *et al.* [354].

Table 6.2 Values of adsorption energy and molecule-sheet distance of H_2S above IG, PG and SG sheets

System	IG	PG	SG
E_{ad} in eV	-0.023	-0.037	-0.011
d in Å	3.33	3.97	4.23

6.3.3.2 N_2O on graphene

The energetic behaviour of N_2O adsorptions on IG, BG, NG, SiG, PG, GG, CG and MG sheets are studied by calculating the adsorption energies and are presented in Table 6.3. The N_2O-graphene binding distance of 3.5 Å and small adsorption energies of N_2O molecule adsorbed on IG *via* N-end (E_{ad} = -0.011 eV) and O-end (E_{ad} = -0.015 eV) show that only weak interactions exist between N_2O molecule and IG, which are in agreement with the results reported by Lv *et al*. [54]. The low absorption energy (-0.027 eV for BG and -0.022 eV for NG) and long binding distance (3.72 Å for BG and 3.58 Å for NG) implies weak forces and physisorption of N_2O on BG and NG. The adsorption energies of N_2O adsorbed on BG and NG are found to be slightly greater than that observed in IG and thus doping of graphene with B and N atoms improve the interactions between N_2O and graphene sheet. The calculated adsorption energies for N_2O on SiG and PG are found to be almost the same (-0.030 eV), which clearly shows physisorption of N_2O on SiG and PG. N_2O adsorbed onto the top site of the Ga atom of GG *via* N-end (E_{ad} = -0.239 eV) and O-end (E_{ad} = -0.160 eV) with corresponding dopant atom-gas molecule distance of 2.28 Å (Figure 6.6 (g)) and 2.43 Å (Figure 6.6 (h)) respectively show that the interaction of Ga atom with N_2O is stronger for N-end adsorbed on GG. The obtained E_{ad} values for N_2O adsorbed on GG *via* N-end and O-end are close to the reported values of -0.27 eV and -0.17 eV respectively [54]. The calculated adsorption energies of N_2O on CG and MG listed in Table 6.3 suggest that, for CG, the structure bonded by O and N atoms is the most stable one (Figure 6.6 (j)), whereas for MG, the structure bonded by N atoms is the most stable one (Figure 6.6 (k)), as they have the largest E_{ad}. The above results show that N_2O is chemisorbed on both CG and MG with large adsorption energies and small binding distances (Table 6.3). These results indicate that the interactions of N_2O with graphene are significantly enhanced by doping graphene with transition metal atoms such as Cr and Mn. The adsorption energy of N_2O was found to be largest on CG, which is followed by MG, GG and then SiG, PG, BG, NG.

Table 6.3 Values of adsorption energy and molecule-sheet distance of N_2O above IG, BG, NG, SiG, PG, GG, CG and MG sheets

System	IG	BG	NG	SiG	PG	GG	CG *via* N-end	CG *via* O and N-end	MG *via* N-end	MG *via* O-end
E_{ad} in eV	-0.015	-0.027	-0.022	-0.030	-0.030	-0.239	-1.168	-2.406	-1.088	-0.478
d in Å	3.5	3.72	3.58	3.41	4.28	2.28	2.01	1.7	1.97	2.12

6.3.4 Electronic Properties of gas-adsorbed intrinsic, and doped graphene systems

6.3.4.1 H_2S on graphene

Table 6.4 illustrates the Hirshfeld charge distribution analysis results of H_2S-adsorbed IG, PG and SG systems. When H_2S is adsorbed on IG, the C-site in the graphene lattice and nearest C neighbours gain a small amount of charge and the adsorbed H_2S molecule obtain a charge state of -0.005. The observed slight variation in the charge states of the C atoms in graphene lattice implies that the H_2S adsorption only results in negligible charge transfer between IG and adsorbed gas molecule. Upon H_2S adsorption on PG and SG, it was observed that there is only a slight increase and decrease in the electronic charge states of the nearest C neighbours and the dopant atoms respectively. As the adsorption of H_2S does not result in significant change in the charge state of dopant atoms in PG and SG, the charge transfer between the doped graphene sheets and H_2S is negligible. The negligible charge transfer between H_2S and IG, SG that point towards a weak interaction between H_2S and IG, SG is in agreement with the results reported in Ref. [354]. Figure 6.7 (a)-(c) present the band structures of H_2S adsorbed on IG, PG and SG systems. The band structure of H_2S-adsorbed IG system remains similar to that of IG (Figure 6.7 (a)). The band structures of PG and SG are also found to be unaffected by their interaction with H_2S molecule as seen in Figure 6.7 (b), (c). These results show that H_2S adsorption does not change the electronic structures of IG, PG and SG.

Table 6.4 Hirshfeld charge distribution analysis of the dopant atom, three C atoms around dopant atom and the adsorbed H_2S molecule on the surface of IG, PG and SG sheets [a]

System	C_1	C_2	C_3	C	P	S	H_2S
IG	0	0	0	0	-	-	-
PG	-0.046	-0.046	-0.046	-	0.172	-	-
SG	-0.037	-0.037	-0.037	-	-	0.300	-
H_2S-IG	-0.001	-0.002	-0.002	-0.002	-	-	-0.005
H_2S-PG	-0.046	-0.046	-0.047	-	0.180	-	-0.014
H_2S-SG	-0.037	-0.037	-0.038	-	-	0.301	-0.008

[a] A negative sign indicates electrons gained, whereas positive sign implies electron lost by the atom (the unit of charge is electron)

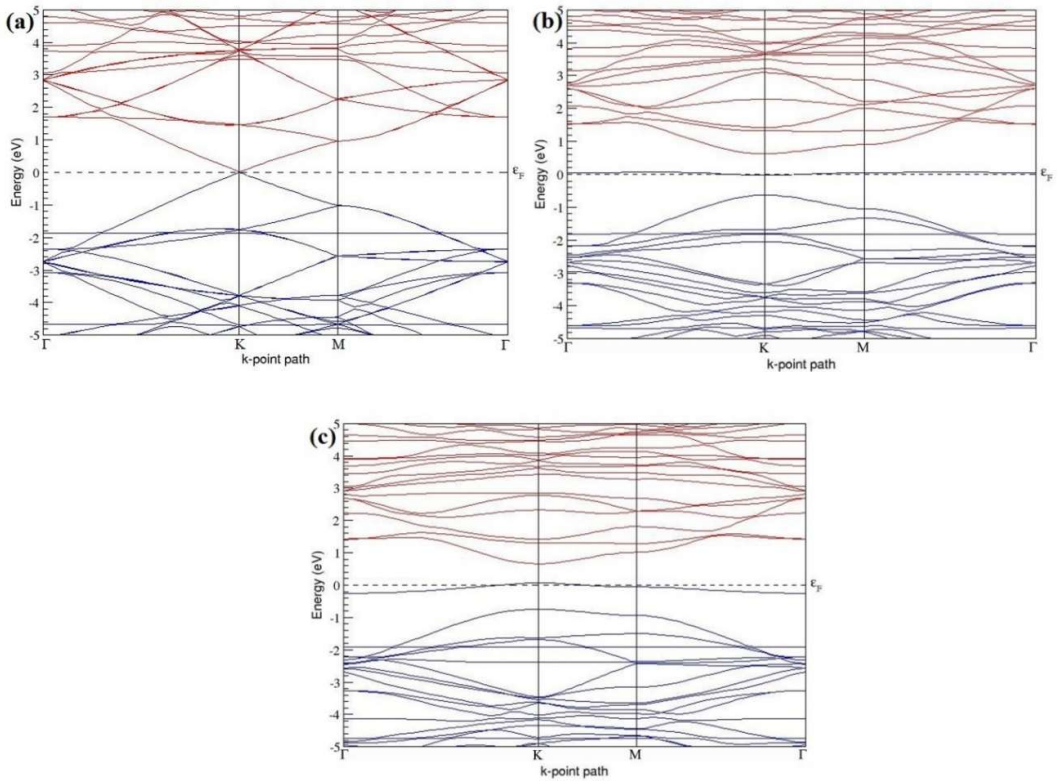

Figure 6.7 Electronic band structures of **(a)** H_2S adsorbed IG **(b)** H_2S adsorbed PG and **(c)** H_2S adsorbed SG

The DOS of H_2S-adsorbed IG, PG and SG systems are shown in Figure 6.8 (a)–(c).

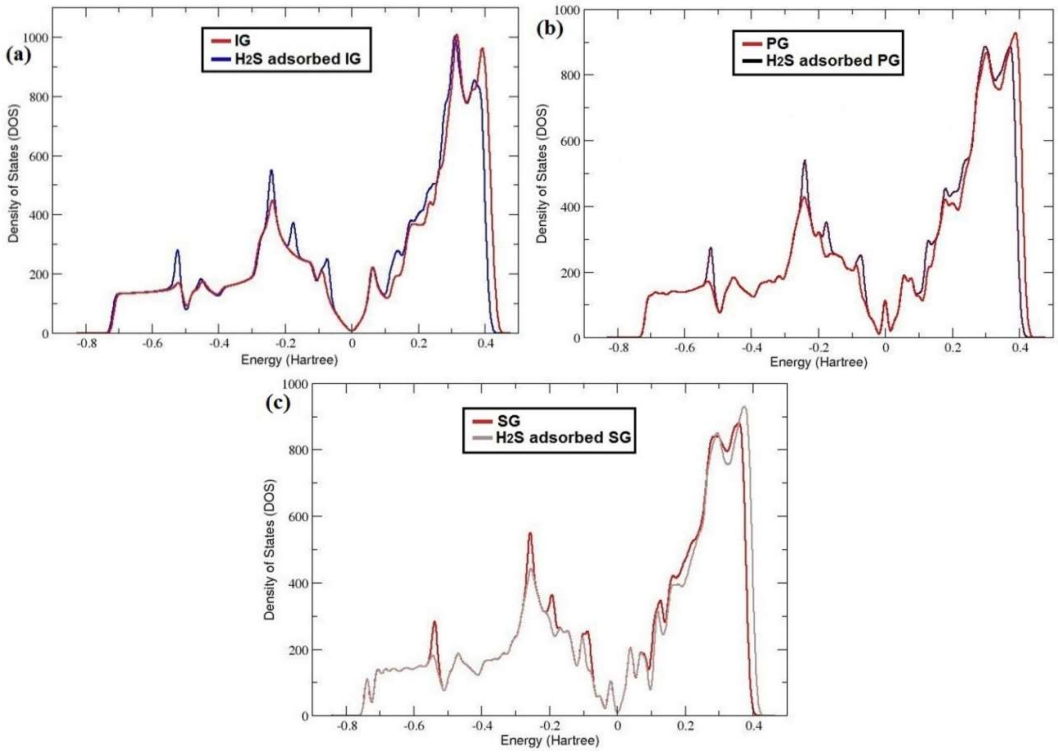

Figure 6.8 The DOS of **(a)** IG and H_2S adsorbed IG **(b)** PG and H_2S adsorbed PG and **(c)** SG and H_2S adsorbed SG

The suggested weak interactions between IG, PG and SG and H_2S molecule from the calculations of adsorption energies are also evident in their DOS structures. The DOS structures show little change near E_F after H_2S adsorption and the DOS of H_2S on IG, PG and SG systems are similar to that of IG, PG and SG respectively. The observed overlapping of the DOS profiles of SG and H_2S adsorbed SG system are similar to that reported in other studies [354]. These results show that the adsorption of H_2S on IG, PG and SG systems would not result in dramatic changes in their electrical conductivities and hence IG, PG and SG are not sensitive to the presence of H_2S molecule.

6.3.4.2 N_2O on graphene

Table 6.5 shows the results from the Hirshfeld charge distribution analysis of BG, NG, SiG, PG, GG, CG and MG sheets before and after N_2O adsorption. The charge states of the dopant atoms, three nearest carbon atoms around the dopant atom (C_1, C_2 and C_3) and the adsorbed N_2O molecule are presented in Table 6.5. In BG, NG, SiG and PG, the charge state of the dopant atom and the C neighbours do not show significant changes after N_2O adsorption. These results indicate that there is negligible charge transfer between these doped graphene systems and N_2O molecule. But when N_2O molecule is adsorbed on the top site of GG, the three carbon atoms surrounding the Ga atom attain electrons and the Ga atom loses valence electrons, which suggests that a chemical bond is formed between Ga and N_2O molecule.

Upon N_2O adsorption on both CG and MG, it was found that the charge state of both Cr and Mn atoms reduce significantly. For N-end adsorbing on CG and MG, the carbon neighbours loses electrons. For the scheme of N_2O adsorbed on CG and MG through the O-end, both C_1 and C_2 neighbours around the Cr and Mn-dopants loses electronic charge, whereas the third C neighbour attain more electrons (Table 6.5). Thus, the adsorption of N_2O on CG and MG result in significant change in the charge state of the dopant atoms, which could be attributed to the charge transfer between the Cr- or Mn-dopant and the N_2O molecule. These results imply that a chemical bond exists in the region between N_2O and the Cr- and Mn-dopants.

The band structures of N_2O adsorbed on GG, CG and MG systems are shown in Figure 6.9 (a)-(c). N_2O-adsorbed GG system exhibit a band gap of 0.218 eV (Figure 6.9 (a)) and on comparing with band structure of GG before N_2O adsorption, there is a small reduction in band gap of about ~0.020 eV after N_2O adsorption. In the case of N_2O adsorbed on CG and MG systems, the observed band gaps are 0.278 eV (Figure 6.9 (b)) and 0.429 eV (Figure 6.9 (c)) respectively. On comparing the band gap in MG before and after N_2O adsorption, it was

observed that the band gap has increased by ~0.044 eV, upon N_2O adsorption. Thus, it could be concluded that the electronic structures of GG and MG are sensitive to N_2O adsorption.

The adsorption of N_2O on CG opens up an energy band gap in graphene due to the strong interactions between Cr and the adsorbed N_2O molecule (Figure 6.9 (b)). These results illustrate that N_2O adsorption strongly influences the electronic properties of CG.

To further investigate the effect of N_2O adsorption on the electronic structures of GG, CG and MG systems, the electronic DOS before and after N_2O adsorption were calculated and are presented in Figure 6.10 (a)-(c). For N_2O adsorbed on GG *via* N-end, as shown in Figure 6.10 (a), a small peak of N_2O appears at the Fermi level, which indicates that 2*p* orbitals of N_2O take part in the formation of N-Ga bond [54]. The obtained DOS profile of N_2O adsorbed GG system and that reported in a similar study [54] are in good agreement. The increase in the DOS of GG above E_F after N_2O adsorption is expected to increase the electrical conductivity of GG.

Table 6.5 Hirshfeld charge distribution analysis of the dopant atom, three C atoms around the doped atom and the adsorbed N_2O molecule on the surface of BG, NG, SiG, PG, GG, CG and MG sheets[a]

System	C_1	C_2	C_3	B	N	Si	P	Ga	Cr	Mn	N_2O
IG	0	0	0	-	-	-	-	-	-	-	-
BG	-0.061	-0.061	-0.061	0.023	-	-	-	-	-	-	-
NG	0.045	0.045	0.045	-	0.030	-	-	-	-	-	-
SiG	-0.084	-0.084	-0.084	-	-	0.205	-	-	-	-	-
PG	-0.046	-0.046	-0.046	-	-	-	0.172	-	-	-	-
GG	-0.028	-0.028	-0.028	-	-	-	-	0.020	-	-	-
CG	-0.067	-0.067	-0.076	-	-	-	-	-	0.327	-	-
MG	-0.037	-0.037	-0.037	-	-	-	-	-	-	0.151	-
N_2O-BG	-0.061	-0.061	-0.065	0.018	-	-	-	-	-	-	0.015
N_2O-NG	0.044	0.044	0.041	-	0.028	-	-	-	-	-	0.011
N_2O-SiG	-0.085	-0.085	-0.088	-	-	0.222	-	-	-	-	0.007
N_2O-PG	-0.046	-0.046	-0.046	-	-	-	0.170	-	-	-	-0.003
N_2O-GG	-0.033	-0.033	-0.040	-	-	-	-	0.006	-	-	0.139
N-end N_2O-CG	-0.062	-0.062	-0.055	-	-	-	-	-	0.277	-	-0.219
O-end N_2O-CG	-0.052	-0.052	-0.100	-	-	-	-	-	0.303	-	-0.198
N-end N_2O-MG	-0.025	-0.025	-0.022	-	-	-	-	-	-	0.064	-0.132
O-end N_2O-MG	-0.035	-0.035	-0.040	-	-	-	-	-	-	0.084	0.098

[a] A negative sign indicates electrons gained, whereas positive sign implies electron lost by the atom (the unit of charge is electron)

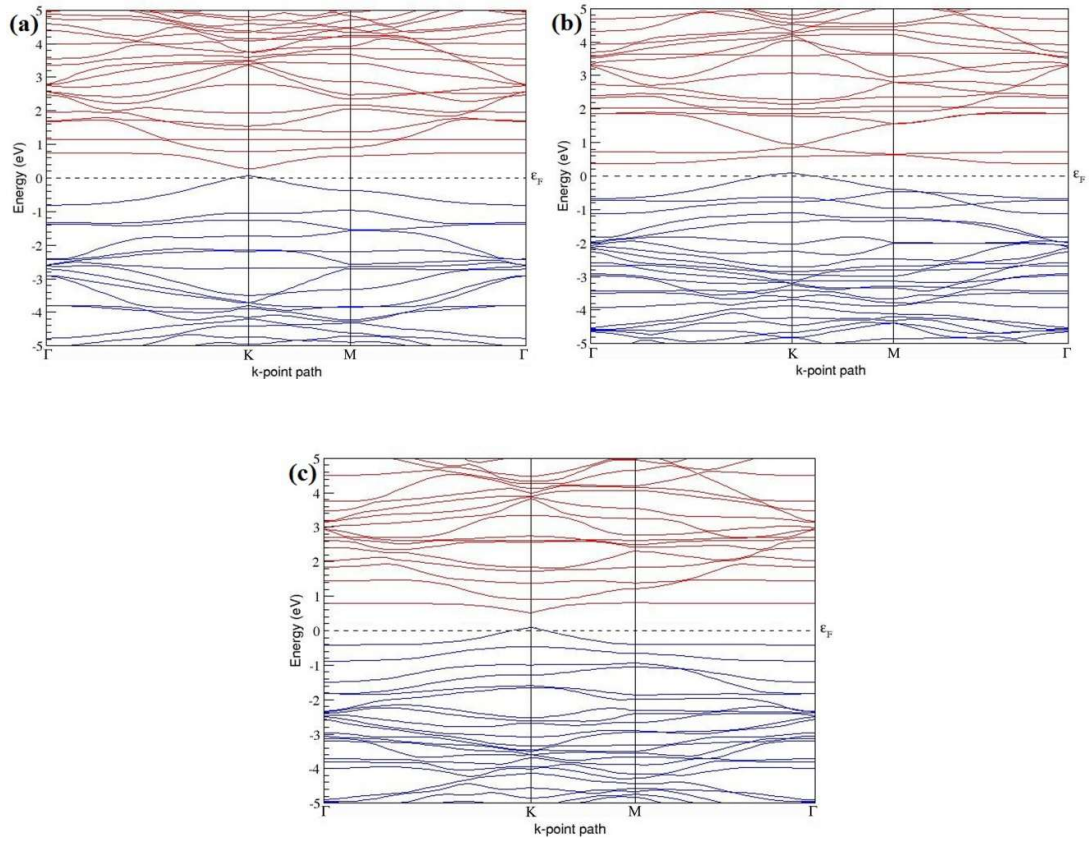

Figure 6.9 Electronic band structures of **(a)** N_2O adsorbed GG **(b)** N_2O adsorbed CG and **(c)** N_2O adsorbed MG

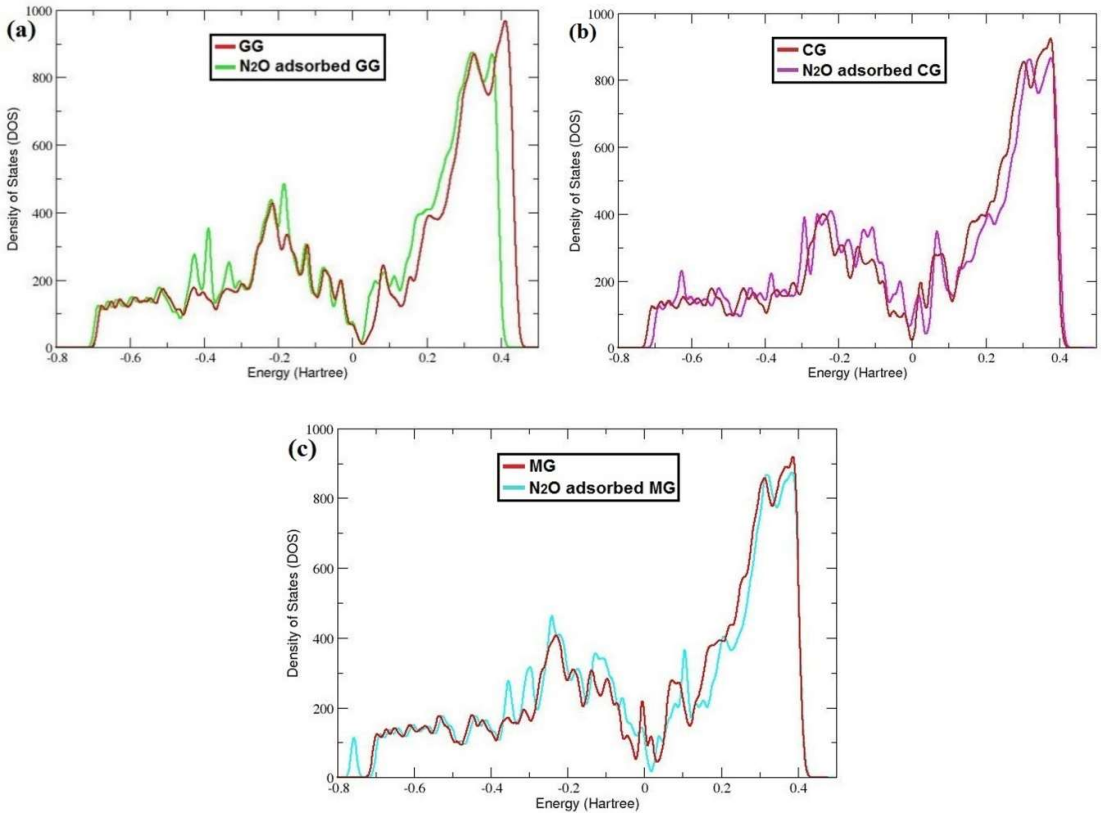

Figure 6.10 The DOS of **(a)** GG and N_2O adsorbed GG **(b)** CG and N_2O adsorbed CG and **(c)** MG and N_2O adsorbed MG

The DOS of CG and MG after N_2O adsorption have changed significantly compared to that of CG (Figure 6.10 (b)) and MG (Figure 6.10 (c)) due to the much stronger interactions between CG or MG and N_2O molecule. The adsorption of N_2O on CG and MG causes the major band features to shift towards higher energy which results in shifting of E_F towards lower energy. The DOS profiles of N_2O adsorbed CG and MG systems show that the chemisorbed N_2O on CG and MG will give rise to dramatic changes in the electrical conductivities of CG and MG sheets. These results illustrate that CG and MG are more likely to be become good candidates as N_2O gas sensors.

6.4 Summary

The adsorption properties of H_2S on IG, PG and SG sheets have been investigated using first-principles DFT method to study the effect of P and S dopants on the reactivity of graphene towards H_2S molecule. First-principles studies have also been carried out to analyze the adsorption of N_2O on intrinsic, heteroatom-doped (B, N, Si, P, Ga, Cr and Mn) graphene sheets.

6.4.1 Outcome

The structural and electronic properties of IG, PG and SG are found to be insensitive to the adsorption of H_2S. The presence of P and S atoms has negligible effect on the H_2S gas sensing properties of graphene. H_2S molecule is found to be physisorbed on PG and SG sheets with small adsorption energies and long binding distances. The Hirshfeld charge distribution analysis of the structures also showed negligible charge transfer between H_2S and IG or doped graphene sheets. The electronic band structures and DOS of PG, SG before and after H_2S adsorption indicate that H_2S adsorption would not result in significant change in the electrical conductivities of PG and SG. It was observed that the local curvature induced by P and S doping resulting from the larger size of the dopant than that of carbon, does not enhance the reactivity of graphene to H_2S. From the obtained results, it could be suggested that graphene doped with P and S atoms are not suitable for the detection of H_2S gas.

The stable adsorption geometries and adsorption energies of N_2O on intrinsic, heteroatom-doped (B, N, Si, P, Ga, Cr and Mn) graphene sheets are obtained on the basis of DFT calculations. The calculations indicate that IG, BG, NG, SiG and PG are not sensitive for N_2O molecule, due to weak interactions. In contrast, GG was found to be sensitive towards N_2O molecule, due to the strong interaction of N_2O with Ga-dopant. CG and MG show chemisorption of N_2O on their surface with comparatively high adsorption energies and short binding distances. The charge distribution analysis, band structure and DOS plots show that

the electronic properties of GG, CG and MG are sensitive to the adsorption of a single N_2O molecule. The results also indicate that CG and MG are suitable sensing materials for the detection of N_2O gas.

6.4.2 Applications

The observed high sensitivity of CG and MG towards N_2O indicate that both CG and MG can be used as novel gas sensors that can detect the presence of N_2O, which helps in controlling the global warming effects and protecting the stratospheric ozone-layer.

6.4.3 Limitations

This work is limited to intrinsic and graphene doped with B, N, Si, P, S, Ga, Cr and Mn atoms. In this work, the adsorption of H_2S on intrinsic and graphene doped with P and S atoms has been investigated. The effect of other dopant atoms such as Cr and Mn atoms on the H_2S gas sensing properties of graphene has not been considered. The work also focuses on the analysis of the adsorption of N_2O on intrinsic and graphene doped with B, N, Si, P, S, Ga, Cr and Mn atoms. The work can be extended to graphene doped with other transition metal atoms such as Fe, Co, Ni, Cu, Zn, Ag, Au etc. for analysing the N_2O gas sensing properties of these transition metal doped graphenes. The work only identified the best suitable dopants on graphene for developing highly sensitive N_2O sensors out of the considered dopants. The N_2O sensing response has not been optimized for high selectivity. The influence of atmospheric constituents on the properties of these doped graphenes need to be investigated for realizing their potential applications as N_2O gas sensors in air.

Graphene possess many interesting features such as room-temperature half integer quantum Hall effect [3, 65], high charge carrier mobility even at high carrier concentrations [64], finite electrical conductivity even at zero charge carrier concentration [5], massless relativistic carriers [2] and ballistic transport on submicrometer level even at room temperature [66], which make it an excellent candidate for applications in electronics [9, 67]. These peculiar physical properties of graphene arise from its unique zero energy band gap with linear energy-momentum relation around the Dirac point [296, 363]. But the minimum conductivity of graphene [5] is a major limitation for enabling graphene-based electronics. The lack of inherent band gap in the electronic structure of pure graphene, makes it impossible to turn off devices such as *p-n* junction diodes, FETs and limits its applications in other energy-related devices such as supercapacitors, solar cells, fuel cells etc. In order to exploit the potential of graphene for electronics, a sizeable band gap should open up in graphene. Until now, various approaches such as application of an external electric field [68], chemical functionalization

[69], use of GNRs [70], doping with heteroatoms etc. [72-75, 77-84] have been proposed for opening a band gap in graphene. Among these, substitutional doping is suggested to be the most effective method for modifying the electronic properties of graphene, due to the strong dependency of the material properties on the structure. This method is described in detail in chapter 7.

CHAPTER 7

ENERGETIC STABILITIES, STRUCTURAL AND ELECTRONIC PROPERTIES OF GRAPHENE DOPED WITH BORON AND NITROGEN ATOMS

7.1 Introduction

Doping of graphene with other elements has proved to be an effective functionalization technique that would open the zero energy band gap in IG without significant degradation of other favourable features of graphene. Among various dopant atoms, B and N atoms have got significant research attention being the nearest neighbours to carbon that provide strong probability of entering the graphene lattice and due to the electron acceptor and donor nature of B and N atoms that produces *p*-type and *n*-type graphene respectively. The *p*-type and *n*-type graphene sheet produced by B- and N-doping could be employed for the fabrication of complementary devices in future graphene-based electronic circuits [77-79, 81]. As the introduction of dopants into the graphene lattice could also lead to important modifications of physical and chemical properties, this could be tailored for developing various graphene-based devices with applications in energy storage [219, 364-366], gas storage [367-369] etc.

There have many reports on band gap engineering of graphene using substitutional doping [72-75, 77, 78, 80, 82, 84, 207, 370, 371]. For instance, Wu *et al.* investigated the geometry, electronic structure and magnetic properties of graphene doped with light non-metallic atoms such as B, N, O and F [75]. An *ab initio* study on the band gap opening in graphene by single B- and N-atom doping in 8, 18, 32 and 50 host C atoms has also been reported [77]. All these works on doped graphene systems have shown that dopant atoms modify the electronic band structure of graphene [78] by introducing an energy gap so that the behaviour of graphene changes from semi-metallic to semiconducting. But one B- and N-atom doping in 3N × 3N (where N is an integer) graphene supercells have shown zero band gap at the Dirac point [77, 80], whereas in the case of one B- and N-atom doping in the (3N-1) × (3N-1) and (3N+1) × (3N+1) supercells of IG, there is a band gap which can be tunable by the dopant concentration [80]. Zhou *et al.* discovered an interesting 3N rule for periodically doped graphene sheets [80], which suggests that when the primitive cell is 3N × 3N, the doped graphene has a zero gap or neglectable gap and the properties of doped graphene can be predicted by their primitive cell sizes [80].

The effect of doping graphene with B and N concentrations varying from 2% to 12% (simulated by varying the number of dopants from one to six in 50 host atoms) on the geometry and electronic structure of graphene has been systematically analyzed by Rani and Jindal [78]. They observed a dependence of the band gap not only on the concentration of dopants, but also on the position of dopant atom in the graphene sheet. The results showed a maximum band gap upon placing the dopants at the same sublattice locations and minimum band gap upon placing the dopants at alternate sublattice locations of graphene [78]. Another study presented the electronic and magnetic properties of graphene doped with N atoms and analyzed the dependence of magnetic moments and band gaps in graphene on N-substitutional doping configurations by considering two N atoms in graphene supercells containing 8, 18 and 32 C atoms [84].

Despite all the above works, a systematic analysis of the structural and electronic properties of N-doped graphene with two N-substitutional dopants in 3N × 3N graphene supercells by considering different doping configurations has not been reported. A similar study on B-doped graphene with more than one dopant in 3N × 3N graphene supercells has also still not appeared in the literature.

The atomic structures, energetic stabilities and electronic properties, specifically the band structures of graphene doped with B and N atoms in 8, 18, 32 and 72 host C atoms are investigated in this chapter. As B and N atoms can be placed at C sites of the crystal lattice in many different configurations, several B- and N-substitutional dopant sites in the graphene sheet are analyzed. The effect of B- and N-doping on the structural and electronic properties of graphene is analyzed by varying the dopant concentrations from 1.39% to 25% and by considering different configurations for the same doping concentration. The dependence of the cohesive energy per atom on the doping concentration and the different doping configurations are also studied to understand the stabilities and to compare the energetics of the B- and N-doped systems. Fourteen dopant concentrations between 1.39% and 25% are considered for the study [372].

7.2 Computational Details

The GGA XC functional in the PBE form [361] is adopted in structural optimization and electronic structure calculations of both IG, different doped graphenes. Norm-conserving Troullier-Martins type pseudopotentials [313] are used for describing the electron-ion interactions. The energy convergence criterion is chosen to be ~10 meV/atom. Plane-wave basis set with converged cutoff energy of 816 eV are used in the calculations. The sampling

of Brillouin zone is done using the k-point mesh generated by the MP scheme [328]. Converged k-point grids corresponding to a 24 × 24 × 1 grid for a graphene unit cell are used for different graphene supercells. For all systems, the relaxation of basis vectors and atomic coordinates are done by minimizing the total energy. Structural optimization has been conducted using the BFGS minimization [329] until the residual forces on atoms are lower than 0.0025 eV/Å.

7.2.1 Model building

A single layer graphene sheet is modelled using four different supercell sizes *i.e.*, 2 × 2 ((3N-1) × (3N-1), where N=1) supercell with 8 C atoms, 3 × 3 (3N × 3N, where N=1) supercell with 18 C atoms, 4 × 4 ((3N+1) × (3N+1), where N=1) supercell with 32 C atoms and 6 × 6 (3N × 3N, where N=2) supercell with 72 C atoms where the distance between the adjacent graphene layers along the perpendicular direction is taken as 10 Å to avoid the interlayer interactions due to the periodic boundary conditions. B- and N-doped graphenes are simulated by replacing the C atom in the supercell structure by a B or N atom and by choosing the corresponding pseudopotentials. B- and N-doping concentrations from 1.39% to 25% are modelled through the substitution of one and two C atoms in the 2 × 2 supercell by dopant atoms which corresponds to 12.5% and 25% dopant concentrations, respectively; the substitution of one, two, three and four C atoms in the 3 × 3 supercell by dopant atoms which corresponds to 5.56% 11.11%, 16.67%, and 22.22% dopant concentrations, respectively; the substitution of one and two C atoms in the 6 × 6 supercell by dopant atoms which corresponds to 1.39% and 2.78% dopant concentrations, respectively; the substitution of one, two, three, four, five and six C atoms in the 4 × 4 supercell by dopant atoms which corresponds to 3.13%, 6.25%, 9.38%, 12.5%, 15.63% and 18.75% dopant concentrations, respectively.

7.2.2 Cohesive energy

In all cases, first the geometries of the B- and N-doped systems were optimized, and then the cohesive energy per atom (E_{coh}) is calculated as [78]:

$$E_{coh} = \frac{(E_{tot} - n_i E_i)}{n}, i = C, B, N \quad (7.1)$$

where E_{tot} and E_i represent the total energies of the considered doped system and of the individual elements present within the doped system. The total energies of the individual elements (C, B or N) are calculated by defining a large supercell and adding the element (C, B or N) at (0, 0, 0). n is the total number of atoms present in the system and n_i is the total

number of species i present in the configuration. The values of E_{coh} indicate the energetic stability of the systems. The lesser the value, the more stable the system is.

Finally, electronic band structures are computed for the optimized doped structures from which the widths of the band gap are determined. The dependence of band gap and the cohesive energy per atom on the concentration and position of dopant atoms are explained in the following section.

7.3 Results and Discussions

7.3.1 Structural and Electronic Properties of IG sheets

Upon structural optimization of IG, the lattice constant and the C-C bond length were observed to be 2.458 Å and 1.42 Å (Figure 7.1 (a)-(d)), which are in agreement with the reported values of 2.46 Å [331] and 1.421 Å [8, 289, 331] respectively. The relaxed geometries and band structures of 2 × 2, 3 × 3, 4 × 4 and 6 × 6 graphene supercells obtained from the calculations are shown in Figure 7.1 (a)-(d) and Figure 7.2 (a)-(d) respectively.

In the band structures of 2 × 2 and 4 × 4 graphene supercells, the top of the valence band and the bottom of the conduction band degenerate at the K-point as seen in Figure 7.2 (a), (c)), whereas in 3 × 3, and 6 × 6 supercells, the degeneracy is observed at the Γ-point as presented in Figure 7.2 (b), (d)). This agrees well with earlier reports that the Dirac point moves into the Γ-point, when the supercells are dimensions of three (3 × 3, 6 × 6, 9 × 9 supercells etc.) [80].

After successful reproduction of the structures and the electronic band structures of IG, IG is doped with 14 different concentrations of B and N atoms. The investigation of the change in the geometries and electronic structures of graphene upon doping with varying B- and N-atom concentrations and the analysis of the band gap for each doping concentration and for different dopant sites of the same doping concentration are carried out as described below.

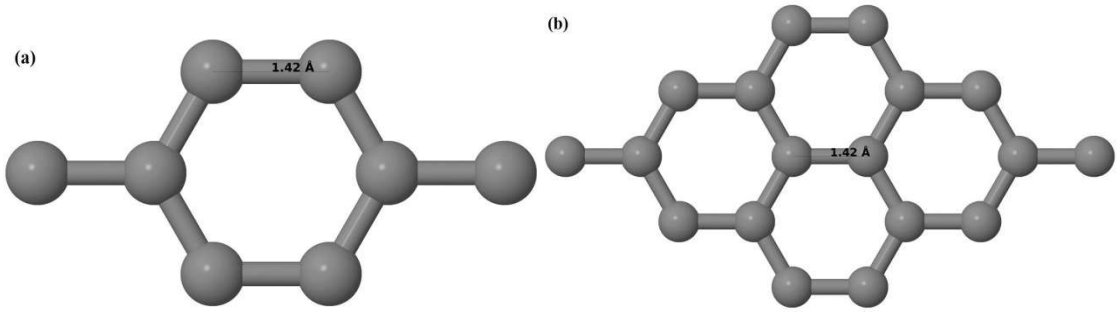

Figure 7.1 (a)-(b) Optimized structures of **(a)** 2 × 2 and **(b)** 3 × 3 supercells of IG, the carbon atoms are shown in grey colour.

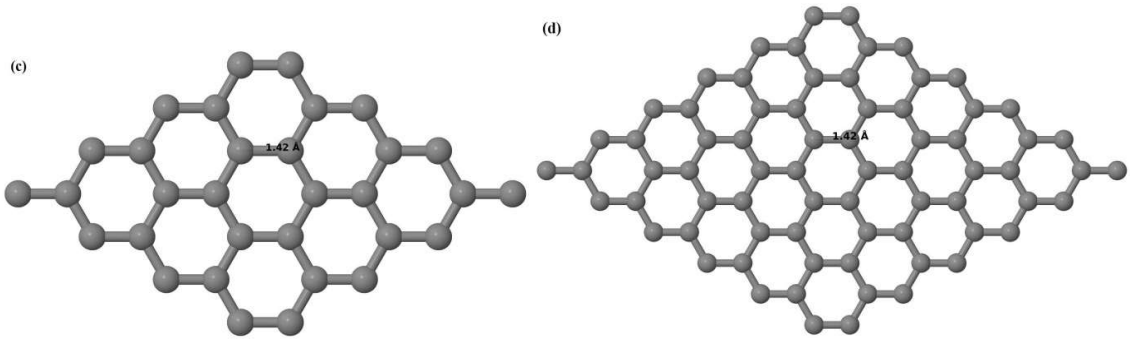

Figure 7.1 (c)-(d) Optimized structures of **(c)** 4 × 4, and **(d)** 6 × 6 supercells of IG, the carbon atoms are shown in grey colour.

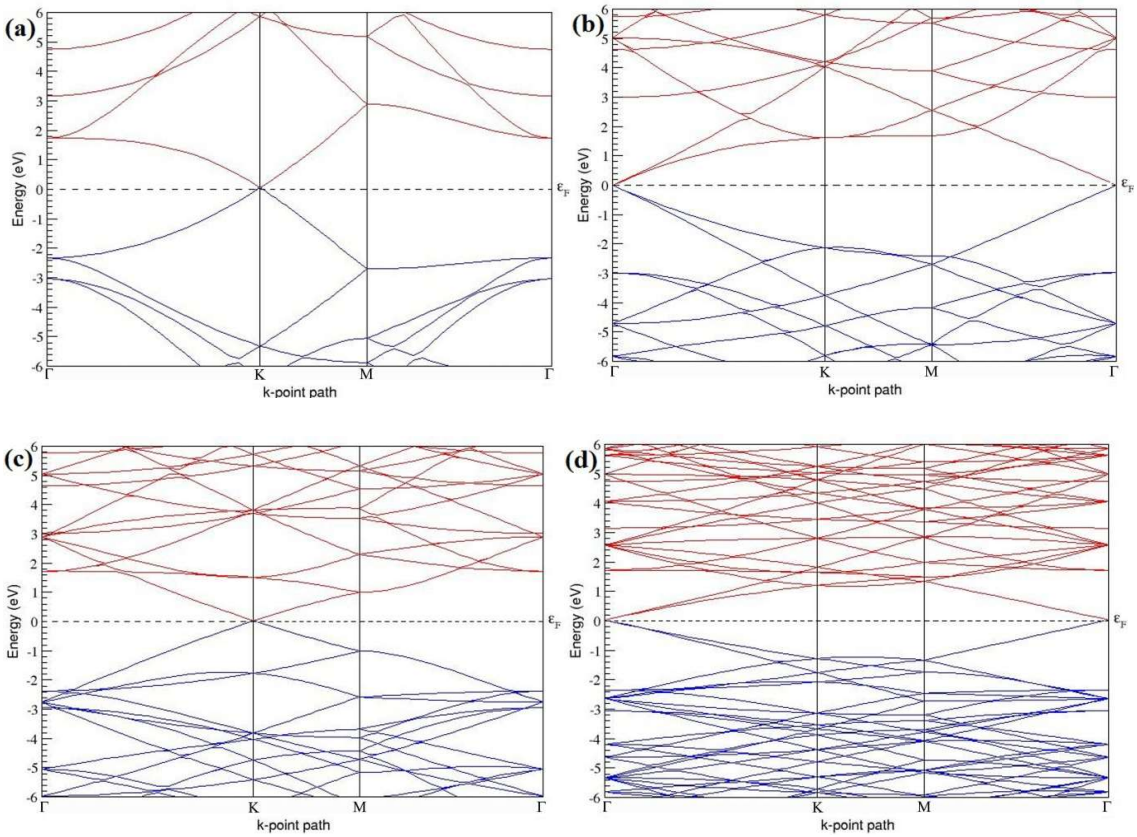

Figure 7.2 Band structures of **(a)** 2 × 2, **(b)** 3 × 3, **(c)** 4 × 4, and **(d)** 6 × 6 supercells of IG.

7.3.2 B-doped graphene

7.3.2.1 B-doped graphene system with one B atom per supercell

Here one B substitutional dopant is considered in 2 × 2, 3 × 3, 4 × 4 and 6 × 6 graphene supercells. Upon structural optimization of all graphene supercells doped with one B atom, it was observed that the planar geometry of IG remains undisturbed (Figure 7.3 (a)-(d)) even after the introduction of B atom, as B also undergoes sp^2 hybridization like the other C atoms in the crystal lattice, which is in accordance with earlier results [75, 78]. The optimized lattice

constant increases from 2.458 Å to 2.464 Å, 2.471 Å, 2.482 Å and 2.514 Å for 6 × 6, 4 × 4, 3 × 3 and 2 × 2 supercells doped with one B atom (1.39%, 3.13%, 5.56%, 12.5% B concentrations) respectively. Since the atomic radius of B is larger than that of C, the lattice constant increases with increase in the B-doping concentration, showing agreement with previous reports [78].

Figure 7.3 (a)-(d) depict the optimized geometries of 2 × 2, 3 × 3, 4 × 4 and 6 × 6 graphene supercells doped with one B atom respectively. The large covalent radius of B compared to that of C results in the expansion of the C-B bond length [75, 78] to 1.5 Å for one B doping in 2 × 2 and 3 × 3 supercell sizes (Figure 7.3 (a),(b)), whereas in 4 × 4 and 6 × 6 supercells, the C-B bond length got extended to 1.49 Å (Figure 7.3 (c), (d))) [75, 78] from the ideal C-C bond length of 1.42 Å. The C-C bond lengths adjacent to the B-dopant got reduced from 1.42 Å to 1.41 Å in 3 × 3 and 4 × 4 graphene supercells (Figure 7.3 (b), (c)), whereas in the case of 6 × 6 graphene supercell, it got reduced to 1.4 Å (Figure 7.3 (d)), in order to compensate for the long C-B bond in the crystal structure so as to retain the planar geometry. The observed reduction in the C-C bond length in the close proximity to the B-dopant agrees well with that reported in Ref. [78]. In larger supercells such as 4 × 4 and 6 × 6 graphene supercells, the C-C bond lengths far away from the dopant are found to be 1.42 Å, same as that in IG.

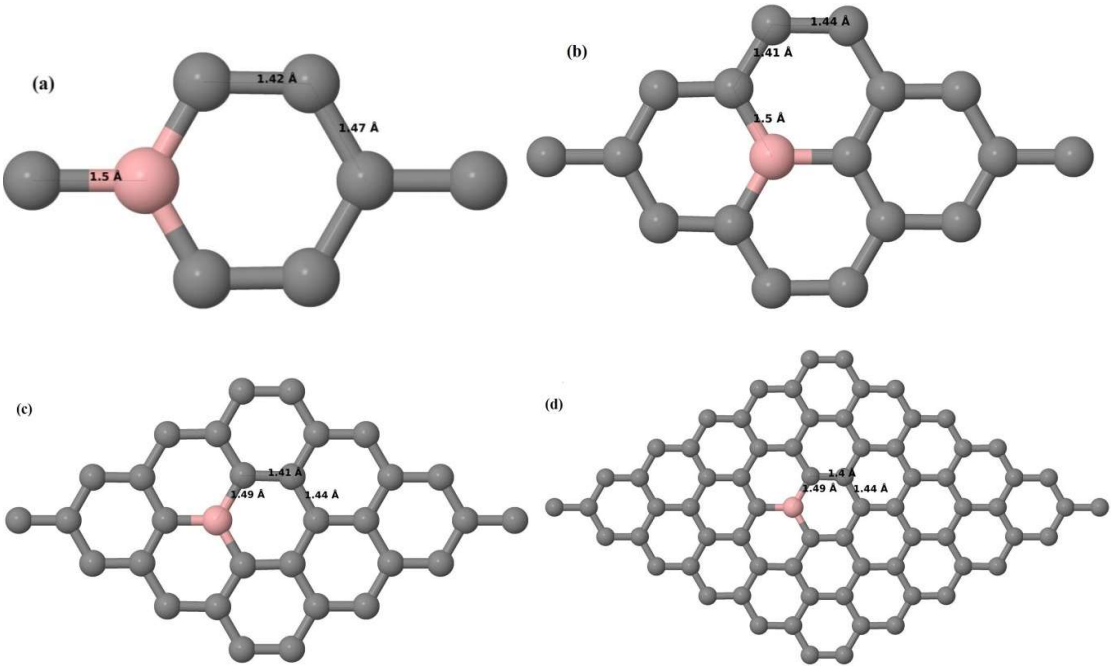

Figure 7.3 Optimized structures of various graphene systems doped with one B atom, the B atoms are shown in rose colour; **(a)** 2 × 2 graphene supercell with 12.5% B concentration, **(b)** 3 × 3 graphene supercell with 5.56% B concentration, **(c)** 4 × 4 graphene supercell with 3.13% B concentration, **(d)** 6 × 6 graphene supercell with 1.39% B concentration.

The calculated cohesive energies per atom of the relaxed geometries of graphene systems doped with one B atom are presented in Table 7.1. Figure 7.4 (a)-(d) present the band structures computed for the optimized structures of different graphene systems doped with one B atom shown in Figure 7.3 (a)-(d). Since the planar geometry of graphene is well preserved even after one B doping, the linear energy dispersion remains unaltered along the high symmetry points of the Brillouin zone as seen in Figure 7.4 (a)-(d), similar to reported literature [75, 78]. Due to the symmetry breaking of the graphene sublattices by the introduction of the B atom, the band structures of 2 × 2 and 4 × 4 graphene supercells show a band gap of ~0.66 eV (Figure 7.4 (a)) and ~0.19 eV (Figure 7.4 (c)) at the Dirac point for one B atom doping (corresponding to 12.5% and 3.13% B concentrations) respectively. The present results are slightly greater that the values reported in Ref. [77], probably due to the variation in the employed computational method. The 3 × 3 and 6 × 6 graphene supercells doped with one B atom (corresponding to 5.56% and 1.39% B concentrations) do not show any band gap (Figure 7.4 (b) and (d)), which is found to be agreement with the zero band gap phenomenon observed in 3N × 3N graphene supercells [77, 80].

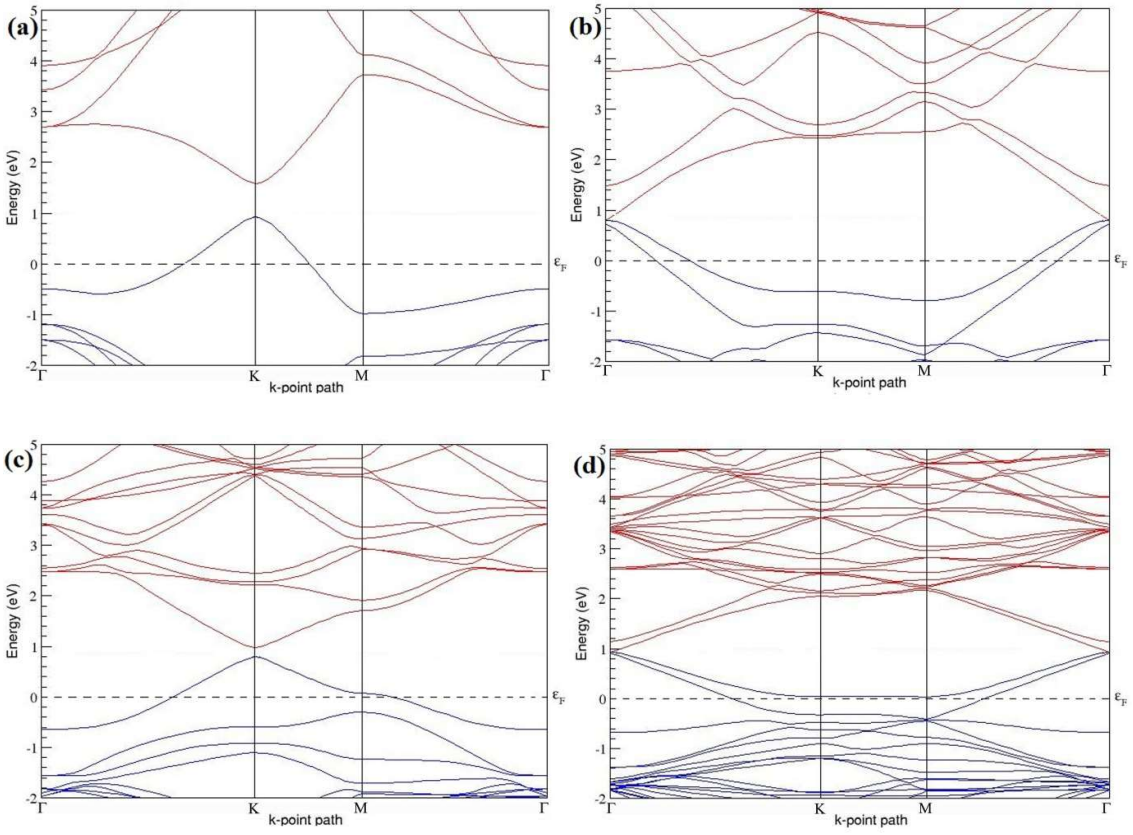

Figure 7.4 Band structures of graphene systems doped with one B atom corresponding to the optimized structures shown in **Figure 7.3 (a)-(d)**; **(a)** 2 × 2 graphene supercell with 12.5% B concentration, **(b)** 3 × 3 graphene supercell with 5.56% B concentration, **(c)** 4 × 4 graphene supercell with 3.13% B concentration and **(d)** 6 × 6 graphene supercell with 1.39% B concentration.

In general, the energy gap increases from ~0.19 eV to ~0.66 eV for 4 × 4 and 2 × 2 supercells doped with one B atom (3.13% and 12.5% B concentrations), respectively (Table 7.1).

Both 2 × 2 and 4 × 4 graphene supercells doped with one B atom exhibit *p*-type doping electronic properties with band gaps, whereas the 3 × 3 and 6 × 6 graphene supercells doped with one B atom show *p*-type doping properties with zero band gap [372].

Table 7.1 The B concentrations, cohesive energies and the band gap introduced for various supercells doped with one B atom.

Model	B Concentration (%)	E_{coh} (eV/atom)	Band gap (eV)
2 × 2	12.5	-8.795	0.658
3 × 3	5.56	-9.088	0
4 × 4	3.13	-9.197	0.190
6 × 6	1.39	-9.270	0

7.3.2.2 B-doped graphene system with two B atoms per supercell

As graphene's honeycomb lattice consists of two interpenetrating triangular sublattices as shown in Figure 7.5, several isomers of the same doping concentration are possible. A few isomers with configurations of three doping sites *i.e.* when all the dopant atoms are adjacent, when they are at same sublattice positions [78] (all in either sublattice "A" or in sublattice "B") and when they are at different sublattice positions (in sublattice "A" and "B") are only presented here for simplicity, as all possible doping configurations of any atomic doping concentration will fall under these three categories only. Hence, the cohesive energies and the band structures for the above mentioned geometries corresponding to the same doping concentration are also calculated to analyse the influence of the dopant sites on the stabilities and the band gap values.

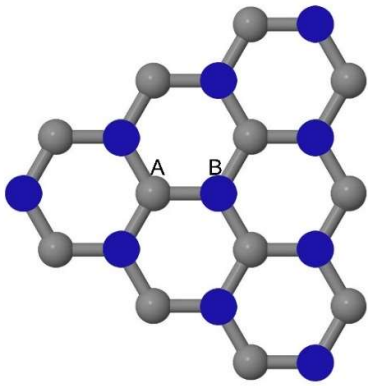

Figure 7.5 Schematic illustration of the honeycomb lattice of graphene. Atoms in sublattices A (B) points are shown in grey (blue) colour.

Here the substitution of two C atoms by two B atoms in 2 × 2, 3 × 3, 4 × 4 and 6 × 6 graphene supercells (Figure 7.6 (a)-(l)) are considered. Similar to graphene systems doped with one B atom, the graphene systems doped with two B atoms also retain the planar geometry of IG as seen in Figure 7.6 (a)-(l). The optimized lattice constant increases from 2.458 Å to 2.469 Å, 2.484 Å, 2.504 Å and 2.576 Å for 6 × 6, 4 × 4, 3 × 3 and 2 × 2 supercells doped with two B atoms (2.78%, 6.25%, 11.11%, 25% B concentrations) respectively, which also shows increase in lattice constant with increasing B-doping concentrations similar to that observed for graphene systems doped with one B atom.

Figure 7.6 (a)-(l) depict the optimized geometries of 2 × 2, 3 × 3, 4 × 4 and 6 × 6 graphene supercell doped with two B atoms. Three doping configurations of 2 × 2, 3 × 3, 4 × 4 and 6 × 6 supercells doped with two B atoms (corresponding to 25%, 11.11%, 6.25% and 2.78% B concentrations respectively) are considered with the dopant atoms at adjacent positions, (Figure 7.6 (a), (d), (g), (j)), same (Figure 7.6 (b), (e), (h), (k)), and alternate sublattice points (Figure 7.6 (c), (f), (i), (l)). The C-B bond length got expanded significantly (Figure 7.6 (a)-(l)) as compared to graphene systems doped with one B atom, due to the presence of two B atoms having bigger size compared to the other C atoms in the lattice, whereas the C-C bond length in the close proximity of the dopant got shortened from 1.42 Å to 1.41 Å or 1.4 Å or even to 1.39 Å in most of the optimized structures, based on the position of the B-dopants, in an attempt to the preserve the planar lattice structure.

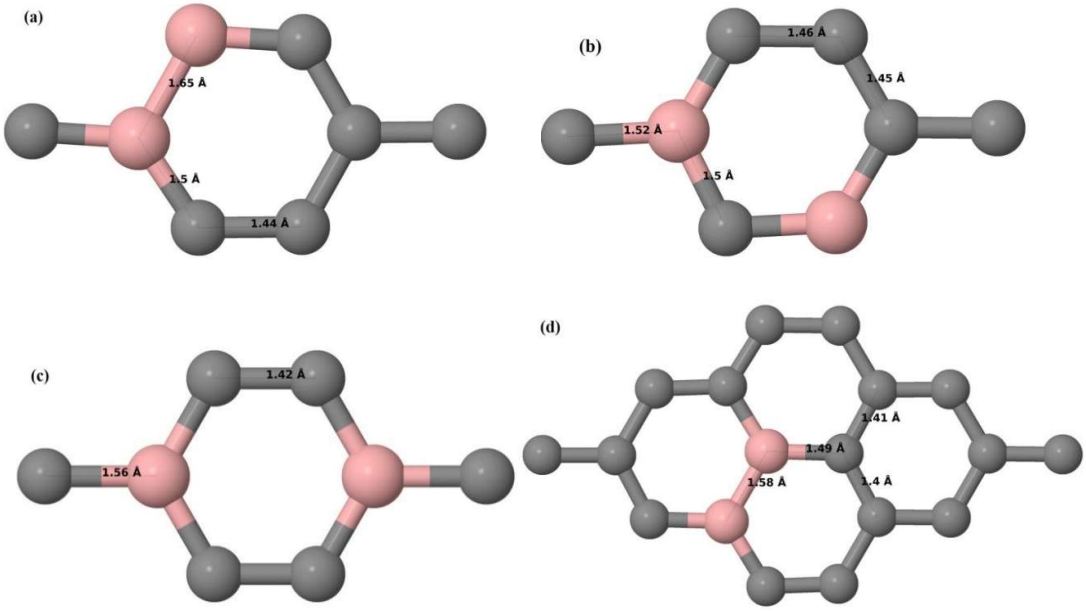

Figure 7.6 (a)-(d) Optimized structures of various graphene systems doped with two B atoms with different doping configurations, **(a), (b)** and **(c)** 2 × 2 graphene supercell with 25% B concentration, **(d)** 3 × 3 graphene supercell with 11.11% B concentration.

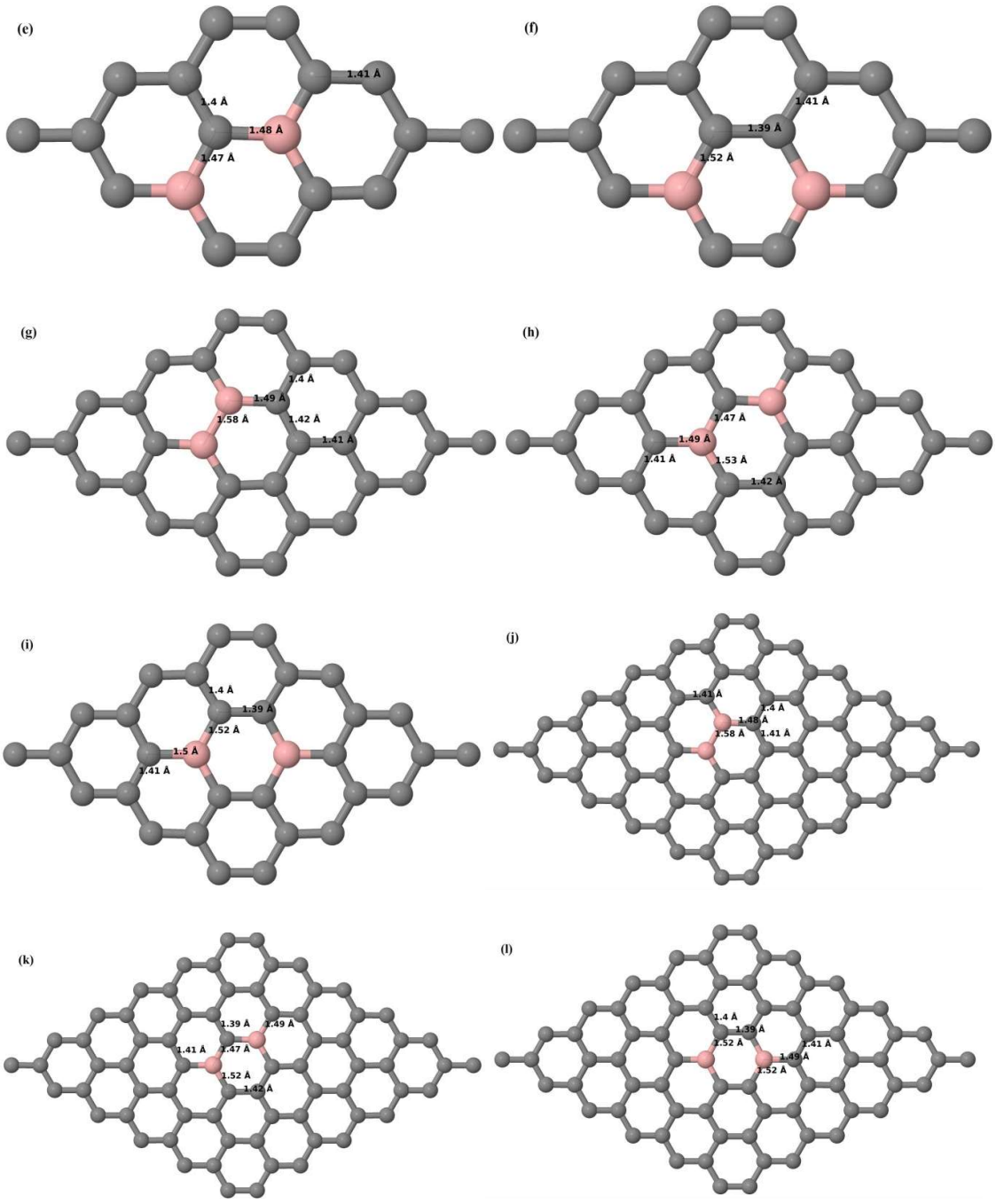

Figure 7.6 (e)-(l) Optimized structures of various graphene systems doped with two B atoms with different doping configurations, **(e)** and **(f)** 3 × 3 graphene supercell with 11.11% B concentration, **(g), (h)** and **(i)** 4 × 4 graphene supercell with 6.25% B concentration, **(j), (k)** and **(l)** 6 × 6 graphene supercell with 2.78% B concentration.

After obtaining the stable geometries, the cohesive energies are calculated for all the considered graphene systems doped with two B atoms and are listed in Table 7.2.

Figure 7.7 (a)-(l) present the band structures computed for the optimized structures of different graphene systems doped with two B atoms shown in Figure 7.6 (a)-(l). As seen in Figure 7.7 (a)-(l), the linear dispersion around the Dirac point is not completely destroyed but

an energy band gap opens in all cases except for graphene doped with two B atoms into 2 × 2 graphene supercell with dopant atoms at the alternate sublattice points (Figure 7.7 (c)). 2 × 2 graphene supercell doped with two B atoms (corresponding to 25% B concentration) show band gaps of ~0.49 eV (Figure 7.7 (a)) and ~1.28 eV (Figure 7.7 (b)), on placing the B atoms at adjacent and same sublattice positions respectively in graphene. B-doped graphene with 25% B concentration has a zero gap (Figure 7.7 (c)), when the B atoms are at alternate sublattice positions, due to the symmetry formed by the B atoms situated in two graphene sublattices ("A" and "B"). At 6.25% B concentration, band gaps of 0.13 eV (Figure 7.7 (g)), 0.375 eV (Figure 7.7 (h)) and ~0.05 eV (Figure 7.7 (i)) open up in graphene, when the B atoms are placed at the adjacent, same and alternate sublattice positions in graphene respectively.

The band structures of 3 × 3 and 6 × 6 graphene supercells doped with two B atoms are characterized by a non-zero band gap, which is different from the zero band gap behaviour observed for the 3 × 3 and 6 × 6 graphene supercells doped with one B atom. 3 × 3 graphene supercell doped with two B atoms (corresponding to 11.11% B concentration) exhibit band gaps of 0.265 eV (Figure 7.7 (d)), 0.274 eV (Figure 7.7 (e)) and ~0.05 eV (Figure 7.7 (f)) for the configurations with dopants at adjacent locations, same and alternate sublattice points in graphene respectively. Doping of graphene with 2.78% concentration of B results in band gap opening of 0.10 eV (Figure 7.7 (j)), ~0.11 eV (Figure 7.7 (k)) and 0.008 eV (Figure 7.7 (l)) respectively in graphene, upon placing the B atoms at adjacent, same and alternate sublattice sites in graphene. 2 × 2, 3 × 3, 4 × 4 and 6 × 6 graphene supercells doped with two B atoms have exhibited *p*-type semiconducting behaviours. 2 × 2 graphene supercell doped with two B atoms also exhibit *p*-type electronic behaviour, but does not show any band gap when the dopants are at alternate sublattice sites (Figure 7.7 (c)).

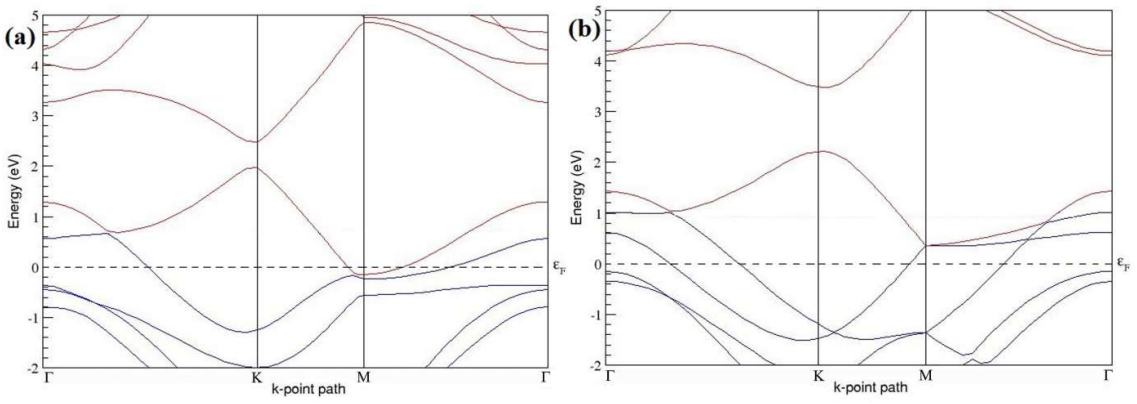

Figure 7.7 (a)-(b) Band structures of graphene systems doped with two B atoms corresponding to the optimized structures shown in **Figure 7.6 (a)** and **(b)** for 2 × 2 graphene supercell with 25% B concentration.

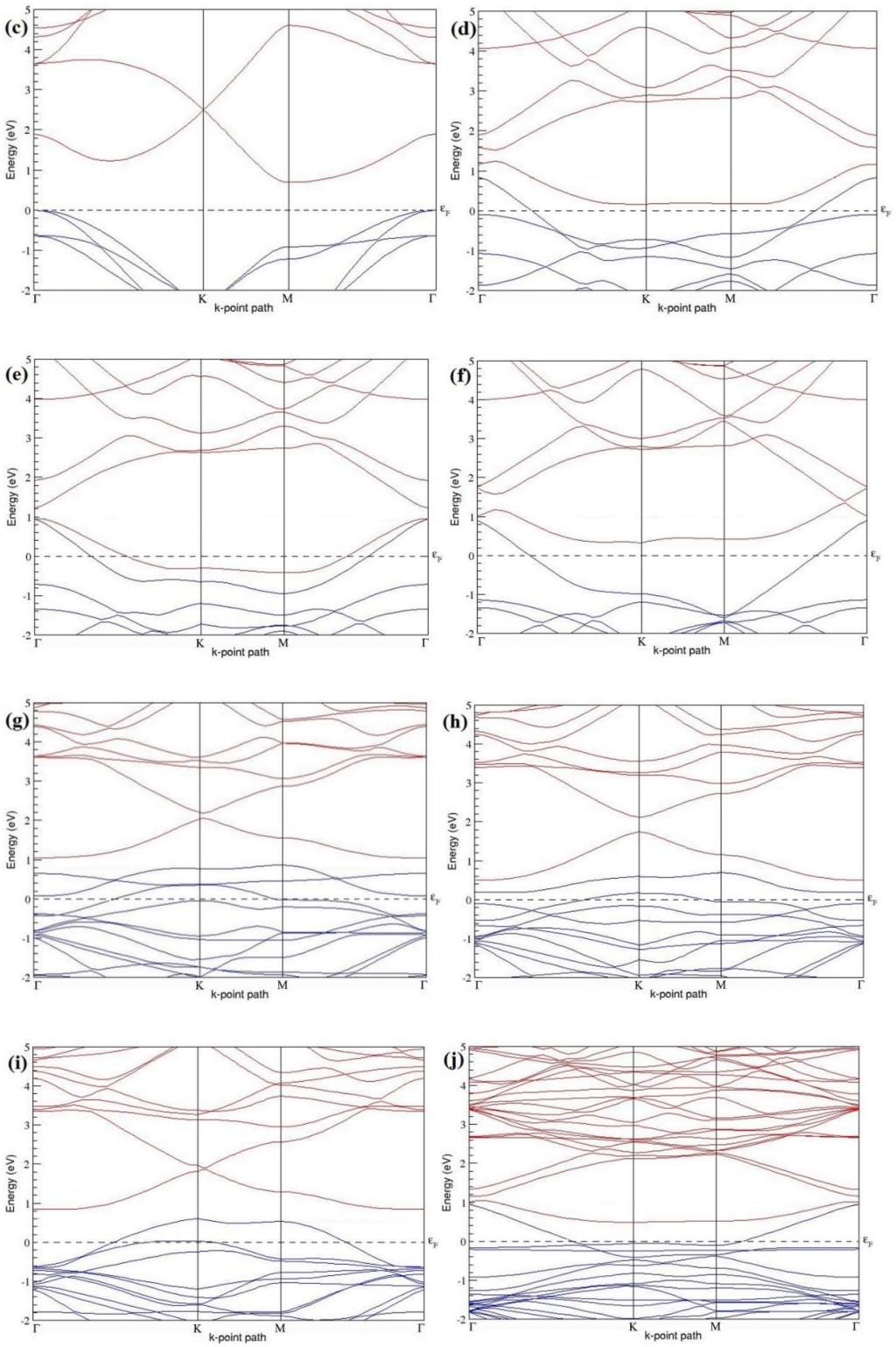

Figure 7.7 (c)-(j) Band structures of graphene systems doped with two B atoms corresponding to the optimized structures shown in **Figure 7.6 (c)-(j); (c)** for 2 × 2 graphene supercell with 25% B concentration, **(d), (e) and (f)** 3 × 3 graphene supercell with 11.11% B concentration **(g), (h) and (i)** 4 × 4 graphene supercell with 6.25% B concentration, **(j)** 6 × 6 graphene supercell with 2.78% B concentration

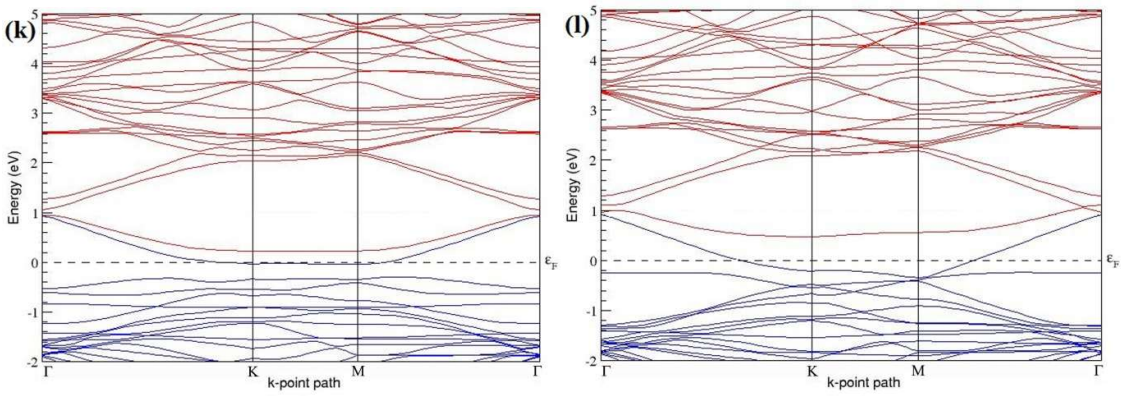

Figure 7.7 (k)-(l) Band structures of graphene systems doped with two B atoms corresponding to the optimized structures shown in **Figure 7.6 (k)** and **(l)** 6 × 6 graphene supercell with 2.78% B concentration.

The considered B concentrations, the doping configurations along with the selected sublattices, the calculated cohesive energies and the band gaps observed for all considered graphene systems doped with two B atoms are summarized in Table 7.2.

Table 7.2 The B concentrations, doping configurations with considered sublattice, cohesive energies and the band gap introduced for various supercells doped with two B atoms.

Model	B Concentration (%)	Configuration	Considered Sublattices for dopants	E_{coh} (eV/atom)	Band gap (eV)
2 × 2	25	Figure 7.6 (a)	"B" and "A" (adjacent)	-8.284	0.492
		Figure 7.6 (b)	Both in "B" (same)	-8.353	1.282
		Figure 7.6 (c)	"B" and "A" (alternate)	-8.493	0
3 × 3	11.11	Figure 7.6 (d)	"B" and "A" (adjacent)	-8.842	0.265
		Figure 7.6 (e)	Both in "B" (same)	-8.874	0.274
		Figure 7.6 (f)	"B" and "A" (alternate)	-8.921	0.046
4 × 4	6.25	Figure 7.6 (g)	"B" and "A" (adjacent)	-9.058	0.130
		Figure 7.6 (h)	Both in "B" (same)	-9.079	0.375
		Figure 7.6 (i)	"B" and "A" (alternate)	-9.095	0.047
6 × 6	2.78	Figure 7.6 (j)	"B" and "A" (adjacent)	-9.202	0.100
		Figure 7.6 (k)	Both in "B" (same)	-9.212	0.114
		Figure 7.6 (l)	"B" and "A" (alternate)	-9.219	0.008

7.3.2.3 B-doped graphene system with three B atoms per supercell

Here the substitution of three C atoms by three B atoms is considered in 3 × 3 and 4 × 4 graphene supercells. Similar to graphene systems doped with one and two B atoms, the planar lattice structure of graphene remains the same (Figure 7.8 (a)-(f)) even after the introduction of three B atoms. Figure 7.8 (a)-(f) present the relaxed geometries of 3 × 3 and 4 × 4 graphene supercells doped with three B atoms at adjacent, same and alternate sublattices respectively. After structural optimization, it was found that graphene structures doped with three B atoms at adjacent locations experience significant geometrical distortion (Figure 7.8 (a), (d)) due to the positioning of three B atoms in the same six-membered carbon ring, as compared to the other graphene systems doped with three B atoms. But still the three adjacent B atoms are seen to lie within the plane with large adjustments in the adjoining bond lengths, as presented in Figure 7.8 (a) and (d).

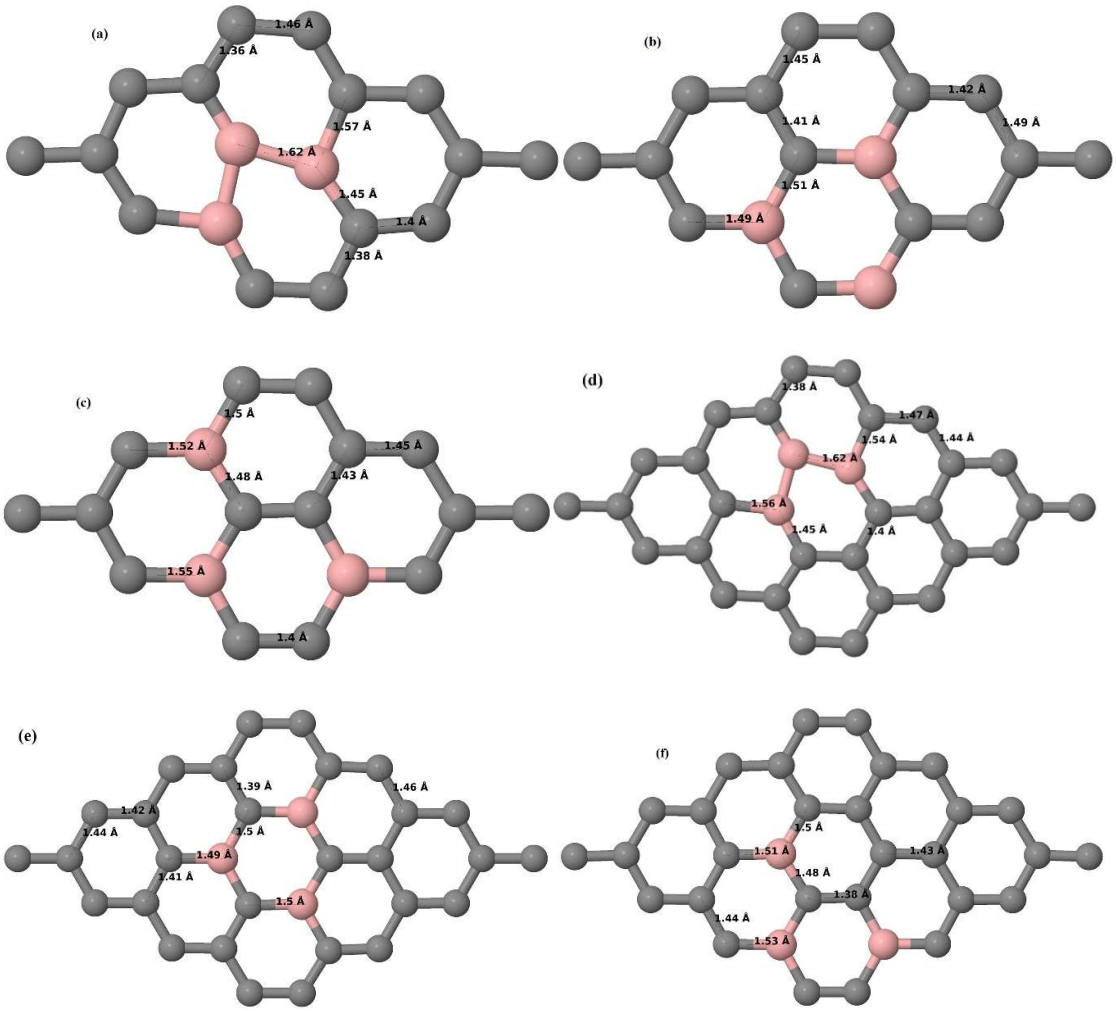

Figure 7.8 Optimized structures of various graphene systems doped with three B atoms with different doping configurations. **(a), (b)** and **(c)** 3 × 3 graphene supercell with 16.67% B concentration, **(d)**, **(e)** and **(f)** 4 × 4 graphene supercell with 9.38% B concentration.

The optimized lattice constant increases from 2.458 Å to 2.475 Å and 2.528 Å for 4 × 4 and 3 × 3 supercells doped with three B atoms (9.38% and 16.67% B concentrations) respectively, which indicates increase in lattice constant with doping concentration similar to that seen in graphene systems doped with one and two B atoms.

Figure 7.9 (a)-(f) present the band structures computed for the optimized structures of different graphene systems with three B atoms shown in Figure 7.8 (a)-(f). The band structures of both 3 × 3 and 4 × 4 graphene supercells doped with three B atoms show non-zero band gaps as seen in Figure 7.9. The linear energy dispersion at the Dirac point in the band structures of graphene systems doped with three B atoms is found to be greatly affected (Figure 7.9 (a), (d)) for those structures in which the B-substitutional dopants are placed at the adjacent positions (Figure 7.8 (a), (d)), which could be attributed to their highly distorted geometries. The observation of highly deformed band structures of B-doped graphene with odd number of dopants in adjacent positions is consistent with that reported in Ref. [78]. At 16.67% B concentration, the observed band gaps are ~0.03 eV (Figure 7.9 (a)) and ~0.11 eV (Figure 7.9 (c)), when the dopant atoms are placed at the adjacent positions and alternate sublattices respectively. The positioning of the three B atoms at same sublattice leads to opening of a large band gap of ~0.90 eV (Figure 7.9 (b)) at 16.67% B concentration. Graphene with 9.38% B concentration shows band gaps of 0.235 eV (Figure 7.9 (d)), ~0.57 eV (Figure 7.9 (e)) and ~0.16 eV ((Figure 7.9 (f)), for the doping configurations of adjacent, same and alternate sublattices respectively. Graphene with three B-doping atoms in 3 × 3 and 4 × 4 graphene supercells exhibit *p*-type semiconducting behaviours. Table 7.3 presents the models used, the B concentrations, considered doping configurations with sublattices, the calculated cohesive energies and the band gap introduced for all graphene systems doped with three B atoms.

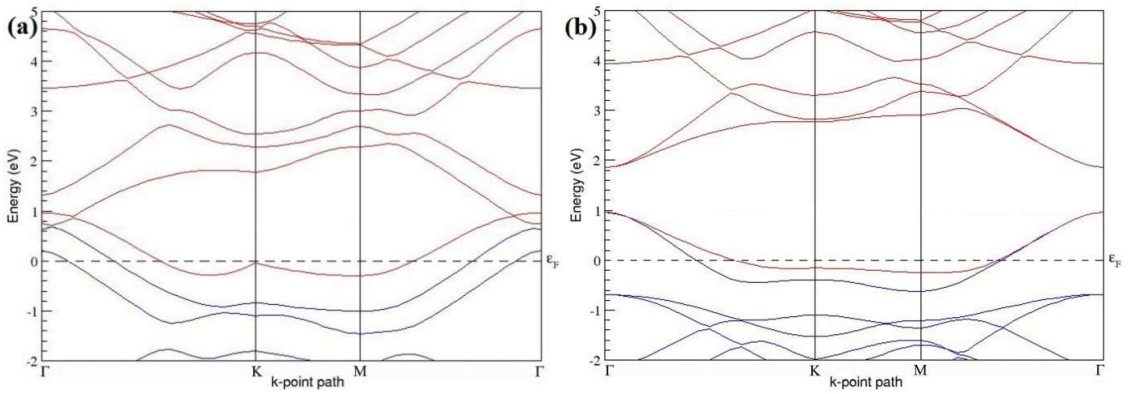

Figure 7.9 (a)-(b) Band structures of graphene systems doped with three B atoms corresponding to the optimized structures shown in **Figure 7.8 (a)** and **(b)** for 3 × 3 graphene supercell with 16.67% B concentration.

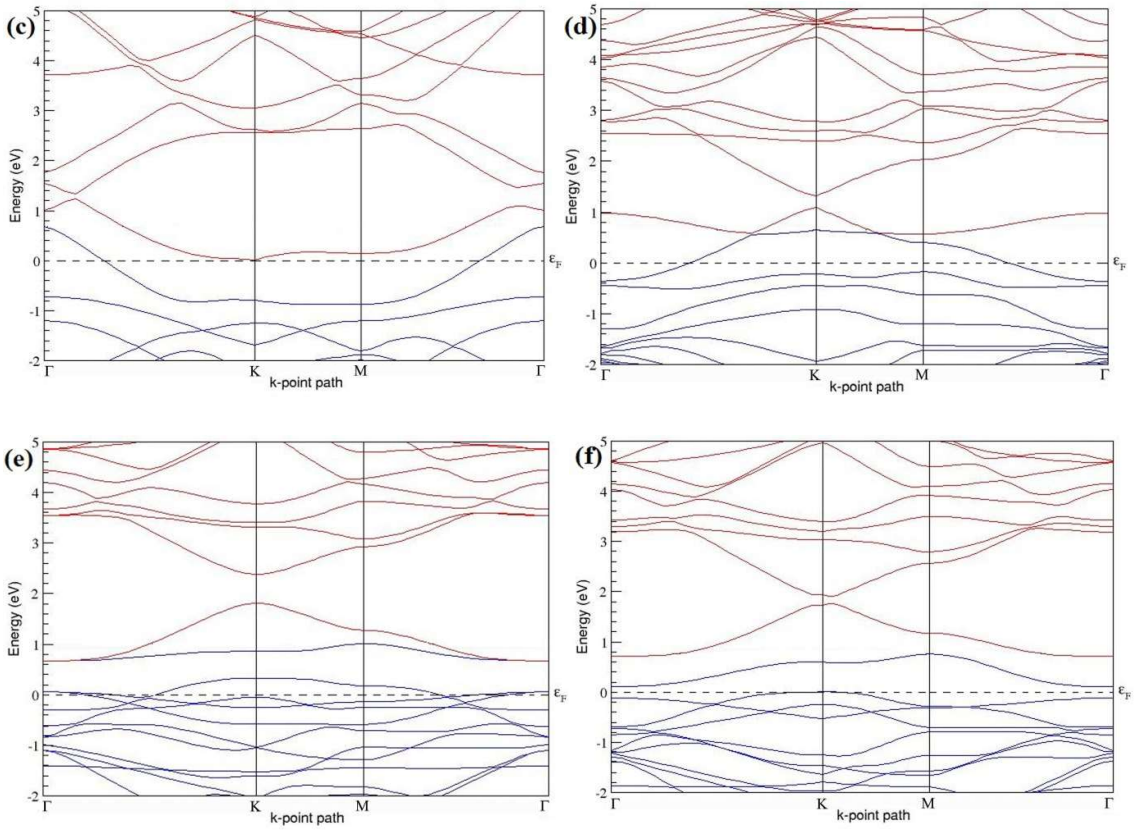

Figure 7.9 (c)-(f) Band structures of graphene systems doped with three B atoms corresponding to the optimized structures shown in **Figure 7.8 (c)-(f)**; **(c)** for 3 × 3 graphene supercell with 16.67% B concentration, **(d), (e)** and **(f)** 4 × 4 graphene supercell with 9.38% B concentration.

Table 7.3 The B concentrations, doping configurations with considered sublattice, cohesive energies and the band gap introduced for various supercells doped with three B atoms.

Model	B Concentration (%)	Configuration	Considered Sublattices for dopants	E_{coh} (eV/atom)	Band gap (eV)
3 × 3	16.67	Figure 7.8 (a)	"B", "A" and "B" (adjacent)	-8.587	0.032
		Figure 7.8 (b)	All in "B" (same)	-8.658	0.900
		Figure 7.8 (c)	"B", "B" and "A" (alternate)	-8.688	0.107
4 × 4	9.38	Figure 7.8 (d)	"B", "A" and "B" (adjacent)	-8.914	0.235
		Figure 7.8 (e)	All in "B" (same)	-8.952	0.568
		Figure 7.8 (f)	"B", "B" and "A" (alternate)	-8.966	0.156

7.3.2.4 B-doped graphene system with four B atoms per supercell

Here the substitutions of four C atoms by four B atoms are considered in 3 × 3 and 4 × 4 graphene supercells. After structural relaxation, all graphene systems doped with four B atoms appear to have the same planar configuration of IG by adjusting the associated bond lengths (Figure 7.10 (a)-(f)). Figure 7.10 (a)-(f) present the relaxed structures of 3 × 3 and 4 × 4 supercells doped with four B atoms at adjacent, same and alternate sublattices respectively. As compared with graphene systems doped with three B atoms, graphene systems doped with four B atoms experience much less structural distortion when the B atoms are placed at the adjacent positions in the lattice (Figure 7.10 (a) and (d)).

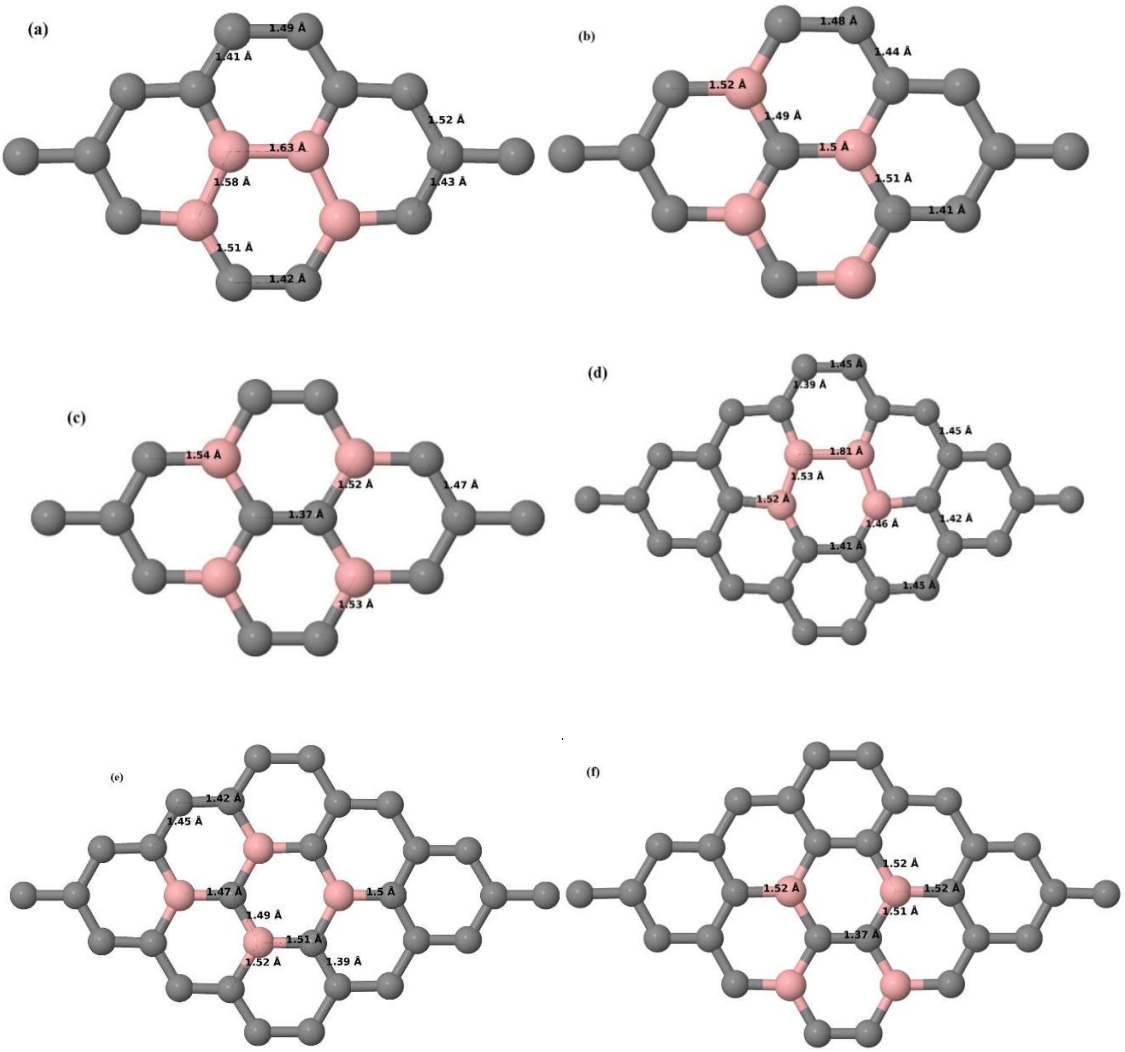

Figure 7.10 Optimized structures of various graphene systems doped with four B atoms with different doping configurations. **(a), (b)** and **(c)** 3 × 3 graphene supercell with 22.22% B concentration, **(d)**, **(e)** and **(f)** 4 × 4 graphene supercell with 12.5% B concentration.

The relaxed lattice constant increases from 2.458 Å to 2.512 Å and 2.557 Å for 4 × 4 and 3 × 3 supercells doped with four B atoms (corresponding to 12.5% and 22.22% B concentrations), respectively, similar to that observed in other B-doped graphene systems.

Figure 7.11 (a)-(f) present the band structures computed for the optimized structures of different graphene systems doped with four B atoms shown in Figure 7.10 (a)-(f). The band structures of both 3 × 3 and 4 × 4 graphene supercells doped with four B atoms depicted in Fig. 7.11 (a)-(f) show non-zero band gap values. At 22.22% B concentration, doped graphene exhibit band gaps of 0.096 eV (Figure 7.11 (a)), ~0.73 eV (Figure 7.11 (b)) and ~0.06 eV ((Figure 7.11 (c)), when B atoms are at adjacent positions, same and alternate sublattices respectively. Graphene with 12.5% B concentration shows band gaps of ~0.12 eV (Figure 7.11 (d)) and ~0.05 eV (Figure 7.11 (f)) for the doping configurations of adjacent and alternate sublattices respectively. Maximum band gap of 0.66 eV (Figure 7.11 (e)) opens up in graphene at 12.5% B concentration, when the dopant atoms are at the same sublattice.

All graphene structures doped with four B atoms exhibit *p*-type semiconducting behaviours. Table 7.4 presents the models used, the doping concentrations with selected sublattices, calculated cohesive energies and the band gap introduced for all graphene systems doped with four B atoms.

Table 7.4 The B concentrations, doping configurations with considered sublattice, cohesive energies and the band gap introduced for various supercells doped with four B atoms.

Model	B Concentration (%)	Configuration	Considered Sublattices for dopants	E_{coh} (eV/atom)	Band gap (eV)
3 × 3	22.22	Figure 7.10 (a)	"B", "A", "B" and "A" (adjacent)	-8.364	0.096
		Figure 7.10 (b)	All in "B" (same)	-8.455	0.728
		Figure 7.10 (c)	"B", "B", "A" and "A" (alternate)	-8.508	0.062
4 × 4	12.5	Figure 7.10 (d)	"B", "A", "B" and "A" (adjacent)	-8.773	0.118
		Figure 7.10 (e)	All in "A" (same)	-8.829	0.662
		Figure 7.10 (f)	"B", "B", "A" and "A" (alternate)	-8.856	0.050

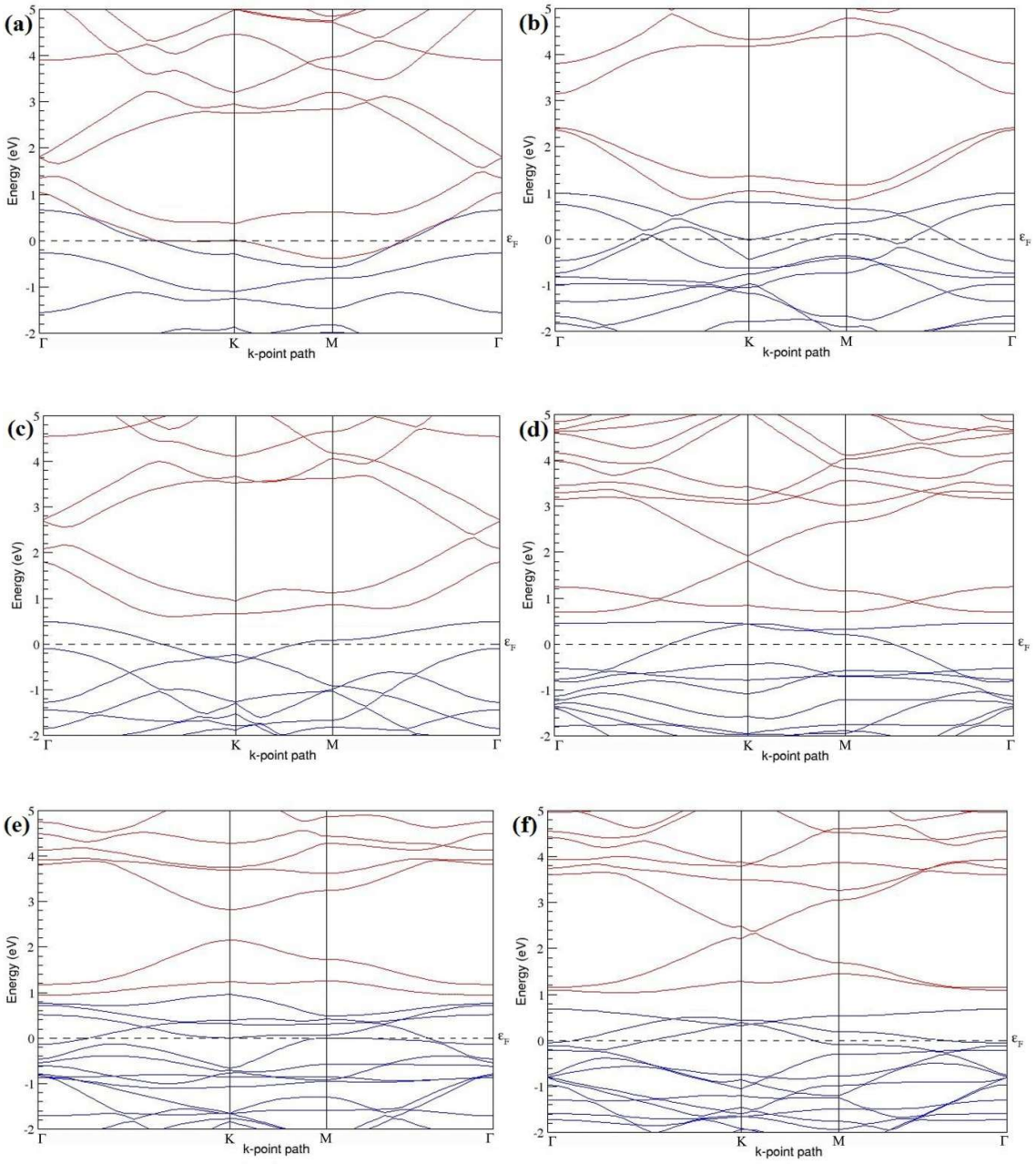

Figure 7.11 (a)-(f) Band structures of graphene systems doped with four B atoms corresponding to the optimized structures shown in **Figure 7.10 (a)-(f)**; **(a), (b)** and **(c)** for 3 × 3 graphene supercell with 22.22% B concentration, **(d), (e)** and **(f)** 4 × 4 graphene supercell with 12.5% B concentration.

7.3.2.5 B-doped graphene system with five B atoms per supercell

Here the substitutions of five C atoms by five B atoms are considered in 4 × 4 graphene supercell. After structural relaxation, it was observed that all graphene systems doped with five B atoms exhibit planar geometry (Figure 7.11 (a)-(c)), similar to other B-doped graphene systems. The relaxed lattice constant increases from 2.458 Å to 2.527 Å for 4 × 4 graphene supercell doped with five B atoms (corresponding to 15.63% B concentration), as observed in other B-doped graphene systems. Similar to graphene systems doped with three B atoms,

graphene systems doped with five B atoms at adjacent positions experience significant structural distortion, but the planar configuration is maintained by adjusting the C-B and adjacent C-C bond lengths (Figure 7.12 (a)). The observed structural distortion is larger than that observed in systems doped with four B atoms.

The band structures computed for the optimized structures of different graphene systems doped with five B atoms shown in Figure 7.13 (a)-(c), show *p*-type semiconducting nature. The observations of disturbed linear energy dispersion at the Dirac point and highly deformed band structure (Figure 7.13 (a)), for the doping configuration with five dopants at adjacent positions, is in agreement with similar previous reports [78]. Table 7.5 summarizes the observed band gaps and the calculated cohesive energies for different doping configurations corresponding to 15.63% B concentration in graphene.

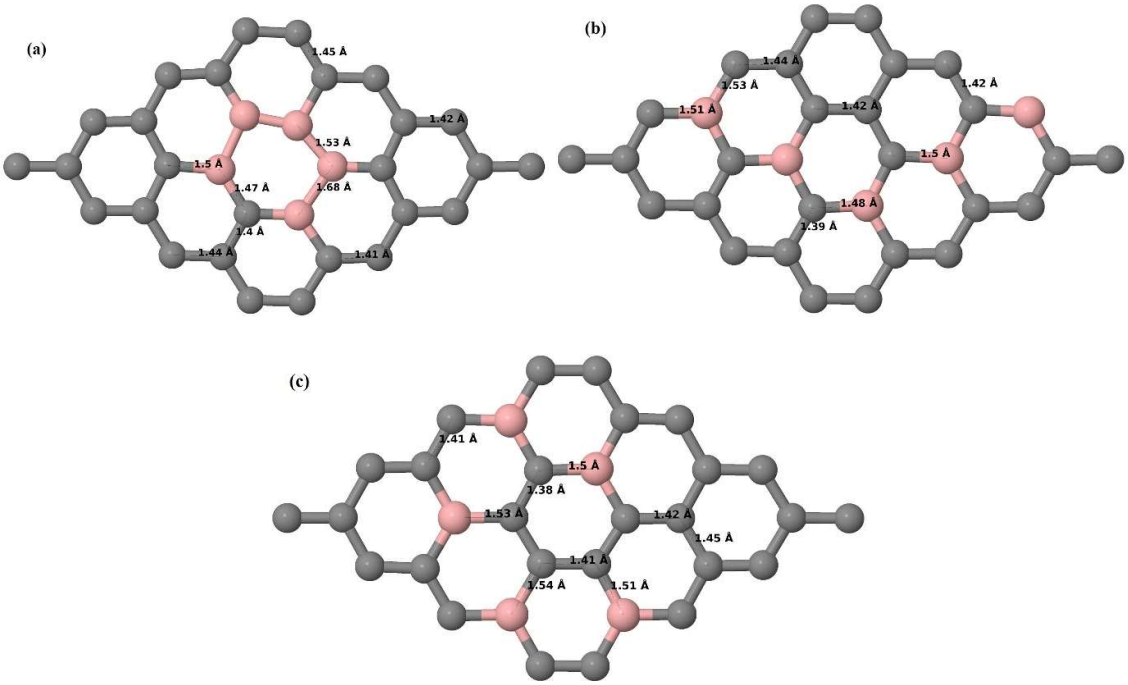

Figure 7.12 (a)-(c) Optimized structures of 4 × 4 graphene supercell doped with five B atoms (15.63% B concentration) with different doping configurations.

Table 7.5 The B concentrations, doping configurations with considered sublattice, cohesive energies and the band gap introduced for 4 × 4 supercell doped with five B atoms.

Model	B Concentration (%)	Configuration	Considered Sublattices for dopants	E_{coh} (eV/atom)	Band gap (eV)
4 × 4	15.63	Figure 7.12 (a)	"B", "A", "B", "A" and "B" (adjacent)	-8.643	0.245
		Figure 7.12 (b)	All in "B" (same)	-8.714	0.756
		Figure 7.10 (c)	"B", "A", "B", "A" and "B" (alternate)	-8.746	0.133

At 15.63% B concentration, B atoms located at adjacent, same and alternate sublattices open band gaps of 0.245 eV (Figure 7.13 (a)), ~0.76 eV (Figure 7.13 (b)) and ~0.13 eV (Figure 7.13 (c)) respectively in graphene.

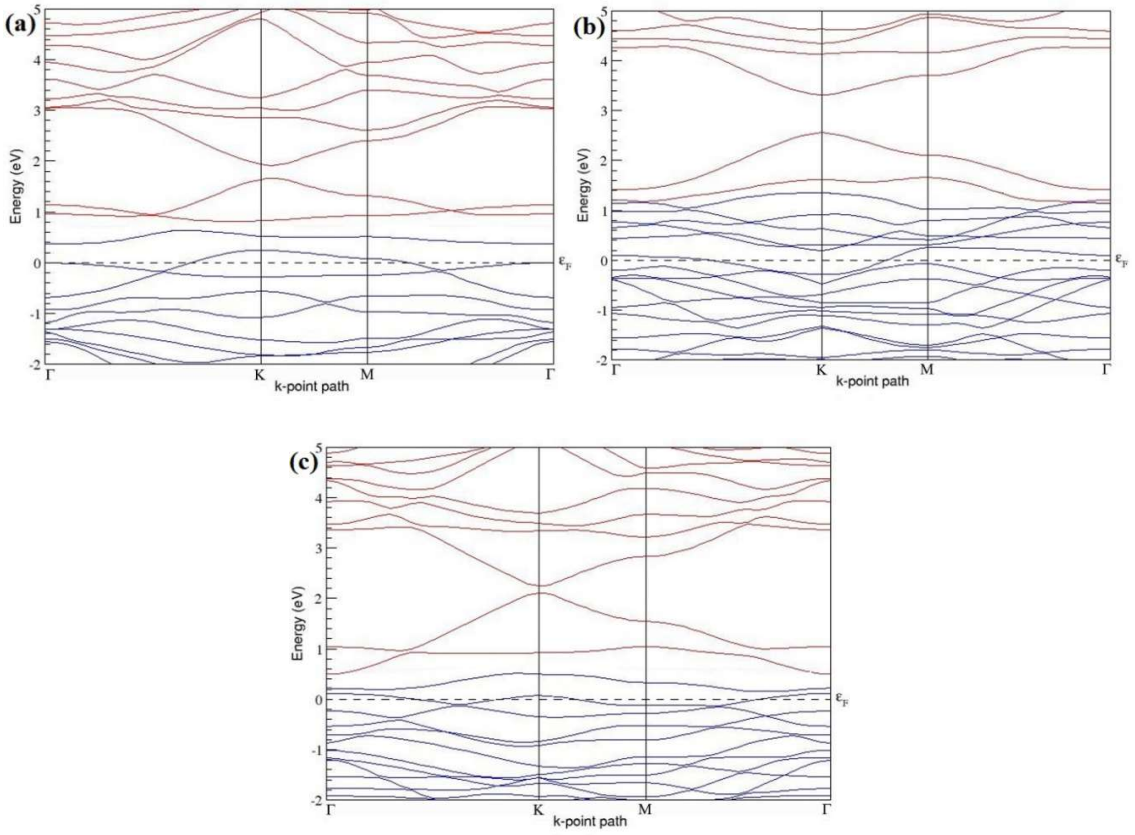

Figure 7.13 (a)-(c) Band structures of 4 × 4 graphene supercell doped with five B atoms (15.63% B concentration) corresponding to the optimized structures shown in **Figure 7.12 (a)-(c)**.

7.3.2.6 B-doped graphene system with six B atoms per supercell

Here six C atoms at adjacent, same and alternate sublattices in a 4 × 4 graphene supercell are substituted by six B atoms. The planar structure is preserved even after the introduction of six B atoms in the lattice (Figure 7.14 (a)-(c)). The relaxed lattice constant increases from 2.458 Å to 2.543 Å for the 4 × 4 graphene supercell doped with six B atoms (corresponding to 18.75% B concentration), as observed in other B-doped graphene systems. Similar to graphene systems doped with four B atoms, the considered 4 × 4 graphene supercell doped with six B atoms at adjacent positions experience less structural distortion (Figure 7.14 (a)) compared to systems doped with three and five B atoms.

The band structures of all graphene systems doped with six B atoms shown in Figure 7.15 (a)-(c) indicate *p*-type semiconducting behaviours. At 18.75% concentration, B-doped graphene does not show a band gap (Figure 7.15 (a), (c)) when the B atoms are located at

adjacent and alternate sublattice sites, whereas a band gap of ~0.99 eV opens up in graphene (Figure 7.15 (b)), when the six B dopants are located at the same sublattice sites of graphene as summarized in Table 7.6. The observed closed band gap in graphene doped with six B atoms (Figure 7.15 (a), (c)) upon placing the dopants at adjacent and alternate sublattices could be attributed to the symmetry formed by the B dopants in two triangular sublattices [78].

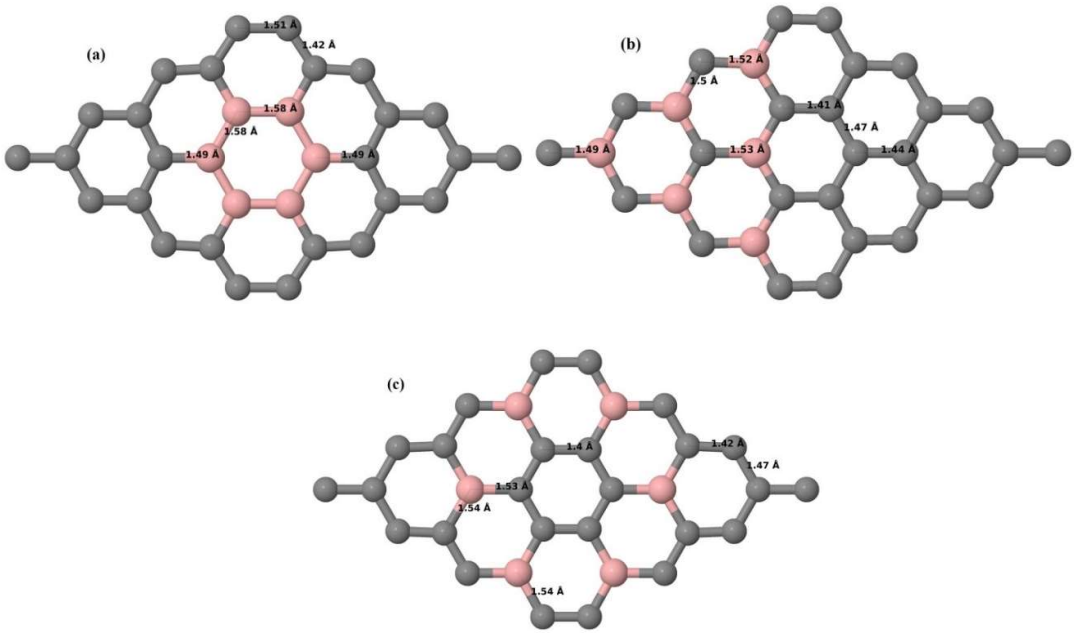

Figure 7.14 (a)-(c) Optimized structures of 4 × 4 graphene supercell doped with six B atoms (18.75% B concentration) with different doping configurations.

Table 7.6 The B concentrations, doping configurations with considered sublattice, cohesive energies and the band gap introduced for 4 × 4 supercell doped with six B atoms.

Model	B Concentration (%)	Configuration	Considered Sublattices for dopants	E_{coh} (eV/atom)	Band gap (eV)
4 × 4	18.75	Figure 7.14 (a)	"B", "A", "B", "A", "B" and "A" (adjacent)	-8.478	0
		Figure 7.14 (b)	All in "B" (same)	-8.593	0.988
		Figure 7.14 (c)	"A", "B", "B", "A", "A" and "B" (alternate)	-8.661	0

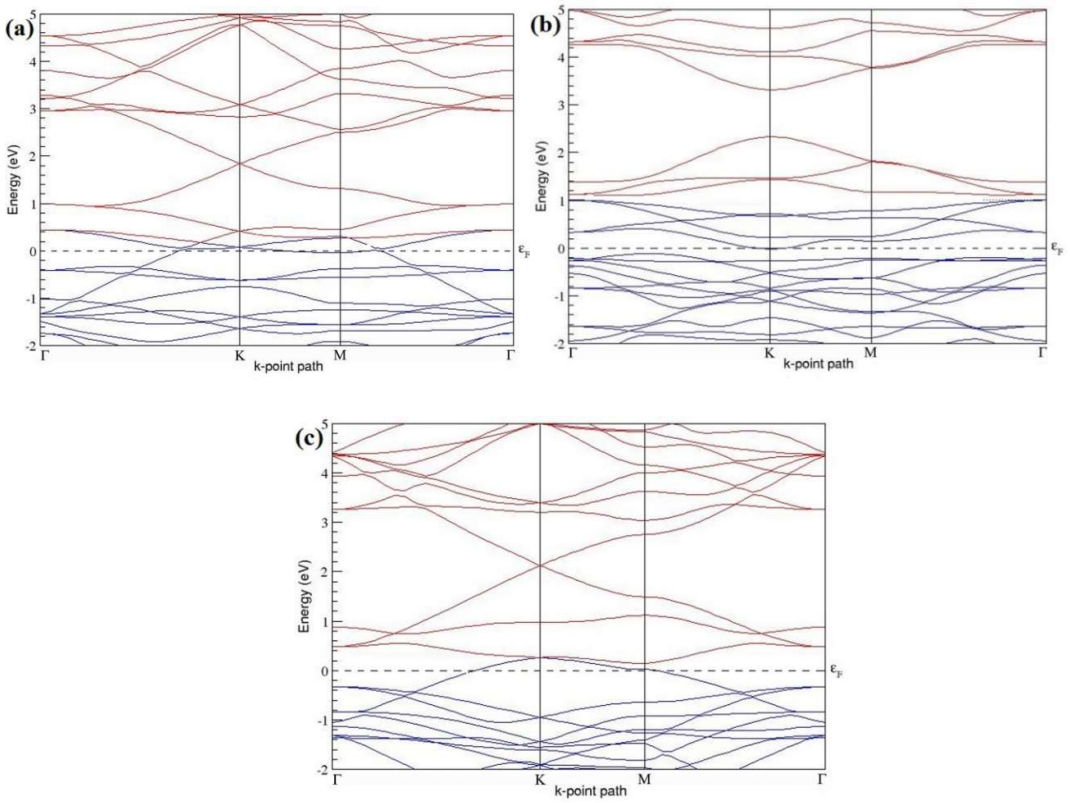

Figure 7.15 (a)-(c) Band structures of 4 × 4 graphene supercell doped with six B atoms (18.75% B concentration) corresponding to the optimized structures shown in **Figure 7.14 (a)-(c).**

7.3.3 N-doped graphene

7.3.3.1 N-doped graphene system with one N atom per supercell

Here one N-substitutional dopant is considered in 2 × 2, 3 × 3, 4 × 4 and 6 × 6 graphene supercells. Similar to that of graphene systems doped with one B atom, all relaxed graphene systems doped with one N atom remain planar (Figure 7.16 (a)-(d)) due to similar size of the C and introduced N atom, showing good accordance with both theoretical [75, 78] and experimental results [211]. Similar to the B atom, as the N atom also undergoes sp^2 hybridization and strongly binds with the three neighbouring C atoms through σ-bonds, there is no distortion in the graphene lattice after N doping. The optimized lattice constant decreases from 2.458 Å to 2.456 Å, 2.454 Å, 2.450 Å and 2.441 Å for 6 × 6, 4 × 4, 3 × 3 and 2 × 2 graphene supercells doped with one N atom (1.39%, 3.13%, 5.56% and 12.5% N concentrations) respectively. This decrease in the optimized lattice constant with the increase in the N-doping concentration is due to the smaller covalent radius of N compared to C, which is in agreement with previous reports [78].

Figure 7.16 (a)-(d) depict the optimized geometries of 2 × 2, 3 × 3 and 4 × 4 and 6 × 6 graphene supercells doped with one N atom. The small covalent radius of N compared to that

of C results in the reduction of the C-N bond length to 1.41 Å for 2 × 2, 3 × 3, 4 × 4 and 6 × 6 graphene supercells doped with one N atom (Figure 7.16 (a)-(d)), consistent with that reported in Ref. [75]. The adjoining C-C bond length also got reduced from 1.42 Å to 1.41 Å in graphene systems doped with one N atom (Figure 7.16 (a)-(d)) in order to preserve the planar geometry.

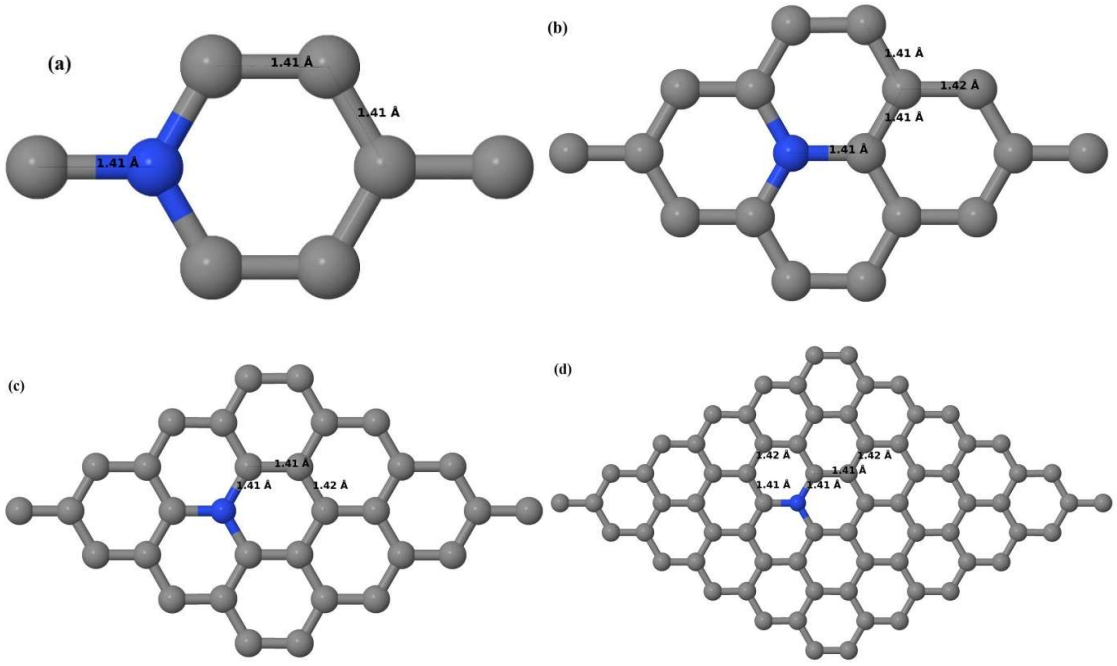

Figure 7.16 Optimized structures of various graphene systems doped with one N atom, the dark blue colour represents N atoms; **(a)** 2 × 2 graphene supercell with 12.5% N concentration, **(b)** 3 × 3 graphene supercell with 5.56% N concentration, **(c)** 4 × 4 graphene supercell with 3.13% N concentration, **(d)** 6 × 6 graphene supercell with 1.39% N concentration.

Figure 7.17 (a)-(d) depict the band structures computed for the relaxed geometries of different graphene systems doped with one N atom shown in Figure 7.16 (a)-(d), in which the linear energy dispersion at the Dirac point is seen unaffected. The observation of the preserved linear energy dispersion near the Dirac point is in good agreement with previous theoretical results [75]. The obtained band structures are compared with those reported in earlier works [75, 78, 84] and are found to be in excellent agreement.

2 × 2 and 4 × 4 graphene supercells doped with one N atom (corresponding to 12.5% and 3.13% N concentrations) show band gaps of ~0.67 eV and ~0.20 eV respectively as evident from Figure 7.17 (a) and (c), due to the symmetry breaking of graphene sublattices similar to that observed in corresponding B-doped graphene systems. The band gap value observed for a 2 × 2 graphene supercell doped with one N atom is in agreement with the existing value of 0.67 eV [80]. Similar to 3 × 3 and 6 × 6 supercells doped with one B atom, there is no band gap opening for 3 × 3 and 6 × 6 supercells doped with one N atom (Figure 7.17 (b), and (d)).

The observed zero band gap in 3 × 3 and 6 × 6 graphene supercells doped with one N atom is consistent with similar theoretical reports [77, 80]. For other supercells, the energy gap increases from ~0.20 eV to ~0.67 eV for 4 × 4 and 2 × 2 supercells doped with one N atom (corresponding to N concentrations of 3.13% and 12.5%), respectively (Table 27). All these graphene systems doped with one N atom exhibit *n*–type metallic nature as evident from the band structures in Figure 7.17, which is consistent with that reported by Wang *et al*. [84]. Both 2 × 2 and 4 × 4 graphene supercells doped with one N atom exhibit *n*-type metallic character [372] with band gap values listed in Table 7.7.

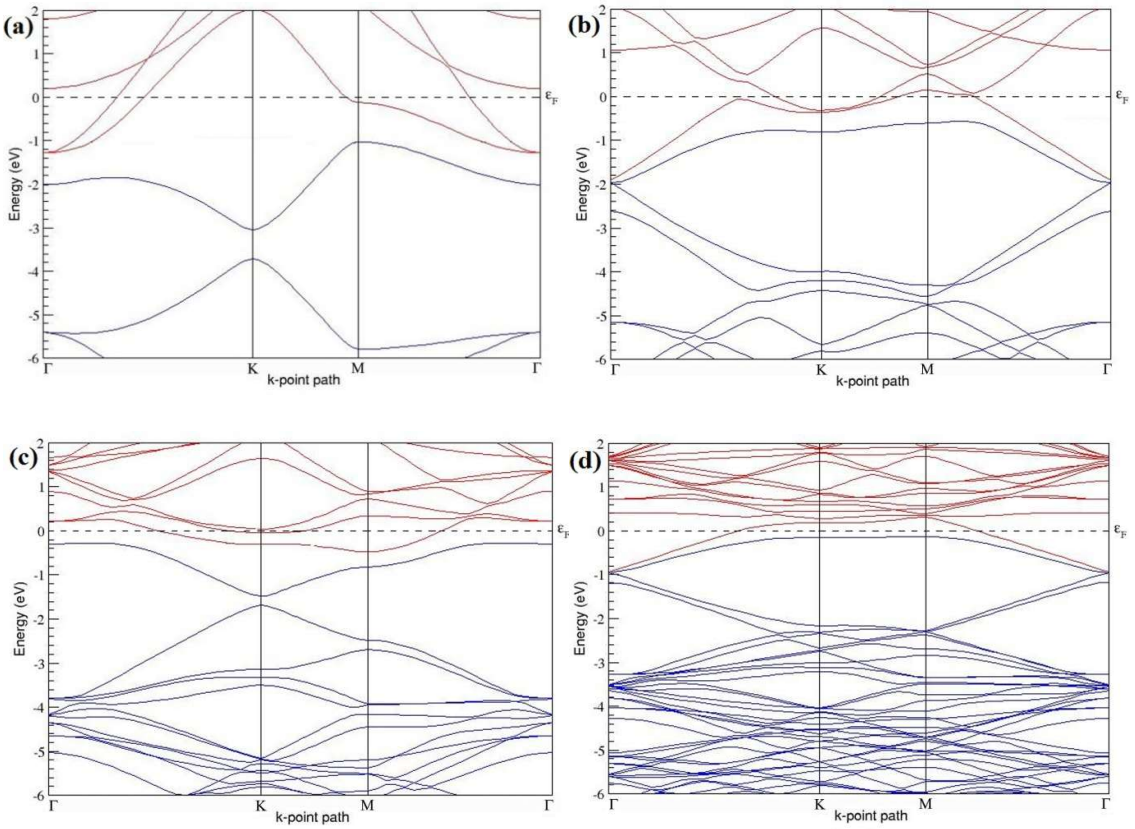

Figure 7.17 Band structures of graphene systems doped with one N atom corresponding to the optimized structures shown in **Figure 7.16 (a)-(d)**; for **(a)** 2 × 2 graphene supercell with 12.5% N concentration, **(b)** 3 × 3 graphene supercell with 5.56% N concentration, **(c)** 4 × 4 graphene supercell with 3.13% N concentration and **(d)** 6 × 6 graphene supercell with 1.39% N concentration.

Table 7.7 The N concentrations, cohesive energies and the band gap introduced for various supercells doped with one N atom.

Model	N Concentration (%)	E_{coh} (eV/atom)	Band gap (eV)
2 × 2	12.5	-9.029	0.668
3 × 3	5.56	-9.193	0
4 × 4	3.13	-9.254	0.202
6 × 6	1.39	-9.291	0

7.3.3.2 N-doped graphene system with two N atoms per supercell

Here the substitution of two C atoms by two N atoms in in 2 × 2, 3 × 3, 4 × 4 and 6 × 6 graphene supercells (Figure 7.18 (a)-(l)) are considered. Similar to graphene systems doped with one N atom, the optimized structures of graphene systems doped with two N atoms preserve the planar geometry of IG (Figure 7.18 (a)-(l)) even after the introduction of two N atoms. The relaxed lattice constant decreases from 2.458 Å to 2.454 Å, 2.449 Å, 2.441 Å and 2.422 Å for 6 × 6, 4 × 4, 3 × 3 and 2 × 2 graphene supercells doped with two N atoms (2.78%, 6.25%, 11.11%, 25% N concentrations) respectively, which shows decrease in lattice constant with increasing N-doping concentration, similar to that observed for graphene systems doped with one N atom.

Figure 7.18 (a)-(l) present the optimized geometries of the 2 × 2, 3 × 3, 4 × 4 and 6 × 6 graphene supercells doped with two N atoms, in which the same configurations taken for graphene systems doped with two B atoms are considered. Three doping configurations of 2 × 2, 3 × 3, 4 × 4 and 6 × 6 supercells doped with two N atoms (corresponding to 25%, 11.11%, 6.25% and 2.78% B concentrations respectively) are selected with the dopant atoms at adjacent positions, (Figure 7.18 (a), (d), (g), (j)), same (Figure 7.18 (b), (e), (h), (k)), and alternate sublattice points (Figure 7.18 (c), (f), (i), (l)). In graphene systems doped with two N atoms, the C-N and C-C bond lengths got reduced significantly (Figure 7.18 (a)-(l)) as compared to graphene systems doped with one N atom for retaining the structure.

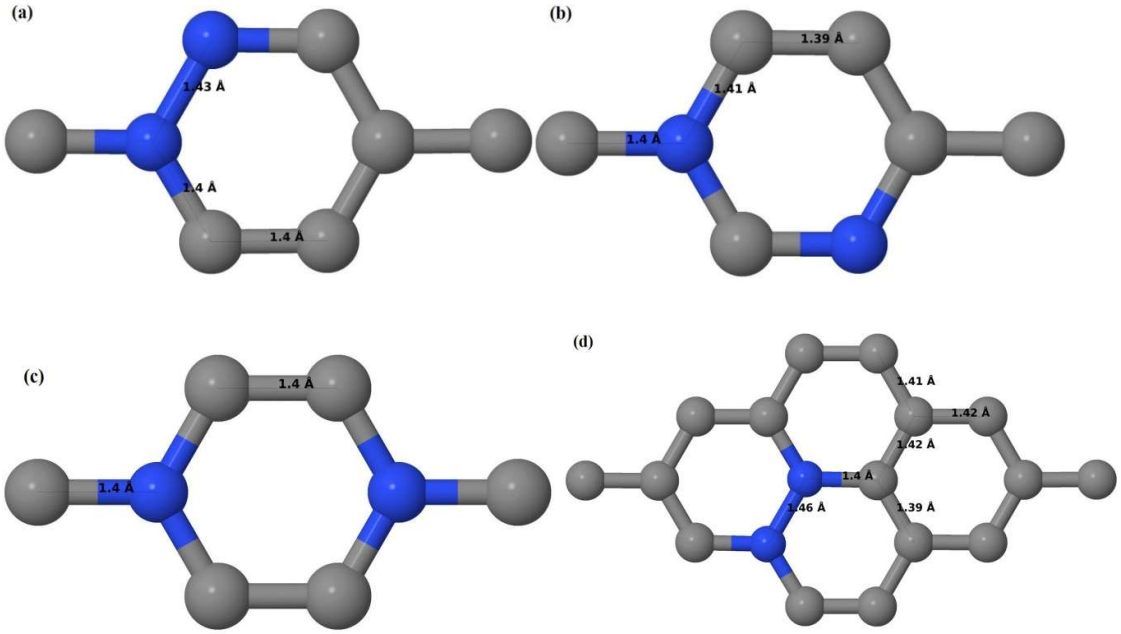

Figure 7.18 (a)-(d) Optimized structures of various graphene systems doped with two N atoms with different doping configurations; **(a), (b)** and **(c)** 2 × 2 graphene supercell with 25% N concentration, **(d)** 3 × 3 graphene supercell with 11.11% N concentration.

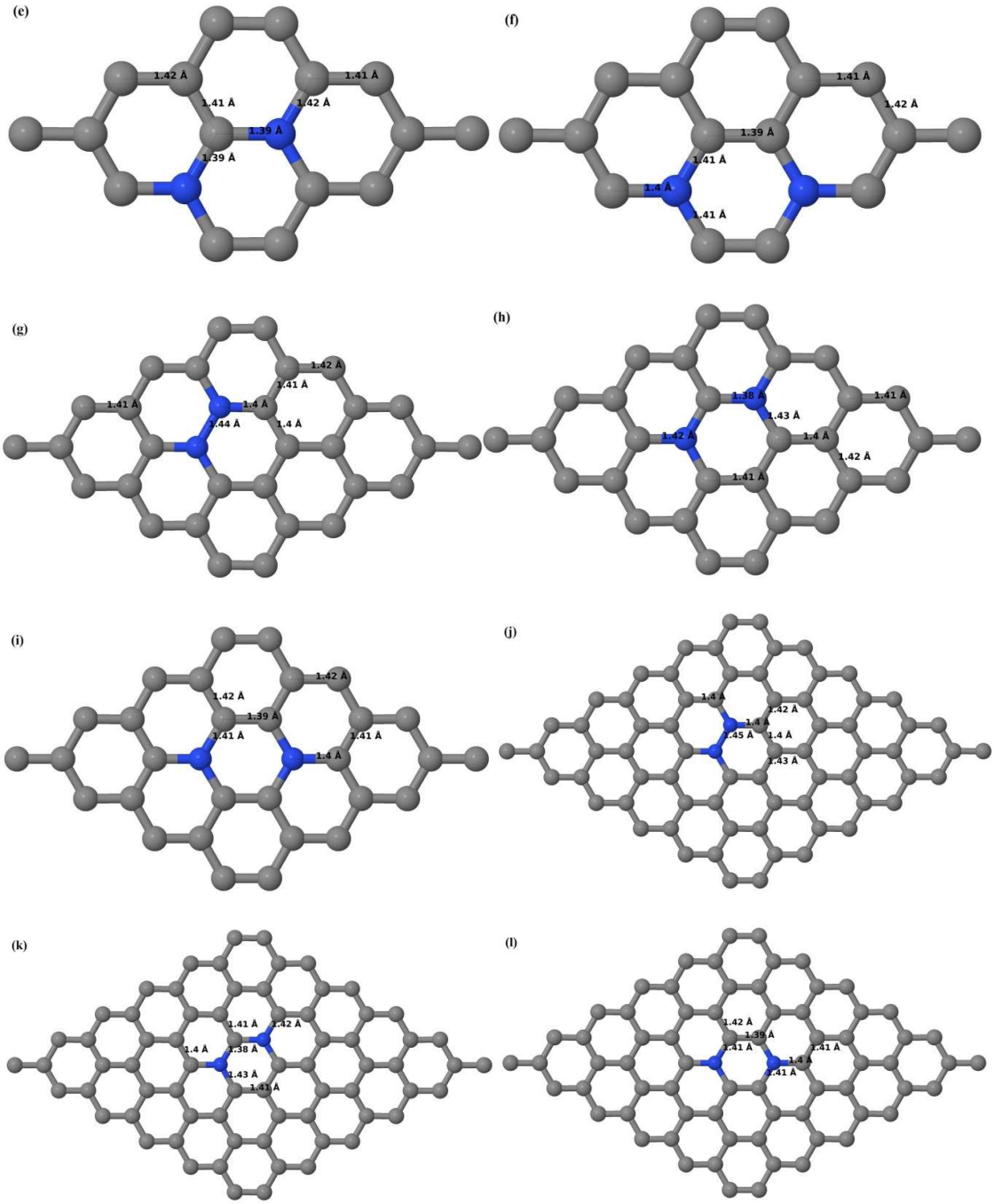

Figure 7.18 (e)-(l) Optimized structures of various graphene systems doped with two N atoms with different doping configurations **(e)** and **(f)** 3 × 3 graphene supercell with 11.11% N concentration, **(g), (h)** and **(i)** 4 × 4 graphene supercell with 6.25% N concentration, **(j), (k)** and **(l)** 6 × 6 graphene supercell with 2.78% N concentration.

After obtaining the stable geometries, the cohesive energies are calculated for all the considered graphene systems doped with two N atoms and are listed in Table 7.8.

Figure 7.19 (a)-(l) present the band structures computed for the optimized structures of different graphene systems doped with two N atoms shown in Figure 7.18 (a)-(l). The band structures of 2 × 2, 3 × 3 and 4 × 4 graphene supercells doped with two N atoms are found to

be in good agreement with those reported in Ref. [84]. Similar to systems doped with two B atoms, the linear dispersion near the Dirac point is not completely destroyed (Figure 7.19 (a)-(l)) but an energy band gap opens in all cases except for 2 × 2 graphene supercell doped with two N atoms at the alternate sublattice points (Figure 7.19 (c)). At 25% N concentration, N-doped graphene has band gaps of 0.40 eV (Figure 7.19 (a)) and ~1.32 eV (Figure 7.19 (b)), on placing the N atoms at adjacent and same sublattice positions in graphene respectively. But the band gap is found to be closed (Figure 7.19 (c)) for the configuration in which the N atoms are at alternate sublattices of a 2 × 2 graphene supercell, even though it corresponds to a high N-doping concentration of 25%.

In 4 × 4 graphene supercell doped with two N atoms (corresponding to 6.25% N concentration), band gaps of ~0.17 eV (Figure 7.19 (g)), ~0.40 eV (Figure 7.19 (h)) and ~0.01 eV (Figure 7.19 (i)) are observed for the configurations with N atoms at adjacent, same and alternate sublattices respectively. The large band gap opening in 2 × 2 and 4 × 4 graphene supercells doped with two N atoms by the positioning of the dopant atoms at the same sublattice is due to the combined effect of the symmetry breaking of sublattices, similar to that observed for graphene systems doped with two B atoms and are in accordance with that reported in Ref. [78]. Similar to 3 × 3 and 6 × 6 graphene supercells doped with two B atoms, the band structures of 3 × 3 and 6 × 6 graphene supercells doped with two N atoms are characterized by non-zero band gaps as shown in Figure 7.19 (d)-(f) and (j)-(l). 3 × 3 graphene supercell doped with two N atoms (corresponding to 11.11% N concentration) exhibit band gaps of ~0.25 eV (Figure 7.19 (d)), ~0.27 eV (Figure 7.19 (e) and ~0.04 eV (Figure 7.19 (f)) for the configuration with N atoms at adjacent positions, same and alternate sublattices respectively. In N-doped graphene with 2.78% N concentration, band gaps of 0.085 eV (Figure 7.19 (j)), ~0.11 eV (Figure 7.19 (k)) and ~0.02 eV (Figure 7.19 (l)) appear when the dopants are at adjacent, same and alternate sublattice sites in graphene. All these doped systems with two N-atoms doping in 2 × 2, 3 × 3, 4 × 4 and 6 × 6 graphene supercells exhibit *n*-type metallic behaviour.

The analysis of the electronic properties of 2 × 2 and 4 × 4 graphene supercells doped with two N atoms are in contrary to that have been inferred in Ref. [84]. Table 7.8 presents a summary of the considered N-doping concentrations with doping configurations, the sublattices selected for the N atoms, the calculated cohesive energies and the band gaps observed in each of these cases.

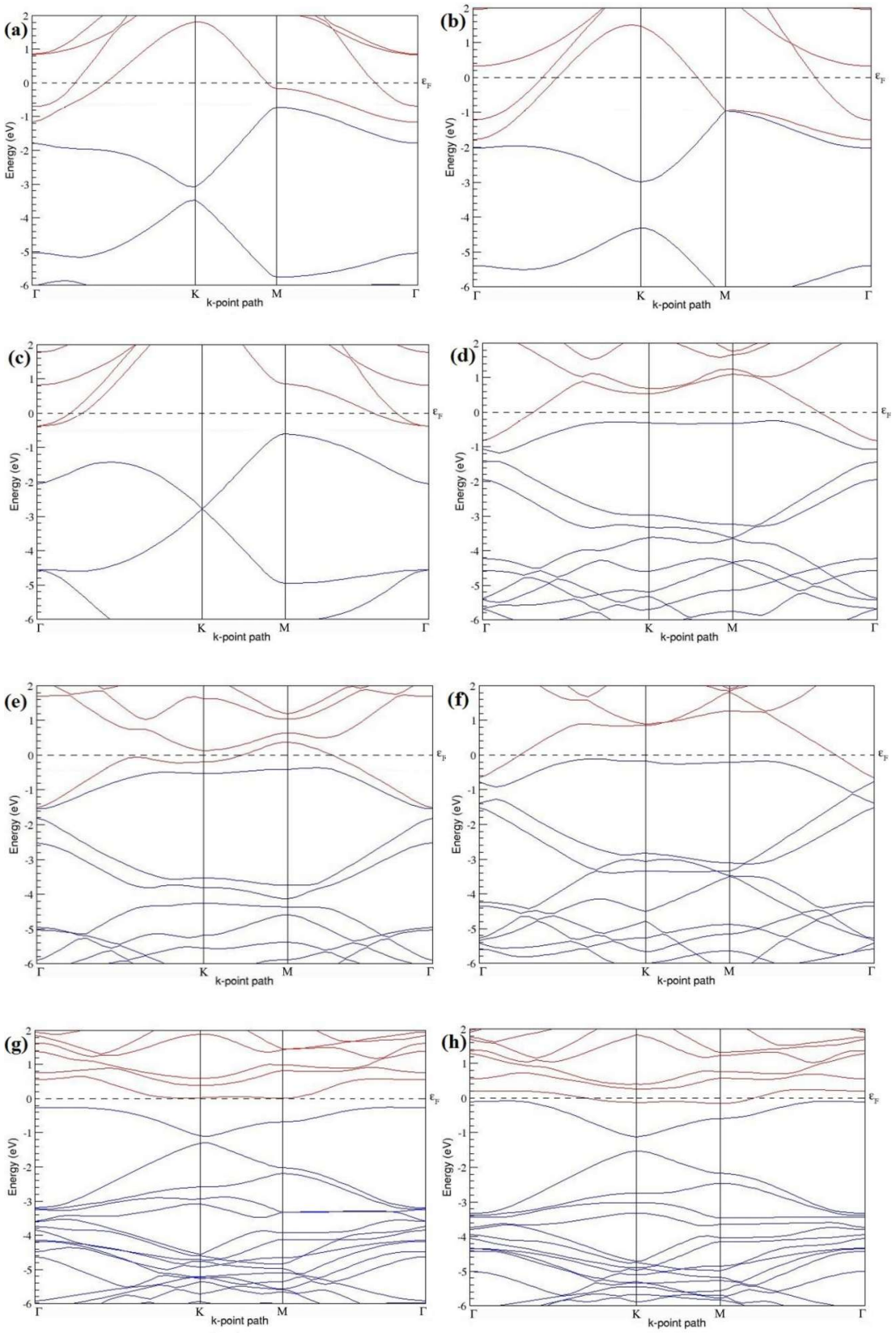

Figure 7.19 (a)-(h) Band structures of graphene systems doped with two N atoms corresponding to the optimized structures shown in **Figure 7.18 (a)-(h); (a), (b)** and **(c)** for 2 × 2 graphene supercell with 25% N concentration, **(d), (e)** and **(f)** 3 × 3 graphene supercell with 11.11% N concentration **(g)** and **(h)** 4 × 4 graphene supercell with 6.25% N concentration.

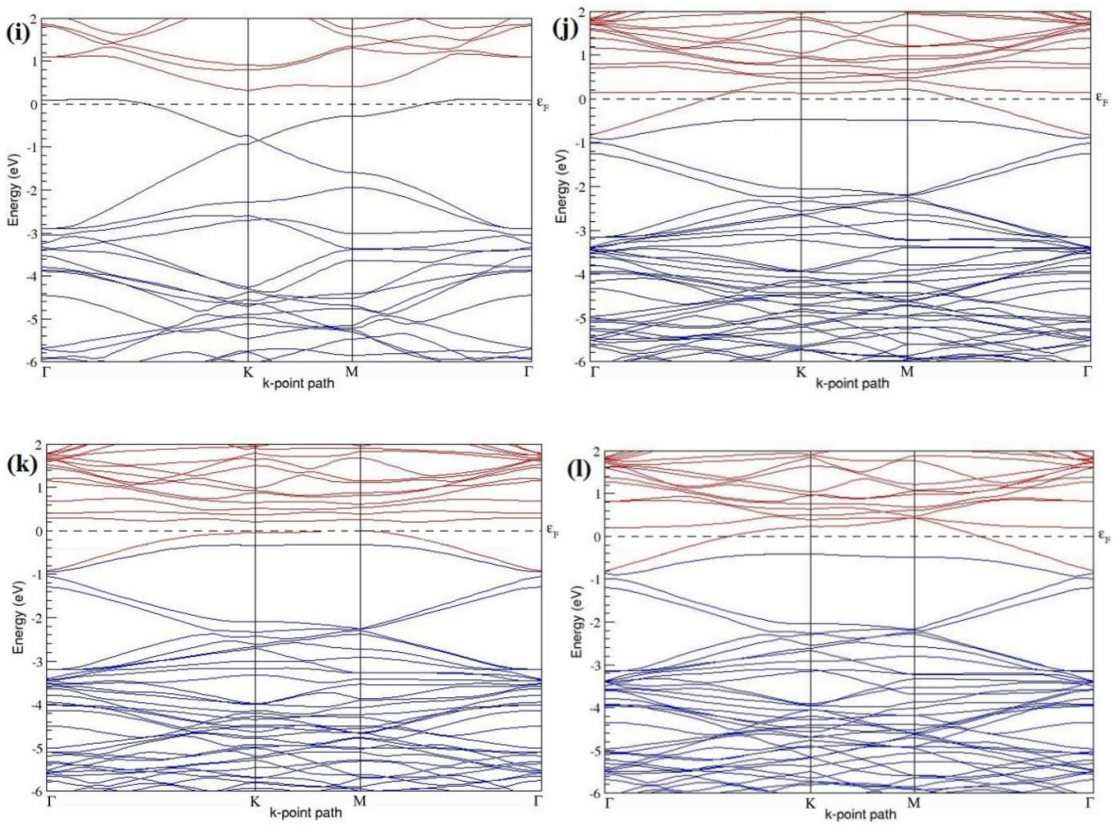

Figure 7.19 (i)-(l) Band structures of graphene systems doped with two N atoms corresponding to the optimized structures shown in **Figure 7.18 (i)-(l)**; **(i)** for 4 × 4 graphene supercell with 6.25% N concentration, **(j), (k)** and **(l)** 6 × 6 graphene supercell with 2.78% N concentration.

Table 7.8 The N concentrations, doping configurations with considered sublattice, cohesive energies and the band gap introduced for various supercells doped with two N atoms.

Model	N Concentration (%)	Configuration	Considered Sublattices for dopants	E_{coh} (eV/atom)	Band gap (eV)
2 × 2	25	Figure 7.18 (a)	"B" and "A" (adjacent)	-8.717	0.400
		Figure 7.18 (b)	Both in "B" (same)	-8.780	1.324
		Figure 7.18 (c)	"B" and "A" (alternate)	-8.875	0
3 × 3	11.11	Figure 7.18 (d)	"B" and "A" (adjacent)	-9.048	0.252
		Figure 7.18 (e)	Both in "B" (same)	-9.079	0.271
		Figure 7.18 (f)	"B" and "A" (alternate)	-9.112	0.039
4 × 4	6.25	Figure 7.18 (g)	"B" and "A" (adjacent)	-9.172	0.174
		Figure 7.18 (h)	Both in "B" (same)	-9.191	0.403
		Figure 7.18 (i)	"B" and "A" (alternate)	-9.203	0.012
6 × 6	2.78	Figure 7.18 (j)	"B" and "A" (adjacent)	-9.253	0.085
		Figure 7.18 (k)	Both in "B" (same)	-9.262	0.110
		Figure 7.18 (l)	"B" and "A" (alternate)	-9.268	0.023

7.3.3.3 N-doped graphene system with three N atoms per supercell

Here the substitutions of three C atoms by three N atoms are considered in 3 × 3 and 4 × 4 graphene supercells. All graphene systems doped with three N atoms have planar hexagonal structure as seen in Figure 7.20 (a)-(f). The relaxed lattice constant decreases from 2.458 Å to 2.445 Å and 2.434 Å for 4 × 4 and 3 × 3 graphene supercells doped with three N atoms (9.38% and 16.67% N concentrations) respectively, similar to that observed in graphene systems doped with one and two N atoms.

Figure 7.20 (a)-(f) present the relaxed geometries of 3 × 3 and 4 × 4 graphene supercells doped with three N atoms at adjacent positions, same and alternate sublattices respectively.

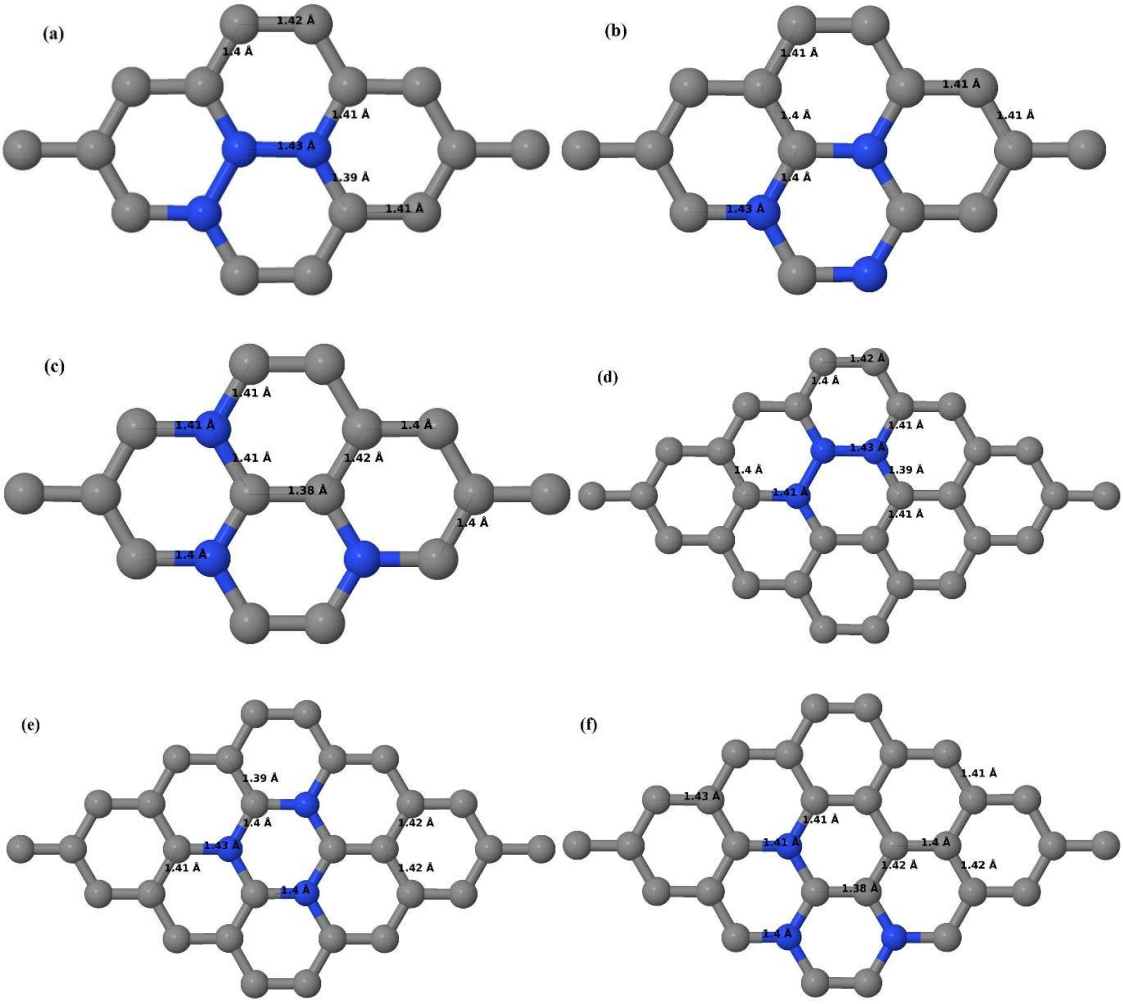

Figure 7.20 Optimized structures of various graphene systems doped with three N atoms with different doping configurations; **(a), (b) and (c)** 3 × 3 graphene supercell with 16.67% N concentration; **(d), (e) and (f)** 4 × 4 graphene supercell with 9.38% N concentration.

Compared with their B counterparts, graphene systems doped with three N atoms are found to have significantly less structural distortion, even when the three N atoms are placed at adjacent locations (Figure 7.20 (a), (d)), due to the comparable size of C and N atoms.

Figure 7.21 (a)-(f) present the band structures computed for the optimized structures of different graphene systems doped with three N atoms shown in Figure 7.20 (a)-(f). Graphene systems doped with three N atoms in 3 × 3 and 4 × 4 graphene supercells exhibit *n*-type metallic behaviour with band gaps indicated in Table 7.9. Similar to graphene systems doped with three B atoms at adjacent positions, deformed band structures were obtained (Figure 7.21 (a), (d)) for those structures in which the N-substitutional dopants are placed at the adjacent positions (Figure 7.20 (a), (d)).

In 3 × 3 graphene systems doped with three N atoms (corresponding to 16.67% N concentration), band gaps of 0.93 eV (Figure 7.21 (b)) appears when the dopant atoms are placed at the same sublattice, whereas band gap values of ~0.29 eV (Figure 7.21 (a)) and 0.16 eV (Figure 7.21 (c)) appear when the dopant atoms are placed at the adjacent positions and alternate sublattice positions respectively. 4 × 4 graphene supercell doped with three N atoms (corresponding to 9.38% N concentration) induce band gaps of 0.27 eV ((Figure 105 (d)), ~0.61 eV (Figure 105 (e)) and ~0.18 eV ((Figure 7.21 (f)), for the configurations with N atoms at adjacent, same and alternate sublattices. Table 7.9 presents the models used, the dopant concentrations, considered dopant concentrations with sublattices, cohesive energies and the band gap introduced for all graphene systems doped with three N atoms.

Table 7.9 The N concentrations, doping configurations with considered sublattice, cohesive energies and the band gap introduced for various supercells doped with three N atoms.

Model	N Concentration (%)	Configuration	Considered Sublattices for dopants	E_{coh} (eV/atom)	Band gap (eV)
3 × 3	16.67	Figure 7.20 (a)	"B", "A" and "B" (adjacent)	-8.876	0.294
		Figure 7.20 (b)	All in "B" (same)	-8.957	0.930
		Figure 7.20 (c)	"B", "B" and "A" (alternate)	-8.984	0.160
4 × 4	9.38	Figure 7.20 (d)	"B, "A and "B" (adjacent)	-9.072	0.270
		Figure 7.20 (e)	All in "B" (same)	-9.120	0.608
		Figure 7.20 (f)	"B", "B" and "A" (alternate)	-9.132	0.176

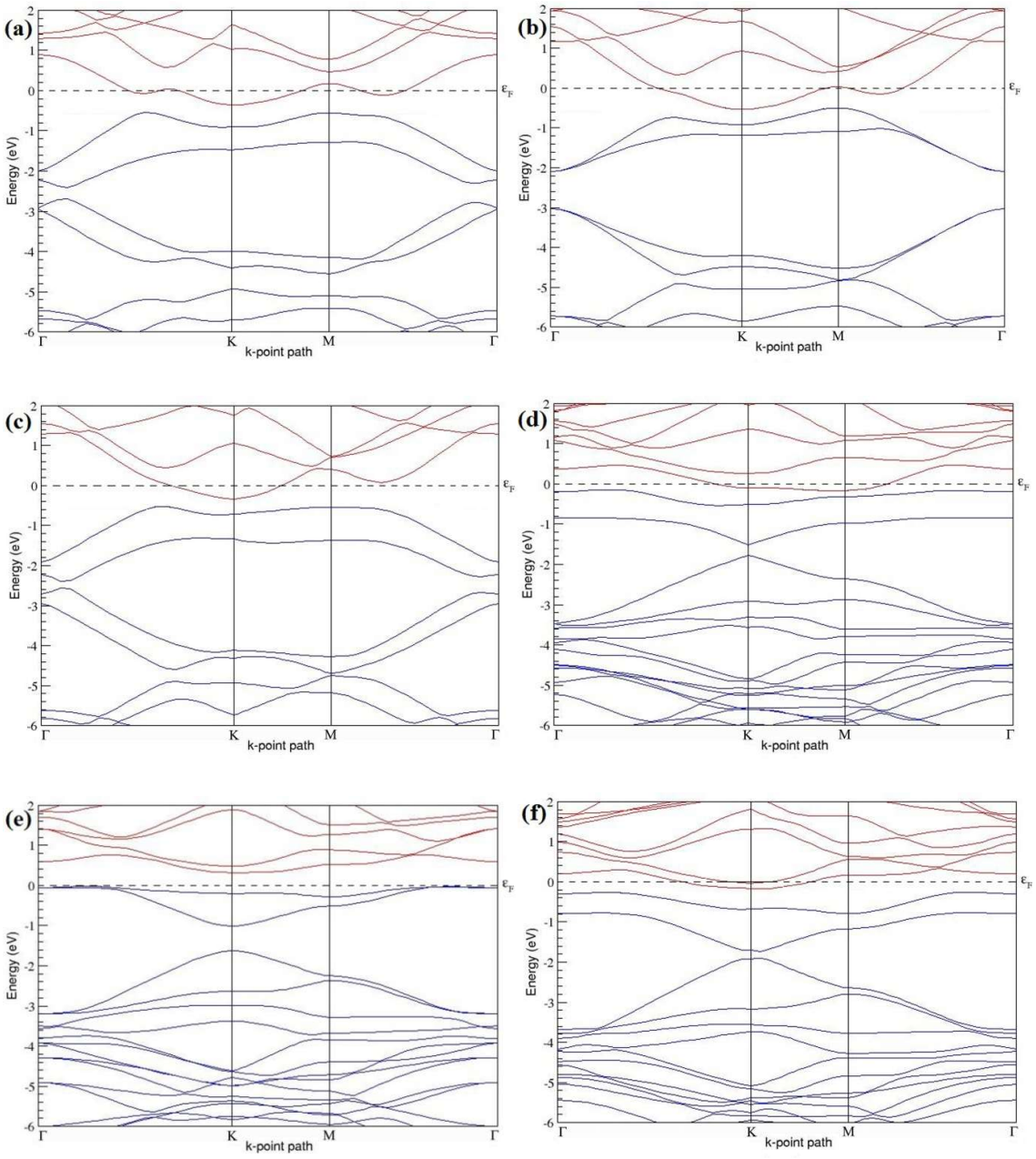

Figure 7.21 Band structures of graphene systems doped with three N atoms corresponding to the configurations shown in **Figure 7.20 (a)-(f)**; for **(a)**, **(b)** and **(c)** 3 × 3 graphene supercell with 16.67% N concentration, **(d), (e)** and **(f)** 4 × 4 graphene supercell with 9.38% N concentration

7.3.3.4 N-doped graphene system with four N atoms per supercell

Here the substitutions of four C atoms by four N atoms are considered in 3 × 3 and 4 × 4 graphene supercells. After structural relaxation, all graphene systems doped with four N atoms appear to be planar by adjusting the adjoining bond lengths (Figure 7.22 (a)-(f)). The relaxed lattice constant decreases from 2.458 Å to 2.441 Å and 2.427 Å for 4 × 4 and 3 × 3 graphene supercells doped with four N atoms (corresponding to 12.5% and 22.22% N

concentrations) respectively, which also indicates decrease in lattice constant with increase in the N-doping concentration as observed with other B-doped graphene systems.

Figure 7.22 (a)-(f) present the relaxed structures of 3 × 3 and 4 × 4 supercells doped with four N atoms at adjacent, same and alternate sublattices respectively. As compared to graphene systems doped with four B atoms, graphene systems doped with four N atoms experience almost negligible structural distortion even upon placing the N atoms at the adjacent positions in the lattice (Figure 7.22 (a) and (d)).

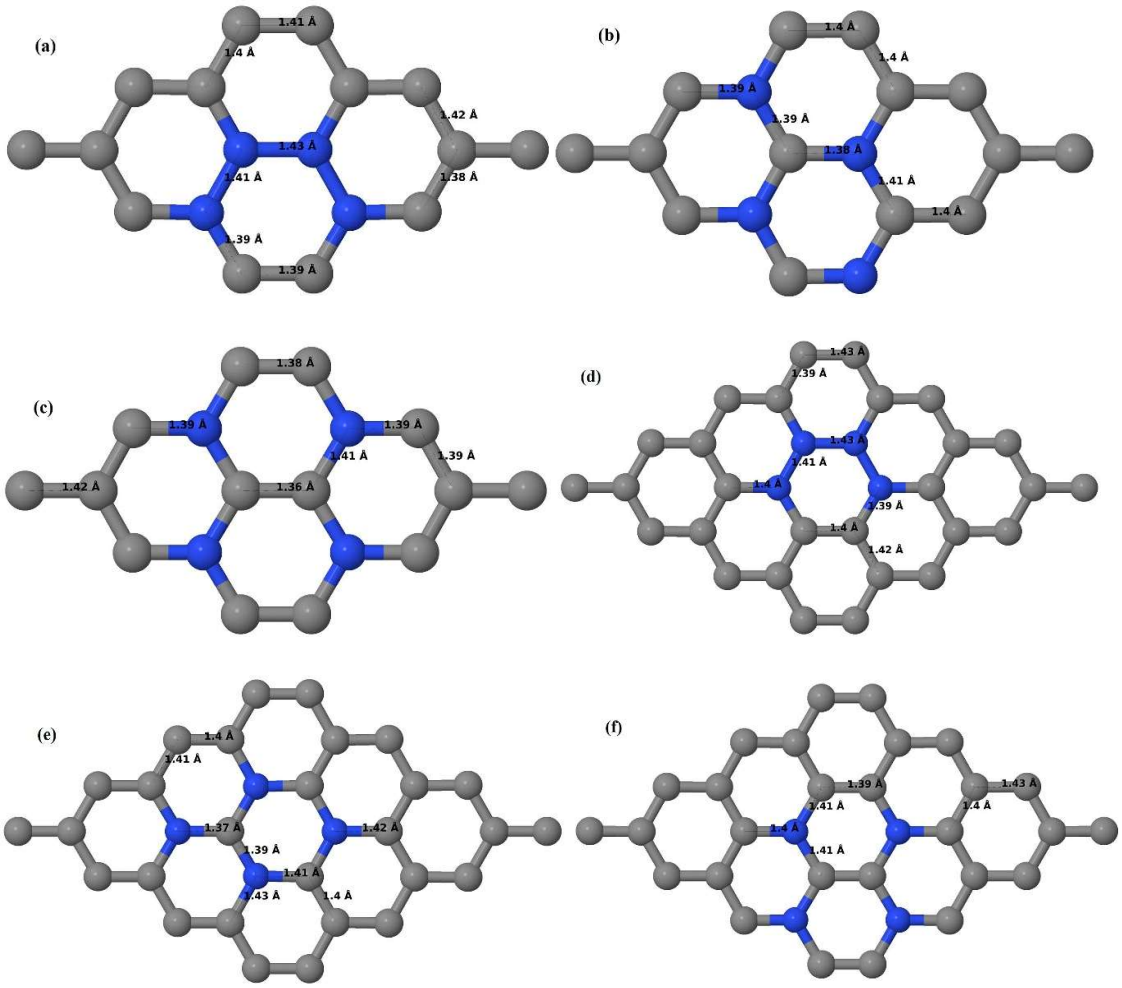

Figure 7.22 Optimized structures of various graphene systems doped with four N atoms with different doping configurations. **(a)**, **(b)** and **(c)** 3 × 3 graphene supercell with 22.22% N concentration; **(d)**, **(e)** and **(f)** 4 × 4 graphene supercell with 12.5% N concentration.

Figure 7.23 (a)-(f) present the band structures computed for the optimized structures of different graphene systems doped with four N atoms shown in Figure 7.22 (a)-(f). Similar to graphene systems doped with three N atoms, all graphene structures doped with four N atoms exhibit *n*-type metallic electronic properties with band gaps (Figure 7.23 (a)-(f)). In 3 × 3 graphene systems doped with four N atoms (corresponding to 22.22%), highest band gap

value of ~0.80 eV (Figure 7.23 (b)) appears when the dopant atoms are placed at the same sublattices, whereas band gaps of 0.20 eV (Figure 7.23 (a)) and ~0.11 eV (Figure 7.23 (c)) are induced in graphene when the dopant atoms are placed at the adjacent positions and alternate sublattices respectively. At 12.5% N concentration, maximum band gap of 0.70 eV (Figure 7.23 (e)) opens up when the dopant atoms are at the same sublattice and the minimum band gap value of ~0.004 eV ((Figure 7.23 (f)) appears when the dopant atoms are at alternate sublattice positions.

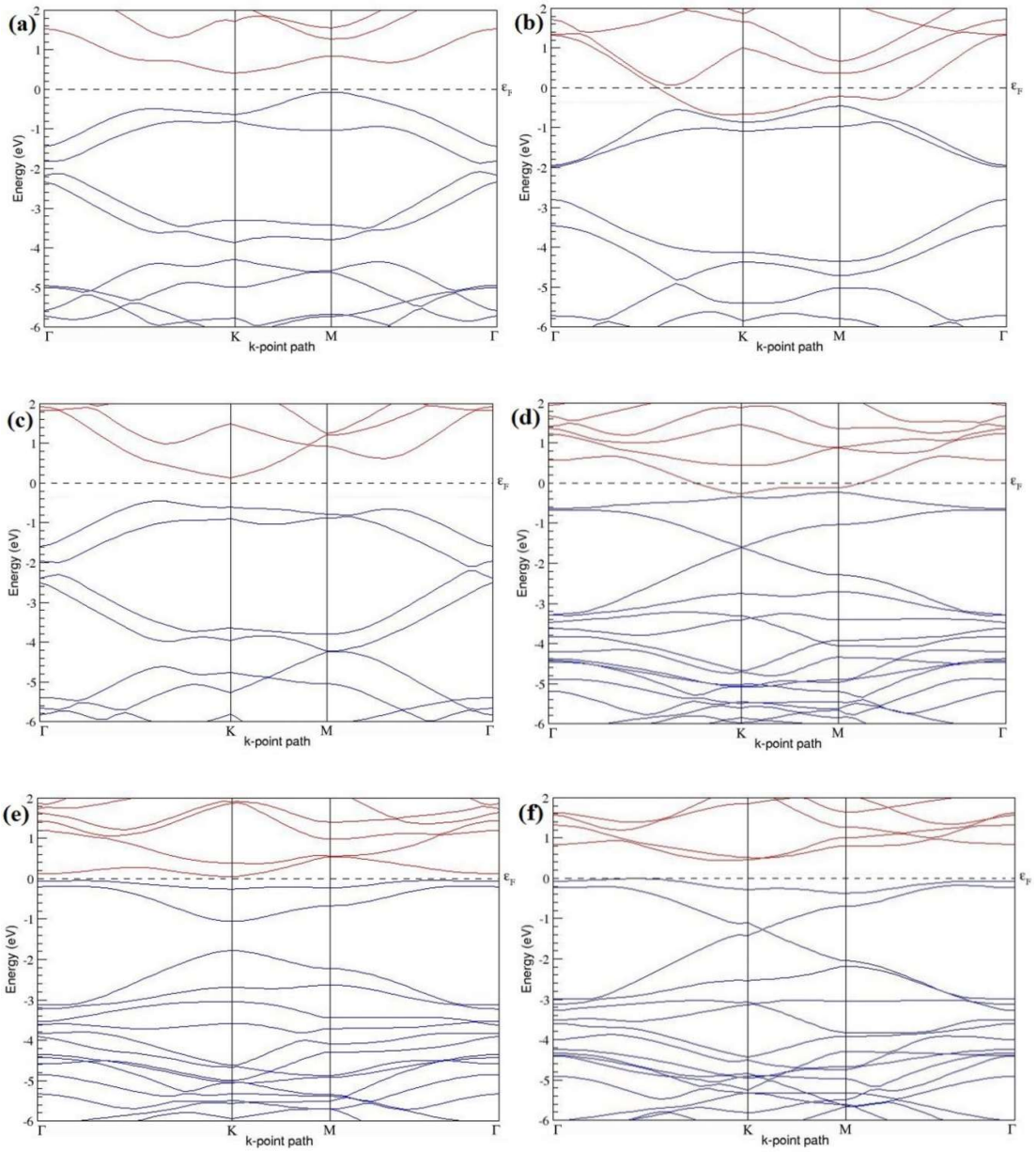

Figure 7.23 Band structures of graphene systems doped with four N atoms corresponding to the optimized structures shown in **Figure 7.22 (a)-(f)**; **(a)**, **(b)** and **(c)** 3 × 3 graphene supercell with 22.22% N concentration; **(d)**, **(e)** and **(f)** 4 × 4 graphene supercell with 12.5% N concentration.

The observed very small band gap for the doping configuration with N atoms at adjacent locations (Figure 7.23 (d) corresponding to 12.5% N-doping concentration could be ascribed to the symmetry formed by the N dopants in the two triangular sublattices. Table 7.10 presents the models used, the doping concentrations with selected sublattices, the cohesive energies and the band gap introduced for all graphene systems doped with four N atoms.

Table 7.10 The N concentrations, doping configurations with considered sublattice, cohesive energies and the band gap introduced for various supercells doped with four N atoms.

Model	N Concentration (%)	Configuration	Considered Sublattices for dopants	E_{coh} (eV/atom)	Band gap (eV)
3 × 3	22.22	Figure 7.22 (a)	"B", "A", "B" and "A" (adjacent)	-8.741	0.200
		Figure 7.22 (b)	All in "B" (same)	-8.844	0.804
		Figure 7.22 (c)	"B", "B", "A" and "A" (alternate)	-8.894	0.106
4×4	12.5	Figure 7.22 (d)	"B", "A", "B" and "A" (adjacent)	-8.987	0.020
		Figure 7.22 (e)	All in "A" (same)	-9.052	0.700
		Figure 7.22 (f)	"B", "B", "A" and "A" (alternate)	-9.077	0.004

7.3.3.5 N-doped graphene system with five N atoms per supercell

Here the substitution of five C atoms by five N atoms in 4 × 4 graphene supercell are considered with the dopant positions of adjacent, same and alternate sublattices. After structural relaxation, it was observed that all graphene systems doped with five N atoms exhibit planar geometry (Figure 7.24 (a)-(c)), similar to other N-doped graphene systems. The relaxed lattice constant decreases from 2.458 Å to 2.435 Å for five N-doped 4 × 4 graphene supercell (corresponding to 15.63% N concentration), as observed in other N-doped graphene systems. Similar to graphene systems doped with three N atoms, there is no structural distortion in all the considered structures of graphene systems doped with five N atoms. The planar configuration is maintained by adjusting the associated bond lengths as indicated in Figure 7.24 (a)-(c)). The band structures presented in Figure 7.25 (a)-(c) indicate that all graphene structures doped with five N atoms show *n*-type metallic character. At 15.63% N concentration, N atoms located at adjacent, same and alternate sublattices induce band gaps of ~0.36 eV (Figure 7.25 (a)), ~0.79 eV (Figure 7.25 (b)) and ~0.14 eV (Figure 7.25 (c)) respectively in graphene as summarized in Table 7.11. Table 7.11 summarizes the

observed band gaps and the calculated cohesive energies for different doping configurations corresponding to 15.63% N concentration in graphene.

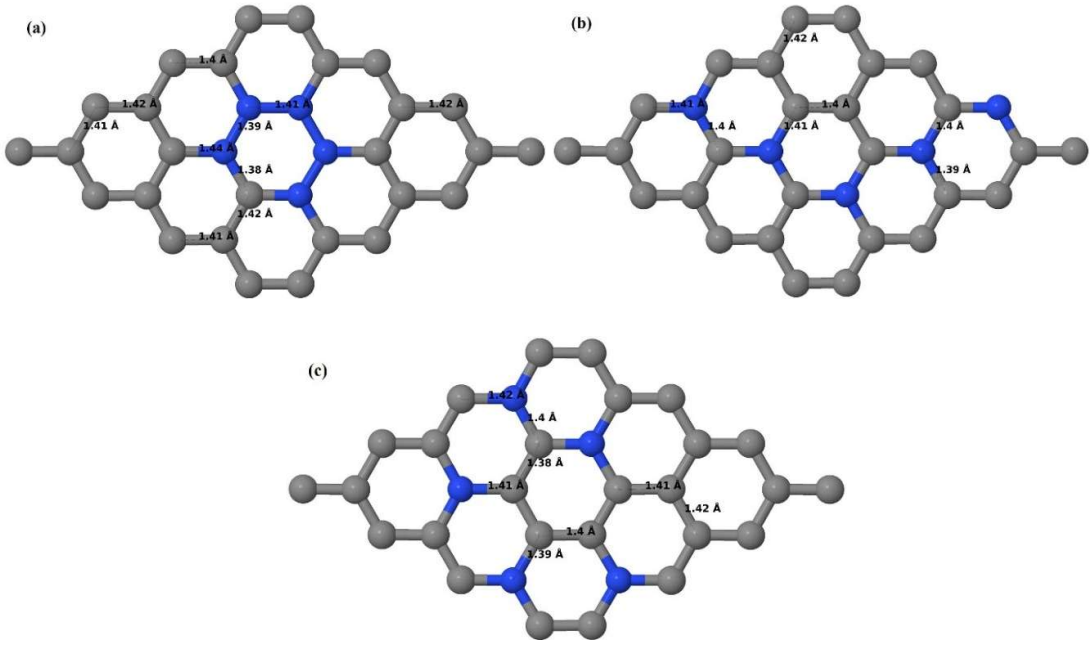

Figure 7.24 (a)-(c) Optimized structures of 4 × 4 graphene supercell doped with five N atoms (15.63% N concentration) with different doping configurations.

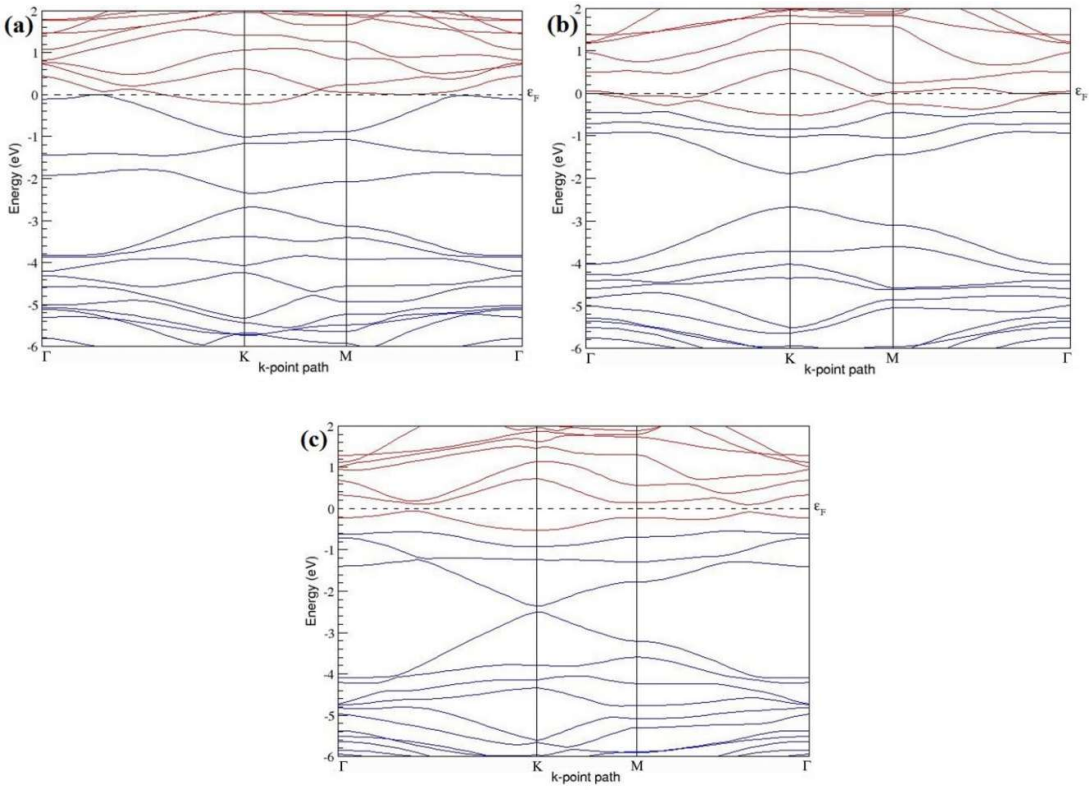

Figure 7.25 (a)-(c) Band structures of 4 × 4 graphene supercell doped with five N atoms (15.63% N concentration) corresponding to the optimized structures shown in **Figure 7.24 (a)-(c).**

Table 7.11 The N concentrations, doping configurations with considered sublattice, cohesive energies and the band gap introduced for 4 × 4 supercell doped with five N atoms.

Model	N Concentration (%)	Configuration	Considered Sublattices for dopants	E_{coh} (eV/atom)	Band gap (eV)
4 × 4	15.63	Figure 7.24 (a)	"B", "A", "B", "A" and "B" (adjacent)	-8.884	0.357
		Figure 7.24 (b)	All in "B" (same)	-8.988	0.792
		Figure 7.24 (c)	"B", "A", "B", "A" and "B" (alternate)	-9.017	0.141

7.3.3.6 N-doped graphene system with six N atoms per supercell

Here the substitutions of six C atoms by six N atoms are considered in the 4 × 4 graphene supercell with the dopant positions of adjacent, same and alternate sublattices. The planar structure is preserved even after the introduction of six N atoms in the lattice (Figure 7.26 (a)-(c)).

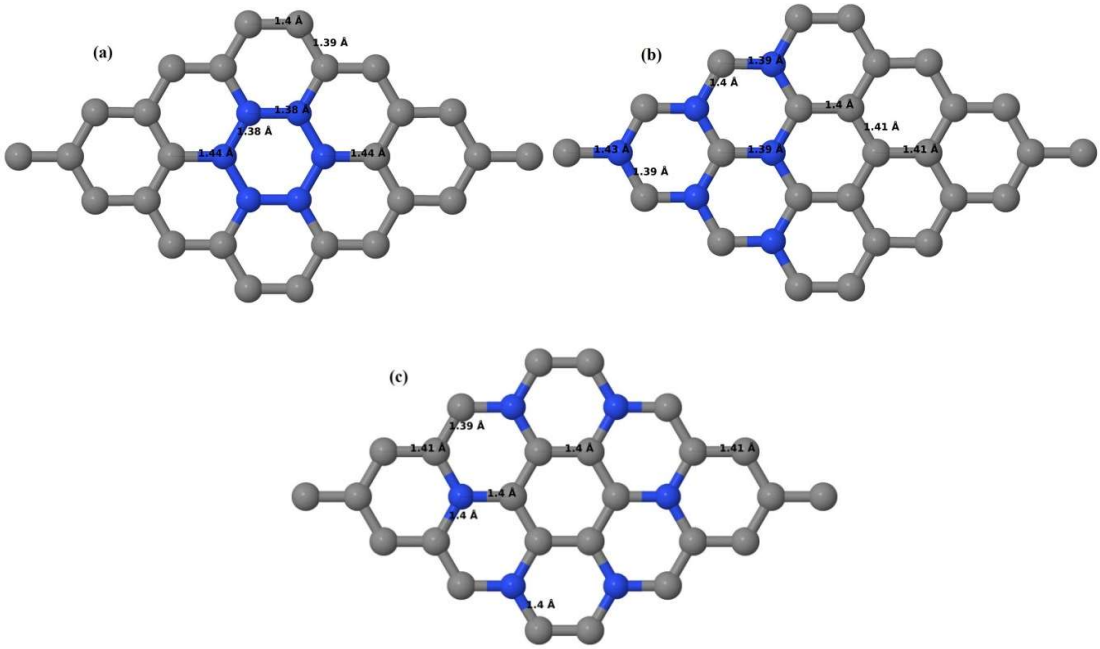

Figure 7.26 (a)-(c) Optimized structures of 4 × 4 graphene supercell doped with six N atoms (18.75% nitrogen concentration) with different doping configurations.

The relaxed lattice constant decreases from 2.458 Å to 2.431 Å for six N-doped 4 × 4 graphene supercell (corresponding to 18.75% N concentration), as observed in other N-doped graphene systems. Similar to other N-doped graphene systems, there is no geometrical distortion in the graphene systems doped with six N atoms.

All these 4 × 4 graphene systems doped with six N atoms show *n*-type metallic behaviour. At 18.75% concentration, band gap of ~1.04 eV (Figure 7.27 (b)) opens up in graphene, when

the six N atoms are located at the same sublattice sites of graphene. Upon placing the N atoms at adjacent and alternate sublattices, there is no band gap opening as evident from Figure 7.27 (a), (c), similar to that observed in graphene systems doped with six B atoms.

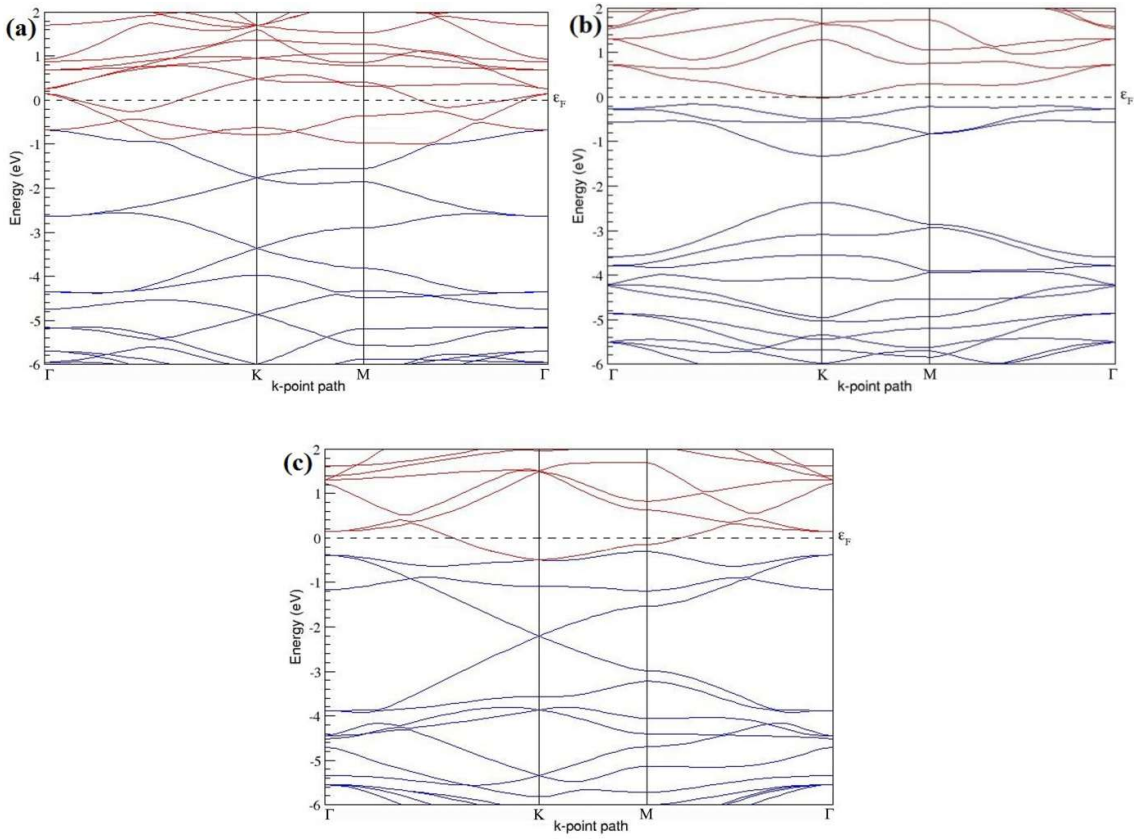

Figure 7.27 (a)-(c) Band structures of 4 × 4 graphene supercell doped with six N atoms (18.75% N concentration) corresponding to the optimized structures shown in **Figure 7.26 (a)-(c).**

Table 7.12 The N concentrations, doping configurations with considered sublattice, cohesive energies and the band gap introduced for 4 × 4 supercell doped with six N atoms.

Model	N Concentration (%)	Configuration	Considered Sublattices for dopants	E_{coh} (eV/atom)	Band gap (eV)
4 × 4	18.75	Figure 7.26 (a)	"B", A", "B", "A", "B" and "A" (adjacent)	-8.753	0
		Figure 7.26 (b)	All in "B" (same)	-8.920	1.042
		Figure 7.26 (c)	"A", "B", "B", "A", "A" and "B" (alternate)	-8.976	0

The changes in the bond lengths after B-doping can be read from the optimized structures shown in Figures 7.3, 7.6, 7.8, 7.10, 7.12, 7.14. In all B-doped graphene systems, the bond lengths are adjusted to retain the planar geometry i.e., with long C-B bonds and relatively short adjacent C-C bonds based on the number and location of B atoms in graphene

supercells. The placement of B atoms at adjacent locations results in large B-B bond lengths in B-doped graphene systems. The large B-B bond lengths observed for the configurations with B atoms at adjacent locations (Figures 7.6 (a), 7.6 (d), 7.6 (g), 7.6 (j), 7.8 (a), 7.8 (d), 7.10 (a), 7.10 (d), 7.12 (a), 7.14 (a) could be ascribed to the large covalent radius of B than the host C atoms. The changes in the bond lengths after N doping can be read from the optimized structures shown in Figures 7.16, 7.18, 7.20, 7.22, 7.24, 7.26. The planar configuration is also maintained in all N-doped graphene systems by adjusting the associated bond lengths i.e., with short C-N and C-C bond lengths.

The obtained negative values of cohesive energies presented in Table 7.1-7.6 and Table 7.7-7.12 indicate that all the considered B- and N-doped graphene systems are energetically stable. It was also observed that the cohesive energy increases with increase in B- and N-doping concentration (Tables 7.1-7.6 and 7.7-7.12), which shows that energetic stability decreases with increasing B- and N-doping concentration. For the same doping concentration, the cohesive energy was found to be lowest for the doping configuration with dopants at alternate sublattice and highest for the doping configuration with dopants at adjacent positions. These results show that B- and N-doped graphene with dopants at alternate sublattices are more stable than that with dopants placed at adjacent and same sublattice positions.

Tables 7.1-7.6 and 7.7-7.12 show that the band gap in general increases with increase in the B- and N-doping concentration for the doping configuration with highest band gap, which is in agreement with previous reports [78]. Except in 3 × 3 and 6 × 6 graphene supercells doped with two B atoms, the band gap was found to be maximum when the B atoms are at the same sublattice and minimum when they are at adjacent positions or alternate sublattices, which is in agreement with that reported by Rani *et al.* [78]. Even though 3 × 3 and 6 × 6 graphene supercells doped with two B atoms show band gap between the valence and conduction bands, no specific dependence of band gap on the B-atom positioning could be highlighted. Apart from the presented isomers of 3 × 3 and 6 × 6 graphene supercells doped with two B atoms (corresponding to 11.11% and 2.78% B concentrations), the band structures of several other isomers for the doping configurations of adjacent, same and alternate sublattices are also calculated (which are not presented here) to check for the observed variation of band gap dependency on dopant positioning from that found in other B-doped graphene systems. The calculated band gaps in all cases of 3 × 3 and 6 × 6 graphene supercells doped with two B atoms do not follow any specific dependency on the B-doping configurations. The nature of this anomaly is still being investigated. On the other hand, 3 × 3 graphene supercell doped

with three and four B or N atoms showed highest band gap for the doping configurations with dopant atoms at same sublattices and lowest band gap for the doping configuration with dopant atoms at alternate sublattices or adjacent positions. The trend of band gap dependency on the doping configurations in all N-doped graphene systems was similar with that of corresponding B-doped graphene systems. Similar to the exception observed in the case of 3 × 3 and 6 × 6 graphene supercells doped with two B atoms, no specific correlation between band gap and doping configuration could be determined for 3 × 3 and 6 × 6 graphene supercells doped with two N atoms (corresponding to 11.11% and 2.78% N concentrations). The band gaps of 2 × 2 graphene doped with two N atoms (1.323 eV at 25% N concentration) and 4 × 4 graphene doped with six N atoms (1.042 eV at 18.75% N concentration) are found to be very close to the band gap of silicon (1.1 eV).

The observed band gaps for the considered B or N concentrations corresponding to the most stable configurations are summarized in Table 7.13. For the most probable configuration corresponding to the doping concentrations ranging from 2.78% to 22.22%, the observed band gaps lie within the range of 0.008-0.190 eV and 0.004-0.202 eV in B- and N-doped systems, respectively, while the most stable configuration corresponding to B- or N-concentrations of 1.39%, 5.56%, 18.75% and 25% do not show a band gap. Thus the band gap of graphene could be tailored from 0.008 eV to 0.190 eV by B-doping and from 0.004 eV to 0.202 eV by N-doping, within the concentration range of 2.78%-22.22%, excluding 5.56% and 18.75% concentrations [372].

As 2 × 2 graphene supercells doped with one B atom or one N atom and 4 × 4 graphene supercells doped with four B atoms or four N atoms correspond to the same doping concentration of 12.5%, the cohesive energies and electronic band structures of three different configurations of 4 × 4 graphene sheet doped with four B atoms or four N atoms are compared with those of the 2 × 2 graphene sheet doped with one B atom or one N atom. The widths of the band gaps for a 12.5% doping concentration simulated by 2 × 2 graphene supercell doped with one B atom or N atom and 4 × 4 graphene supercell doped with four B atoms or four N atoms are found to be almost the same only for the configuration of 4 × 4 graphene supercell doped with four B atoms or four N atoms at the same sublattice. The band gaps introduced for other configurations of 4 × 4 graphene supercell doped with four B atoms or four N atoms (adjacent and alternate sublattice positions) were observed to be comparatively small. However, the comparison of the cohesive energies of 2 × 2 graphene sheet doped with one B atom or N atom (-8.795 eV/atom and -9.029 eV/atom respectively) and 4 × 4 graphene supercell doped with four B atoms or N atoms at the same sublattice (-

8.829 eV/atom and -9.052 eV/atom respectively) indicate that cohesive energy is strongly dependent on the supercell size considered for the doping concentration. Thus, to achieve a 12.5% B or N doping concentration, 4 × 4 graphene supercell doped with four B atoms or four N atoms is more stable than 2 × 2 graphene supercell doped with one B atom or one N atom [372].

Table 7.13 The doping concentrations, most stable doping configuration and the observed band gaps.

Concentration (%)	Most stable configuration (B-doped)	Band gap (eV) (B-doped)	Most stable configuration (N-doped)	Band gap (eV) (N-doped)
1.39	Figure 7.3 (d)	0	Figure 7.16 (d)	0
2.78	Figure 7.6 (l)	0.008	Figure 7.18 (l)	0.023
3.13	Figure 7.3 (c)	0.190	Figure 7.16 (c)	0.202
5.56	Figure 7.3 (b)	0	Figure 7.16 (b)	0
6.25	Figure 7.6 (i)	0.047	Figure 7.18 (i)	0.012
9.38	Figure 7.8 (f)	0.156	Figure 7.20 (f)	0.176
11.11	Figure 7.6 (f)	0.046	Figure 7.18 (f)	0.039
12.5	Figure 7.10 (f)	0.050	Figure 7.22 (f)	0.004
15.63	Figure 7.12 (c)	0.133	Figure 7.24 (c)	0.141
16.67	Figure 7.8 (c)	0.107	Figure 7.20 (c)	0.160
18.75	Figure 7.14 (c)	0	Figure 7.26 (c)	0
22.22	Figure 7.10 (c)	0.062	Figure 7.22 (c)	0.106
25	Figure 7.6 (c)	0	Figure 7.18 (c)	0

7.4 Summary

The energetic stabilities, structural and electronic properties of B- and N-doped graphene with varying doping concentrations and several doping configurations in different graphene supercell sizes have been calculated using first-principles DFT based calculations.

7.4.1 Outcome

It was observed that both B- and N-doped graphene maintain the planar geometry of IG with a slight distortion with longer C-B and shorter C-N bonds, which is in agreement with previous reports. The doped structures with dopant atoms placed at adjacent locations have been found to be highly distorted, with less distortion in N-doped graphene systems compared to that of the corresponding B-doped graphene systems.

The stability was found to be decreasing with increase in B- and N-doping concentration. For a particular doping concentration, stability is found to be higher for the atomic configuration

with dopant atoms at alternate sublattice positions than other configurations and decreases in the order of alternate > same > adjacent. The cohesive energies of the N-doped graphene systems are found to be lower than that of similar B-doped graphene systems and hence N-doped graphene structures are considered to be more stable than their B-doped counterparts. As the doping concentration decreases, the cohesive energy difference between similar N- and B-doped graphene structures also decrease, which indicate that graphene structures with light doping of B and N atoms are highly stable.

All B-doped graphene systems exhibit *p*-type doping electronic properties as the Fermi level shifts into the valence band, whereas all N-doped graphene systems exhibit *n*-type doping electronic properties as the Fermi level shifts into the conduction band. The results also show that graphene with one B- and N-atom doping in any size of supercells have exhibited *p*-type semiconducting and *n*-type metallic characters respectively with or without band gaps based on the doping concentration. The analysis of the electronic structures of 3 × 3 and 6 × 6 graphene supercells with more than one B- or N-atoms have shown non-zero band gaps around the Dirac point, different from the zero band gap observed for one B- or N-doped 3 × 3 and 6 × 6 graphene supercells. It was also observed that for the same B- and N-doping concentration, the distribution of the dopant atoms in the crystal lattice determines the width of the introduced band gap around the Dirac point and also affect the electronic band structures. The calculations show that B- and N-doped graphene systems with more than one doping atom have exhibited *p*-type semiconducting and *n*-type metallic behaviour with or without band gaps based on the doping concentrations and doping configurations.

Except in 3 × 3 and 6 × 6 graphene supercells with two B and N dopants (corresponding to 11.11% and 2.87% doping concentrations), the band gap dependency on the dopant sites was observed to be the same, where a maximum band gap opens up when the dopant atoms are at the same sublattice and a minimum band gap opens up when the dopants are at alternate sublattices. No conceivable correlation between the band gap and the doping configurations could be deduced from the band structures of graphene with two B and N doping in 3 × 3 and 6 × 6 graphene supercells. Three and four B- and N- doped 3 × 3 graphene supercells show similar band gap dependency on the dopant locations that has been observed with other supercells which are non-multiples of three. The results from the calculations indicate that band gap can be adjusted as required using B- and N-substitutional dopants based on the doping concentration and the doping configuration.

For the most probable configuration corresponding to the doping concentrations ranging from 2.78% to 22.22%, the observed band gaps lie within the range of 0.008-0.190 eV and 0.004-0.202 eV in B- and N-doped graphene systems, respectively, while the most stable configurations corresponding to B- or N-concentrations of 1.39%, 5.56%, 18.75% and 25% do not show a band gap. Thus, the band gap of graphene could be tailored from 0.008 eV to 0.190 eV by B-doping and from 0.004 eV to 0.202 eV by N-doping, within the concentration range of 2.78%-22.22%, excluding 5.56% and 18.75% concentrations.

7.4.2 Applications

The opening of a tunable band gap in graphene using B- and N-substitutional dopant atoms is beneficial for enabling graphene applications in electronics. The tailoring of band gap of graphene by varying the doping concentration and the doping configurations could be used for design and development of future graphene-based electronic devices such as p-n junction diodes, field effect transistors and in energy storage devices such as solar cells, fuel cells, supercapacitors etc.

7.4.3 Limitations

This work is limited to the investigation of the structural, energetic, and electronic properties of B- and N-doped graphene. This work can be extended to other experimentally demonstrated doped graphenes such as Si-, S- and P-doped graphene. In this work, simulation of doped graphene systems with varying doping concentrations have been performed by introducing B- and N-substitutional dopants in 3N × 3N graphene supercells where N = 1, 2, (3N-1) × (3N-1), and (3N+1) × (3N+1) graphene supercells where N=1. Hence, B- and N-dopant concentrations between 1.39% and 25% are only considered in the work. Other dopant concentrations can be simulated by varying the number of dopants in larger supercells. The simulation of larger graphene supercells with several dopant atoms require access to advanced computational facilities. Only cohesive energies and energy band gap between the valence and conduction bands have been calculated for all the considered doped systems. The estimation of electron effective mass and electron mobility can provide more insights into the applicability of the doped graphene systems for device applications. Therefore, apart from the calculations of cohesive energies and energy gap, the effective mass and the mobility of doped graphene systems also need to be explored.

CONCLUSIONS

Gas sensing technology is emerging as one of the prominent application in intelligent systems and is receiving increasing attention in both industry and academia. With ever-growing environmental concerns, the detection and monitoring of various gaseous species released during industrial, greenhouse processes are of critical importance in environmental monitoring, industrial chemical processing, public safety, food, agriculture, medicine and indoor air quality control. The standard metal oxide semiconductor based gas sensors used now-a-days for gas detection suffer from long recovery periods, low selectivity and demand elevated temperature operation (200° to 600° C), which restricted their applications in rapidly changing gaseous environments. The increasing demand for highly sensitive, selective, cost-effective, low power consuming, stable and portable sensors has stimulated extensive research on new sensing materials.

Graphene, a one-atom-thick sheet of carbon atoms arranged in a hexagonal crystal structure, has shown great promise for gas sensing applications owing to its excellent structural and electrical properties. Endowed with high surface area, chemically reactive sites and tunable chemical and electronic properties, graphene derivatives such as graphene oxide and reduced graphene oxide have already demonstrated a superior gas sensing activity over pristine nanostructured metal oxide, CNTs and conductive polymers. Even though both carbon-based nanomaterials such as CNTs and graphene possess peculiar electrical properties that suit them for promising gas sensing applications, the demonstrated higher sensitivity of graphene based materials over CNTs could be attributed to the greatest possible surface area per unit volume (sensing area greater than of CNTs having 1D structure). Moreover, the planar structure of graphene is more suitable to use in standard microlithography systems which make device integration with graphene easier than that of CNTs. In further advancement, the modification of the graphene surface was found to be highly successful in achieving high sensitivity and providing selectivity for a specific gas. The inclusion of the active functionality on the graphene surface was reported to enhance the detection limit, response time at ambient temperatures which are key parameters for enhanced gas sensor system. These great improvements in sensor parameters compared to unmodified graphene are due to the combined effect of the advantages of individual properties of graphene and modifiers.

Modelling of graphene-gas molecule adsorption systems has verified weak physisorption of gas molecules on intrinsic graphene, which poses a major limitation for future applications of graphene-based gas sensors. Graphene oxide and reduced graphene oxide have shown highly

sensitive sensing response compared to intrinsic graphene, by virtue of the surface rich oxygen-containing functional groups. Both experimental and theoretical studies have revealed that the interactions of graphene with gas molecules could be improved by heteroatom doping of graphene.

Quantum mechanical based theoretical calculations on gas molecular adsorption on intrinsic and different heteroatom-doped graphene enable us to better understand the processes involved in the sensing mechanisms and help us in identifying suitable doping on graphene that can lead to high sensitivity sensing of gas molecules, before carrying out the costly experimental analysis. The objective of this thesis was to investigate the influence of the adsorption of various gas molecules on the structural and electronic properties of intrinsic and different heteroatom-doped graphene for analyzing the doping effects on the reactivity of graphene towards gas molecules and thus for utilizing the unique characteristics of graphene in designing highly sensitive gas sensors for practical gas detection applications.

The adsorptions of small gas molecules (CO, NO, NO_2 and H_2O) on B-, Al- and Ga-doped graphene studied using DFT calculations for enabling their potential usage as toxic gas sensing materials in the presence of water vapour have shown that B-doped graphene exhibits similar structural and electronic properties before and after CO and H_2O adsorption, suggesting weak physisorption of CO and H_2O on its surface. The structural and electronic properties of B-doped graphene are found to be strongly affected by the adsorption of NO and NO_2, due to strong molecule-graphene interactions. Hence B-doped graphene could be used as a good gas sensor for detecting NO and NO_2 molecules in the presence of water vapour. Also, B-doped graphene is not a suitable choice for detecting the presence of CO.

The large adsorption energies and short binding distances of CO, NO, NO_2 and H_2O on Al- and Ga-doped graphene indicate the chemisorption of CO, NO, NO_2 and H_2O on Al- or Ga-doped graphene. The Hirshfeld charge distribution analysis, electronic band structures and density of states of the CO-, NO-, NO_2- and H_2O-adsorbed-doped graphene systems proved that the electronic properties of Al- and Ga-doped graphene are sensitive to CO, NO, NO_2 and H_2O molecules. The local curvature in the ground state configuration of graphene doped with Al and Ga due to the large dopant atom-carbon bond length results in high reactivity of Al- and Ga-doped graphene towards these gas molecules. The observed high sensitivity of Al- and Ga-doped graphene to toxic gas molecules such as CO, NO and NO_2 can be exploited for developing highly selective CO, NO and NO_2 sensors. But the presence of water vapour basically limits the practical applications of Al- and Ga-doped graphene structures as efficient toxic-gas sensing materials.

Density functional calculations on the adsorption of O_2 on Ga-doped graphene performed to analyze the sensitivity of Ga-doped graphene to O_2 molecule in air have shown the chemisorption of O_2 on Ga-doped graphene. The dramatic change of atomic and electronic structures of Ga-doped graphene by the adsorbed O_2 molecule reveals the sensitivity of Ga-doped graphene to O_2, which affects its sensing response towards other harmful gases and thus prevents the potential usage of Ga-doped graphene as toxic gas sensors.

The adsorption of H_2S on intrinsic graphene, P- and S-doped graphene sheets was explored using first-principles density functional approach to analyse the influence of P and S dopants on the reactivity of graphene towards H_2S molecule. The structural and electronic properties of intrinsic graphene, P- and S-doped graphene are found to be insensitive to the adsorption of H_2S. The presence of P and S atoms has negligible effect on the H_2S gas sensing properties of graphene. H_2S molecule is found to be physisorbed on intrinsic graphene, P- and S-doped graphene sheets with small adsorption energies and large binding distances. The Hirshfeld charge distribution analysis of the structures also showed negligible charge transfer between H_2S and intrinsic or doped graphene sheets. The analysis of the electronic band structures and DOS of P- and S-doped graphene before and after H_2S adsorption indicate that H_2S adsorption would not result in significant change in their electrical conductivities. It was observed that the local curvature induced by P and S doping resulting from the larger size of the dopant than that of carbon, does not enhance the reactivity of graphene to H_2S.

DFT calculations for the adsorption of N_2O on intrinsic, heteroatom-doped (B, N, Si, P, Ga, Cr and Mn) graphene sheets performed to investigate the effects of these dopants on the N_2O gas sensing properties of graphene have shown weak interactions of intrinsic, B-, N-, Si- and P-doped graphenes with N_2O molecule. The results suggest that intrinsic, B-, N-, Si- and P-doped graphene are not sensitive for N_2O molecule. The interaction between graphene and N_2O was found to be greatly improved by the introduction of Ga-dopant in the graphene structure. The large adsorption energies and short binding distances observed for N_2O adsorbed on Cr- and Mn-doped graphenes suggest that the interactions between N_2O and Cr- or Mn-doped graphene involve chemisorption. The charge distribution analysis, band structure and DOS plots of Ga-, Cr- and Mn-doped graphene without and with adsorbed N_2O molecule show that the electronic properties of Ga-, Cr- and Mn-doped graphenes are sensitive to the adsorption of a single N_2O molecule. The results also indicate that Cr- and Mn-doped graphene are most suitable choices as sensing materials for the detection of N_2O gas.

From the DFT based analysis of the structural properties of B- and N-doped graphene with varying doping concentrations and several doping configurations, it was found that the planar

hexagonal geometry of the graphene sheet remains unchanged even after substitutional B- and N-doping, but experiences large changes in the associated bond lengths. The cohesive energies of the doped graphene systems increase with increasing doping concentration and thus the energetic stabilities of doped systems decrease with increase in doping concentration. N-doped graphene structures are more stable than their B-doped counterparts. For all the doping concentrations considered, the structures with the dopant atoms at alternate sublattices of graphene have been found to have the lowest cohesive energies and therefore form the most stable structures. For a particular doping concentration, stability decreases in the order of alternate > same > adjacent. As the doping concentration decreases, the cohesive energy difference between similar N- and B-doped graphene structures also decrease, which indicate that graphene structures with light doping of B and N atoms are highly stable.

The band gap increases with increase in B- and N-dopant concentration (for the configuration with the highest band gap). The distribution of the dopant atoms in the crystal lattice also determines the stabilities and width of the introduced band gap in the electronic structure. The analysis of the electronic structures of 3 × 3 and 6 × 6 graphene supercells with more than one B- or N-atoms have shown non-zero band gaps around the Dirac point, different from the zero band gap observed for one B- or N-doped 3 × 3 and 6 × 6 graphene supercells. The calculations show that all B- and N-doped graphene systems have exhibited *p*-type semiconducting and *n*-type metallic behaviour with or without band gaps based on the doping concentrations and doping configurations.

Except in 3 × 3 and 6 × 6 graphene supercells with two B and N dopants (corresponding to 11.11% and 2.87% doping concentrations), the band gap dependency on the dopant sites was observed to be the same, where a maximum band gap opens up when the dopant atoms are at the same sublattice and a minimum band gap opens up when the dopants are at alternate sublattices. No conceivable correlation between the band gap and the doping configurations could be deduced from the band structures of graphene with two B and N doping in 3 × 3 and 6 × 6 graphene supercells. Three and four B- and N-doped 3 × 3 graphene supercells show similar band gap dependency on the dopant locations that has been observed with other supercells which are non-multiples of three. The results from the first-principles simulations indicate that the band gap of graphene can be tailored as required using B- and N-dopants according to the choice of the supercell *i.e.* the dopant density and substitutional dopant configurations, which would be helpful for fabricating graphene-based nano-electronic devices.

SPECIFIC CONTRIBUTIONS

The contributions of this thesis are predictions on the applicability of different doped graphenes as sensitive gas sensing materials for the detection of several toxic gases by investigating the influence of adsorption of gas molecules on the structural and electronic properties of different doped graphenes.

The predictions from the simulation based studies of the adsorption of several gas molecules on intrinsic and doped graphenes using quantum mechanical calculations within the framework of DFT are the following:

a) The electronic properties of B-doped graphene are sensitive to NO and NO_2 molecules, but not influenced much by the adsorption of CO and H_2O molecules. Therefore B-doped graphene could be used as a good gas sensor for detecting NO and NO_2 molecules in the presence of water vapour. The weak sensitivity of B-doped graphene towards CO molecule suggests that B-doped graphene is not suitable for CO gas sensing applications.
b) Al- and Ga-doped graphene show significantly enhanced interactions with CO, NO and NO_2 through the formation of strong chemical bonds between the dopant atom (Al or Ga) and the adsorbed gas molecule. The chemisorptions of CO, NO and NO_2 on Al- and Ga-doped graphene induce notable changes in their electronic properties and hence they are expected to be used as promising sensing materials for detecting toxic gases such as CO, NO and NO_2. The strong interactions between H_2O and Al- and Ga-doped graphene significantly affect the sensitivity of these doped graphenes towards other gas molecules, which practically limit their applications as novel toxic-gas sensors.
c) Molecular oxygen present in the air also get strongly adsorbed on the surface of Ga-doped graphene which leads to false alarm and thus affects its sensitivity to other toxic gases, preventing the utilization of Ga-doped graphene as toxic gas sensors.
d) The physisorption of H_2S on intrinsic, P- and S-doped graphene sheets show weak sensitivity of intrinsic, P- and S-doped graphene towards H_2S molecule and hence it could be suggested that graphene doped with P and S atoms are not suitable for sensing H_2S gas.
e) The weak interactions of N_2O with intrinsic, B-, N-, Si-, P-doped graphene sheets indicate that they are not suitable for sensing N_2O molecule. The chemisorption of

N_2O on Ga-doped graphene indicates that Ga-doped graphene can be used to detect N_2O. The structural and electronic properties of Cr- and Mn-doped graphene are also found to be highly sensitive to the adsorption of N_2O, which make Cr- and Mn-doped graphene as promising gas sensing materials for detecting N_2O.

This thesis also discusses the recent advancements in graphene based gas sensors with emphasis on the use of modified graphene materials. Experimental works on the applications of intrinsic and modified graphene as gas sensors and theoretical researches on structural modifications of graphene for its effective utilization as sensitive and selective gas sensing materials have been reviewed in the article entitled "Recent advances in graphene based gas sensors" published in Sensors and Actuators B: Chemical (2015), 218, 160-183. Chapter 2 of the thesis which is based on the published review article describes various graphene modification methods such as the introduction of dopants and defects, decoration with metal/metal oxide nanoparticles, and functionalization with polymers. The most recent progress in first-principles simulation works on gas molecular adsorption on graphene, doped and defected graphene for exploiting their potential as gas sensors that have been discussed in a submitted book chapter is also included in Chapter 2 of the thesis. The latest developments in the area of gas sensors by employing graphene and other 2D materials beyond graphene as sensing materials, with emphasis on various sensing performance indicators have been described in detail in the published article entitled "Two-Dimensional Materials for Sensing: Graphene and Beyond" published in Multidisciplinary Digital Publishing Institute's Electronics (2015), 4(3), 651-687.

Chapter 5 of the thesis is based on the work entitled "Ab initio study on gas sensing properties of group III (B, Al, Ga) doped graphene" published in Elsevier's Computational Condensed Matter (2016), 9, 40-55 in which the adsorptions of several small gas molecules such as CO, NO, NO_2 and H_2O on B-, Al- and Ga-doped graphene have been investigated to evaluate their potential usage as toxic gas sensing elements in the atmosphere with water vapour. This chapter also describes the work entitled "Molecular Oxygen Adsorbed on Gallium Doped Graphene: A First-Principles Study", which was accepted for publication in Materials Science Forum, Trans Tech Publications, Switzerland in which the sensitivity of Ga-doped graphene to the presence of O_2 are described.

Chapter 6 of the thesis is based on a submitted book chapter in which the effect of different dopants on the N_2O gas sensing properties of graphene is discussed. This chapter also

discusses the work entitled "DFT based simulation of H_2S gas sensing properties of doped graphene", which was accepted for presentation in 8th International Conference on Nanotechnology: Fundamentals and Applications (ICNFA' 2017), June 6-8, 2017, Rome, Italy in which the effect of P and S dopants on the H_2S gas sensing properties have been described.

Chapter 7 is based on the work entitled "Energetic Stabilities, Structural and Electronic Properties of Monolayer Graphene doped with Boron and Nitrogen Atoms" published in Multidisciplinary Digital Publishing Institute's Electronics Journal (2016), 5(4), 91 in which the structural, energetic and electronic properties of monolayer graphene doped with boron and nitrogen at varying concentrations and with different configurations are investigated. The contributions of chapter 7 of the thesis on the calculations of energetic stabilities, structural and electronic properties of graphene doped with B and N atoms are as follows:

a) The energetic stabilities decrease with increasing B- and N-dopant concentration. N-doped graphene structures are more stable than corresponding B-doped counterparts. The doped structures with dopant atoms placed at adjacent locations have been found to be highly distorted, with less distortion in N-doped graphene systems compared to that of the corresponding B-doped graphene systems. For a particular doping concentration, stability is found to be higher for the atomic configuration with dopant atoms at alternate sublattice positions than other configurations and decreases in the order of alternate > same > adjacent.
b) The analysis of the electronic structures of 3 × 3 and 6 × 6 graphene supercells with more than one B- or N-atoms have shown non-zero band gaps around the Dirac point, different from the zero band gap observed for one B- or N-doped 3 × 3 and 6 × 6 graphene supercells.
c) From the electronic band structure calculations of all considered B- and N-doped graphene systems, it was found that B- and N-doped graphene systems have exhibited *p*-type semiconducting and *n*-type metallic behaviour with or without band gaps based on the doping concentrations and doping configurations.
d) Except in 3 × 3 and 6 × 6 graphene supercells with two B and N dopants (corresponding to 11.11% and 2.87% doping concentrations), the band gap dependency on the dopant sites was observed to be the same, where a maximum band gap opens up when the dopant atoms are at the same sublattice and a minimum band gap opens up when the dopants are at alternate sublattices. No conceivable correlation between the band gap and the doping configurations could be deduced from the band

structures of graphene with two B and N doping in 3 × 3 and 6 × 6 graphene supercells. Three and four B- and N- doped 3 × 3 graphene supercells show similar band gap dependency on the dopant locations that has been observed with other supercells which are non-multiples of three.

FUTURE SCOPE OF WORK

In spite of the great advancements in the field of graphene-based gas sensors during the past 10 years, there are some major challenges that need to overcome to meet the increasing demands of the industry for developing high performance gas sensors. Stronger binding of gas molecules required for gas sensing applications, achieved by doped graphenes would result in noticeable changes in electrical conductivity of doped graphenes upon exposure to gases. The main drawback with doped graphene-based gas sensors is the long recovery period, as the thermal energy at room temperature is not sufficient to overcome the activation energy required for releasing the strongly adsorbed gas molecules from the surface. The adsorption and desorption processes on intrinsic graphene are energetically viable as compared to the chemisorption on doped graphenes. Strong adsorption on the surface of doped graphenes makes gas desorption extremely difficult without the assistance of ultra-violet light illumination or annealing at high temperatures or by the application of an electric field. These treatments make the adsorption process reversible in practical time periods. Thus, a proper balance should be maintained between sensitivity and recovery of the doped graphene-based gas sensors. Doped graphene-based gas sensors are best choices for ultrahigh sensitivity detection of gas molecules, but as just “on off” sensors. Hence future work needs to focus on functionalization schemes that could control the binding energy of the gas molecules on doped graphenes which could enable fast regeneration of the sensor at room temperature.

As most of the doped graphenes get strongly influenced by a range of different gas species and mixtures, specific identification of gases by selective adsorption is challenging. The high sensitivity of the several doped graphene structures to most of the gases makes them uninteresting for developing selective gas sensing devices. For example, Al- and Ga-doped graphene have shown high chemical reactivity to almost all gases and hence Al- and Ga-doped graphene-based sensing devices are not suitable choices for the detection of a particular gas of interest in atmospheric air, as the other constituent gases of air strongly affect the sensing signal of Al- and Ga-doped graphene for the desired gas. Similar is the case with other doped graphenes, except with a few exceptions. Several doped graphenes have demonstrated high selectivity. Among these, S-doped graphene is highly selective to NO_2, B-doped graphene is selective to NO and NO_2 in the presence of other common gas molecules, pyridinic-like N-doped graphene has shown high selectivity for CO in the presence of N_2, O_2 and NO.

Until now, most of the previous reports have investigated different modifications of graphene for improving the interactions between gas molecules and graphene and thus have focused on the analysis of sensitivity of modified graphene towards gas molecules. Only few theoretical reports have considered both sensitivity and selectivity as the key performance metrics of graphene-based gas sensors in the choice of suitable modification on graphene for achieving highly sensitive and selective gas sensors. Although single molecule NO_2 detection was demonstrated with graphene, the requirement of specialized working conditions (ultra-high vacuum) limits practical realization of ultra-high sensitive graphene based gas sensors. In addition to the focus on increased reactivity, theoretical works need to focus on selectivity aspects of graphene-based gas sensors and also on the suitability of using them under practical environments. Hence, future work on graphene-based gas sensor technology is more likely to focus on functionalization of graphene with appropriate capture agents that specifically bind the target gas to graphene's surface. Considering sensitivity and selectivity as performance indicators, newer dopants, functional molecules and fabrication methods need to be explored.

Graphene-based sensing materials need to be combined with suitable transduction platforms for enabling the development of next generation graphene-based gas sensing devices. Modelling of transducer for conductometric graphene-based gas sensors, which measures the conductance change of graphene-based sensing materials after gas adsorption, and simulations of electron transport properties of graphene-based gas sensors are required for quantitative evaluation of gas sensing characteristics of different graphenes. Hence future theoretical studies need to focus on the calculations of electrical conductance of modified graphene before and after gas adsorption to investigate the detection capability of conductometric graphene gas sensors.

The realization of highly sensitive, selective and reversible graphene-based gas sensors through hybridizing graphene with functional materials having improved activity can ultimately lead to single molecule detection of specific toxic or polluting gases at room temperature and under ambient pressure conditions. However, large scale production of graphene with high and uniform quality is still challenging. For improved approaches, comparison of existing graphene-based sensing technologies with other gas sensing materials is also critical.

Most of the sensing studies are based on the lab-scale tests, to achieve high performance devices to an industrial level; it needs graphene hybrids, which should be environmentally stable in electronic and chemical characteristics during operation. The potential of graphene-

based composites obtained by hybridizing graphene with metal, metal oxide nanoparticles, polymers, quantum dots and nanowires have been verified a number of times through large amounts of exciting research being performed for the detection of a wide range of gases over designated temperatures with enhanced sensing response and high selectivity. With a possibility of a wide range of such combinations, extremely high performance gas sensors can be expected in future using materials that have not been explored yet. Research on graphene-based ternary composites are underway and we can also expect quaternary composites based on graphene with excellent synergistic effects to come up in the future that could resolve the selectivity issue associated with graphene.

Further insights on theoretical studies are also needed to better understand the interaction mechanism between various gases and graphene-based functional nanohybrids which could facilitate the experimental/device fabrication process in advent of production of enhanced gas sensors. While such studies exist for doped and defective graphene systems, they are however either very limited or lacking for metal oxide-graphene and polymer-graphene hybrid systems. Quantum mechanical calculations and atomic scale simulation tools could be further extended to the design and modelling of metal oxide- and polymer-graphene hybrid gas sensors.

Quantum detection of gas molecules using graphene under practical conditions is not so far away from reality as the progress of research in this regime is very fast and future advances would be more centred on more efficient graphene-based composites, fabrication techniques, different preparation strategies and improved sensor designs.

REFERENCES

[1] K. S. Novoselov, A. K. Geim, S. V. Morozov, D. Jiang, Y. Zhang, S. V. Dubonos, I. V. Grigorieva, and A. A. Firsov, "Electric Field Effect in Atomically Thin Carbon Films," *Science,* vol. 306, pp. 666-669, 2004.

[2] K. S. Novoselov, A. K. Geim, S. V. Morozov, D. Jiang, M. I. Katsnelson, I. V. Grigorieva, S. V. Dubonos, and A. A. Firsov, "Two-dimensional gas of massless Dirac fermions in graphene," *Nature,* vol. 438, pp. 197-200, 2005.

[3] Y. Zhang, Y.-W. Tan, H. L. Stormer, and P. Kim, "Experimental observation of the quantum Hall effect and Berry's phase in graphene," *Nature,* vol. 438, pp. 201-204, 2005.

[4] M. I. Katsnelson, "Graphene: carbon in two dimensions," *Materials Today,* vol. 10, pp. 20-27, 2007.

[5] A. K. Geim and K. S. Novoselov, "The rise of graphene," *Nature Materials,* vol. 6, pp. 183-191, 2007.

[6] C. Lee, X. Wei, J. W. Kysar, and J. Hone, "Measurement of the Elastic Properties and Intrinsic Strength of Monolayer Graphene," *Science,* vol. 321, pp. 385-388, 2008.

[7] R. R. Nair, P. Blake, A. N. Grigorenko, K. S. Novoselov, T. J. Booth, T. Stauber, N. M. R. Peres, and A. K. Geim, "Fine Structure Constant Defines Visual Transparency of Graphene," *Science,* vol. 320, pp. 1308-1308, 2008.

[8] A. H. Castro Neto, F. Guinea, N. M. R. Peres, K. S. Novoselov, and A. K. Geim, "The electronic properties of graphene," *Reviews of Modern Physics,* vol. 81, pp. 109-162, 2009.

[9] A. K. Geim, "Graphene: Status and Prospects," *Science,* vol. 324, pp. 1530-1534, 2009.

[10] M. F. Craciun, S. Russo, M. Yamamoto, and S. Tarucha, "Tuneable electronic properties in graphene," *Nano Today,* vol. 6, pp. 42-60, 2011.

[11] K. S. Novoselov, V. I. Falko, L. Colombo, P. R. Gellert, M. G. Schwab, and K. Kim, "A roadmap for graphene," *Nature,* vol. 490, pp. 192-200, 2012.

[12] V. Singh, D. Joung, L. Zhai, S. Das, S. I. Khondaker, and S. Seal, "Graphene based materials: Past, present and future," *Progress in Materials Science,* vol. 56, pp. 1178-1271, 2011.

[13] F. Bonaccorso, Z. Sun, T. Hasan, and A. C. Ferrari, "Graphene photonics and optoelectronics," *Nature Photonics,* vol. 4, pp. 611-622, 2010.

[14] I. Lahiri, V. P. Verma, and W. Choi, "An all-graphene based transparent and flexible field emission device," *Carbon,* vol. 49, pp. 1614-1619, 2011.

[15] G. Zhao, T. Wen, C. Chen, and X. Wang, "Synthesis of graphene-based nanomaterials and their application in energy-related and environmental-related areas," *RSC Advances,* vol. 2, pp. 9286-9303, 2012.

[16] N. O. Weiss, H. Zhou, L. Liao, Y. Liu, S. Jiang, Y. Huang, and X. Duan, "Graphene: An Emerging Electronic Material," *Advanced Materials,* vol. 24, pp. 5782-5825, 2012.

[17] J. Zhu, D. Yang, Z. Yin, Q. Yan, and H. Zhang, "Graphene and Graphene-Based Materials for Energy Storage Applications," *Small,* vol. 10, pp. 3480-3498, 2014.

[18] L. Tao, D. Wang, S. Jiang, Y. Liu, Q. Xie, H. Tian, N. Deng, X. Wang, Y. Yang, and T.-L. Ren, "Fabrication techniques and applications of flexible graphene-based electronic devices," *Journal of Semiconductors,* vol. 37, p. 041001, 2016.

[19] S. S. Varghese, S. Lonkar, K. K. Singh, S. Swaminathan, and A. Abdala, "Recent advances in graphene based gas sensors," *Sensors and Actuators B: Chemical,* vol. 218, pp. 160-183, 2015.

[20] S. Varghese, S. Varghese, S. Swaminathan, K. Singh, and V. Mittal, "Two-Dimensional Materials for Sensing: Graphene and Beyond," *Electronics,* vol. 4, p. 651, 2015.
[21] Y. Shao, J. Wang, H. Wu, J. Liu, I. A. Aksay, and Y. Lin, "Graphene Based Electrochemical Sensors and Biosensors: A Review," *Electroanalysis,* vol. 22, pp. 1027-1036, 2010.
[22] Q. He, S. Wu, Z. Yin, and H. Zhang, "Graphene-based electronic sensors," *Chemical Science,* vol. 3, pp. 1764-1772, 2012.
[23] Y. Liu, X. Dong, and P. Chen, "Biological and chemical sensors based on graphene materials," *Chemical Society Reviews,* vol. 41, pp. 2283-2307, 2012.
[24] S. Basu and P. Bhattacharyya, "Recent developments on graphene and graphene oxide based solid state gas sensors," *Sensors and Actuators B: Chemical,* vol. 173, pp. 1-21, 2012.
[25] W. Yuan and G. Shi, "Graphene-based gas sensors," *Journal of Materials Chemistry A,* vol. 1, pp. 10078-10091, 2013.
[26] T. Wang, D. Huang, Z. Yang, S. Xu, G. He, X. Li, N. Hu, G. Yin, D. He, and L. Zhang, "A Review on Graphene-Based Gas/Vapor Sensors with Unique Properties and Potential Applications," *Nano-Micro Letters,* vol. 8, pp. 95-119, 2016.
[27] E. W. Hill, A. Vijayaragahvan, and K. Novoselov, "Graphene Sensors," *IEEE Sensors Journal,* vol. 11, pp. 3161-3170, 2011.
[28] F. Yavari and N. Koratkar, "Graphene-Based Chemical Sensors," *The Journal of Physical Chemistry Letters,* vol. 3, pp. 1746-1753, 2012.
[29] U. Latif and F. L. Dickert, "Graphene Hybrid Materials in Gas Sensing Applications," *Sensors,* vol. 15, pp. 30504-30524, 2015.
[30] F. Schedin, A. K. Geim, S. V. Morozov, E. W. Hill, P. Blake, M. I. Katsnelson, and K. S. Novoselov, "Detection of individual gas molecules adsorbed on graphene," *Nature Materials,* vol. 6, pp. 652-655, 2007.
[31] Y. Dan., "Nanowire and Graphene-Based Vapor Sensors for Electronic Nose Applications," Ph. D. dissertation, Department of Electrical and Systems Engineering, University of Pennsylvania, Ann Arbor, Michigan, USA, 2008.
[32] O. Leenaerts, B. Partoens, and F. M. Peeters, "Adsorption of H_2O, NH_3, CO, NO_2, and NO on graphene: A first-principles study," *Physical Review B,* vol. 77, p. 125416, 2008.
[33] P. Giannozzi, R. Car, and G. Scoles, "Oxygen adsorption on graphite and nanotubes," *The Journal of Chemical Physics,* vol. 118, pp. 1003-1006, 2003.
[34] J. Dai, P. Giannozzi, and J. Yuan, "Adsorption of pairs of NO_x molecules on single-walled carbon nanotubes and formation of NO + NO_3 from NO_2," *Surface Science,* vol. 603, pp. 3234-3238, 2009.
[35] Y. Zou, F. Li, Z. H. Zhu, M. W. Zhao, X. G. Xu, and X. Y. Su, "An ab initio study on gas sensing properties of graphene and Si-doped graphene," *The European Physical Journal B,* vol. 81, pp. 475-479, 2011.
[36] Z. Yong-Hui, C. Ya-Bin, Z. Kai-Ge, L. Cai-Hong, Z. Jing, Z. Hao-Li, and P. Yong, "Improving gas sensing properties of graphene by introducing dopants and defects: a first-principles study," *Nanotechnology,* vol. 20, p. 185504, 2009.
[37] Z. M. Ao, J. Yang, S. Li, and Q. Jiang, "Enhancement of CO detection in Al doped graphene," *Chemical Physics Letters,* vol. 461, pp. 276-279, 2008.
[38] M. Chi and Y.-P. Zhao, "Adsorption of formaldehyde molecule on the intrinsic and Al-doped graphene: A first principle study," *Computational Materials Science,* vol. 46, pp. 1085-1090, 2009.
[39] J. Dai, J. Yuan, and P. Giannozzi, "Gas adsorption on graphene doped with B, N, Al, and S: A theoretical study," *Applied Physics Letters,* vol. 95, p. 232105, 2009.

[40] L. Shao, G. Chen, H. Ye, Y. Wu, Z. Qiao, Y. Zhu, and H. Niu, "Sulfur dioxide adsorbed on graphene and heteroatom-doped graphene: a first-principles study," *The European Physical Journal B,* vol. 86, pp. 1-5, 2013.

[41] Y.-H. Zhang, L.-F. Han, Y.-H. Xiao, D.-Z. Jia, Z.-H. Guo, and F. Li, "Understanding dopant and defect effect on H_2S sensing performances of graphene: A first-principles study," *Computational Materials Science,* vol. 69, pp. 222-228, 2013.

[42] H.-p. Zhang, X.-g. Luo, X.-y. Lin, X. Lu, Y. Leng, and H.-t. Song, "Density functional theory calculations on the adsorption of formaldehyde and other harmful gases on pure, Ti-doped, or N-doped graphene sheets," *Applied Surface Science,* vol. 283, pp. 559-565, 2013.

[43] S. Sharma and A. S. Verma, "A theoretical study of H_2S adsorption on graphene doped with B, Al and Ga," *Physica B: Condensed Matter,* vol. 427, pp. 12-16, 2013.

[44] Y. Avila, G. H. Cocoletzi, and M. T. Romero, "First principles calculations of phenol adsorption on pristine and group III (B, Al, Ga) doped graphene layers," *Journal of Molecular Modeling,* vol. 20, pp. 1-9, 2014.

[45] X.-Y. Liu and J.-M. Zhang, "Formaldehyde molecule adsorbed on doped graphene: A first-principles study," *Applied Surface Science,* vol. 293, pp. 216-219, 2014.

[46] B. Wanno and C. Tabtimsai, "A DFT investigation of CO adsorption on VIIIB transition metal-doped graphene sheets," *Superlattices and Microstructures,* vol. 67, pp. 110-117, 2014.

[47] L. Ma, J.-M. Zhang, K.-W. Xu, and V. Ji, "A first-principles study on gas sensing properties of graphene and Pd-doped graphene," *Applied Surface Science,* vol. 343, pp. 121-127, 2015.

[48] A. S. Rad, "First principles study of Al-doped graphene as nanostructure adsorbent for NO_2 and N_2O: DFT calculations," *Applied Surface Science,* vol. 357, Part A, pp. 1217-1224, 2015.

[49] A. Shokuhi Rad and V. Pouralijan Foukolaei, "Density functional study of Al-doped graphene nanostructure towards adsorption of CO, CO_2 and H_2O," *Synthetic Metals,* vol. 210, Part B, pp. 171-178, 2015.

[50] A. S. Rad, "Al-doped graphene as a new nanostructure adsorbent for some halomethane compounds: DFT calculations," *Surface Science,* vol. 645, pp. 6-12, 2016.

[51] A. S. Rad, S. S. Shabestari, S. Mohseni, and S. A. Aghouzi, "Study on the adsorption properties of O_3, SO_2, and SO_3 on B-doped graphene using DFT calculations," *Journal of Solid State Chemistry,* vol. 237, pp. 204-210, 2016.

[52] A. Shokuhi Rad, M. Esfahanian, S. Maleki, and G. Gharati, "Application of carbon nanostructures toward SO_2 and SO_3 adsorption: a comparison between pristine graphene and N-doped graphene by DFT calculations," *Journal of Sulfur Chemistry,* vol. 37, pp. 176-188, 2016.

[53] W. Wang, Y. Zhang, C. Shen, and Y. Chai, "Adsorption of CO molecules on doped graphene: A first-principles study," *AIP Advances,* vol. 6, p. 025317, 2016.

[54] Y.-a. Lv, G.-l. Zhuang, J.-g. Wang, Y.-b. Jia, and Q. Xie, "Enhanced role of Al or Ga-doped graphene on the adsorption and dissociation of N_2O under electric field," *Physical Chemistry Chemical Physics,* vol. 13, pp. 12472-12477, 2011.

[55] Y. Chen, B. Gao, J.-X. Zhao, Q.-H. Cai, and H.-G. Fu, "Si-doped graphene: an ideal sensor for NO- or NO_2-detection and metal-free catalyst for N_2O-reduction," *Journal of Molecular Modeling,* vol. 18, pp. 2043-2054, 2012.

[56] H.-p. Zhang, X.-g. Luo, H.-t. Song, X.-y. Lin, X. Lu, and Y. Tang, "DFT study of adsorption and dissociation behavior of H_2S on Fe-doped graphene," *Applied Surface Science,* vol. 317, pp. 511-516, 2014.

[57] H.-p. Zhang, X.-g. Luo, X.-y. Lin, X. Lu, and Y. Leng, "Density functional theory calculations of hydrogen adsorption on Ti-, Zn-, Zr-, Al-, and N-doped and intrinsic

graphene sheets," *International Journal of Hydrogen Energy,* vol. 38, pp. 14269-14275, 2013.
[58] Y. Sun, L. Chen, F. Zhang, D. Li, H. Pan, and J. Ye, "First-principles studies of HF molecule adsorption on intrinsic graphene and Al-doped graphene," *Solid State Communications,* vol. 150, pp. 1906-1910, 2010.
[59] A. S. Rad, "Al-doped graphene as modified nanostructure sensor for some ether molecules: Ab-initio study," *Synthetic Metals,* vol. 209, pp. 419-425, 2015.
[60] D. Borisova, V. Antonov, and A. Proykova, "Hydrogen sulfide adsorption on a defective graphene," *International Journal of Quantum Chemistry,* vol. 113, pp. 786-791, 2013.
[61] Q. Zhou, L. Yuan, X. Yang, Z. Fu, Y. Tang, C. Wang, and H. Zhang, "DFT study of formaldehyde adsorption on vacancy defected graphene doped with B, N, and S," *Chemical Physics,* vol. 440, pp. 80-86, 2014.
[62] C. Ma, X. Shao, and D. Cao, "Nitrogen-doped graphene as an excellent candidate for selective gas sensing," *Science China Chemistry,* vol. 57, pp. 911-917, 2014.
[63] Q. Zhou, C. Wang, Z. Fu, Y. Tang, and H. Zhang, "Adsorption of formaldehyde molecule on Stone–Wales defected graphene doped with Cr, Mn, and Co: A theoretical study," *Computational Materials Science,* vol. 83, pp. 398-402, 2014.
[64] K. I. Bolotin, K. J. Sikes, Z. Jiang, M. Klima, G. Fudenberg, J. Hone, P. Kim, and H. L. Stormer, "Ultrahigh electron mobility in suspended graphene," *Solid State Communications,* vol. 146, pp. 351-355, 2008.
[65] K. I. Bolotin, F. Ghahari, M. D. Shulman, H. L. Stormer, and P. Kim, "Observation of the fractional quantum Hall effect in graphene," *Nature,* vol. 462, pp. 196-199, 2009.
[66] X. Du, I. Skachko, A. Barker, and E. Y. Andrei, "Approaching ballistic transport in suspended graphene," *Nature Nanotechnology,* vol. 3, pp. 491-495, 2008.
[67] P. Avouris, Z. Chen, and V. Perebeinos, "Carbon-based electronics," *Nature Nanotechnology,* vol. 2, pp. 605-615, 2007.
[68] K. F. Mak, C. H. Lui, J. Shan, and T. F. Heinz, "Observation of an Electric-Field-Induced Band Gap in Bilayer Graphene by Infrared Spectroscopy," *Physical Review Letters,* vol. 102, p. 256405, 2009.
[69] D. W. Boukhvalov and M. I. Katsnelson, "Tuning the gap in bilayer graphene using chemical functionalization: Density functional calculations," *Physical Review B,* vol. 78, p. 085413, 2008.
[70] M. Y. Han, B. Özyilmaz, Y. Zhang, and P. Kim, "Energy Band-Gap Engineering of Graphene Nanoribbons," *Physical Review Letters,* vol. 98, p. 206805, 2007.
[71] Y. H. Lu, W. Chen, Y. P. Feng, and P. M. He, "Tuning the Electronic Structure of Graphene by an Organic Molecule," *The Journal of Physical Chemistry B,* vol. 113, pp. 2-5, 2009.
[72] L. S. Panchakarla, K. S. Subrahmanyam, S. K. Saha, A. Govindaraj, H. R. Krishnamurthy, U. V. Waghmare, and C. N. R. Rao, "Synthesis, Structure, and Properties of Boron- and Nitrogen-Doped Graphene," *Advanced Materials,* vol. 21, pp. 4726-4730, 2009.
[73] P. A. Denis, "Band gap opening of monolayer and bilayer graphene doped with aluminium, silicon, phosphorus, and sulfur," *Chemical Physics Letters,* vol. 492, pp. 251-257, 2010.
[74] A. Lherbier, X. Blase, Y.-M. Niquet, F. Triozon, and S. Roche, "Charge Transport in Chemically Doped 2D Graphene," *Physical Review Letters,* vol. 101, p. 036808, 2008.
[75] M. Wu, C. Cao, and J. Z. Jiang, "Light non-metallic atom (B, N, O and F)-doped graphene: a first-principles study," *Nanotechnology,* vol. 21, p. 505202, 2010.

[76] J. M. García-Lastra, "Strong dependence of band-gap opening at the Dirac point of graphene upon hydrogen adsorption periodicity," *Physical Review B,* vol. 82, p. 235418, 2010.
[77] M. WoiŃSka, K. Milowska, and J. A. Majewski, "Ab Initio Modeling of Graphene Functionalized with Boron and Nitrogen," *Acta Physica Polonica, A.,* vol. 122, pp. 1087-1089, 2012.
[78] P. Rani and V. K. Jindal, "Designing band gap of graphene by B and N dopant atoms," *RSC Advances,* vol. 3, pp. 802-812, 2013.
[79] P. Lazar, R. Zboril, M. Pumera, and M. Otyepka, "Chemical nature of boron and nitrogen dopant atoms in graphene strongly influences its electronic properties," *Physical Chemistry Chemical Physics,* vol. 16, pp. 14231-14235, 2014.
[80] Z. Ye-Cheng, Z. Hao-Li, and D. Wei-Qiao, "A 3 N rule for the electronic properties of doped graphene," *Nanotechnology,* vol. 24, p. 225705, 2013.
[81] B. Huang, "Electronic properties of boron and nitrogen doped graphene nanoribbons and its application for graphene electronics," *Physics Letters A,* vol. 375, pp. 845-848, 2011.
[82] S. Mukherjee and T. P. Kaloni, "Electronic properties of boron- and nitrogen-doped graphene: a first principles study," *Journal of Nanoparticle Research,* vol. 14, pp. 1-5, 2012.
[83] Z. Wang, J. Xiao, and X. Li, "Effects of heteroatom (boron or nitrogen) substitutional doping on the electronic properties of graphene nanoribbons," *Solid State Communications,* vol. 152, pp. 64-67, 2012.
[84] Z. Wang, S. Qin, and C. Wang, "Electronic and magnetic properties of single-layer graphene doped by nitrogen atoms," *The European Physical Journal B,* vol. 87, pp. 1-6, 2014.
[85] B. Jürgen, "Nanotechnology impact on sensors," *Nanotechnology,* vol. 20, p. 430206, 2009.
[86] X. Liu, S. Cheng, H. Liu, S. Hu, D. Zhang, and H. Ning, "A survey on gas sensing technology," *Sensors,* vol. 12, pp. 9635-9665, 2012.
[87] H. E. Endres, W. Göttler, R. Hartinger, S. Drost, W. Hellmich, G. Müller, C. B.-v. Braunmühl, A. Krenkow, C. Perego, and G. Sberveglieri, "A thin-film SnO_2 sensor system for simultaneous detection of CO and NO_2 with neural signal evaluation," *Sensors and Actuators B: Chemical,* vol. 36, pp. 353-357, 1996.
[88] T. Siyama and A. Kato, "A new detector for gaseous components using semiconductor thin film," *Analytical Chemistry,* vol. 34, pp. 1502-1503, 1962.
[89] A. A. Tomchenko, G. P. Harmer, B. T. Marquis, and J. W. Allen, "Semiconducting metal oxide sensor array for the selective detection of combustion gases," *Sensors and Actuators B: Chemical,* vol. 93, pp. 126-134, 2003.
[90] M. M. Arafat, B. Dinan, S. A. Akbar, and A. S. M. A. Haseeb, "Gas Sensors Based on One Dimensional Nanostructured Metal-Oxides: A Review," *Sensors,* vol. 12, p. 7207, 2012.
[91] N. Barsan and U. Weimar, "Conduction Model of Metal Oxide Gas Sensors," *Journal of Electroceramics,* vol. 7, pp. 143-167, 2001.
[92] S. Capone, A. Forleo, L. Francioso, R. Rella, P. Siciliano, J. Spadavecchia, D. Presicce, and A. Taurino, "Solid state gas sensors: state of the art and future activities," *Journal of Optoelectronics and Advanced Materials,* vol. 5, pp. 1335-1348, 2003.
[93] M. Patra, K. Manzoor, M. Manoth, S. Negi, S. Vadera, and N. Kumar, "Nanotechnology applications for chemical and biological sensors," *Defence Science Journal,* vol. 58, p. 636, 2008.

[94] S. Sharma and M. Madou, "A new approach to gas sensing with nanotechnology," *Philosophical Transactions of the Royal Society of London A: Mathematical, Physical and Engineering Sciences,* vol. 370, pp. 2448-2473, 2012.
[95] K. Kalantar-zadeh and B. Fry, *Nanotechnology-enabled sensors*. New York: Springer Science & Business Media, 2008.
[96] R. Rathi, *Core concept of nanotechnology with application spectrum*. New Delhi: SBS Publishers, 2007.
[97] G. Jimenez-Cadena, J. Riu, and F. X. Rius, "Gas sensors based on nanostructured materials," *Analyst,* vol. 132, pp. 1083-1099, 2007.
[98] Y. Cui, Q. Wei, H. Park, and C. M. Lieber, "Nanowire Nanosensors for Highly Sensitive and Selective Detection of Biological and Chemical Species," *Science,* vol. 293, pp. 1289-1292, 2001.
[99] J. Kong, N. R. Franklin, C. Zhou, M. G. Chapline, S. Peng, K. Cho, and H. Dai, "Nanotube Molecular Wires as Chemical Sensors," *Science,* vol. 287, pp. 622-625, 2000.
[100] X.-J. Huang and Y.-K. Choi, "Chemical sensors based on nanostructured materials," *Sensors and Actuators B: Chemical,* vol. 122, pp. 659-671, 2007.
[101] S. Hanna Varghese, R. Nair, B. G Nair, T. Hanajiri, T. Maekawa, Y. Yoshida, and D. Sakthi Kumar, "Sensors based on carbon nanotubes and their applications: a review," *Current Nanoscience,* vol. 6, pp. 331-346, 2010.
[102] S. Mao, G. Lu, and J. Chen, "Nanocarbon-based gas sensors: progress and challenges," *Journal of Materials Chemistry A,* vol. 2, pp. 5573-5579, 2014.
[103] E. Llobet, "Gas sensors using carbon nanomaterials: A review," *Sensors and Actuators B: Chemical,* vol. 179, pp. 32-45, 2013.
[104] P. Hu, J. Zhang, L. Li, Z. Wang, W. O'Neill, and P. Estrela, "Carbon nanostructure-based field-effect transistors for label-free chemical/biological sensors," *Sensors,* vol. 10, pp. 5133-5159, 2010.
[105] W. Choi, I. Lahiri, R. Seelaboyina, and Y. S. Kang, "Synthesis of Graphene and Its Applications: A Review," *Critical Reviews in Solid State and Materials Sciences,* vol. 35, pp. 52-71, 2010.
[106] X. Li, G. Zhang, X. Bai, X. Sun, X. Wang, E. Wang, and H. Dai, "Highly conducting graphene sheets and Langmuir-Blodgett films," *Nature Nanotechnology,* vol. 3, pp. 538-542, 2008.
[107] K. S. Subrahmanyam, L. S. Panchakarla, A. Govindaraj, and C. N. R. Rao, "Simple Method of Preparing Graphene Flakes by an Arc-Discharge Method," *The Journal of Physical Chemistry C,* vol. 113, pp. 4257-4259, 2009.
[108] C. Berger, Z. Song, X. Li, X. Wu, N. Brown, C. Naud, D. Mayou, T. Li, J. Hass, A. N. Marchenkov, E. H. Conrad, P. N. First, and W. A. de Heer, "Electronic Confinement and Coherence in Patterned Epitaxial Graphene," *Science,* vol. 312, pp. 1191-1196, 2006.
[109] I. Janowska, O. Ersen, T. Jacob, P. Vennégues, D. Bégin, M.-J. Ledoux, and C. Pham-Huu, "Catalytic unzipping of carbon nanotubes to few-layer graphene sheets under microwaves irradiation," *Applied Catalysis A: General,* vol. 371, pp. 22-30, 2009.
[110] K. S. Kim, Y. Zhao, H. Jang, S. Y. Lee, J. M. Kim, K. S. Kim, J.-H. Ahn, P. Kim, J.-Y. Choi, and B. H. Hong, "Large-scale pattern growth of graphene films for stretchable transparent electrodes," *Nature,* vol. 457, pp. 706-710, 2009.
[111] A. Reina, X. Jia, J. Ho, D. Nezich, H. Son, V. Bulovic, M. S. Dresselhaus, and J. Kong, "Large area, few-layer graphene films on arbitrary substrates by chemical vapor deposition," *Nano letters,* vol. 9, pp. 30-35, 2008.
[112] X. Fan, W. Peng, Y. Li, X. Li, S. Wang, G. Zhang, and F. Zhang, "Deoxygenation of Exfoliated Graphite Oxide under Alkaline Conditions: A Green Route to Graphene Preparation," *Advanced Materials,* vol. 20, pp. 4490-4493, 2008.

[113] S. Stankovich, D. A. Dikin, R. D. Piner, K. A. Kohlhaas, A. Kleinhammes, Y. Jia, Y. Wu, S. T. Nguyen, and R. S. Ruoff, "Synthesis of graphene-based nanosheets via chemical reduction of exfoliated graphite oxide," *Carbon,* vol. 45, pp. 1558-1565, 2007.
[114] S. K. Vashist and A. Venkatesh, "Advances in graphene-based sensors and devices," *Journal of Nanomedicine & Nanotechnology,* vol. 4, p. e127, 2013.
[115] J. Wu, H. A. Becerril, Z. Bao, Z. Liu, Y. Chen, and P. Peumans, "Organic solar cells with solution-processed graphene transparent electrodes," *Applied Physics Letters,* vol. 92, p. 263302, 2008.
[116] M. D. Stoller, S. Park, Y. Zhu, J. An, and R. S. Ruoff, "Graphene-based ultracapacitors," *Nano letters,* vol. 8, pp. 3498-3502, 2008.
[117] B. Luo, S. Liu, and L. Zhi, "Chemical Approaches toward Graphene-Based Nanomaterials and their Applications in Energy-Related Areas," *Small,* vol. 8, pp. 630-646, 2012.
[118] Y. Wang, Z. Li, J. Wang, J. Li, and Y. Lin, "Graphene and graphene oxide: biofunctionalization and applications in biotechnology," *Trends in Biotechnology,* vol. 29, pp. 205-212, 2011.
[119] P. Avouris, "Graphene: electronic and photonic properties and devices," *Nano letters,* vol. 10, pp. 4285-4294, 2010.
[120] F. Liu, P. Ming, and J. Li, "*Ab initio* calculation of ideal strength and phonon instability of graphene under tension," *Physical Review B,* vol. 76, p. 064120, 2007.
[121] A. A. Balandin, S. Ghosh, W. Bao, I. Calizo, D. Teweldebrhan, F. Miao, and C. N. Lau, "Superior Thermal Conductivity of Single-Layer Graphene," *Nano letters,* vol. 8, pp. 902-907, 2008.
[122] J. S. Bunch, S. S. Verbridge, J. S. Alden, A. M. Van Der Zande, J. M. Parpia, H. G. Craighead, and P. L. McEuen, "Impermeable atomic membranes from graphene sheets," *Nano letters,* vol. 8, pp. 2458-2462, 2008.
[123] R. Danneau, F. Wu, M. F. Craciun, S. Russo, M. Y. Tomi, J. Salmilehto, A. F. Morpurgo, and P. J. Hakonen, "Shot Noise in Ballistic Graphene," *Physical Review Letters,* vol. 100, p. 196802, 2008.
[124] Y. Zhu, S. Murali, W. Cai, X. Li, J. W. Suk, J. R. Potts, and R. S. Ruoff, "Graphene and graphene oxide: synthesis, properties, and applications," *Advanced Materials,* vol. 22, pp. 3906-24, 2010.
[125] W. A. de Heer, C. Berger, X. Wu, P. N. First, E. H. Conrad, X. Li, T. Li, M. Sprinkle, J. Hass, M. L. Sadowski, M. Potemski, and G. Martinez, "Epitaxial graphene," *Solid State Communications,* vol. 143, pp. 92-100, 2007.
[126] M. Dankerl, M. V. Hauf, A. Lippert, L. H. Hess, S. Birner, I. D. Sharp, A. Mahmood, P. Mallet, J.-Y. Veuillen, M. Stutzmann, and J. A. Garrido, "Graphene Solution-Gated Field-Effect Transistor Array for Sensing Applications," *Advanced Functional Materials,* vol. 20, pp. 3117-3124, 2010.
[127] P. Hyung Goo, H. Sukju, L. Juhwan, K. Duck-Hwan, S. In Sang, K. Jae Hun, W. Deok Ha, L. Seok, and J. Seong Chan, "Comparison of Chemical Vapor Sensing Properties between Graphene and Carbon Nanotubes," *Japanese Journal of Applied Physics,* vol. 51, p. 045101, 2012.
[128] J. Z. Zhang, "Improved Sensing with Nanostructures," *The Journal of Physical Chemistry Letters,* vol. 3, pp. 1806-1807, 2012.
[129] Y. Dan, Y. Lu, N. J. Kybert, Z. Luo, and A. T. C. Johnson, "Intrinsic Response of Graphene Vapor Sensors," *Nano letters,* vol. 9, pp. 1472-1475, 2009.
[130] E. R. Hugo, J. Prasoon, K. G. Awnish, R. G. Humberto, W. C. Milton, A. T. Srinivas, and C. E. Peter, "Adsorption of ammonia on graphene," *Nanotechnology,* vol. 20, p. 245501, 2009.

[131] G. Ko, H. Y. Kim, J. Ahn, Y. M. Park, K. Y. Lee, and J. Kim, "Graphene-based nitrogen dioxide gas sensors," *Current Applied Physics,* vol. 10, pp. 1002-1004, 2010.
[132] C. W. Chen, S. C. Hung, M. D. Yang, C. W. Yeh, C. H. Wu, G. C. Chi, F. Ren, and S. J. Pearton, "Oxygen sensors made by monolayer graphene under room temperature," *Applied Physics Letters,* vol. 99, p. 243502, 2011.
[133] H. J. Yoon, D. H. Jun, J. H. Yang, Z. Zhou, S. S. Yang, and M. M.-C. Cheng, "Carbon dioxide gas sensor using a graphene sheet," *Sensors and Actuators B: Chemical,* vol. 157, pp. 310-313, 2011.
[134] G. Chen, T. M. Paronyan, and A. R. Harutyunyan, "Sub-ppt gas detection with pristine graphene," *Applied Physics Letters,* vol. 101, p. 053119, 2012.
[135] S. Rumyantsev, G. Liu, M. S. Shur, R. A. Potyrailo, and A. A. Balandin, "Selective Gas Sensing with a Single Pristine Graphene Transistor," *Nano letters,* vol. 12, pp. 2294-2298, 2012.
[136] K. R. Nemade and S. A. Waghuley, "Chemiresistive Gas Sensing by Few-Layered Graphene," *Journal of Electronic Materials,* vol. 42, pp. 2857-2866, 2013.
[137] A. Fattah and S. Khatami, "Selective H_2S Gas Sensing With a Graphene/n-Si Schottky Diode," *IEEE Sensors Journal,* vol. 14, pp. 4104-4108, 2014.
[138] S. Kumar, S. Kaushik, R. Pratap, and S. Raghavan, "Graphene on Paper: A Simple, Low-Cost Chemical Sensing Platform," *ACS Applied Materials & Interfaces,* vol. 7, pp. 2189-2194, 2015.
[139] F. Ricciardella, B. Alfano, F. Loffredo, F. Villani, T. Polichetti, M. L. Miglietta, E. Massera, and G. D. Francia, "Inkjet printed graphene-based chemi-resistors for gas detection in environmental conditions," in *2015 XVIII AISEM Annual Conference*, Trento, Italy, 2015, pp. 1-4.
[140] M. R. Axet, R. R. Bacsa, B. F. Machado, and P. Serp, "Adsorption on and reactivity of carbon nanotubes and graphene," in *Handbook of Carbon Nano Materials,* K. Kadish and F. D'souza, Eds. Singapore: World Scientific, 2014, pp. 39-183.
[141] P. Dutta and P. M. Horn, "Low-frequency fluctuations in solids: 1/f noise," *Reviews of Modern Physics,* vol. 53, pp. 497-516, 1981.
[142] V. Aroutiounian, "Band Gap Opening in Graphene," *Armenian Journal of Physics,* vol. 6, pp. 141-148, 2013.
[143] L. Ganhua, E. O. Leonidas, and C. Junhong, "Reduced graphene oxide for room-temperature gas sensors," *Nanotechnology,* vol. 20, p. 445502, 2009.
[144] D. R. Dreyer, S. Park, C. W. Bielawski, and R. S. Ruoff, "The chemistry of graphene oxide," *Chemical Society Reviews,* vol. 39, pp. 228-240, 2010.
[145] S. Pei and H.-M. Cheng, "The reduction of graphene oxide," *Carbon,* vol. 50, pp. 3210-3228, 2012.
[146] D. Chen, H. Feng, and J. Li, "Graphene Oxide: Preparation, Functionalization, and Electrochemical Applications," *Chemical Reviews,* vol. 112, pp. 6027-6053, 2012.
[147] S. Prezioso, F. Perrozzi, L. Giancaterini, C. Cantalini, E. Treossi, V. Palermo, M. Nardone, S. Santucci, and L. Ottaviano, "Graphene Oxide as a Practical Solution to High Sensitivity Gas Sensing," *The Journal of Physical Chemistry C,* vol. 117, pp. 10683-10690, 2013.
[148] J. Wang, B. Singh, J.-H. Park, S. Rathi, I.-y. Lee, S. Maeng, H.-I. Joh, C.-H. Lee, and G.-H. Kim, "Dielectrophoresis of graphene oxide nanostructures for hydrogen gas sensor at room temperature," *Sensors and Actuators B: Chemical,* vol. 194, pp. 296-302, 2014.
[149] M. Proceka, Z. Opilskia, J. Jagiellob, and L. Lipinskab, "Investigations of SAW Structures with oxide graphene layer to detection of selected gases," *Acta Physica Polonica, A.,* vol. 124, pp. 402-405, 2013.
[150] T. Pustelny, S. Drewniak, M. Setkiewicz, E. Maciak, M. Urbańczyk, M. Procek, K. Gut, Z. Opilski, J. Jagiello, and L. Lipinska, "The sensitivity of sensor structures with

oxide graphene exposed to selected gaseous atmospheres," *Bulletin of the Polish Academy of Sciences: Technical Sciences*, vol. 61, p. 705, 2013.
[151] S. Some, Y. Xu, Y. Kim, Y. Yoon, H. Qin, A. Kulkarni, T. Kim, and H. Lee, "Highly Sensitive and Selective Gas Sensor Using Hydrophilic and Hydrophobic Graphenes," *Scientific Reports,* vol. 3, p. 1868, 2013.
[152] H. Bi, K. Yin, X. Xie, J. Ji, S. Wan, L. Sun, M. Terrones, and M. S. Dresselhaus, "Ultrahigh humidity sensitivity of graphene oxide," *Scientific Reports,* vol. 3, p. 2714, 2013.
[153] H. S. Ahn, H. J. Park, J. H. Oh, J. C. Joo, and D. J. Kim, "VOCs sensing property of graphene oxide thin film by reduction rate," *Applied Mechanics and Materials*, vol. 440, pp. 64-68, 2014.
[154] Y. Yao, X. Chen, H. Guo, Z. Wu, and X. Li, "Humidity sensing behaviors of graphene oxide-silicon bi-layer flexible structure," *Sensors and Actuators B: Chemical,* vol. 161, pp. 1053-1058, 2012.
[155] C. K. Chua and M. Pumera, "Chemical reduction of graphene oxide: a synthetic chemistry viewpoint," *Chemical Society Reviews,* vol. 43, pp. 291-312, 2014.
[156] J. T. Robinson, F. K. Perkins, E. S. Snow, Z. Wei, and P. E. Sheehan, "Reduced Graphene Oxide Molecular Sensors," *Nano letters,* vol. 8, pp. 3137-3140, 2008.
[157] J. D. Fowler, M. J. Allen, V. C. Tung, Y. Yang, R. B. Kaner, and B. H. Weiller, "Practical Chemical Sensors from Chemically Derived Graphene," *ACS Nano,* vol. 3, pp. 301-306, 2009.
[158] V. Dua, S. P. Surwade, S. Ammu, S. R. Agnihotra, S. Jain, K. E. Roberts, S. Park, R. S. Ruoff, and S. K. Manohar, "All-Organic Vapor Sensor Using Inkjet-Printed Reduced Graphene Oxide," *Angewandte Chemie International Edition,* vol. 49, pp. 2154-2157, 2010.
[159] G. Lu, S. Park, K. Yu, R. S. Ruoff, L. E. Ocola, D. Rosenmann, and J. Chen, "Toward Practical Gas Sensing with Highly Reduced Graphene Oxide: A New Signal Processing Method To Circumvent Run-to-Run and Device-to-Device Variations," *ACS Nano,* vol. 5, pp. 1154-1164, 2011.
[160] A. Lipatov, A. Varezhnikov, P. Wilson, V. Sysoev, A. Kolmakov, and A. Sinitskii, "Highly selective gas sensor arrays based on thermally reduced graphene oxide," *Nanoscale,* vol. 5, pp. 5426-5434, 2013.
[161] J. Hassinen, J. Kauppila, J. Leiro, A. Määttänen, P. Ihalainen, J. Peltonen, and J. Lukkari, "Low-cost reduced graphene oxide-based conductometric nitrogen dioxide-sensitive sensor on paper," *Analytical and Bioanalytical Chemistry,* vol. 405, pp. 3611-3617, 2013.
[162] H. Nantao, Y. Zhi, W. Yanyan, Z. Liling, W. Ying, H. Xiaolu, W. Hao, W. Liangmin, and Z. Yafei, "Ultrafast and sensitive room temperature NH_3 gas sensors based on chemically reduced graphene oxide," *Nanotechnology,* vol. 25, p. 025502, 2014.
[163] D. H. Wang, Y. Hu, J. J. Zhao, L. L. Zeng, X. M. Tao, and W. Chen, "Holey reduced graphene oxide nanosheets for high performance room temperature gas sensing," *Journal of Materials Chemistry A,* vol. 2, pp. 17415-17420, 2014.
[164] H. K. Lee, J. Lee, N. J. Choi, S. E. Moon, H. Lee, and W. S. Yang, "Efficient Reducing Method of Graphene Oxide for Gas Sensor Applications," *Procedia Engineering,* vol. 25, pp. 892-895, 2011.
[165] G. Lu, K. Yu, L. E. Ocola, and J. Chen, "Ultrafast room temperature NH_3 sensing with positively gated reduced graphene oxide field-effect transistors," *Chemical Communications,* vol. 47, pp. 7761-7763, 2011.
[166] J. Wang, B. Singh, S. Maeng, H.-I. Joh, and G.-H. Kim, "Assembly of thermally reduced graphene oxide nanostructures by alternating current dielectrophoresis as hydrogen-gas sensors," *Applied Physics Letters,* vol. 103, p. 083112, 2013.

[167] J. Wang, Y. Kwak, I.-y. Lee, S. Maeng, and G.-H. Kim, "Highly responsive hydrogen gas sensing by partially reduced graphite oxide thin films at room temperature," *Carbon,* vol. 50, pp. 4061-4067, 2012.
[168] L.-S. Zhang, W. D. Wang, X.-Q. Liang, W.-S. Chu, W.-G. Song, W. Wang, and Z.-Y. Wu, "Characterization of partially reduced graphene oxide as room temperature sensor for H_2," *Nanoscale,* vol. 3, pp. 2458-2460, 2011.
[169] F. Niu, L.-M. Tao, Y.-C. Deng, Q.-H. Wang, and W.-G. Song, "Phosphorus doped graphene nanosheets for room temperature NH_3 sensing," *New Journal of Chemistry,* vol. 38, pp. 2269-2272, 2014.
[170] F. Niu, J.-M. Liu, L.-M. Tao, W. Wang, and W.-G. Song, "Nitrogen and silica co-doped graphene nanosheets for NO_2 gas sensing," *Journal of Materials Chemistry A,* vol. 1, pp. 6130-6133, 2013.
[171] C. Liang, Y. L. Wang, and T. Li, "Sulfur-doping in graphene and its high selectivity gas sensing in NO_2," in *2015 Transducers - 2015 18th International Conference on Solid-State Sensors, Actuators and Microsystems (TRANSDUCERS)*, Alaska, USA, 2015, pp. 1421-1424.
[172] R. Lv, G. Chen, Q. Li, A. McCreary, A. Botello-Méndez, S. V. Morozov, L. Liang, X. Declerck, N. Perea-López, D. A. Cullen, S. Feng, A. L. Elías, R. Cruz-Silva, K. Fujisawa, M. Endo, F. Kang, J.-C. Charlier, V. Meunier, M. Pan, A. R. Harutyunyan, K. S. Novoselov, and M. Terrones, "Ultrasensitive gas detection of large-area boron-doped graphene," *Proceedings of the National Academy of Sciences,* vol. 112, pp. 14527-14532, 2015.
[173] A. Kaniyoor, R. Imran Jafri, T. Arockiadoss, and S. Ramaprabhu, "Nanostructured Pt decorated graphene and multi walled carbon nanotube based room temperature hydrogen gas sensor," *Nanoscale,* vol. 1, pp. 382-386, 2009.
[174] W. Li, X. Geng, Y. Guo, J. Rong, Y. Gong, L. Wu, X. Zhang, P. Li, J. Xu, G. Cheng, M. Sun, and L. Liu, "Reduced Graphene Oxide Electrically Contacted Graphene Sensor for Highly Sensitive Nitric Oxide Detection," *ACS Nano,* vol. 5, pp. 6955-6961, 2011.
[175] A. Gutes, B. Hsia, A. Sussman, W. Mickelson, A. Zettl, C. Carraro, and R. Maboudian, "Graphene decoration with metal nanoparticles: Towards easy integration for sensing applications," *Nanoscale,* vol. 4, pp. 438-440, 2012.
[176] M. G. Chung, D.-H. Kim, D. K. Seo, T. Kim, H. U. Im, H. M. Lee, J.-B. Yoo, S.-H. Hong, T. J. Kang, and Y. H. Kim, "Flexible hydrogen sensors using graphene with palladium nanoparticle decoration," *Sensors and Actuators B: Chemical,* vol. 169, pp. 387-392, 2012.
[177] Y. Pak, S.-M. Kim, H. Jeong, C. G. Kang, J. S. Park, H. Song, R. Lee, N. Myoung, B. H. Lee, S. Seo, J. T. Kim, and G.-Y. Jung, "Palladium-Decorated Hydrogen-Gas Sensors Using Periodically Aligned Graphene Nanoribbons," *ACS Applied Materials & Interfaces,* vol. 6, pp. 13293-13298, 2014.
[178] L. Huang, Z. Wang, J. Zhang, J. Pu, Y. Lin, S. Xu, L. Shen, Q. Chen, and W. Shi, "Fully Printed, Rapid-Response Sensors Based on Chemically Modified Graphene for Detecting NO_2 at Room Temperature," *ACS Applied Materials & Interfaces,* vol. 6, pp. 7426-7433, 2014.
[179] S. Cui, S. Mao, Z. Wen, J. Chang, Y. Zhang, and J. Chen, "Controllable synthesis of silver nanoparticle-decorated reduced graphene oxide hybrids for ammonia detection," *Analyst,* vol. 138, pp. 2877-2882, 2013.
[180] B. Cho, J. Yoon, M. G. Hahm, D.-H. Kim, A. R. Kim, Y. H. Kahng, S.-W. Park, Y.-J. Lee, S.-G. Park, J.-D. Kwon, C. S. Kim, M. Song, Y. Jeong, K.-S. Nam, and H. C. Ko, "Graphene-based gas sensor: metal decoration effect and application to a flexible device," *Journal of Materials Chemistry C,* vol. 2, pp. 5280-5285, 2014.

[181] J. Wang, S. Rathi, B. Singh, I. Lee, S. Maeng, H.-I. Joh, and G.-H. Kim, "Dielectrophoretic assembly of Pt nanoparticle-reduced graphene oxide nanohybrid for highly-sensitive multiple gas sensor," *Sensors and Actuators B: Chemical,* vol. 220, pp. 755-761, 2015.

[182] S. Mao, S. Cui, G. Lu, K. Yu, Z. Wen, and J. Chen, "Tuning gas-sensing properties of reduced graphene oxide using tin oxide nanocrystals," *Journal of Materials Chemistry,* vol. 22, pp. 11009-11013, 2012.

[183] L. Zhou, F. Shen, X. Tian, D. Wang, T. Zhang, and W. Chen, "Stable Cu_2O nanocrystals grown on functionalized graphene sheets and room temperature H_2S gas sensing with ultrahigh sensitivity," *Nanoscale,* vol. 5, pp. 1564-1569, 2013.

[184] S. Liu, B. Yu, H. Zhang, T. Fei, and T. Zhang, "Enhancing NO_2 gas sensing performances at room temperature based on reduced graphene oxide-ZnO nanoparticles hybrids," *Sensors and Actuators B: Chemical,* vol. 202, pp. 272-278, 2014.

[185] H. Zhang, J. Feng, T. Fei, S. Liu, and T. Zhang, "SnO_2 nanoparticles-reduced graphene oxide nanocomposites for NO_2 sensing at low operating temperature," *Sensors and Actuators B: Chemical,* vol. 190, pp. 472-478, 2014.

[186] A. Esfandiar, S. Ghasemi, A. Irajizad, O. Akhavan, and M. R. Gholami, "The decoration of TiO_2/reduced graphene oxide by Pd and Pt nanoparticles for hydrogen gas sensing," *International Journal of Hydrogen Energy,* vol. 37, pp. 15423-15432, 2012.

[187] G. Singh, A. Choudhary, D. Haranath, A. G. Joshi, N. Singh, S. Singh, and R. Pasricha, "ZnO decorated luminescent graphene as a potential gas sensor at room temperature," *Carbon,* vol. 50, pp. 385-394, 2012.

[188] H. Meng, W. Yang, K. Ding, L. Feng, and Y. Guan, "Cu_2O nanorods modified by reduced graphene oxide for NH_3 sensing at room temperature," *Journal of Materials Chemistry A,* vol. 3, pp. 1174-1181, 2015.

[189] D. Zhang, A. Liu, H. Chang, and B. Xia, "Room-temperature high-performance acetone gas sensor based on hydrothermal synthesized SnO_2-reduced graphene oxide hybrid composite," *RSC Advances,* vol. 5, pp. 3016-3022, 2015.

[190] D. Zhang, J. Liu, H. Chang, A. Liu, and B. Xia, "Characterization of a hybrid composite of SnO_2 nanocrystal-decorated reduced graphene oxide for ppm-level ethanol gas sensing application," *RSC Advances,* vol. 5, pp. 18666-18672, 2015.

[191] P.-G. Su and S.-L. Peng, "Fabrication and NO_2 gas-sensing properties of reduced graphene oxide/WO_3 nanocomposite films," *Talanta,* vol. 132, pp. 398-405, 2015.

[192] A. S. M. I. Uddin and G.-S. Chung, "Synthesis of highly dispersed ZnO nanoparticles on graphene surface and their acetylene sensing properties," *Sensors and Actuators B: Chemical,* vol. 205, pp. 338-344, 2014.

[193] C. Wang, J. Zhu, S. Liang, H. Bi, Q. Han, X. Liu, and X. Wang, "Reduced graphene oxide decorated with CuO-ZnO hetero-junctions: towards high selective gas-sensing property to acetone," *Journal of Materials Chemistry A,* vol. 2, pp. 18635-18643, 2014.

[194] Z. Zhang, X. Zou, L. Xu, L. Liao, W. Liu, J. Ho, X. Xiao, C. Jiang, and J. Li, "Hydrogen gas sensor based on metal oxide nanoparticles decorated graphene transistor," *Nanoscale,* vol. 7, pp. 10078-10084, 2015.

[195] X. Huang, N. Hu, R. Gao, Y. Yu, Y. Wang, Z. Yang, E. Siu-Wai Kong, H. Wei, and Y. Zhang, "Reduced graphene oxide-polyaniline hybrid: Preparation, characterization and its applications for ammonia gas sensing," *Journal of Materials Chemistry,* vol. 22, pp. 22488-22495, 2012.

[196] M. Parmar, C. Balamurugan, and D.-W. Lee, "PANI and graphene/PANI nanocomposite films—comparative toluene gas sensing behavior," *Sensors,* vol. 13, pp. 16611-16624, 2013.

[197] X. L. Huang, N. T. Hu, Y. Y. Wang, and Y. F. Zhang, "Ammonia gas sensor based on aniline reduced graphene oxide," *Advanced Materials Research*, vol. 669, pp. 79-84, 2013.
[198] Z. Ye, Y. Jiang, H. Tai, and Z. Yuan, "The Investigation of Reduced Graphene Oxide/P3HT Composite Films for Ammonia Detection," *Integrated Ferroelectrics,* vol. 154, pp. 73-81, 2014.
[199] S. K. Mishra, S. N. Tripathi, V. Choudhary, and B. D. Gupta, "SPR based fibre optic ammonia gas sensor utilizing nanocomposite film of PMMA/reduced graphene oxide prepared by in situ polymerization," *Sensors and Actuators B: Chemical,* vol. 199, pp. 190-200, 2014.
[200] T. Xie, G. Xie, Y. Zhou, J. Huang, M. Wu, Y. Jiang, and H. Tai, "Thin film transistors gas sensors based on reduced graphene oxide poly(3-hexylthiophene) bilayer film for nitrogen dioxide detection," *Chemical Physics Letters,* vol. 614, pp. 275-281, 2014.
[201] Y. Yang, X. Yang, W. Yang, S. Li, J. Xu, and Y. Jiang, "Porous conducting polymer and reduced graphene oxide nanocomposites for room temperature gas detection," *RSC Advances,* vol. 4, pp. 42546-42553, 2014.
[202] Y. Seekaew, S. Lokavee, D. Phokharatkul, A. Wisitsoraat, T. Kerdcharoen, and C. Wongchoosuk, "Low-cost and flexible printed graphene–PEDOT:PSS gas sensor for ammonia detection," *Organic Electronics,* vol. 15, pp. 2971-2981, 2014.
[203] Y. Zhou, Y. Jiang, G. Xie, M. Wu, and H. Tai, "Gas sensors for CO_2 detection based on RGO–PEI films at room temperature," *Chinese Science Bulletin,* vol. 59, pp. 1999-2005, 2014.
[204] R. A. G. Rañola, J. M. Kalaw, and F. B. Sevilla, "Graphene/Nylon-6 chemiresistor sensor for trimethylamine gas sensing," *Applied Mechanics and Materials*, vol. 492, pp. 321-325, 2014.
[205] W.-D. Lin, H.-M. Chang, and R.-J. Wu, "Applied novel sensing material graphene/polypyrrole for humidity sensor," *Sensors and Actuators B: Chemical,* vol. 181, pp. 326-331, 2013.
[206] W.-K. Jang, J. Yun, H.-I. Kim, and Y.-S. Lee, "Improvement of ammonia sensing properties of polypyrrole by nanocomposite with graphitic materials," *Colloid and Polymer Science,* vol. 291, pp. 1095-1103, 2013.
[207] D. Usachov, O. Vilkov, A. Grüneis, D. Haberer, A. Fedorov, V. K. Adamchuk, A. B. Preobrajenski, P. Dudin, A. Barinov, M. Oehzelt, C. Laubschat, and D. V. Vyalikh, "Nitrogen-Doped Graphene: Efficient Growth, Structure, and Electronic Properties," *Nano letters,* vol. 11, pp. 5401-5407, 2011.
[208] X.-K. Kong, C.-L. Chen, and Q.-W. Chen, "Doped graphene for metal-free catalysis," *Chemical Society Reviews,* vol. 43, pp. 2841-2857, 2014.
[209] H. Liu, Y. Liu, and D. Zhu, "Chemical doping of graphene," *Journal of Materials Chemistry,* vol. 21, pp. 3335-3345, 2011.
[210] Y. Shao, S. Zhang, M. H. Engelhard, G. Li, G. Shao, Y. Wang, J. Liu, I. A. Aksay, and Y. Lin, "Nitrogen-doped graphene and its electrochemical applications," *Journal of Materials Chemistry,* vol. 20, pp. 7491-7496, 2010.
[211] Y. Wang, Y. Shao, D. W. Matson, J. Li, and Y. Lin, "Nitrogen-Doped Graphene and Its Application in Electrochemical Biosensing," *ACS Nano,* vol. 4, pp. 1790-1798, 2010.
[212] R. Lv and M. Terrones, "Towards new graphene materials: Doped graphene sheets and nanoribbons," *Materials Letters,* vol. 78, pp. 209-218, 2012.
[213] H. Wang, T. Maiyalagan, and X. Wang, "Review on Recent Progress in Nitrogen-Doped Graphene: Synthesis, Characterization, and Its Potential Applications," *ACS Catalysis,* vol. 2, pp. 781-794, 2012.

[214] C. Zhang, N. Mahmood, H. Yin, F. Liu, and Y. Hou, "Synthesis of Phosphorus-Doped Graphene and its Multifunctional Applications for Oxygen Reduction Reaction and Lithium Ion Batteries," *Advanced Materials,* vol. 25, pp. 4932-4937, 2013.
[215] C. N. R. Rao, K. Gopalakrishnan, and A. Govindaraj, "Synthesis, properties and applications of graphene doped with boron, nitrogen and other elements," *Nano Today,* vol. 9, pp. 324-343, 2014.
[216] J. S. Oh, K. N. Kim, and G. Y. Yeom, "Graphene Doping Methods and Device Applications," *Journal of Nanoscience and Nanotechnology,* vol. 14, pp. 1120-1133, 2014.
[217] Y. Lu, Y. Huang, M. Zhang, and Y. Chen, "Nitrogen-Doped Graphene Materials for Supercapacitor Applications," *Journal of Nanoscience and Nanotechnology,* vol. 14, pp. 1134-1144, 2014.
[218] X. Wang, G. Sun, P. Routh, D.-H. Kim, W. Huang, and P. Chen, "Heteroatom-doped graphene materials: syntheses, properties and applications," *Chemical Society Reviews,* vol. 43, pp. 7067-7098, 2014.
[219] T. F.-L. FENG Ya-Qiang, LANG Jun-Wei, LIU Wen-Wen, YAN Xing-Bin, "Facile Approach to Preparation of Nitrogen-doped Graphene and Its Supercapacitive Performance," *Journal of Inorganic Materials,* vol. 28, pp. 677-682, 2013.
[220] T. Humberto, L. Ruitao, T. Mauricio, and S. D. Mildred, "The role of defects and doping in 2D graphene sheets and 1D nanoribbons," *Reports on Progress in Physics,* vol. 75, p. 062501, 2012.
[221] P.-G. Su and H.-C. Shieh, "Flexible NO_2 sensors fabricated by layer-by-layer covalent anchoring and in situ reduction of graphene oxide," *Sensors and Actuators B: Chemical,* vol. 190, pp. 865-872, 2014.
[222] S. Yoo, X. Li, Y. Wu, W. Liu, X. Wang, and W. Yi, "Ammonia Gas Detection by Tannic Acid Functionalized and Reduced Graphene Oxide at Room Temperature," *Journal of Nanomaterials,* vol. 2014, p. 6, 2014.
[223] X. Chen, F. M. Yasin, P. K. Eggers, R. A. Boulos, X. Duan, R. N. Lamb, K. S. Iyer, and C. L. Raston, "Non-covalently modified graphene supported ultrafine nanoparticles of palladium for hydrogen gas sensing," *RSC Advances,* vol. 3, pp. 3213-3217, 2013.
[224] M. G. Chung, D. H. Kim, H. M. Lee, T. Kim, J. H. Choi, D. k. Seo, J.-B. Yoo, S.-H. Hong, T. J. Kang, and Y. H. Kim, "Highly sensitive NO_2 gas sensor based on ozone treated graphene," *Sensors and Actuators B: Chemical,* vol. 166–167, pp. 172-176, 2012.
[225] Y. Kim, T. K. An, J. Kim, J. Hwang, S. Park, S. Nam, H. Cha, W. J. Park, J. M. Baik, and C. E. Park, "A composite of a graphene oxide derivative as a novel sensing layer in an organic field-effect transistor," *Journal of Materials Chemistry C,* vol. 2, pp. 4539-4544, 2014.
[226] N. Hu, Y. Wang, J. Chai, R. Gao, Z. Yang, E. S.-W. Kong, and Y. Zhang, "Gas sensor based on p-phenylenediamine reduced graphene oxide," *Sensors and Actuators B: Chemical,* vol. 163, pp. 107-114, 2012.
[227] S. Cui, Z. Wen, E. C. Mattson, S. Mao, J. Chang, M. Weinert, C. J. Hirschmugl, M. Gajdardziska-Josifovska, and J. Chen, "Indium-doped SnO_2 nanoparticle-graphene nanohybrids: simple one-pot synthesis and their selective detection of NO_2," *Journal of Materials Chemistry A,* vol. 1, pp. 4462-4467, 2013.
[228] Q. Huang, D. Zeng, H. Li, and C. Xie, "Room temperature formaldehyde sensors with enhanced performance, fast response and recovery based on zinc oxide quantum dots/graphene nanocomposites," *Nanoscale,* vol. 4, pp. 5651-5658, 2012.
[229] K. Nemade and S. Waghuley, "Highly responsive carbon dioxide sensing by graphene/Al_2O_3 quantum dots composites at low operable temperature," *Indian Journal of Physics,* vol. 88, pp. 577-583, 2014.

[230] T. Quang Trung, H. Tran My Hoa, T. Duc Tai, T. Van Tam, and N. Nang Dinh, "Synthesis and application of graphene–silver nanowires composite for ammonia gas sensing," *Advances in Natural Sciences: Nanoscience and Nanotechnology,* vol. 4, p. 045012, 2013.

[231] H. Y. Jeong, D.-S. Lee, H. K. Choi, D. H. Lee, J.-E. Kim, J. Y. Lee, W. J. Lee, S. O. Kim, and S.-Y. Choi, "Flexible room-temperature NO_2 gas sensors based on carbon nanotubes/reduced graphene hybrid films," *Applied Physics Letters,* vol. 96, p. 213105, 2010.

[232] L. Zhu, Y. Jia, G. Gai, X. Ji, J. Luo, and Y. Yao, "Ambipolarity of large-area Pt-functionalized graphene observed in H_2 sensing," *Sensors and Actuators B: Chemical,* vol. 190, pp. 134-140, 2014.

[233] J. Yu, M. Shafiei, J. Ou, K. Shin, and W. Wlodarski, "A study of hydrogen gas sensing performance of Pt/Graphene/GaN devices," in *2011 IEEE Sensors*, Limerick, Ireland, 2011, pp. 1017-1020.

[234] X. Liu, J. Cui, J. Sun, and X. Zhang, "3D graphene aerogel-supported SnO_2 nanoparticles for efficient detection of NO_2," *RSC Advances,* vol. 4, pp. 22601-22605, 2014.

[235] S. Shubhda, J. Kiran, V. N. Singh, S. Sukhvir, N. Vijayan, D. Nita, G. Govind, and T. D. Senguttuvan, "Faster response of NO_2 sensing in graphene–WO_3 nanocomposites," *Nanotechnology,* vol. 23, p. 205501, 2012.

[236] Y. Yang, C. Tian, J. Wang, L. Sun, K. Shi, W. Zhou, and H. Fu, "Facile synthesis of novel 3D nanoflower-like Cu(x)O/multilayer graphene composites for room temperature NO(x) gas sensor application," *Nanoscale,* vol. 6, pp. 7369-7378, 2014.

[237] Z. Jiang, J. Li, H. Aslan, Q. Li, Y. Li, M. Chen, Y. Huang, J. P. Froning, M. Otyepka, R. Zboril, F. Besenbacher, and M. Dong, "A high efficiency H_2S gas sensor material: paper like Fe_2O_3/graphene nanosheets and structural alignment dependency of device efficiency," *Journal of Materials Chemistry A,* vol. 2, pp. 6714-6717, 2014.

[238] K. R. Nemade and S. A. Waghuley, "Role of defects concentration on optical and carbon dioxide gas sensing properties of Sb_2O_3/graphene composites," *Optical Materials,* vol. 36, pp. 712-716, 2014.

[239] K. R. Nemade and S. A. Waghuley, "LPG sensing application of graphene/Bi_2O_3 quantum dots composites," *Solid State Sciences,* vol. 22, pp. 27-32, 2013.

[240] J. Zhang, C. Zhao, P. A. Hu, Y. Q. Fu, Z. Wang, W. Cao, B. Yang, and F. Placido, "A UV light enhanced TiO_2/graphene device for oxygen sensing at room temperature," *RSC Advances,* vol. 3, pp. 22185-22190, 2013.

[241] X. Li, X. Chen, Y. Yao, N. Li, and X. Bi, "Multi-Walled Carbon Nanotubes/Graphene Oxide Composites for Humidity Sensing," *IEEE Sensors Journal,* vol. 13, pp. 4749-4756, 2013.

[242] L. T. Hoa, H. N. Tien, V. H. Luan, J. S. Chung, and S. H. Hur, "Fabrication of a novel 2D-graphene/2D-NiO nanosheet-based hybrid nanostructure and its use in highly sensitive NO_2 sensors," *Sensors and Actuators B: Chemical,* vol. 185, pp. 701-705, 2013.

[243] K. Anand, O. Singh, M. P. Singh, J. Kaur, and R. C. Singh, "Hydrogen sensor based on graphene/ZnO nanocomposite," *Sensors and Actuators B: Chemical,* vol. 195, pp. 409-415, 2014.

[244] N. Chen, X. Li, X. Wang, J. Yu, J. Wang, Z. Tang, and S. A. Akbar, "Enhanced room temperature sensing of Co_3O_4-intercalated reduced graphene oxide based gas sensors," *Sensors and Actuators B: Chemical,* vol. 188, pp. 902-908, 2013.

[245] S. Liu, L. Zhou, L. Yao, L. Chai, L. Li, G. Zhang, Kankan, and K. Shi, "One-pot reflux method synthesis of cobalt hydroxide nanoflake-reduced graphene oxide hybrid and their NO_x gas sensors at room temperature," *Journal of Alloys and Compounds,* vol. 612, pp. 126-133, 2014.

[246] X. Zhou, X. Wang, B. Wang, Z. Chen, C. He, and Y. Wu, "Preparation, characterization and NH_3-sensing properties of reduced graphene oxide/copper phthalocyanine hybrid material," *Sensors and Actuators B: Chemical,* vol. 193, pp. 340-348, 2014.
[247] K. R. Nemade and S. A. Waghuley, "Preparation of MnO_2 immobilized graphene nanocomposite by solid state diffusion route for LPG sensing," *Journal of Luminescence,* vol. 153, pp. 194-197, 2014.
[248] A. Esfandiar, A. Irajizad, O. Akhavan, S. Ghasemi, and M. R. Gholami, "Pd–WO_3/reduced graphene oxide hierarchical nanostructures as efficient hydrogen gas sensors," *International Journal of Hydrogen Energy,* vol. 39, pp. 8169-8179, 2014.
[249] S.-J. Choi, B.-H. Jang, S.-J. Lee, B. K. Min, A. Rothschild, and I.-D. Kim, "Selective Detection of Acetone and Hydrogen Sulfide for the Diagnosis of Diabetes and Halitosis Using SnO_2 Nanofibers Functionalized with Reduced Graphene Oxide Nanosheets," *ACS Applied Materials & Interfaces,* vol. 6, pp. 2588-2597, 2014.
[250] X. An, J. C. Yu, Y. Wang, Y. Hu, X. Yu, and G. Zhang, "WO_3 nanorods/graphene nanocomposites for high-efficiency visible-light-driven photocatalysis and NO_2 gas sensing," *Journal of Materials Chemistry,* vol. 22, pp. 8525-8531, 2012.
[251] F. Liu, X. Chu, Y. Dong, W. Zhang, W. Sun, and L. Shen, "Acetone gas sensors based on graphene-$ZnFe_2O_4$ composite prepared by solvothermal method," *Sensors and Actuators B: Chemical,* vol. 188, pp. 469-474, 2013.
[252] M. Shafiei, R. Arsat, J. Yu, K. Kalantar-zadeh, W. Wlodarski, S. Dubin, and R. B. Kaner, "Pt/graphene nano-sheet based hydrogen gas sensor," in *2009 IEEE Sensors*, Christchurch, New Zealand, 2009, pp. 295-298.
[253] M. Raghu, R. Suresh, and P. S. Vijay, "MWCNT–polymer composites as highly sensitive and selective room temperature gas sensors," *Nanotechnology,* vol. 22, p. 215502, 2011.
[254] S. Srivastava, S. S. Sharma, S. Agrawal, S. Kumar, M. Singh, and Y. K. Vijay, "Study of chemiresistor type CNT doped polyaniline gas sensor," *Synthetic Metals,* vol. 160, pp. 529-534, 2010.
[255] F. Yavari, Z. Chen, A. V. Thomas, W. Ren, H.-M. Cheng, and N. Koratkar, "High sensitivity gas detection using a macroscopic three-dimensional graphene foam network," *Scientific Reports,* vol. 1, No. 166, 2011.
[256] S. G. Pawar, M. A. Chougule, S. L. Patil, B. T. Raut, P. R. Godse, S. Sen, and V. B. Patil, "Room Temperature Ammonia Gas Sensor Based on Polyaniline-TiO_2 Nanocomposite," *IEEE Sensors Journal,* vol. 11, pp. 3417-3423, 2011.
[257] J. Hong, S. Lee, J. Seo, S. Pyo, J. Kim, and T. Lee, "A Highly Sensitive Hydrogen Sensor with Gas Selectivity Using a PMMA Membrane-Coated Pd Nanoparticle/Single-Layer Graphene Hybrid," *ACS Applied Materials & Interfaces,* vol. 7, pp. 3554-3561, 2015.
[258] Z. Wu, X. Chen, S. Zhu, Z. Zhou, Y. Yao, W. Quan, and B. Liu, "Enhanced sensitivity of ammonia sensor using graphene/polyaniline nanocomposite," *Sensors and Actuators B: Chemical,* vol. 178, pp. 485-493, 2013.
[259] Y. M. Cai, Z. Y. Qin, and Z. Zhou, "Nanocoating of polyaniline layer on the surface of graphene sheets for ammonia gas detection," *Advanced Materials Research*, vol. 557-559, pp. 1803-1806, 2012.
[260] T. Alizadeh and L. H. Soltani, "Graphene/poly(methyl methacrylate) chemiresistor sensor for formaldehyde odor sensing," *Journal of Hazardous Materials,* vol. 248–249, pp. 401-406, 2013.
[261] L. Al-Mashat, K. Shin, K. Kalantar-zadeh, J. D. Plessis, S. H. Han, R. W. Kojima, R. B. Kaner, D. Li, X. Gou, S. J. Ippolito, and W. Wlodarski, "Graphene/Polyaniline Nanocomposite for Hydrogen Sensing," *The Journal of Physical Chemistry C,* vol. 114, pp. 16168-16173, 2010.

[262] T. O. Wehling, K. S. Novoselov, S. V. Morozov, E. E. Vdovin, M. I. Katsnelson, A. K. Geim, and A. I. Lichtenstein, "Molecular Doping of Graphene," *Nano letters,* vol. 8, pp. 173-177, 2008.
[263] S. M. Seyed-Talebi and J. Beheshtian, "Computational study of ammonia adsorption on the perfect and rippled graphene sheet," *Physica B: Condensed Matter,* vol. 429, pp. 52-56, 2013.
[264] B. Huang, Z. Li, Z. Liu, G. Zhou, S. Hao, J. Wu, B.-L. Gu, and W. Duan, "Adsorption of Gas Molecules on Graphene Nanoribbons and Its Implication for Nanoscale Molecule Sensor," *The Journal of Physical Chemistry C,* vol. 112, pp. 13442-13446, 2008.
[265] M. Rostam, M. Yawar, and G. Nader, "Investigation of gas sensing properties of armchair graphene nanoribbons," *Journal of Physics: Condensed Matter,* vol. 20, p. 425211, 2008.
[266] K. K. Paulla and A. A. Farajian, "Concentration Effects of Carbon Oxides on Sensing by Graphene Nanoribbons: Ab Initio Modeling," *The Journal of Physical Chemistry C,* vol. 117, pp. 12815-12825, 2013.
[267] E. Akbari, R. Yousof, M. T. Ahmadi, M. J. Kiani, M. Rahmani, H. K. Feiz Abadi, and M. Saeidmanesh, "The effect of concentration on gas sensor model based on graphene nanoribbon," *Neural Computing and Applications,* vol. 24, pp. 143-146, 2014.
[268] A. Fathalian, J. Jalilian, and S. Shahidi, "Effects of gas adsorption on the electronic properties of graphene nanoribbons," *Physica B: Condensed Matter,* vol. 417, pp. 75-78, 2013.
[269] Y. Peng and J. Li, "Ammonia adsorption on graphene and graphene oxide: a first-principles study," *Frontiers of Environmental Science & Engineering,* vol. 7, pp. 403-411, 2013.
[270] S. Tang and Z. Cao, "Adsorption of nitrogen oxides on graphene and graphene oxides: Insights from density functional calculations," *The Journal of Chemical Physics,* vol. 134, p. 044710, 2011.
[271] E. C. Mattson, K. Pande, M. Unger, S. Cui, G. Lu, M. Gajdardziska-Josifovska, M. Weinert, J. Chen, and C. J. Hirschmugl, "Exploring Adsorption and Reactivity of NH_3 on Reduced Graphene Oxide," *The Journal of Physical Chemistry C,* vol. 117, pp. 10698-10707, 2013.
[272] J. Dai and J. Yuan, "Adsorption of molecular oxygen on doped graphene: Atomic, electronic, and magnetic properties," *Physical Review B,* vol. 81, p. 165414, 2010.
[273] D. Jiayu and Y. Jianmin, "Modulating the electronic and magnetic structures of P-doped graphene by molecule doping," *Journal of Physics: Condensed Matter,* vol. 22, p. 225501, 2010.
[274] H. Tavakol and A. Mollaei-Renani, "DFT, AIM, and NBO study of the interaction of simple and sulfur-doped graphenes with molecular halogens, CH_3OH, CH_3SH, H_2O, and H_2S," *Structural Chemistry,* vol. 25, pp. 1659-1667, 2014.
[275] F. Nasehnia and M. Seifi, "Adsorption of molecular oxygen on VIIIB transition metal-doped graphene: A DFT study," *Modern Physics Letters B,* vol. 28, p. 1450237, 2014.
[276] T. Hussain, P. Panigrahi, and R. Ahuja, "Enriching physisorption of H_2S and NH_3 gases on a graphane sheet by doping with Li adatoms," *Physical Chemistry Chemical Physics,* vol. 16, pp. 8100-8105, 2014.
[277] H. Tanveer, P. Puspamitra, and A. Rajeev, "Sensing propensity of a defected graphane sheet towards CO, H_2O and NO_2," *Nanotechnology,* vol. 25, p. 325501, 2014.
[278] M. J. Allen, V. C. Tung, and R. B. Kaner, "Honeycomb Carbon: A Review of Graphene," *Chemical Reviews,* vol. 110, pp. 132-145, 2010.

[279] E. H. L. Falcao and F. Wudl, "Carbon allotropes: beyond graphite and diamond," *Journal of Chemical Technology & Biotechnology,* vol. 82, pp. 524-531, 2007.
[280] H.-S. P. Wong and D. Akinwande, *Carbon nanotube and graphene device physics*. New York: Cambridge University Press, 2011.
[281] O. Leenaerts, "An ab initio study of the adsorption of atoms and molecules graphene," Ph. D. dissertation, Department of Physics, University of Antwerp Antwerp, Belgium, 2010.
[282] M. O. Goerbig, "Electronic properties of graphene in a strong magnetic field," *Reviews of Modern Physics,* vol. 83, pp. 1193-1243, 2011.
[283] S. Iijima, "Helical microtubules of graphitic carbon," *Nature,* vol. 354, pp. 56-58, 1991.
[284] R. E. Smalley, "Discovering the fullerenes," *Reviews of Modern Physics,* vol. 69, pp. 723-730, 1997.
[285] R. Peierls, "Quelques propriétés typiques des corps solides," in *Annales de l'institut Henri Poincaré*, 1935, pp. 177-222.
[286] L. Landau, "Zur Theorie der phasenumwandlungen II," *Phys. Z. Sowjetunion,* vol. 11, pp. 26-35, 1937.
[287] A. Kekulé, "Sur la constitution des substances aromatiques," *Bulletin mensuel de la Société Chimique de Paris,* vol. 3, p. 98, 1865.
[288] L. Pauling, *The nature of the chemical bond and the structure of molecules and crystals: an introduction to modern structural chemistry*, 3rd ed. New York: Cornell University Press, 1960.
[289] A. Dato, Z. Lee, K.-J. Jeon, R. Erni, V. Radmilovic, T. J. Richardson, and M. Frenklach, "Clean and highly ordered graphene synthesized in the gas phase," *Chemical Communications,* pp. 6095-6097, 2009.
[290] N. Choudhary and W. Choi, "Graphene Synthesis and Applications," in *Handbook of Carbon Nano Materials*, K. Kadish and F. D'Souza, Eds. Singapore: World Scientific, 2015, pp. 1-49.
[291] M. T. Dove, "Structure and Dynamics — An Atomic View of Materials," *Materials Today,* vol. 6, p. 59, 2003.
[292] F. Han, "Reciprocal Lattice," in *Problems in Solid State Physics with Solutions*, Singapore: World Scientific, 2012, pp. 103-122.
[293] M. S. Dresselhaus, G. Dresselhaus, and A. Jorio, *Group theory: application to the physics of condensed matter*. Heidelberg: Springer Science & Business Media, 2007.
[294] M. Masir, O. Leenaerts, B. Partoens, and F. Peeters, "Theory of the Structural, Electronic and Transport Properties of Graphene," in *2D Materials for Nanoelectronics*, M. Houssa, A. Dimoulas, and A. Molle, Eds. Florida: CRC Press, 2016, pp. 3-36.
[295] M. Machón, S. Reich, C. Thomsen, D. Sánchez-Portal, and P. Ordejón, "*Ab initio* calculations of the optical properties of 4-Å-diameter single-walled nanotubes," *Physical Review B,* vol. 66, p. 155410, 2002.
[296] P. R. Wallace, "The Band Theory of Graphite," *Physical Review,* vol. 71, pp. 622-634, 1947.
[297] S. Reich, J. Maultzsch, C. Thomsen, and P. Ordejón, "Tight-binding description of graphene," *Physical Review B,* vol. 66, p. 035412, 2002.
[298] I. Gierz, C. Riedl, U. Starke, C. R. Ast, and K. Kern, "Atomic Hole Doping of Graphene," *Nano letters,* vol. 8, pp. 4603-4607, 2008.
[299] B. N. Harmon, "Computational materials science: challenges, opportunities," *Journal of Physics: Conference Series,* vol. 16, p. 273, 2005.
[300] M. Steinhauser and S. Hiermaier, "A Review of Computational Methods in Materials Science: Examples from Shock-Wave and Polymer Physics," *International Journal of Molecular Sciences,* vol. 10, p. 5135, 2009.

[301] P. Hohenberg and W. Kohn, "Inhomogeneous Electron Gas," *Physical Review,* vol. 136, pp. B864-B871, 1964.
[302] T. van Mourik, M. Bühl, and M.-P. Gaigeot, "Density functional theory across chemistry, physics and biology," *Philosophical Transactions of the Royal Society A: Mathematical, Physical and Engineering Sciences,* vol. 372, p. 20120488, 2014.
[303] K. Burke, "Perspective on density functional theory," *The Journal of Chemical Physics,* vol. 136, p. 150901, 2012.
[304] W. Kohn and L. J. Sham, "Self-Consistent Equations Including Exchange and Correlation Effects," *Physical Review,* vol. 140, pp. A1133-A1138, 1965.
[305] R. M. Martin, *Electronic structure: basic theory and practical methods*. New York: Cambridge University Press, 2004.
[306] D. M. Ceperley and B. J. Alder, "Ground State of the Electron Gas by a Stochastic Method," *Physical Review Letters,* vol. 45, pp. 566-569, 1980.
[307] F. Tran and P. Blaha, "Accurate Band Gaps of Semiconductors and Insulators with a Semilocal Exchange-Correlation Potential," *Physical Review Letters,* vol. 102, p. 226401, 2009.
[308] J. P. Perdew and Y. Wang, "Accurate and simple analytic representation of the electron-gas correlation energy," *Physical Review B,* vol. 45, pp. 13244-13249, 1992.
[309] A. D. Becke, "Density-functional exchange-energy approximation with correct asymptotic behavior," *Physical Review A,* vol. 38, pp. 3098-3100, 1988.
[310] J. P. Perdew and K. Burke, "Comparison shopping for a gradient-corrected density functional," *International Journal of Quantum Chemistry,* vol. 57, pp. 309-319, 1996.
[311] D. R. Hamann, M. Schlüter, and C. Chiang, "Norm-Conserving Pseudopotentials," *Physical Review Letters,* vol. 43, pp. 1494-1497, 1979.
[312] D. Vanderbilt, "Soft self-consistent pseudopotentials in a generalized eigenvalue formalism," *Physical Review B,* vol. 41, pp. 7892-7895, 1990.
[313] N. Troullier and J. L. Martins, "Efficient pseudopotentials for plane-wave calculations," *Physical Review B,* vol. 43, pp. 1993-2006, 1991.
[314] X. Gonze, J. M. Beuken, R. Caracas, F. Detraux, M. Fuchs, G. M. Rignanese, L. Sindic, M. Verstraete, G. Zerah, F. Jollet, M. Torrent, A. Roy, M. Mikami, P. Ghosez, J. Y. Raty, and D. C. Allan, "First-principles computation of material properties: the ABINIT software project," *Computational Materials Science,* vol. 25, pp. 478-492, 2002.
[315] V. Milman, B. Winkler, J. A. White, C. J. Pickard, M. C. Payne, E. V. Akhmatskaya, and R. H. Nobes, "Electronic structure, properties, and phase stability of inorganic crystals: A pseudopotential plane-wave study," *International Journal of Quantum Chemistry,* vol. 77, pp. 895-910, 2000.
[316] B. Delley, "From molecules to solids with the DMol3 approach," *The Journal of Chemical Physics,* vol. 113, pp. 7756-7764, 2000.
[317] G. Paolo, B. Stefano, B. Nicola, C. Matteo, C. Roberto, C. Carlo, C. Davide, L. C. Guido, C. Matteo, D. Ismaila, C. Andrea Dal, G. Stefano de, F. Stefano, F. Guido, G. Ralph, G. Uwe, G. Christos, K. Anton, L. Michele, M.-S. Layla, M. Nicola, M. Francesco, M. Riccardo, P. Stefano, P. Alfredo, P. Lorenzo, S. Carlo, S. Sandro, S. Gabriele, P. S. Ari, S. Alexander, U. Paolo, and M. W. Renata, "QUANTUM ESPRESSO: a modular and open-source software project for quantum simulations of materials," *Journal of Physics: Condensed Matter,* vol. 21, p. 395502, 2009.
[318] J. Hafner, "Ab-initio simulations of materials using VASP: Density-functional theory and beyond," *Journal of Computational Chemistry,* vol. 29, pp. 2044-2078, 2008.
[319] X. Gonze, "A brief introduction to the ABINIT software package," *Zeitschrift für Kristallographie - Crystalline Materials* vol. 220, pp. 558-562, 2005.
[320] X. Gonze, B. Amadon, P. M. Anglade, J. M. Beuken, F. Bottin, P. Boulanger, F. Bruneval, D. Caliste, R. Caracas, M. Côté, T. Deutsch, L. Genovese, P. Ghosez, M.

Giantomassi, S. Goedecker, D. R. Hamann, P. Hermet, F. Jollet, G. Jomard, S. Leroux, M. Mancini, S. Mazevet, M. J. T. Oliveira, G. Onida, Y. Pouillon, T. Rangel, G. M. Rignanese, D. Sangalli, R. Shaltaf, M. Torrent, M. J. Verstraete, G. Zerah, and J. W. Zwanziger, "ABINIT: First-principles approach to material and nanosystem properties," *Computer Physics Communications,* vol. 180, pp. 2582-2615, 2009.

[321] X. Gonze, F. Jollet, F. Abreu Araujo, D. Adams, B. Amadon, T. Applencourt, C. Audouze, J. M. Beuken, J. Bieder, A. Bokhanchuk, E. Bousquet, F. Bruneval, D. Caliste, M. Côté, F. Dahm, F. Da Pieve, M. Delaveau, M. Di Gennaro, B. Dorado, C. Espejo, G. Geneste, L. Genovese, A. Gerossier, M. Giantomassi, Y. Gillet, D. R. Hamann, L. He, G. Jomard, J. Laflamme Janssen, S. Le Roux, A. Levitt, A. Lherbier, F. Liu, I. Lukačević, A. Martin, C. Martins, M. J. T. Oliveira, S. Poncé, Y. Pouillon, T. Rangel, G. M. Rignanese, A. H. Romero, B. Rousseau, O. Rubel, A. A. Shukri, M. Stankovski, M. Torrent, M. J. Van Setten, B. Van Troeye, M. J. Verstraete, D. Waroquiers, J. Wiktor, B. Xu, A. Zhou, and J. W. Zwanziger, "Recent developments in the ABINIT software package," *Computer Physics Communications,* vol. 205, pp. 106-131, 2016.

[322] M. Torrent, F. Jollet, F. Bottin, G. Zérah, and X. Gonze, "Implementation of the projector augmented-wave method in the ABINIT code: Application to the study of iron under pressure," *Computational Materials Science,* vol. 42, pp. 337-351, 2008.

[323] W. Z. n. A. Q. Y. Meng, "Adsorption of Methane on Pristine and Al-Doped Graphene: A Comparative Study via First-Principles Calculation," *Advanced Materials Research,* vol. 602-604, pp. 870-873, 2013.

[324] A. S. Rad and O. R. Kashani, "Adsorption of acetyl halide molecules on the surface of pristine and Al-doped graphene: Ab initio study," *Applied Surface Science,* vol. 355, pp. 233-241, 2015.

[325] S. S. Varghese, S. Swaminathan, K. K. Singh, and V. Mittal, "*Ab initio* study on gas sensing properties of group III (B, Al and Ga) doped graphene," *Computational Condensed Matter,* vol. 9, pp. 40-55, 2016.

[326] F. Tournus and J. C. Charlier, "Ab initio study of benzene adsorption on carbon nanotubes," *Physical Review B,* vol. 71, p. 165421, 2005.

[327] S. Goedecker, M. Teter, and J. Hutter, "Separable dual-space Gaussian pseudopotentials," *Physical Review B,* vol. 54, pp. 1703-1710, 1996.

[328] H. J. Monkhorst and J. D. Pack, "Special points for Brillouin-zone integrations," *Physical Review B,* vol. 13, pp. 5188-5192, 1976.

[329] H. B. Schlegel, "Optimization of equilibrium geometries and transition structures," *Journal of Computational Chemistry,* vol. 3, pp. 214-218, 1982.

[330] F. L. Hirshfeld, "Bonded-atom fragments for describing molecular charge densities," *Theoretica chimica acta,* vol. 44, pp. 129-138, 1977.

[331] M. S. Dresselhaus, G. Dresselhaus, R. Saito, and A. Jorio, "Raman spectroscopy of carbon nanotubes," *Physics Reports,* vol. 409, pp. 47-99, 2005.

[332] J. C. Slonczewski and P. R. Weiss, "Band Structure of Graphite," *Physical Review,* vol. 109, pp. 272-279, 1958.

[333] I. M. Katsnelson, "Zitterbewegung, chirality, and minimal conductivity in graphene," *The European Physical Journal B - Condensed Matter and Complex Systems,* vol. 51, pp. 157-160, 2006.

[334] D. R. Lide, "CRC Handbook of Chemistry and Physics, 81st ed. Boca Raton, FL: CRC Press, 2000.

[335] J. B. Hasted, "Liquid Water: Dielectric Properties," in *The Physics and Physical Chemistry of Water*, F. Franks, Ed. Boston, MA: Springer, 1972, pp. 255-309.

[336] A. G. Garcia, S. E. Baltazar, A. H. R. Castro, J. F. P. Robles, and A. Rubio, "Influence of S and P Doping in a Graphene Sheet," *Journal of Computational and Theoretical Nanoscience,* vol. 5, pp. 2221-2229, 2008.

[337] National Center for Biotechnology Information. PubChem Compound Database; CID=402, https://pubchem.ncbi.nlm.nih.gov/compound/402 (accessed Jan. 7, 2017).
[338] D. C. Glass, "A review of the health effects of hydrogen sulphide exposure," *Annals of Occupational Hygiene,* vol. 34, pp. 323-327, 1990.
[339] T. W. Lambert, V. M. Goodwin, D. Stefani, and L. Strosher, "Hydrogen sulfide (H_2S) and sour gas effects on the eye. A historical perspective," *Science of The Total Environment,* vol. 367, pp. 1-22, 2006.
[340] B. Doujaiji and J. A. Al-Tawfiq, "Hydrogen sulfide exposure in an adult male," *Annals Saudi Medicine,* vol. 30, pp. 76-80, 2010.
[341] D. Wei, Y. Liu, Y. Wang, H. Zhang, L. Huang, and G. Yu, "Synthesis of N-Doped Graphene by Chemical Vapor Deposition and Its Electrical Properties," *Nano letters,* vol. 9, pp. 1752-1758, 2009.
[342] Z. Jin, J. Yao, C. Kittrell, and J. M. Tour, "Large-Scale Growth and Characterizations of Nitrogen-Doped Monolayer Graphene Sheets," *ACS Nano,* vol. 5, pp. 4112-4117, 2011.
[343] R. Lv, Q. Li, A. R. Botello-Méndez, T. Hayashi, B. Wang, A. Berkdemir, Q. Hao, A. L. Elías, R. Cruz-Silva, H. R. Gutiérrez, Y. A. Kim, H. Muramatsu, J. Zhu, M. Endo, H. Terrones, J.-C. Charlier, M. Pan, and M. Terrones, "Nitrogen-doped graphene: beyond single substitution and enhanced molecular sensing," *Scientific Reports,* vol. 2, p. 586, 2012.
[344] Z. Wang, P. Li, Y. Chen, J. Liu, H. Tian, J. Zhou, W. Zhang, and Y. Li, "Synthesis of nitrogen-doped graphene by chemical vapour deposition using melamine as the sole solid source of carbon and nitrogen," *Journal of Materials Chemistry C,* vol. 2, pp. 7396-7401, 2014.
[345] Y.-B. Tang, L.-C. Yin, Y. Yang, X.-H. Bo, Y.-L. Cao, H.-E. Wang, W.-J. Zhang, I. Bello, S.-T. Lee, H.-M. Cheng, and C.-S. Lee, "Tunable Band Gaps and p-Type Transport Properties of Boron-Doped Graphenes by Controllable Ion Doping Using Reactive Microwave Plasma," *ACS Nano,* vol. 6, pp. 1970-1978, 2012.
[346] H. Wang, Y. Zhou, D. Wu, L. Liao, S. Zhao, H. Peng, and Z. Liu, "Synthesis of Boron-Doped Graphene Monolayers Using the Sole Solid Feedstock by Chemical Vapor Deposition," *Small,* vol. 9, pp. 1316-1320, 2013.
[347] S. Agnoli and M. Favaro, "Doping graphene with boron: a review of synthesis methods, physicochemical characterization, and emerging applications," *Journal of Materials Chemistry A,* vol. 4, pp. 5002-5025, 2016.
[348] J. Zhang, J. Li, Z. Wang, X. Wang, W. Feng, W. Zheng, W. Cao, and P. Hu, "Low-Temperature Growth of Large-Area Heteroatom-Doped Graphene Film," *Chemistry of Materials,* vol. 26, pp. 2460-2466, 2014.
[349] R. Lv, M. C. dos Santos, C. Antonelli, S. Feng, K. Fujisawa, A. Berkdemir, R. Cruz-Silva, A. L. Elías, N. Perea-Lopez, F. López-Urías, H. Terrones, and M. Terrones, "Large-Area Si-Doped Graphene: Controllable Synthesis and Enhanced Molecular Sensing," *Advanced Materials,* vol. 26, pp. 7593-7599, 2014.
[350] Z. Wang, P. Li, Y. Chen, J. Liu, W. Zhang, Z. Guo, M. Dong, and Y. Li, "Synthesis, characterization and electrical properties of silicon-doped graphene films," *Journal of Materials Chemistry C,* vol. 3, pp. 6301-6306, 2015.
[351] G. Hui, L. Zheng, S. Li, G. Wenhua, G. Wei, C. Lijie, R. Amrita, Q. Weijin, V. Robert, and M. A. Pulickel, "Synthesis of S-doped graphene by liquid precursor," *Nanotechnology,* vol. 23, p. 275605, 2012.
[352] F. Hassani, H. Tavakol, F. Keshavarzipour, and A. Javaheri, "A simple synthesis of sulfur-doped graphene using sulfur powder by chemical vapor deposition," *RSC Advances,* vol. 6, pp. 27158-27163, 2016.

[353] D.-W. Shin, T. S. Kim, and J.-B. Yoo, "Phosphorus doped graphene by inductively coupled plasma and triphenylphosphine treatments," *Materials Research Bulletin,* vol. 82, pp. 71-75, 2016.
[354] O. Faye, A. Raj, V. Mittal, and A. C. Beye, "H_2S adsorption on graphene in the presence of sulfur: A density functional theory study," *Computational Materials Science,* vol. 117, pp. 110-119, 2016.
[355] D. J. Wuebbles, "Nitrous Oxide: No Laughing Matter," *Science,* vol. 326, pp. 56-57, 2009.
[356] J. C. Kramlich and W. P. Linak, "Nitrous oxide behavior in the atmosphere, and in combustion and industrial systems," *Progress in Energy and Combustion Science,* vol. 20, pp. 149-202, 1994.
[357] P. Forster, V. Ramaswamy, P. Artaxo, T. Berntsen, R. Betts, D. W. Fahey, J. Haywood, J. Lean, D. C. Lowe, G. Myhre, J. Nganga, R. Prinn, G. Raga, M. Schultz, and R. Van Dorland, "Changes in atmospheric constituents and in radiative forcing," Cambridge University Press, Cambridge, United Kingdom, 2007.
[358] A. R. Ravishankara, J. S. Daniel, and R. W. Portmann, "Nitrous Oxide (N_2O): The Dominant Ozone-Depleting Substance Emitted in the 21st Century," *Science,* vol. 326, pp. 123-125, 2009.
[359] J. Pérez-Ramírez, "Prospects of N_2O emission regulations in the European fertilizer industry," *Applied Catalysis B: Environmental,* vol. 70, pp. 31-35, 2007.
[360] T. D. Rapson and H. Dacres, "Analytical techniques for measuring nitrous oxide," *TrAC Trends in Analytical Chemistry,* vol. 54, pp. 65-74, 2014.
[361] J. P. Perdew, K. Burke, and M. Ernzerhof, "Generalized Gradient Approximation Made Simple," *Physical Review Letters,* vol. 77, pp. 3865-3868, 1996.
[362] J. Thakur, H. S. Saini, and M. K. Kashyap, "Electronic and magnetic properties of Cr doped graphene; Full potential approach," *AIP Conference Proceedings,* vol. 1675, p. 030032, 2015.
[363] J. C. Charlier, J. P. Michenaud, X. Gonze, and J. P. Vigneron, "Tight-binding model for the electronic properties of simple hexagonal graphite," *Physical Review B,* vol. 44, pp. 13237-13249, 1991.
[364] Z.-S. Wu, W. Ren, L. Xu, F. Li, and H.-M. Cheng, "Doped Graphene Sheets As Anode Materials with Superhigh Rate and Large Capacity for Lithium Ion Batteries," *ACS Nano,* vol. 5, pp. 5463-5471, 2011.
[365] C. Ma, X. Shao, and D. Cao, "Nitrogen-doped graphene nanosheets as anode materials for lithium ion batteries: a first-principles study," *Journal of Materials Chemistry,* vol. 22, pp. 8911-8915, 2012.
[366] H. Fang, C. Yu, T. Ma, and J. Qiu, "Boron-doped graphene as a high-efficiency counter electrode for dye-sensitized solar cells," *Chemical Communications,* vol. 50, pp. 3328-3330, 2014.
[367] S. Gadipelli and Z. X. Guo, "Graphene-based materials: Synthesis and gas sorption, storage and separation," *Progress in Materials Science,* vol. 69, pp. 1-60, 2015.
[368] K. C. Kemp, V. Chandra, M. Saleh, and K. S. Kim, "Reversible CO_2 adsorption by an activated nitrogen doped graphene/polyaniline material," *Nanotechnology,* vol. 24, p. 235703, 2013.
[369] Y. G. Zhou, X. T. Zu, F. Gao, J. L. Nie, and H. Y. Xiao, "Adsorption of hydrogen on boron-doped graphene: A first-principles prediction," *Journal of Applied Physics,* vol. 105, p. 014309, 2009.
[370] L. S. Panchakarla, A. Govindaraj, and C. N. R. Rao, "Boron- and nitrogen-doped carbon nanotubes and graphene," *Inorganica Chimica Acta,* vol. 363, pp. 4163-4174, 2010.

[371] Y. Fujimoto, "Formation, Energetics, and Electronic Properties of Graphene Monolayer and Bilayer Doped with Heteroatoms," *Advances in Condensed Matter Physics,* vol. 2015, Article ID 571490, 14 pages, 2015.
[372] S. Varghese, S. Swaminathan, K. Singh, and V. Mittal, "Energetic Stabilities, Structural and Electronic Properties of Monolayer Graphene Doped with Boron and Nitrogen Atoms," *Electronics,* vol. 5, p. 91, 2016.

LIST OF PUBLICATIONS AND PRESENTATIONS

Journal Articles

1. **Seba Sara Varghese**, Sundaram Swaminathan, Krishna Kumar Singh, Vikas Mittal, "Energetic Stabilities, Structural and Electronic Properties of Monolayer Graphene doped with Boron and Nitrogen Atoms," *Electronics*, vol. 5, p. 91, 2016.
2. **Seba Sara Varghese,** Sundaram Swaminathan, Krishna Kumar Singh, Vikas Mittal, "*Ab initio* study on gas sensing properties of group III (B, Al, Ga) doped graphene," *Computational Condensed Matter*, vol. 9, pp. 40-55, 2016.
3. **Seba Sara Varghese**, Saino Hanna Varghese, Sundaram Swaminathan, Krishna Kumar Singh, Vikas Mittal, "Two-Dimensional Materials for Sensing: Graphene and Beyond," *Electronics*, vol. 4, pp. 651-687, 2015.
4. **Seba S. Varghese**, Sunil Lonkar, K. K. Singh, Sundaram Swaminathan, Ahmed Abdala, "Recent advances in graphene based gas sensors," *Sensors and Actuators B: Chemical*, vol. 218, pp. 160-183, 2015.

Book Chapters

1. **Seba Sara Varghese**, Sundaram Swaminathan, Krishna Kumar Singh, Vikas Mittal "Gas molecular adsorption on graphene: Implications for gas sensing applications" (Submitted to Petroleum Institute).
2. **Seba Sara Varghese**, Sundaram Swaminathan, Krishna Kumar Singh, Vikas Mittal "DFT based investigation of N_2O adsorption on graphene and heteroatom-doped graphene" (Submitted to Petroleum Institute).

Conference Articles and Abstracts

1. **Seba Sara Varghese**, Sundaram Swaminathan, K K Singh, Vikas Mittal, "DFT based simulation of H_2S gas sensing properties of doped graphene," in *8th International Conference on Nanotechnology: Fundamentals and Applications (ICNFA' 2017)*, Rome, Italy, June 2017 (Accepted for presentation).
2. **Seba Sara Varghese**, Sundaram Swaminathan, K K Singh, Vikas Mittal, "Molecular Oxygen Adsorbed on Gallium Doped Graphene: A First-Principles Study," in *5th International Conference on Material Science and Engineering Technology (ICMSET 2016),* Tokyo, Japan, October 2016 (Accepted for publication in Materials Science Forum, Trans Tech Publications, Switzerland, ISSN: 1662-9752).

3. **Seba Sara Varghese**, Sundaram Swaminathan, K K Singh, Vikas Mittal, "*Ab initio* study of H_2S adsorption on graphene doped with P and S," *Journal of Nanomedicine & Nanotechnology,* 2016, 7 (2), P. 42.
4. **Seba Sara Varghese**, Akshay Moudgil, K.K. Singh, Sundaram Swaminathan, Vikas Mittal, "Adsorption of O_2 and N_2O on Phosphorus and Gallium doped graphene: A first-principles study," *in 4th NanoToday Conference*, Dubai, United Arab Emirates, December 2015, P4-13.
5. **Seba Sara Varghese**, Kiran Menon, Sreesha Damodar, K. K. Singh, Neeru Sood, Sundaram Swaminathan, "Graphene: A Promising platform for bio-sensing applications," in *4th Annual International Conference on Advances in Biotechnology (BioTech 2014)*, Dubai, United Arab Emirates, March 2014, pp. 74-80.

BRIEF BIOGRAPHY OF THE CANDIDATE

Name of the Candidate	Seba Sara Varghese
Contact Information	Mob: +971552578505 Email: p2012001@dubai.bits-pilani.ac.in; sebavarghese@gmail.com
Qualification	M. E. Microelectronics from BITS, Pilani-Dubai Campus, Dubai, United Arab Emirates (2012) B. Tech. Electrical and Electronics Engineering from Cochin University of Science and Technology, Kerala, India (2008)
Research Areas	Graphene based gas sensors, Carbon nanotubes, two-dimensional materials for electronics and sensing, Microelectromechanical systems and nanotechnology, Computational quantum mechanics
Work experience (years)	3 years 6 months
Number of publications	12 - 4 peer-reviewed journals - 3 book chapters (under review) - 8 conference proceedings

BRIEF BIOGRAPHY OF THE SUPERVISOR

Name of the Supervisor	Dr. Sundaram Swaminathan
Present Designation and Address	Pro Vice Chancellor DIT University, Dehradun Mussoorie link road Dehradun 248009, India Phone: +917055219111 Fax:+911353000309 Email: pvc@dituniversity.edu.in
Qualification	Ph.D.
Areas of research	Nanosensors, MEMS/NEMS, Graphene
Work experience (Years)	40
Number of publications	111
Number of Ph. D. students supervised	2

BRIEF BIOGRAPHY OF THE CO-SUPERVISOR

Name of the Supervisor	Dr. K. K. Singh
Present Designation and Address	Professor, Department of Physics BITS Pilani Dubai Campus DIAC, Dubai, UAE Phone:009712753700 Fax: 0097144200844 Email: singh@dubai.bits-pilani.ac.in
Qualification	Ph. D.
Areas of research	Graphene based Gas Sensors, Carbon Nano tube, Micro electromechanical Systems and Nanotechnology
Work experience (Years)	18
Number of publications	25
Number of Ph. D. students supervised	Nil